Dark Matter Distributions in Early-type Galaxies from Strong Gravitational Lensing

Thomas Martin Eichner

Dark Matter Distributions in Early-type Galaxies from Strong Gravitational Lensing

Thomas Martin Eichner

Dissertation der Fakultät für Physik
Dissertation of the Faculty of Physics

der Ludwig-Maximilians-Universität München
at the Ludwig Maximilian University of Munich

für den Grad des
for the degree of

Doctor rerum naturalium

vorgelegt von Thomas Martin Eichner
presented by

aus Erding
from

München, 2013

Zusammenfassung

Dunkle Materie macht einen Großteil der Masse von elliptischen Galaxien aus. Jedoch sind die genaue Menge und die räumliche Verteilung dieser dunklen Materie noch unklar. Ferner schrumpfen Galaxien in einer dichten Umgebung, wie sie in Zentren von Galaxienhaufen zu finden ist, da die äußeren Teile ihrer dunklen Materie Halos abgelöst werden. Das Ziel dieser Arbeit ist es, den Anteil dunkler Materie im Zentrum und den Außenbereichen elliptischer Galaxien mit Hilfe des von ihnen verursachten starken Gravitationslinseneffekts zu messen. Gravitationslinsen sind gut geeignet für die Untersuchung dunkler Materie, da sie auf alle Arten von Materie reagieren, ungeachtet ihres dynamischen oder evolutionären Zustandes. Wir stellen Untersuchungen der durch die Sloan Lens ACS Studie entdeckten außergewöhnlichen Gravitationslinsen SDSS J1538+5817 und SDSS J1430+4105 vor. Als Linsen dienen elliptische Galaxien bei Rotverschiebungen $z_l = 0.143$ bzw. $z_l = 0.285$. Für SDSS J1538+5817 zeigen wir, daß beide Quellen die gleiche Rotverschiebung $z_s = 0.531$ haben. Die Mehrfachbilder überdecken einen Bereich von 1 kpc bis 4 kpc in der Linsenebene. Für SDSS J1430+4105 ist die Quelle bei einer Rotverschiebung $z_s = 0.575$ in einen ausgedehnten Einsteinring gelinst, der einen radialen Bereich von 4 kpc bis 10 kpc in der Linsenebene abdeckt. In beiden Fällen können die gelinsten Bilder mit verschiedenen Modelansätzen übereinstimmend reproduziert werden. Wir erhalten für SDSS J1538+5817 eine projizierte Gesamtmasse von $8.11^{+0.27}_{-0.59} \times 10^{10}\ M_\odot$ innerhalb des Einsteinradius von 2.5 kpc, für SDSS J1430+4105 erhalten wir $5.37 \pm 0.06 \times 10^{11} M_\odot$ innerhalb von 6.5 kpc. Die leuchtende und dunkle Materie werden getrennt modelliert, woraus Anteile an dunkler Materie von $0.1^{+0.2}_{-0.1}$ bzw. $0.40^{+0.14}_{-0.10}$ innerhalb des Einsteinradius folgen. Wir nehmen ein De Vaucouleurs–Profil für die Lichtverteilung in jeder der beiden Galaxien an. Aus der stellaren Masse, die mit dieser Lichtverteilung verbunden ist, können wir ein Masse–zu–Leuchtkraft–Verhältnis von $\frac{M_{\mathrm{deVauc}}}{L_B} \approx (5.5 \pm 1.5)\, \frac{M_\odot}{L_{\odot,B}}$ für SDSS J1430+4105 bestimmen. Ähnliche Ergebnisse erhalten wir für das zentrale Masse–zu–Leuchtkraft–Verhältnis von SDSS J1538+5817. Ein Vergleich dieser Masse–zu–Leuchtkraft–Verhältnisse mit denjenigen, welche photometrisch bestimmt werden, zeigt die beste Übereinstimmung bei Verwendung der Salpeter IMF. Außergewöhnliche Gravitationslinsensysteme wie die hier untersuchten mit einem Ansatz aus zwei Komponenten zu modellieren, verbessert deshalb unser Verständnis der Eigenschaften der zentralen dunklen und leuchtenden Materie. Weiterhin wird die dunkle Materie auf mittleren Skalen um elliptische Galaxien in einem Galaxienhaufen untersucht. Mit dem Galaxienhaufen MACSJ1206.2-0847 wird der seltene Fall einer Hintergrundquelle untersucht, die zu einem Arc gelinst und zusätzlich von einigen benachbarten Galaxien verzerrt wird. Diese Verzerrungen erlauben uns die Gesamtmassenverteilung dieser benachbarten Galaxien auf größeren als den üblicherweise mit starken Gravitationslinsen oder Dynamik-Studien zugänglichen Skalen zu bestimmen. Wir beschreiben den Galaxienhaufen mit einem elliptischen NFW–Profil und die Galaxien mit zwei Parametern für die zentrale Masse und Ausdehnung einer Referenzgalaxie. Basierend auf dem beobachteten Nah–Infrarotlicht werden Skalierungsrelationen zwischen dieser Referenzgalaxie und den übrigen Haufengalaxien angenommen. Die Positionen der beobachteten gelinsten Abbildungen von 12 mehrfach abgebildeten Hintergrundgalaxien können mit einer mittleren Abweichung von $0.85''$ reproduziert werden. Darauf aufbauend kann die Flächenhelligkeit des Arcs und seines Gegenbildes mit erstaunlicher Genauigkeit rekonstruiert werden. Die Längenskala für die bestmögliche Bestimmung der eingeschlossenen Galaxienhalomasse beträgt etwa 5 Effektivradien. Die Geschwindigkeitsdispersion und Größe eines Halos mit Helligkeiten $m_{\mathrm{AB},160W} = 19.2$ und $M_{B,\mathrm{Vega}} = -20.7$ betragen $\sigma = 150 \mathrm{kms}^{-1}$ und $r \approx 26 \pm 6 \mathrm{kpc}$. Die in dieser Arbeit durchgeführte Auswertung kann auf andere ähnliche Fälle ausgeweitet werden. Damit wird die Lücke zwischen Ergebnissen geschlossen, welche einerseits auf starken Gravitationslinsen und dynamischen Methoden auf kürzeren Skalen und andererseits auf schwachen Gravitationslinsen auf längeren Skalen basieren.

Abstract

Dark matter constitutes a large fraction of the mass of early–type galaxies. However, the exact amountand spatial distribution of the dark matter, especially in the galaxies' center is still unclear. Furthermore, galaxies in dense environments such as the centers of galaxy clusters shrink in size, since parts of their outer dark matter halo is stripped away. The aim of this thesis is to measure the dark matter content in the centers and outskirts of elliptical galaxies by analyzing the strong gravitational lensing effect they produce. Gravitational lensing is well–suited for investigating dark matter, since it is sensitive to all forms of matter, regardless of its dynamical or evolutionary state.

We present gravitational lensing studies of the exceptional strong lensing systems SDSS J1538+5817 and SDSS J1430+4105, identified by the Sloan Lens ACS survey. The lenses are elliptical galaxies at $z_l = 0.143$ and $z_l = 0.285$, respectively. For SDSS J1538+5817 we show that both multiple imaged sources are located at the same redshift $z_s = 0.531$. Its multiple images span a range from 1 to 4 kpc in the plane of the lens. For SDSS J1430+4105, the source at redshift $z_s = 0.575$ is imaged into a broad Einstein ring, covering radii from $4\,\mathrm{kpc}$ to $10\,\mathrm{kpc}$ in the plane of the lens. In both cases, the lensed images can be accurately and consistently reproduced with different modeling approaches. We get projected total masses of $8.11^{+0.27}_{-0.59} \times 10^{10}\,M_\odot$ within the Einstein radius of 2.5 kpc for SDSS J1538+5817 and $5.37 \pm 0.06 \times 10^{11} M_\odot$ within 6.5 kpc for SDSS J1430+4105. The luminous and dark matter were traced separately, resulting in dark matter fractions within the Einstein radius of $0.1^{+0.2}_{-0.1}$ and $0.40^{+0.14}_{-0.10}$ for SDSS J1538+5817 and SDSS J1430+4105, respectively. We assume a de Vaucouleurs profile to trace the light distribution of both galaxies. From the stellar mass associated with this light, we can explicitly derive a stellar mass–to–light ratio of $\frac{M_{\mathrm{deVauc}}}{L_B} \approx (5.5 \pm 1.5) \frac{M_\odot}{L_{\odot,B}}$ in the case of SDSS J1430+4105. Similar results are obtained for the central mass–to–light ratio of SDSS J1538+5817. Comparing these mass–to–light ratios with photometric estimates for the mass–to–light ratios shows the best agreement with a Salpeter IMF. Modeling extraordinary systems like SDSS J1538+5817 or SDSS J1430+4105 using a two–component approach leads to a better understanding of galaxies' central dark and luminous matter properties.

We also study dark matter on intermediate scales around elliptical galaxies embedded in a cluster environment. In the galaxy cluster MACSJ1206.2-0847, we describe the rare case of a background source lensed into a giant gravitational arc and additionally distorted by several nearby cluster galaxies. These distortions allow us to constrain the total matter distribution of these galaxies beyond regions normally accessible by strong lensing or dynamical studies. We model the cluster mass distribution with an elliptical NFW profile and the cluster galaxies with two parameters for the central mass and extent of a reference halo. We assume scaling relations from the reference halo to the other member galaxies based on their observed NIR-light. We can match the observed lensed positions of 12 multiply lensed background objects at an r.m.s. level of $0.85''$, and can reconstruct the surface brightness distribution of the giant arc and its counterimage to an amazing accuracy. We find the length scale where the enclosed galaxy halo mass is best constrained to be at about 5 effective radii. The velocity dispersion and halo size of a galaxy with $m_{\mathrm{AB,160W}} = 19.2$ or $M_{\mathrm{B,Vega}} = -20.7$ are $\sigma = 150\mathrm{kms}^{-1}$ and $r \approx 26 \pm 6\mathrm{kpc}$. The analysis carried out in this work can be extended to other cases similar to MACSJ1206.2-0847, which constitute ideal objects for the study of total matter distributions of galaxies at intermediate scales. This closes the gap between strong lensing and dynamical studies on shorter scales and weak lensing studies on longer scales.

Contents

List of Figures

List of Tables

Chapter 1

Introduction

When we observe the night sky – with or without telescopes – we see a large variety of different structures: from individual asteroids with diameters over 100 meters, moons, planets, stars, star clusters, and galaxies, to galaxy groups and even clusters of galaxies with sizes of the order of 10^{23} meters. However, all we can directly observe is the electromagnetic radiation emitted, reflected or absorbed by the baryonic components of these objects. All these structures, however, form only less the 5% of the energy content of the universe (Komatsu et al., 2011; Larson et al., 2011). The rest of the universe is filled with two components termed dark matter and dark energy – thus named because as yet we do not have a better description of their nature. Dark matter and dark energy make up approximately 22% and 73% of the universes' current energy content, see Fig. 1.1. Here, a qualitative summary of the framework of the thesis will be given, followed by a more detailed overview in the next chapters.

The dark universe

Dark matter, being approximately 5 times more abundant than baryonic matter, is – almost hundred years after its discovery – still a puzzle to us. We know some of its properties – such as that it interacts gravitationally and exists around all galaxies – and can derive some implications from that, for example how it clumps and forms invisible halos around galaxies, groups, and clusters of galaxies (e.g. Blumenthal et al. 1984, Davis et al. 1985, Kaiser & Squires 1993, Navarro et al. 1997, Clowe et al. 2004), that it formed the first potential wells or that it bends light the same way as barionic matter. Despite that, we still lack a definite answer about its constituents, despite dedicated searches (e.g. Bravin et al. 1999; Bernabei et al. 2004; Sanglard et al. 2005; EDELWEISS Collaboration et al. 2011). Dark matter itself was proposed the first time by Fritz Zwicky in the 1930s to explain how the Coma Cluster can be gravitationally bound despite its large peculiar motions (Zwicky, 1933). After that, dark matter again gained some attention in the 1970s, when Rubin and Ford published their measured rotation curve of M31, showing that it was flat on the outskirts although a decline would be expected according to its light profile (Rubin & Ford, 1970). In 1978, dark matter was also used to explain the mass of the Virgo cluster measured from X-ray observations (Mathews, 1978). Other studies also in the 1970s and earlier confirmed the reality of dark matter, e.g. Kahn & Woltjer (1959), Ostriker & Peebles (1973). Thus, at the beginning of the 1980s most astronomers believed in the existence of dark matter, although they did not have unambiguous evidence of its nature. That dark matter was composed of light, relativistic neutrinos was proposed (e.g. Doroshkevich et al. (1981)) but was soon ruled out by observing
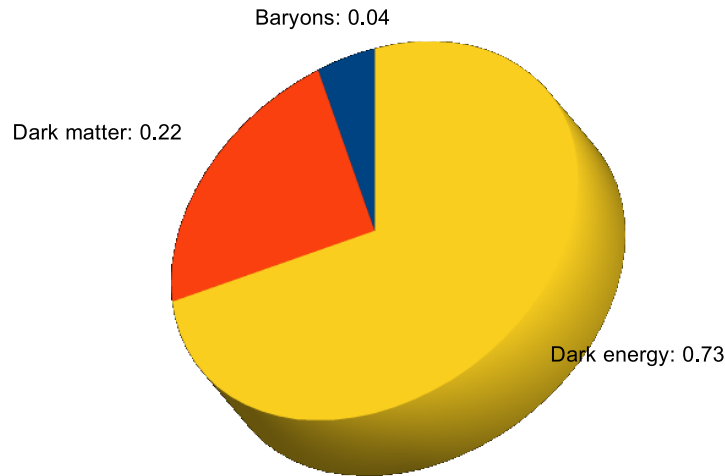
Figure 1.1: The energy content of the universe today as found by Komatsu et al. (2011); Larson et al. (2011).

and predicting the galaxy clustering in the universe (e.g. White et al. (1983)), confirming that a substantial part of dark matter is cold dark matter. Here, cold means that the kinetic energy of the dark matter particles is small compared to the rest energy at the time matter decoupled from radiation, therefore the individual dark matter particles have velocities much smaller than the speed of light. The idea of dark matter being (mainly) composed of compact, massive $M \sim M_\odot$ objects (so called MACHOs) rather than smoothly distributed elementary particles is ruled out by observations (Alcock et al., 2000; Riffeser et al., 2008). This leads to the currently most widely accepted view of dark matter as (predominantly) cold, dark and smoothly distributed. Prior to the discovery of dark energy in 1998, this cold dark matter (CDM) component was considered to dominate the energy content of today's universe.

The history of dark energy, however, is somewhat longer than that. The two starting points are: the discovery of the expansion of the universe by E. Hubble 1929 (Hubble, 1929) and, even earlier, the introduction of the constant Λ in the field equations, see Einstein (1916, 1917). While Einstein introduced Λ to balance gravity and prevent a static universe from collapsing due to its own gravitational attraction, Hubble observed that objects further away from us tend to recess with increasing speed, allowing the universe to be non–static, hence making Λ appear dispensable. Until the detection of acceleration of the expansion of the universe by the High–z Supernova Search Team and the Supernova Cosmology Project(SCP) (Riess et al., 1998; Perlmutter et al., 1998) in 1998, different models for the energy content of the universe and the curvature of spacetime existed. To explain the accelerated expansion, some term was needed in the field equations of the universe that drives it apart, hence Λ was revived and termed the dark energy parameter or cosmological constant. We have as yet no definite knowledge about its nature or even know whether Λ is indeed constant in time. Nonetheless this dark energy must be the dominant energy component in today's universe. Thus, at this point in time, the most accepted picture of the universe is a ΛCDM model with

a dominant dark energy component. Unfortunately, we lack a clear picture of the nature of these dark components. One way ascertain the nature of these dark components of the universe is to measure their properties. E.g. the dark matter density profiles, the distribution of matter on different mass scales, the spatial clustering of structures and the development of these properties over time are some of the probes used nowadays. Another successful probe used is the temperature fluctuation of the Cosmic Microwave Background (CMB), for example measured by the Wilkinson Microwave Anisotropy Probe (WMAP) (Komatsu et al., 2011; Larson et al., 2011). To further our knowledge of the dark components of the universe, we can compare predictions of the above described properties for different physical models of the dark components with observations so as to find the models that best describe the observations.

Gravitational lensing

Although we only see 5% of the energy content of today's universe directly, we can still observe the other 95 % by its influence on the visible, baryonic matter or by its influence on light itself. The dynamics of celestial objects, e.g. stars in galaxies or galaxies in galaxy clusters is influenced by the presence of dark matter, allowing us to determine the dark matter profiles of galaxies and clusters of galaxies. For example, the motion of stars in a galaxy is determined by the gravitational potential of this galaxy, hence the dark matter distribution is imprinted on the motion of the stars, (e.g. Bacon et al. 2001, Cappellari et al. 2011).

Another way of measuring the dark components of the universe is by measuring their influence on the propagation of light itself. The accelerated expansion of the universe was discovered by comparing the redshift and dimming of distant supernovae.

This thesis, however, focuses on another powerful physical effect: the deflection of light by matter present around its propagation path is independent of this matter's baryonic or dark nature. Therefore, this effect is particularly useful for investigating the dark matter component. The effect was described correctly for the first time in the framework of general relativity, (Einstein, 1916, 1922):

$$\alpha(\mathrm{R}) = \frac{4\mathrm{GM}}{\mathrm{c}^2\mathrm{R}} \quad ,$$

with α being the deflection angle of light passing a mass M at a radius R in the weak–field limit. However, the idea of light being deflected when passing a mass is more than a century older. For short reviews of the history of gravitational lensing, see e.g. Wambsganss (1998), Sauer (2010). Although the idea that distant galaxies could act as gravitational lenses was proposed as early at 1937 (Zwicky, 1937a,b), it took more than 40 years until the first extragalactic lens was discovered: The first observed multiple imaged background source was the distant quasar Q0957+561 identified by Walsh, Carswell and Weymann in 1979 as a double image of one quasar, lensed by a galaxy along our line of sight (Walsh et al., 1979). However, it was several years before the first gravitational arcs – highly distorted images of background galaxies by foreground lenses – were observed (Lynds & Petrosian, 1986; Soucail et al., 1987), although interestingly Soucail et al. considered the arc in Abell 370 to be more likely a star formation region in the cluster in their publication. This arc is shown in Fig. 1.2.

Since then, gravitational lensing has developed into a useful tool for investigating mass distribution in galaxies and galaxy clusters. The strong gravitational lensing effect in the centers of galaxies or clusters of galaxies – meaning that one background source is imaged multiple times – can be used to study total mass distributions in these inner regions. In the outer
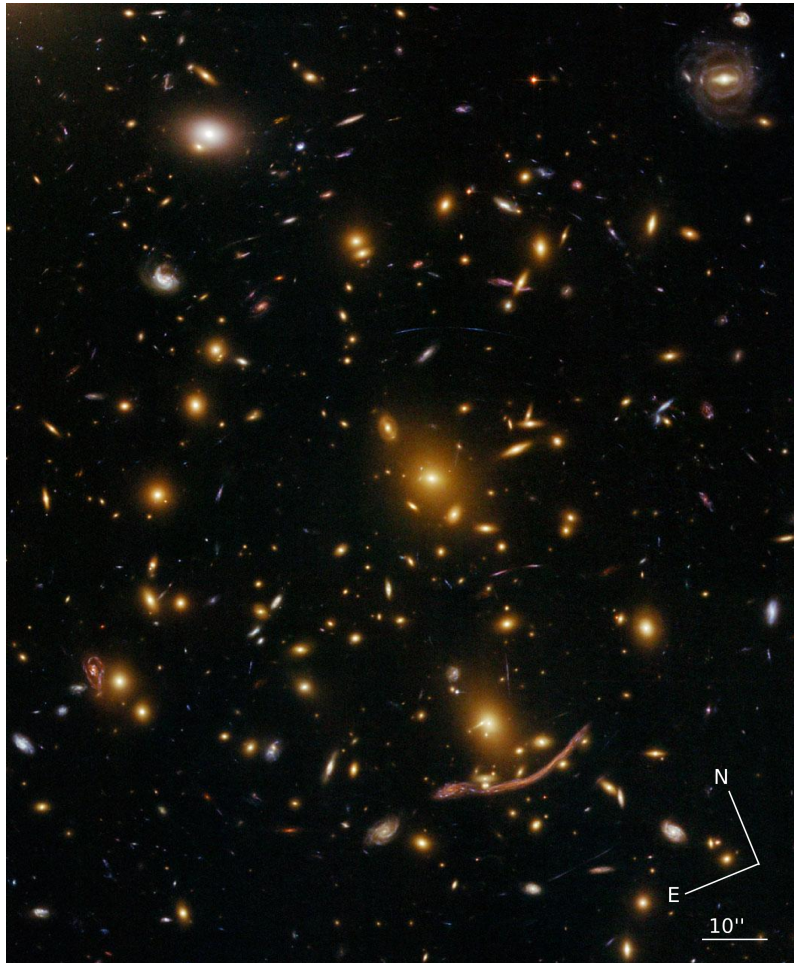
Figure 1.2: A color image of the galaxy cluster Abell 370 located at Ra:02h39m50.5s Dec:-01d35m08s with a redshift of $z = 0.375$, composed of the filters F435W, F625W and F814W, centered at wavelengths of 4297Å, 6318Å and 8333Å, respectively. The giant arc visible in this image was the first detected arc. At the redshift of the cluster, $1'' = 5.13\,\text{kpc}$. Credit: NASA, ESA, the Hubble SM4 ERO Team, and ST-ECF.

regions weak gravitational lensing – measuring only small distortions imprinted on the shapes of background objects which are detected statistically – can be used to study the mass distributions there. Large surveys aim to observe a statistical relevant number of clusters of galaxies so as to increase our knowledge about clusters, e.g. LoCuSS (Zhang et al., 2008) or CLASH (Postman et al., 2012). MACSJ1206.2-0847, which is studied in detail in Chapter 7, is part of the CLASH survey.

As previously mentioned, individual galaxies can also act as gravitational lenses. Since the typical image separation due to galaxy–scale lenses in the strong lensing regime is about $1''$, high resolution images are needed to identify and investigate this effect. This technique is mostly used to derive properties about the lensing galaxies itself (e.g. Bolton et al. 2004, 2006; Belokurov et al. 2007; Smail et al. 2007; Suyu et al. 2009; Suyu & Halkola 2010), especially about its baryonic and dark matter distribution. However, it can also be used to investigate cosmology (Suyu et al., 2010a; Grillo et al., 2008b; Jullo et al., 2010), e.g. to investigate the expansion rate of the universe. Surveys have been carried out in order to find galaxy scale lenses, such as the CASTLe Survey[1] aimed at imaging all known strong gravitational lensing systems on galaxy scales from space so as to provide high resolution images in order to obtain properties of the lens galaxies as well as to learn something about the expansion rate of the universe. The survey collected more than 100 galaxy scale gravitational lensing systems so far. Another survey that should be mentioned here is the SLACS survey[2] (Bolton et al., 2006). It collected approximately 100 lensing systems found in the spectra of the Sloan digital sky survey[3]. SDSS J1538+5817 and SDSS J1430+4105, which are studied in detail as part of this thesis, are part of this survey.

Elliptical galaxies

Elliptical galaxies are, in terms of numbers of galaxies, only a minor member of the family of galaxy types. However, they host the largest fraction of baryonic mass (Fukugita et al., 1998; Bell et al., 2003; Renzini, 2006). Their most striking feature, which is responsible for their name, is the elliptical shape of isophotes (contours of constant surface brightness). In reality this is not entirely true. For example, Bender et al. (1988) measure the shapes of 69 bright elliptical galaxies and find small (disk–like or box–like) deviations from the pure elliptical forms, as well as small twists of the major axis and changes in the ellipticities. However, we stick with this simple approximation of the form. The radial distribution in these galaxies is well-described by a so called de Vaucouleurs profile (de Vaucouleurs, 1948). The light emitted by elliptical galaxies is dominated by wavelength larger than $4000\mathring{A}$, hence these galaxies appear red in the visible spectrum. (e.g. Peletier et al. 1990), pointing to an older stellar population (Thomas et al., 2005). Consequently, elliptical galaxies (or their progenitors) must have existed for long times, making them very interesting objects. Furthermore, elliptical galaxies dominate in dense environments (Dressler, 1980; Bamford et al., 2009) hence, the environment must influence the evolution of (elliptical) galaxies. There are indications that elliptical galaxies are the results of dissipationless mergers of progenitor galaxies (Lacey & Cole, 1993; Baugh et al., 1996). A summary of the properties of elliptical galaxies is given in Chapter 4.

---

[1]http://www.cfa.harvard.edu/castles/
[2]http://www.slacs.org/
[3]http://www.sdss.org/

Motivation for this thesis

Elliptical galaxies represent a class of highly evolved structures in the universe. Mergers with other galaxies and the evolution of their stellar components have lead to their present day appearance. Conversely studying elliptical galaxies as they appear today yields information about their assembly and interaction history. Dark matter contributes the most mass to these galaxies, and thus the evolution of the dark matter distribution is imprinted on the observed distribution of elliptical galaxies. We can therefore learn about the history and the main evolutionary processes of elliptical galaxies by analyzing their total and dark matter distributions. This work focuses on understanding the distribution of total (dark and luminous) matter using strong gravitational lensing because gravitational lensing is sensitive to all kinds of matter, regardless of its nature or state. Consequently, direct information can be obtained about dark matter as well. We investigate the inner mass profiles of 2 extraordinary elliptical lensing galaxies and the truncation of elliptical galaxies in the dense environment of one cluster. To derive the (inner) mass profiles of galaxies by lensing, tracking the signal over a considerable distance is necessary. We therefore search for elliptical galaxies in the SLACS survey that have multiple sources (SDSS J1538+5817, see Chapter 5) or have one source that is lensed over a broad radial range (SDSS J1430+4105, see Chapter 6). We construct the inner mass profile from lensing alone for these 2 objects and dissect their mass profile into a luminous and dark part to gain information about both. We utilize the observed SDSS photometry to compare the stellar masses derived by photometric estimates with the lensing derived ones for these two galaxies. The techniques presented here could be extended to a larger sample size. Chapter 7 takes a slightly different approach: we use the fortunate situation that in MACSJ1206.2-0847 a giant arc, produced by the lensing potential of the galaxy cluster, gets distorted further by some elliptical cluster galaxies. Consequently, the arc light passes the galaxies at various different distances from the galaxies' centers. This allows us to trace the matter distribution of the lenses at radii beyond the visible radii. Reconstructing the surface brightness of this distorted arc, we can learn something about the dark matter distribution of the cluster galaxies. In this rare case, we can study the truncation of the galaxies' dark matter halos by tidal interaction with strong lensing. Furthermore, we can also investigate the basic mass properties of elliptical galaxies in a cluster environment, showing agreement with scaling relations derived independently in local elliptical galaxies. Again, the same methods can be applied on other clusters or groups of galaxies, gaining information about the processes governing the evolution of elliptical galaxies in dense environments.

Organization

This thesis is organized as follows: the Chapters 2, 3 and 4 give a summary of the theoretical framework of this thesis while Chapters 5, 6 and 7 present the results obtained in the course of this work. Chapter 2 presents the foundations of the cosmological framework of this work. Most of the work presented depends heavily on gravitational lensing, hence Chapter 3 describes the basic theory of this. Chapter 4 concludes the more theoretical part of the thesis by summarizing the basic properties of elliptical galaxies as these are the objects studied in this work. The experimental work conducted in the course of this thesis begins with Chapter 5, in which we present the observed inner mass profile measured by gravitational lensing for the early–type galaxy SDSS J1538+5817. This is followed by Chapter 6 where we present a similar analysis for SDSS J1430+4105. Chapter 7 uses strong gravitational lensing by the

galaxy cluster MACSJ1206.2-0847 to constrain scaling relations and sizes of inner cluster members in this galaxy cluster. Finally, Chapter 8 provides a summary of the results and some outlook for subsequent work of the near future.

A short review of cosmology

2.1 The Homogeneous Universe

2.1.1 The Cosmological principle and the Robertson-Walker Metric

Let us begin with the cosmological principle: the universe is homogeneous and isotropic on large scales. Also, we assume that no preferred location exists in the universe[1]. A general form of a metric describing this universe was found by Robertson and Walker, see Robertson (1935), Robertson (1936a), Robertson (1936b), Walker (1937), Peacock (1999), Ryden (2002):

$$\mathrm{d}s^2 = -\mathrm{c}^2\mathrm{d}t^2 + \mathrm{a}(t)^2 \left[\frac{\mathrm{d}x^2}{1 - \mathrm{k}x^2/\mathrm{R}_0^2} + x^2\mathrm{d}\Omega^2 \right] \quad , \tag{2.1}$$

where c is the speed of light, t is the time difference between two events, $\mathrm{a}(t)$ is the scale factor at time t, $\mathrm{k}\,\epsilon\,\{+1, 0, -1\}$ is the curvature parameter, and R_0 is the scale radius of the universe today. x is defined as the comoving distance, meaning that it is constant for observers moving with the expansion (or contraction) of the universe.

A widely used alternative notation (the notations for Eqs. 2.1 and 2.2 follow Ryden 2002) with a somewhat different definition of the comoving distance[2] is:

$$\mathrm{d}s^2 = -\mathrm{c}^2\mathrm{d}t^2 + \mathrm{a}(t)^2 \left[\mathrm{d}r^2 + \mathrm{S}_\mathrm{k}(r)^2\mathrm{d}\Omega^2 \right] \quad , \tag{2.2}$$

with

$$\mathrm{S}_\mathrm{k}(r) = \begin{cases} \mathrm{R}_0 \sin\left(\frac{r}{\mathrm{R}_0}\right) , & \text{for} \quad \mathrm{k} = +1 \\ r , & \text{for} \quad \mathrm{k} = 0 \\ \mathrm{R}_0 \sinh\left(\frac{r}{\mathrm{R}_0}\right) , & \text{for} \quad \mathrm{k} = -1 \end{cases} .$$

Without expansion, $\mathrm{a}(t) = 1$, and curvature, $\mathrm{k} = 0$, this gives the Minkowski metric of special relativity. This notation is also used in Peacock (1999).

---

[1]These 3 assumptions are somewhat redundant, e.g. an isotropic universe with no preferred location must be homogeneous.

[2]$x = \mathrm{S}_\mathrm{k}(r)$, meaning that the radial coordinate is different in curved spaces.

2.1.2 Friedman equation

The Einstein field equations, derived in Einstein (1916) and Einstein (1917), are, written in a compact manner:

$$G_{\mu\nu} + g_{\mu\nu}\Lambda = \frac{8\pi\mathrm{G}}{\mathrm{c}^4}T_{\mu\nu} \quad . \tag{2.3}$$

Here, $G_{\mu\nu}$ denotes the so-called Einstein Tensor, derived from the metric tensor $g_{\mu\nu}$ which is connected to Eq. 2.1 via $\mathrm{d}s^2 = g_{\mu\nu}\mathrm{d}x^\mu\mathrm{d}x^\nu$ ($\mathrm{d}x^\mu$ and $\mathrm{d}x^\nu$ denote the coordinates of space and time where $\mu,\nu \in \{0,1,2,3\}$)[3], Λ the so-called cosmological constant and $T_{\mu\nu}$ the energy momentum tensor. In this case, we use a positive sign for the rhs of the equation, see Peacock (1999).
From Eqs. 2.1 and 2.3 the first Friedman equation can be derived (Friedman, 1922). For that, we assume the universe to be filled with a perfect fluid and use its energy momentum tensor[4]:

$$\left(\frac{\dot{\mathrm{a}}(t)}{\mathrm{a}(t)}\right)^2 = \frac{8\pi\mathrm{G}\varepsilon(t)}{3\mathrm{c}^2} + \frac{\Lambda\mathrm{c}^2}{3} - \frac{\mathrm{kc}^2}{\mathrm{R}_0^2\mathrm{a}(t)^2} \quad . \tag{2.4}$$

This equation describes the expansion of the universe, connecting the change of the scale factor $\mathrm{a}(t)$ with the energy density of the universe ε, its curvature and the cosmological constant.

2.1.3 Cosmic expansion and redshift

First, we define the Hubble parameter as the ratio of the rate of change of the scale parameter and its value at time t:

$$\mathrm{H}(t) = \frac{\dot{\mathrm{a}}(t)}{\mathrm{a}(t)} \quad . \tag{2.5}$$

This quantifies the expansion of the universe, since it provides the ratio between the recession velocity of an object (given by the change of the scale factor $\dot{\mathrm{a}}(t)$) and its distance (given by the scale factor $\mathrm{a}(t)$). The value of $\mathrm{H}(t)$ at present day is abbreviated with H_0 and called the Hubble constant, see Hubble (1929) who described a linear correlation between the distance of an object and its recession velocity observed on earth. Hubble's diagram of this correlation is shown in Fig. 2.1.
Its value today, measured from the CMB, is $\mathrm{H}_0 = 71.0 \pm 2.5\frac{\mathrm{km}}{\mathrm{s\,Mpc}}$, see Komatsu et al. (2011). This expansion of the universe shifts the emitted spectra of all cosmological objects we can observe towards longer wavelengths, that is, redshifting them. The redshift z we measure is defined by the ratio of observed λ_{obs} to emitted wavelength λ_{em}:

$$1 + z := \frac{\lambda_{\mathrm{obs}}}{\lambda_{\mathrm{em}}} = \frac{\mathrm{a}(t_{\mathrm{obs}})}{\mathrm{a}(t_{\mathrm{em}})} \overset{\mathrm{a}(t_{\mathrm{obs}})=1}{=} \frac{1}{\mathrm{a}(t_{\mathrm{em}})} \quad . \tag{2.6}$$

The change in wavelength is given just by the change of the scale factor between emission and observation.

---

[3]For the Robertson Walker metric, Eq. 2.1, we get the following non-zero components for the tensor: $g_{tt} = -1$, $g_{xx} = \frac{\mathrm{a}(t)^2}{1-\mathrm{k}x^2/\mathrm{R}_0^2}$, $g_{\Theta\Theta} = \mathrm{a}(t)^2 x^2$, $g_{\varphi\varphi} = \mathrm{a}(t)^2 x^2 \sin^2 \Theta$, see Weinberg (2008).

[4]For $T_{\mu\nu}$, we get $T_{00} = \frac{\varepsilon}{\mathrm{c}^2}$, $T_{\mathrm{i}0} = 0$ and $T_{\mathrm{ij}} = \mathrm{a}(t)^2 \mathrm{p}\tilde{g}_{\mathrm{ij}}$, p denoting the pressure of the fluid and $\tilde{g}_{\mathrm{ij}}$ the three-metric for $\mathrm{i,j} \in \{1,2,3\}$, see Weinberg (2008).
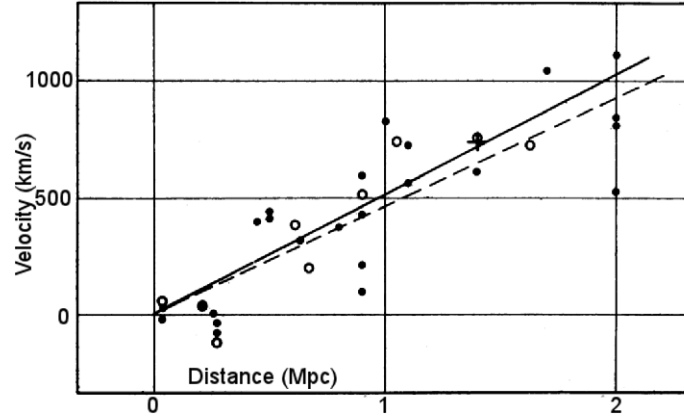
Figure 2.1: The first attempt to measure the Hubble constant. 'Radial velocities, corrected for solar motion, are plotted against distances estimated from involved stars and mean luminosities of nebulae in a cluster. The black discs and full line represent the solution for solar motion using the nebulae individually; the circles and broken line represent the solution combining the nebulae into groups; the cross represents the mean velocity corresponding to the mean distance of 22 nebulae whose distances could not be estimated individually.' Hubble (1929). While the value was wrong by at least an order of magnitude, this indicated the evidence of an expanding universe. Credit: Hubble (1929).

Assuming a flat universe without a cosmological constant that is dominated by cold matter, $\varepsilon \approx \rho c^2$, we can define a critical density from Eq. 2.4.

$$\rho_{\rm c}(t) = \frac{3}{8\pi {\rm G}} {\rm H}(t)^2 \quad .\tag{2.7}$$

We now can give all energy densities in units of this critical density:

$$\Omega_{\rm m} := \frac{\rho_{\rm m}}{\rho_{\rm c}}, \quad \Omega_{\rm r} := \frac{\varepsilon_{\rm r}}{\rho_{\rm c} c^2}, \quad \Omega_{\Lambda} := \frac{\Lambda c^2}{3\rho_{\rm c} {\rm H}(t)^2} \quad .$$

We have three components that possibly contribute to the total energy density Ω of the universe: radiation $\Omega_{\rm r}$, matter $\Omega_{\rm m}$ and the cosmological constant Ω_{Λ}. Therefore, we get an explicit form for the Hubble parameter, see Peacock (1999):

$$ {\rm H(a)}^2 = {\rm H}_0^2 \left[\Omega_{\Lambda} + \Omega_{\rm m} {\rm a}^{-3} + \Omega_{\rm r} {\rm a}^{-4} - (\Omega - 1) {\rm a}^{-2} \right] \quad ,\tag{2.8}$$

where $\Omega = 1$ is true for a flat universe. This dependency is plotted in Fig 2.2.

As can be seen, the Hubble parameter is closely linked to the dominant component of the universe, and it is getting constant in recent times due to the cosmological constant. In the case of a universe dominated by a positive cosmological constant $\Lambda > 0$, Eq. 2.4 gives an exponentially increasing scale factor:

$$ {\rm a} \propto {\rm e}^{\sqrt{\Lambda} t} \quad . $$

This exponential increase of the scale factor has been measured recently, see Riess et al. (1998), Perlmutter et al. (1998). Fig. 2.3 shows one of the 2 measurements suggesting the accelerated increase of the scale parameter in recent history. The driving force for this acceleration is termed dark energy, the simplest explanation which is still in agreement with current observations being a cosmological constant over time. The physical nature of this cosmological constant is as yet unknown.
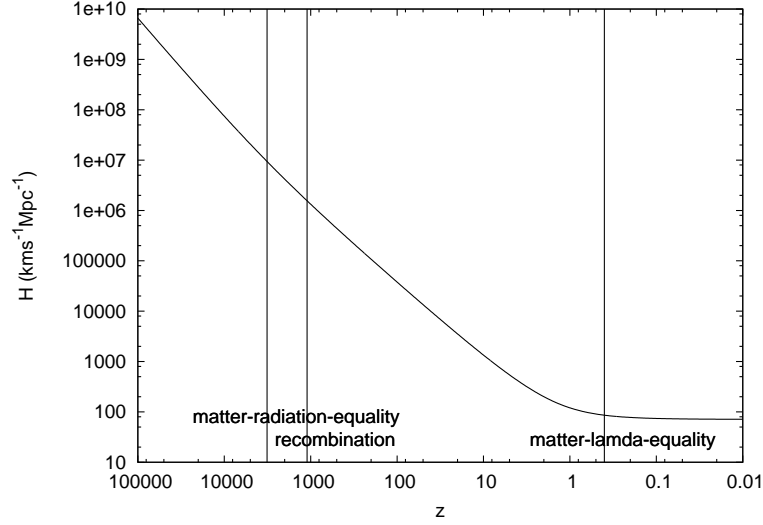
Figure 2.2: Development of the Hubble parameter with redshift, see Eq. 2.8 and Fig. 2.5. The values for Ω_Λ, Ω_m and Ω_r are taken from Eq. 2.17. The Hubble parameter can be seen to be declining with redshift throughout almost the entire history of the universe, only becoming constant in recent times due to the cosmological constant.

2.1.4 Distances in cosmology

Next, we need to define distances between objects in cosmology, e.g., see Peacock (1999), Ryden (2002) and Schneider et al. (2006).

The **proper distance** defines the distance two objects have at one instance of time, if this distance could be measured. We follow the notation of Ryden (2002) for the discussion of distances:

$$D_p(t) := a(t) \int_0^r dr' = a(t)r \quad . \tag{2.9}$$

This is the comoving distance r times the scale factor at that instance of time. This is not a measurable quantity, since we cannot get information of a distant position instantaneously. Since we are interested in observations, we need to define observable distances, taking into account the finite speed of light. For that we calculate the distances between an object emitting light at t_{em} and an observer receiving this light at t_{obs}. The **comoving distance** can be calculated from Eq. 2.2:

$$0 = ds^2 = -c^2 dt^2 + a(t)^2 dr^2 \quad .$$

Using $\dot{a} = \frac{da}{dt}$, we get for the comoving distance:

$$r = \int_{a(t_{em})}^{a(t_{obs})} \frac{c}{a^2 H} da \overset{Eq.2.8}{=} \int_{a(t_{em})}^{a(t_{obs})} \frac{c}{H_0} \left[\Omega_\Lambda a^4 + \Omega_m a + \Omega_r - (\Omega - 1)a^2 \right]^{-1/2} da \quad . \tag{2.10}$$

For the following, we assume $a(t_{obs}) = 1$. First, we introduce the angular diameter distance, since this is the quantity required for lensing. The basic idea is: If we can measure the angular size $\delta\Theta$ of an object for which we know the physical size l_A, we can determine the distance[5]

---

[5]We can safely assume $D_A \gg l_A$, hence $\delta\Theta \ll 1$.
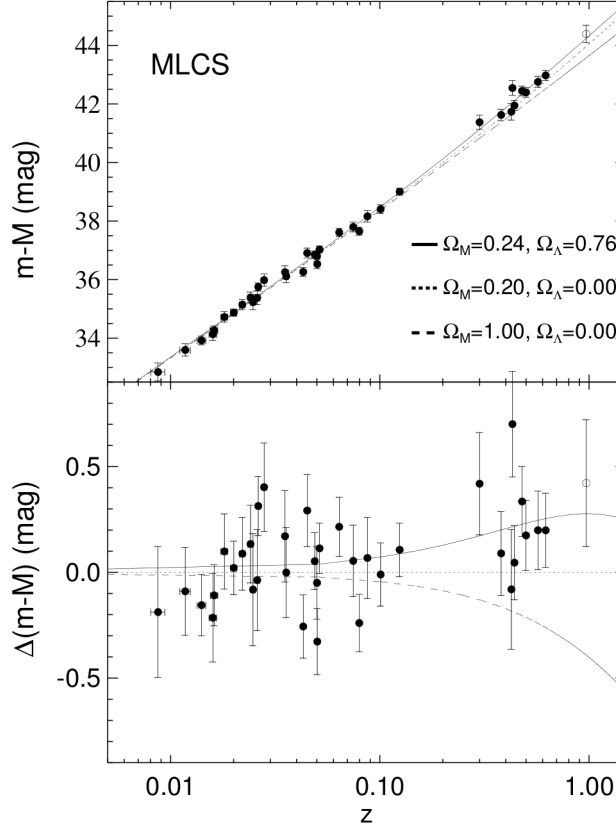
Figure 2.3: In this plot, the distance to Supernovae Ia is plotted, estimated in 2 different ways. On the x-axis, the redshift is plotted. On the y-axis, the distance modulus is plotted, giving the (logarithmic) difference in emitted and observed fluxes. The expected curves for 3 different sets of cosmologies are plotted together with the observed supernovae data. The open symbol marks SN 1997ck ($z = 0.97$). As can be seen, a model with a cosmological constant (solid line) follows the observations best. Credit: Riess et al. (1998). Reproduced by permission of the AAS.

D_A:

$$\tan \delta\Theta \approx \delta\Theta = \frac{l_A}{D_A} \quad .$$

Using Eq. 2.1, we can connect $\delta\Theta$ with ds by putting the object (lets assume a bar with length l_A for now) on the plane of the sky ($dx = 0$) and assuming $dt = 0$, meaning that light rays from both ends of the bar arrive at our position at the same instance of time:

$$l_A = ds = a(t_{em})S_k(r)\delta\Theta \quad .$$

Putting all together, we get the **angular diameter distance**:

$$D_A = a(t_{em})S_k(r) = \frac{S_k(r)}{1 + z_{em}} \quad . \tag{2.11}$$

Another way to define distances is by looking at the flux f received from an object with intrinsic luminosity L at a distance D_L:

$$f = \frac{L}{4\pi D_L^2} \quad .$$
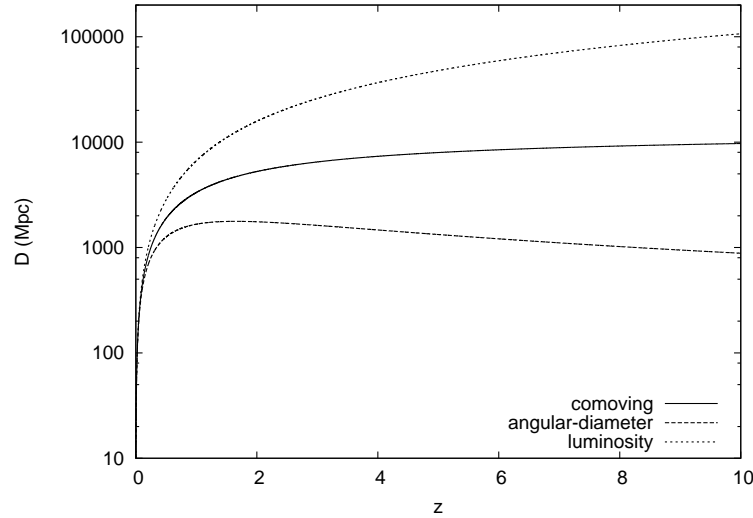
Figure 2.4: The comoving (Eq. 2.10), angular (Eq. 2.11) and luminosity (Eq. 2.12) distance plotted versus redshift. We assume a flat universe with parameters taken from Eq. 2.17. As can be seen, different distance definitions give different results since their dependencies on the scale factors are different.

First, we need the surface area of the sphere A on which the luminosity L is distributed in order to calculate the flux. Again, Eg. 2.1 with $dt = 0$ (since we want the size at one instance of time) and $dx = 0$ (since the radius of the sphere is constant), helps us:

$$A = \int ds^2 = 4\pi S_k(r)^2 \quad .$$

Second, the observed luminosity also changes. Due to the change in scale factor, the wavelength changes, and additionally the time between two consecutive photons changes by the scale factor. This means that the received energy per second changes by a factor $a(t_{em})^2$.

$$L' = a(t_{em})^2 L = \frac{L}{(1 + z_{em})^2} \quad .$$

Again, combining all of these factors we get for the **luminosity distance** D_L:

$$D_L = S_k(r)(1 + z_{em}) \quad . \tag{2.12}$$

For a flat universe, the comoving, angular-diameter and luminosity distances for an observer with $z_{obs} = 0$ are plotted in Fig 2.4.

2.1.5   Today's Universe

We want to describe the development of the universe over time. We omit the very early universe, since we are mainly interested in its later development. In order to do that, we need two more equations, see e.g. Ryden (2002):
First, we need the equation of state for the components of the universe, connecting the pressure P with the energy density ε:

$$P = w\varepsilon \quad . \tag{2.13}$$

w is the proportionality factor and differs for different types of components[6]. Consider a small volume of the comoving universe. With no heat flow in or out of this volume - this is fulfilled, e.g., for a homogeneous and isotropic universe - we get from the first law of thermodynamics as the second equation:

$$\dot{E} + P\dot{V} = 0 \quad .$$

using $E = V\varepsilon$ and $V = (ra)^3$, we get the fluid equation:

$$\dot{\varepsilon} + 3\frac{\dot{a}}{a}(\varepsilon + P) = 0 \quad . \tag{2.14}$$

For the three components matter, radiation and the cosmological constant, we therefore calculate the following scaling with the expansion of the universe:

$$\varepsilon_{\text{radiation}} \propto a^{-4}, \quad \varepsilon_{\text{matter}} \propto a^{-3}, \quad \varepsilon_\Lambda = const \quad . \tag{2.15}$$

This result has already been used for Eq. 2.8. Since these energy densities scale differently with the scale factor, the universe was dominated by different energy densities at different times[7]. From that, we can also calculate the lookback time depending on redshift, using Eq. 2.4:

$$t = \frac{1}{H_0} \int_0^{z_1} \frac{dz}{(1+z)\sqrt{\Omega_r(1+z)^4 + \Omega_m(1+z)^3 + \Omega_\Lambda + (1-\Omega)}} \quad . \tag{2.16}$$

Todays values of the energy densities for a flat ΛCDM universe are, see Larson et al. (2011):

$$\Omega_\Lambda = 0.734 \pm 0.029, \quad \Omega_{\text{CDM}} = 0.222 \pm 0.026, \quad \Omega_{\text{baryons}} = 0.0449 \pm 0.0028,$$

$$\Omega_{\text{matter}} = \Omega_{\text{CDM}} + \Omega_{\text{baryons}} = 0.267 \pm 0.026, \quad \Omega_{\text{radiation}} \overset{z_{\text{eq}}=3196^{+134}_{-133}}{=} (8.4 \pm 0.9) \times 10^{-5} \quad . \tag{2.17}$$

z_{eq} gives the redshift of matter–radiation equality, meaning the point in time at which the energy densities of matter and radiation were the same. This is also marked in Fig. 2.5. The development of these different components over time can be seen in Fig. 2.5.

Since the universe is close to being flat today, see Komatsu et al. (2011), Larson et al. (2011), we do not consider Eq. 2.4 in case of a non-zero curvature here. An observationally important time in cosmology is the era of recombination, in which neutral hydrogen atoms could be formed, making the universe transparent to the background radiation at that time. This took place when the background radiation photons were not energetic enough to reionize this formed hydrogen which is at a background temperature of $\approx 3000\,\text{K}$. From Fixsen et al. (1994), we get a temperature for the CMB today of $2.714 \pm 0.022\,\text{K}$. Therefore, we get $z_{\text{recombination}} \approx 1100$. The CMB provides the earliest cosmic radiation we can still detect today because in earlier times the photons were scattered from the free electrons present before recombination.

---

[6] $w = 0$, $w = 1/3$, $w = -1$ for non-relativistic matter, radiation and Λ respectively.
[7] We could input these dependencies into the Friedman equation, Eq. 2.4, to get the Hubble parameter, Eq. 2.8.
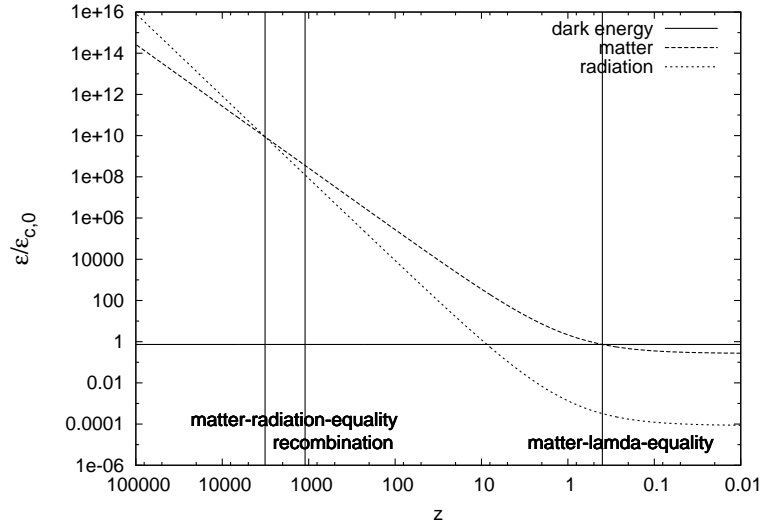
Figure 2.5: The development of the energy density of the different components of the universe. Starting from today's values, Eq. 2.17, the different components scale differently with the scale factor (or redshift) of the universe. Therefore, different components dominate the evolution of the scale factor at different times. While the early universe was dominated by radiation, it is now dominated by dark energy, having passed through an intermediate phase of matter domination. Vertical lines mark the time of matter–radiation equality, the time of recombination and the time of Λ–matter equality.

2.2 Structure formation

2.2.1 Linear theory

Moving from scales of $\geq 100\,\mathrm{Mpc}$ to smaller scales, we see that the universe is not isotropic and homogeneous on these smaller scales. In fact, we find structures on any scales below $\approx 100\,\mathrm{Mpc}$, such as clusters of galaxies, galaxies, globular clusters, stars, planets, moons, and so on, see Fig. 2.6.

From the WMAP (Komatsu et al., 2011), we know that the temperature T of the CMB radiation at the epoch of recombination ($z \approx 1100$) (Jones et al., 2004.) was homogeneous to $\frac{\delta T}{T} = 10^{-5}$. Since the baryonic matter was coupled to the radiation via Thompson scattering, we assume the same temperature fluctuations for the baryonic matter. Hence the density fluctuations of the universe must have been smaller than $\frac{\delta\rho}{\rho} = 3 \times 10^{-5}$, assuming an ideal gas and adiabatic fluctuations. This marks the starting point of observations of structure formation since matter and radiation decouple only at this time.

The growth of structure can be approximated by a linearized perturbation theory, as long as the deviations from an unperturbed expanding universe are small, see Peacock (1999) and Schneider (2006) for the following.

We start with the Euler, energy conservation and Poisson equations for small perturbations in a matter dominated, expanding universe, using $\delta = \frac{\delta\rho}{\rho_0}$:

$$
\begin{aligned}
\frac{\mathrm{d}\delta\vec{v}}{\mathrm{d}t} &= -\frac{\vec{\nabla}\delta p}{\rho_0} - \vec{\nabla}\delta\Phi - (\delta\vec{v}\cdot\vec{\nabla})\vec{v}_0 \\
\frac{\mathrm{d}\delta}{\mathrm{d}t} &= -\vec{\nabla}\cdot\delta\vec{v} \\
\vec{\nabla}^2\delta\Phi &= 4\pi\mathrm{G}\rho_0\delta \\
\mathrm{c}_\mathrm{s}^2 &= \frac{\partial p}{\partial\rho}
\end{aligned}
\qquad .
\tag{2.18}
$$
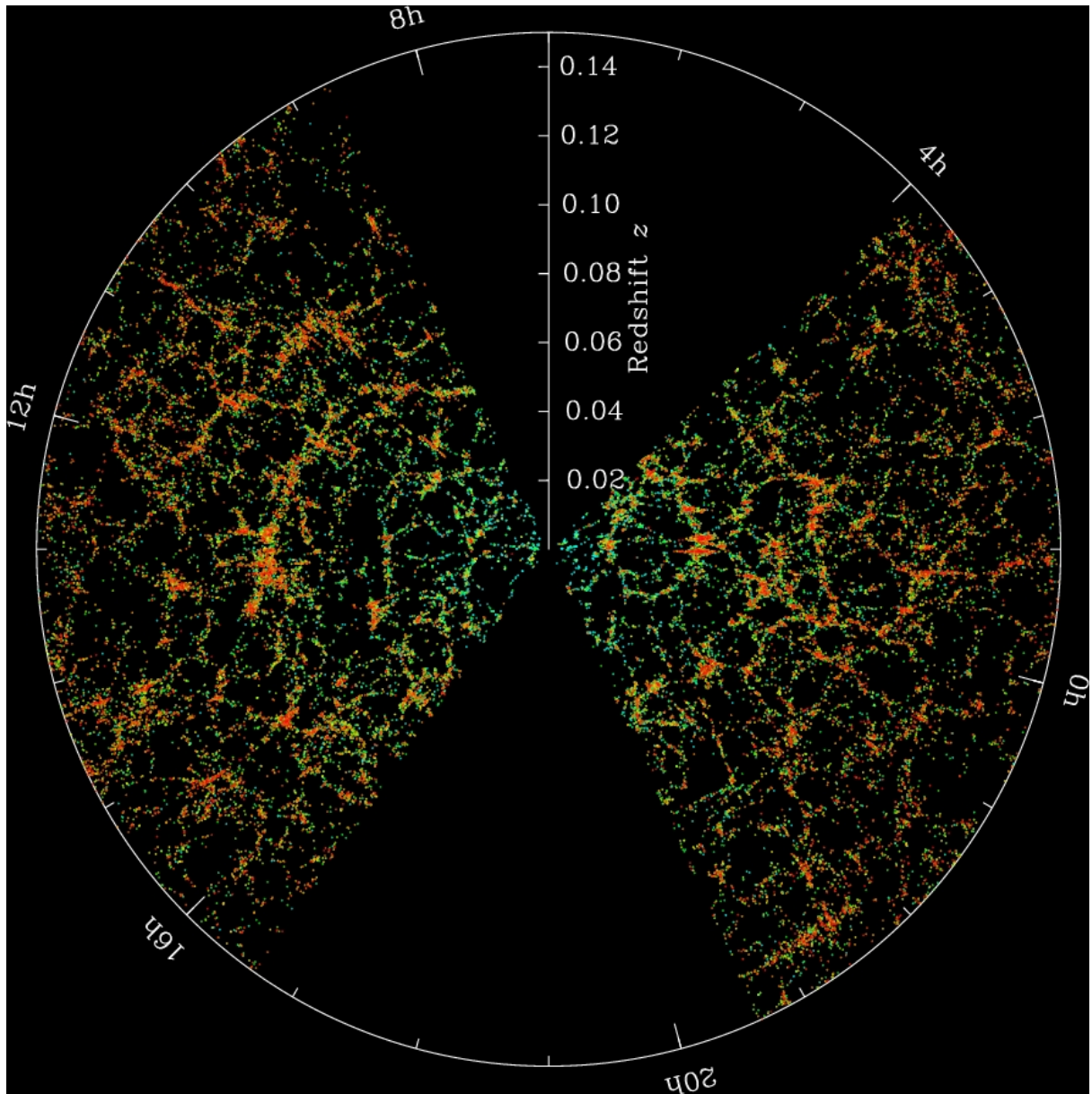
Figure 2.6: Galaxies from a slice around declination $\delta = 0 \pm 1.25°$ form the SDSS 3rd year data release. Each dot marks an observed galaxy. The coloring goes from red (old) to blue (young) according to the age of the stellar population. The outer circle marks a distance of $\approx 650\,\mathrm{Mpc}$. While on large enough scales this distribution tends to be homogeneous and isotropic, this is not the case on scales of $\approx 50\,\mathrm{Mpc}$ and below. Credit: M. Blanton and the Sloan Digital Sky Survey (SDSS) Collaboration, http://www.sdss.org.

All variables with a leading δ ($\delta\vec{v}$, $\delta\Phi$, δp) denote small perturbations to the local undisturbed values of the velocity field $\vec{v}_0$, the density ρ_0, the pressure p_0 and the gravitational potential Φ_0. The last equation defines the sound speed for adiabatic perturbations. After some calculations, see e.g. Peacock (1999), we get the following differential equation for the evolution of the density fluctuations:

$$\ddot{\delta} = \delta(4\pi G\rho_0 - c_s^2 k^2) \quad , \tag{2.19}$$

when using an ansatz for the spatial distribution $\delta \propto e^{-i\vec{k}\cdot\vec{r}}$ with a proper wavevector $\vec{k}$. Depending on the rhs of Eq. 2.19, we get solutions with amplitudes that decay, oscillate or grow over time. Since we study structure growth, we are only interested in the growing solutions, for which the rhs of Eq. 2.19 is positive. Therefore only modes with a wavelength bigger than

$$\lambda > \frac{2\pi}{k} = c_s\sqrt{\frac{\pi}{G\rho_0}} \tag{2.20}$$

can grow in this scenario. This length is also known as the Jeans length. It is governed by two variables: The sound speed c_s and the density of the universe ρ_0. Since the early universe before recombination is mainly radiation-dominated[8], the sound speed is $c_s = \frac{c}{\sqrt{3}}$. For the radiation dominated era, the rhs of Eq. 2.19 changes: 4π changes to $\frac{32\pi}{3}$, see Peacock (1999); this changes the Jeans length by a factor $\sqrt{\frac{3}{8}}$. We see that only large clumps of matter (of the order $10^{16} M_\odot$ or above) can grow (Jones et al., 2004.) continuously up to recombination, while on all other scales overdensities cease to grow at some time before. Furthermore, perturbations in the density field smaller than $\approx 10^{12} M_\odot$ are wiped out by Silk damping (Silk, 1968) before the beginning of recombination. After recombination, the baryonic matter is decoupled from the photons, therefore the sound speed now depends on its temperature:

$$c_s = \sqrt{\frac{dp}{d\rho}} = \sqrt{\frac{5kT}{3m}} \quad , \tag{2.21}$$

for an ideal gas and adiabatic sound waves with m denoting the mass of the gas particles k the Boltzmann constant and T the temperature of the baryonic gas.

The wavelength and therefore the according mass drops to $\approx 10^6 M_\odot$ (Jones et al., 2004.), meaning that structures with this mass[9] and above can now grow. For a matter dominated, flat universe (which was the case for most of the time after recombination), the linear density contrast grows like the scale factor, $\delta \propto a(t)$ (Peacock, 1999). Therefore, the linear density contrast now would be of the order of 10%, much smaller than that observed today. Hence, we need something additional to explain this discrepancy. We can solve that problem by introducing dark matter: Since it does not interact with radiation (hence dark), the density contrast of dark matter can also grow before recombination, giving a higher contrast at recombination than what is observed for the baryonic matter. Depending on its sound speed, this dark matter clumps on different scales: hot dark matter particles are considered to be

---

[8]The epochs of recombination and matter-radiation equality are two different epochs, but this difference does not change this argument since the baryons are coupled to the photons before recombination.

[9]This is the typical mass scale for the oldest structures of the universe: globular clusters and dwarf galaxies.

relativistic at the time of decoupling, therefore this kind of matter forms large structures first. Afterwards smaller structures would be formed by fragmentation of larger structures, that is, clusters of galaxies form first then fragment in groups of galaxies then galaxies and so on. This is also referred to as top–down structure formation.

Cold dark matter particles are non-relativistic, hence, according to Eq. 2.21 and Eq. 2.20, also small scale structures can grow from the beginning. Since smaller scale structures collapse faster, smaller structures form first in this scenario. This is also termed bottom–up structure formation.

2.2.2 Hierarchical growth following Press-Schechter

Press & Schechter (1974) also assumed a hierarchical growth of structure from small scales to larger scales, beginning after recombination. We work in comoving distances, and follow (Peacock, 1999) for the rest of this section. We assume a random density field $\delta(\vec{x})$. for which we can define the following correlation function

$$\xi(\vec{x}, \vec{x}') = \langle \delta(\vec{x}) \delta^*(\vec{x}') \rangle = \xi(|\vec{x} - \vec{x}'|) \quad .$$

The brackets denote averaging over the volume of the density field, δ^* denotes the conjugate of δ. The last equality is only true for a homogeneous and isotropic universe, meaning that the correlation function only depends on the distance between $\vec{x}$ and $\vec{x}'$. We can derive the variance of the density field from the correlation function:

$$\sigma^2(\mathrm{R}) = \int \int \xi(|\vec{x} - \vec{x}'|) f_\mathrm{R}(\vec{x}) f_\mathrm{R}(\vec{x}') \mathrm{d}x^3 \mathrm{d}x'^3 \quad ,$$

where $f_\mathrm{R}(\vec{x})$ denotes a filter or weight function with a characteristic length scale R, e.g. a Gaussian or a Top Hat.

An equivalent description of the correlation function is its Fourier transformation, the power spectrum:

$$\mathrm{P}(k) = \langle |\delta_{\vec{k}}|^2 \rangle \quad ,$$

where the brackets denote the ensemble average and ξ and $|\delta_{\vec{k}}|^2$ are connected by Fourier transformation:

$$\xi(\vec{r}) = \frac{\mathrm{V}}{2\pi^3} \int |\delta_{\vec{k}}|^2 e^{-i\vec{k}\vec{r}} \mathrm{d}^3 k \quad .$$

For the power spectrum, we assume a single, featureless power law:

$$\mathrm{P}(k) \propto k^n \quad . \tag{2.22}$$

In absence of mixing between scales, the linear theory can still represent the mass spectrum of collapsed objects, assuming that an object collapses as it reaches a critical overdensity. For a universe with critical density and no cosmological constant, its value extrapolated to the present is $\delta_\mathrm{c} = 1.68$, derived from a spherical collapse model. According to Mo et al. (2010) this value can be used for all realistic cosmologies, since the dependency on Ω_m is weak in scenarios both with and without a cosmological constant. Objects that form before some redshift z need to have a higher extrapolated density contrast by the linear growth factor:

$\delta_c(z) = (1 + z)\delta_c$. In order to derive the mass of these objects, we smooth the initial density field by the filter function:

$$\delta_R(\vec{x}) = \int \delta(\vec{x}') f_R(\vec{x} - \vec{x}') d^3 x' \quad .$$

Furthermore, we can assign a characteristic mass for this density fluctuations:

$$M \sim \frac{4}{3}\pi \rho_0 R^3 \quad .$$

For the Press-Schechter formula, we now calculate how often regions of a characteristic mass with densities higher than the critical density $\delta_c(z)$ exist for an initial Gaussian density field and get the comoving number density $f(M)dM$. Peacock (1999) states for this:

$$f(M, z) = \sqrt{\frac{2}{\pi}} \left| \frac{d\sigma}{dM} \right| \frac{\rho_0}{M} \left(\frac{\delta_c(z)}{\sigma(M)^2} \right) e^{-\frac{\delta_c(z)^2}{2\sigma(M)^2}} \quad . \tag{2.23}$$

A closer look at Eq. 2.23 shows several different points: First, there will be a characteristic mass $M_\star(z)$ above which the number density will decrease exponentially. Second, since the variance $\sigma(M)^2$ decreases with mass, small mass structures are more frequent than high mass structures. Third, since $\delta_c(z)$ increases with redshift, there is less structure at higher redshift, but smaller structures are more numerous at the same time. Therefore, this gives a bottom up mass assembly, as favored by a cold dark matter scenario. Both Press-Schechter and the linear growth of structures describe the properties of the large scale structure and its formation history well. Thus, we get a basic description of the history of our Universe's structural growth by following this two approaches.

In Fig. 2.7, Girardi et al. (1998) measure this mass function at the high–mass end from cluster measurements. They compare it with different predictions for different variances $\sigma(M)_8^2$, giving the density variation within a sphere of $8h^{-1}$Mpc radius and Γ defining the transfer function of the matter power spectrum.
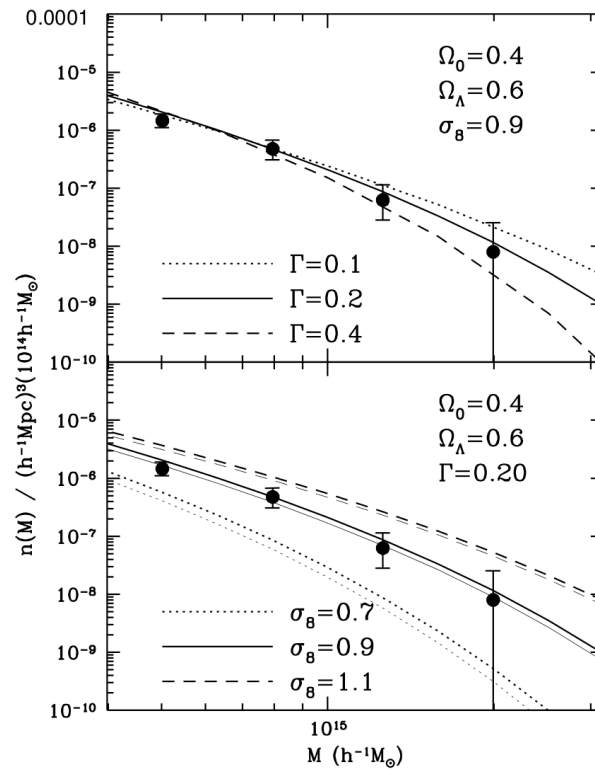
Figure 2.7: This plot shows the mass function, Eq. 2.23, for the Press-Schechter high-mass end. The data points represent different mass bins from cluster measurements. In the upper panel, the effect on the mass function for different shapes of the initial power spectrum is shown, on the lower panel, different rms fluctuations are assumed. Credit: Girardi et al. (1998). Reproduced by permission of the AAS.

Chapter 3

Gravitational Lensing

3.1 Basic theory of gravitational lensing

The theory of gravitational lensing treats light as rays which are deflected by gravitational fields they pass. The deflection angle $\hat{\alpha}$ generated by a mass M passed by a lightray in distance r is given by:

$$\hat{\alpha}(r) = \frac{4GM}{c^2 r} \quad ,$$

(3.1)

where G denotes the gravitational constant and c the speed of light in vacuum, see Einstein (1916, 1922); Schneider et al. (1992); Narayan & Bartelmann (1996); Schneider et al. (2006). This is sketched in Fig. 3.1.
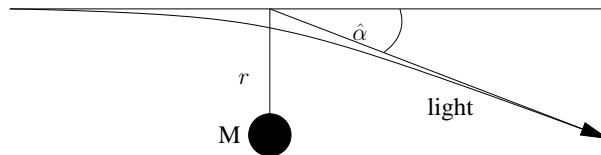
Figure 3.1: The concept of the light deflection: The light ray passes from left to right, passing the deflector with mass M in distance r. The light ray gets deflected by $\hat{\alpha}$.

It is valid in the weak field limit, meaning that r is large compared to the Schwarzschild radius of the mass M, a condition which is always fulfilled in the cosmological cases considered in this work. From that, we can derive the lens equation. Reviews of the theory of gravitational lensing can be found in Schneider et al. (1992); Narayan & Bartelmann (1996); Schneider et al. (2006). This section follows Narayan & Bartelmann (1996). First, we use the so called "thin lens approximation", meaning that we simplify the physics by projecting all the lens' mass onto one sheet and call that the lens plane. This can be done since the distances D_{ds} and D_d (see Fig. 3.2) are large compared to the size of the lens in all cosmologically relevant cases. The following definitions, also of the different angles, are taken from (Narayan & Bartelmann, 1996, pp. 9,10). We define the surface mass density $\Sigma(\vec{\xi})$ on the lens plane by projecting the mass along the line of sight (LOS) l on the lens plane:

$$\Sigma(\vec{\xi}) = \int \rho(\vec{\xi}, l) \mathrm{d}l \quad ,$$

(3.2)

with $\vec{\xi}$ being the position defined in the lens plane. Combining Eqs. 3.1 and 3.2 gives the deflection of each mass element in the lens plane. The deflection angle of an extended mass distribution is simply the integral over all mass elements:

$$\vec{\hat{\alpha}}(\vec{\xi}) = \frac{4G}{c^2} \int_{\mathbb{R}^2} \frac{(\vec{\xi} - \vec{\xi'})\Sigma(\vec{\xi'})}{|\vec{\xi} - \vec{\xi'}|^2} d^2\xi' \quad , \tag{3.3}$$

where $\vec{\xi}$ and $\vec{\xi'}$ are vectors in the lens plane to the intersection of the light ray and the position of the mass element $\Sigma(\vec{\xi'})$, respectively. The origin of the coordinate system and the optical axis can be chosen randomly. A widely used choice for this optical axis is given by the lens' center of mass.

In Fig 3.2, the basic lensing situation is sketched. $\vec{\beta}$ is defined as the angle between the true source position and the optical axis, $\vec{\Theta}$ as the angle between the image position and the optical axis and $\vec{\alpha}$ as the difference between these two (Narayan & Bartelmann, 1996, pp.9,10).
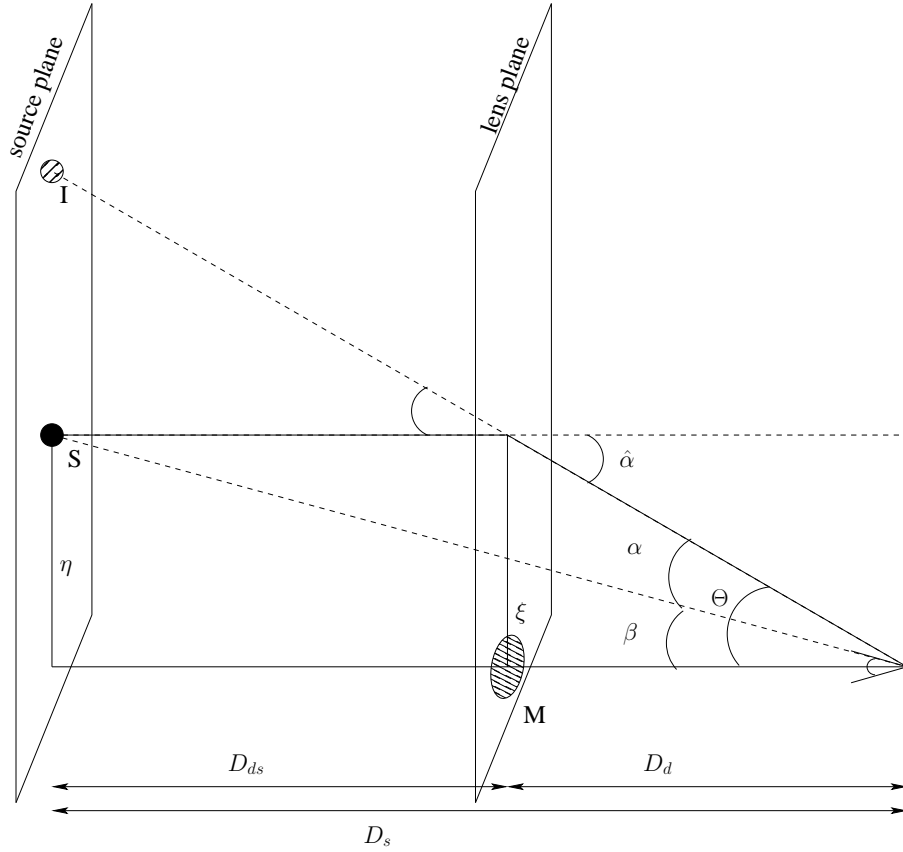
Figure 3.2: The basic lensing situation: The light propagates from the source S to the observer and gets deflected by the angle $\hat{\alpha}$ in the lens plane by the lens by the mass M. Backprojection of the observed ray to the source plane gives the image position I with angle Θ. In angular coordinates, the source position would be seen with angle β, the angular difference between source and image position is called α.

Geometry connects the true deflection angle $\vec{\hat{\alpha}}$ with the reduced deflection angle $\vec{\alpha}$. We refer to the later when using the term deflection angle in the following. We get

$$\vec{\alpha} = \frac{D_{ds}}{D_s} \vec{\hat{\alpha}} \quad . \tag{3.4}$$

For the deflection angle and the lens equation we get

$$\vec{\beta} = \vec{\Theta} - \vec{\alpha}(\vec{\Theta}) \quad , \tag{3.5}$$

which relates the true source angle ($\vec{\beta}$) with the observable image angle ($\vec{\Theta}$) and the deflection angle $\vec{\alpha}$. The deflection angle depends on the mass distribution of the lens, Eq. 3.3, and therefore on $\vec{\xi} = D_{\mathrm{d}}\vec{\Theta}$. All the angles are defined on the plane of the sky, so they all are 2-dimensional vectors.

The following discussions of the gravitational potential, the convergence and shear and the definition of the local Jacobian lens mapping are taken from (Narayan & Bartelmann, 1996, pp. 23,24). Rewriting Eq. 3.3 in angular coordinates and using Eq. 3.4 gives for the deflection angle:

$$\vec{\alpha}(\vec{\Theta}) = \frac{4\mathrm{G}}{\mathrm{c}^2}\frac{\mathrm{D}_{\mathrm{ds}}\mathrm{D}_{\mathrm{d}}}{\mathrm{D}_{\mathrm{s}}} \int_{\mathbb{R}^2} \frac{(\vec{\Theta} - \vec{\Theta}')\Sigma(\mathrm{D}_{\mathrm{d}}\tilde{\Theta}')}{|\vec{\Theta} - \vec{\Theta}'|^2} \mathrm{d}^2\Theta' \quad . \tag{3.6}$$

We now define:

$$\kappa(\vec{\Theta}) = \frac{\Sigma(\vec{\Theta})}{\Sigma_{\mathrm{crit}}} \quad \text{with} \quad \Sigma_{\mathrm{crit}} = \frac{\mathrm{c}^2}{4\pi\mathrm{G}}\frac{\mathrm{D}_{\mathrm{s}}}{\mathrm{D}_{\mathrm{ds}}\mathrm{D}_{\mathrm{d}}} \quad , \tag{3.7}$$

and term $\kappa(\vec{\Theta})$ the convergence and Σ_{crit} the critical surface density of the lens. Thus Eq. 3.6 can be rewritten as

$$\vec{\alpha}(\vec{\Theta}) = \frac{1}{\pi} \int_{\mathbb{R}^2} \kappa(\vec{\Theta}')\frac{(\vec{\Theta} - \vec{\Theta}')}{|\vec{\Theta} - \vec{\Theta}'|^2} \mathrm{d}^2\Theta' \quad . \tag{3.8}$$

Using the derivative of $\nabla \ln|\vec{x}| = \vec{x}/\vec{x}^2$, we can define an effective lensing potential $\psi(\vec{\Theta})$ requesting the condition $\nabla_{\vec{\Theta}}\psi(\vec{\Theta}) = \vec{\alpha}(\vec{\Theta})$:

$$\psi(\vec{\Theta}) = \frac{1}{\pi} \int_{\mathbb{R}^2} \kappa(\vec{\Theta}') \ln|\vec{\Theta} - \vec{\Theta}'|\mathrm{d}^2\Theta' \quad . \tag{3.9}$$

This effective lensing potential can be related back to the Newtonian potential by integrating along the LOS:

$$\psi(\vec{\xi}) = \frac{2\mathrm{D}_{\mathrm{ds}}}{\mathrm{c}^2\mathrm{D}_{\mathrm{d}}\mathrm{D}_{\mathrm{s}}} \int \phi(\vec{\xi}, l)\mathrm{d}l \quad . \tag{3.10}$$

The Laplacian of the potential, Eq. 3.9, gives twice the convergence, using $\nabla^2 \ln(x) = 2\pi\delta(x)$:

$$\nabla_{\vec{\Theta}}^2\psi(\vec{\Theta}) = 2\kappa(\vec{\Theta}) \quad . \tag{3.11}$$

Up to now, we have only examined the deflection of one light ray by an extended mass distribution. Next we want to consider the mapping of an extended light source. Using the abbreviation $\psi_{\mathrm{ij}} = \frac{\partial^2\psi}{\partial\Theta_{\mathrm{i}}\partial\Theta_{\mathrm{j}}}$, we get the local Jacobian matrix of the lens mapping:

$$A = \frac{\partial\vec{\beta}}{\partial\vec{\Theta}} = (\delta_{\mathrm{ij}} - \psi_{\mathrm{ij}}) \quad , \tag{3.12}$$

where we used the lens equation 3.5 and the Kronecker symbol δ_{ij}. This matrix (or more accurately its inverse) gives the change of the image position induced by a change of the source position.

We can rephrase Eq. 3.12 using Eq. 3.11 and the following definition of the shear tensor:

$$
\begin{aligned}
\gamma_1(\vec{\Theta}) &= \frac{1}{2}(\psi_{11} - \psi_{22}) = \gamma(\vec{\Theta})\cos(2\phi(\vec{\Theta})) \\
\gamma_2(\vec{\Theta}) &= \psi_{12} = \psi_{21} = \gamma(\vec{\Theta})\sin(2\phi(\vec{\Theta})) \quad ,
\end{aligned}
\tag{3.13}
$$

with $\gamma(\vec{\Theta}) := |\vec{\gamma}(\vec{\Theta})|$. We get:

$$
A = \begin{pmatrix} 1 - \kappa - \gamma_1 & -\gamma_2 \\ -\gamma_2 & 1 - \kappa + \gamma_1 \end{pmatrix} \quad .
\tag{3.14}
$$

It can be shown that the eigenvalues of this matrix are

$$
\lambda_{1,2} = 1 - \kappa \pm \gamma \quad ,
\tag{3.15}
$$

meaning that a circular source gets (de-)magnified by the convergence[1] and distorted to an ellipse by the shear since it has a different sign for the two eigenvalues, see Fig 3.3 for illustration.
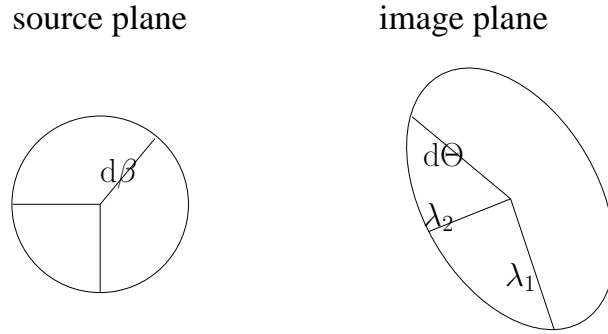
Figure 3.3: The basic image mapping situation in lensing: The source vector $\mathrm{d}\beta$ is mapped into the image vector $\mathrm{d}\Theta$ via Eq. 3.12. In this process, the image gets also distorted. While on the source plane, the two eigenvalues λ_1 λ_2 have the same length, this changes on the image plane according to Eq. 3.15.

The magnification of the image is given by the flux ratios of the source and the image. Since A describes the mapping from the image to the source plane, a circular source with radius r is transformed into an ellipse with the axes: $\frac{r}{\lambda_1}, \quad \frac{r}{\lambda_2}$. Considering a circular small source with homogeneous surface brightness $f^{(i)}$, we get for the magnification:

$$
\mu = \frac{F_\mathrm{I}}{F_\mathrm{S}} = \frac{\pi f^{(i)}}{\pi r^2 f^{(i)}} \frac{rr}{\lambda_1 \lambda_2} = \frac{1}{\lambda_1 \lambda_2} = (\det A)^{-1} \quad .
\tag{3.16}
$$

Let us briefly consider a circular lens. The deflection angle is in this case, using Eq. 3.8, a function of the mean convergence $\langle \kappa \rangle(\Theta)$ within radius Θ :

$$
\alpha(\Theta) = \frac{1}{\pi\Theta}\langle\kappa\rangle(\Theta)\pi\Theta^2 \quad \text{with} \quad \langle\kappa\rangle(\Theta) = \frac{1}{\pi\Theta^2}\int_0^\Theta 2\pi\Theta'\kappa(\Theta')\mathrm{d}\Theta' \quad .
\tag{3.17}
$$

With a source at angular position $\beta = 0$, Eq. 3.5 together with Eq. 3.17 gives

---

[1]Since A describes the mapping of the image to the source plane, a source with radius r has an image radius of $r/(1 - \kappa)$ when only considering the convergence.

$$0 = \Theta - \langle\kappa\rangle(\Theta)\Theta \quad , \tag{3.18}$$

which is only true for $\langle\kappa\rangle(\Theta) = 1$. For a lens with a radially monotonically declining surface density, this only occurs at one value of Θ, the so called Einstein radius or Einstein angle Θ_E. There, the mean surface density equals the critical surface density in Eq. 3.7. This Einstein angle is the most characteristic quantity for a lensing system.

3.2 The regime of strong lensing

Depending on the exact properties of the source–lens–observer system, there are different regimes of the previously outlined theory: Micro-, weak and strong lensing. Since the rest of the work uses the framework of strong lensing, we will briefly discuss its basic concepts. Lensing is termed strong lensing when one source can be imaged multiple times to the observer, resulting in several images of the same source. From Eqs. 3.16 and 3.14, we can calculate the magnification:

$$\mu(\vec{\Theta}) = ((1 - \kappa(\vec{\Theta}))^2 - \gamma(\vec{\Theta})^2)^{-1} \quad . \tag{3.19}$$

Since κ and γ are both functions of the position $\vec{\Theta}$, there can be cases where the magnification μ is infinite[2]. These curves in the image plane are called critical curves, their lens equation mapping back onto the source plane are called caustics. These critical curves separate regions of the image plane where the multiplicity of the images is different, meaning that each time a source crosses the caustic in the source plane, images appear or disappear at the corresponding critical line in the image plane. This is sketched in Figs. 3.4 and 3.7.

3.2.1 The case of an axisymmetric lens

For now, let us again assume a circular lens with an arbitrary mass profile; its deflection angle is defined in Eq. 3.17. We put this into the lens equation 3.5 and get:

$$\beta = \Theta - \langle\kappa\rangle(\Theta)\Theta \quad . \tag{3.20}$$

Assuming a lens with a continuous, monotonic and convex declining radial density profile and some radius where $\langle\kappa\rangle(\Theta) > 1$, we can write down more than one solution for the equation above[3] for some range of β. In general, we get 3 solutions:
One with positive $\Theta_1 = \frac{\beta}{1-\langle\kappa\rangle(\Theta_1)}$ with $\langle\kappa\rangle(\Theta_1) < 1$, one with negative $\Theta_2 = \frac{\beta}{1-\langle\kappa\rangle(\Theta_2)}$ with $\langle\kappa\rangle(\Theta_2) > 1$ meaning that this image is on the opposite side of the lens center with respect to the source position, and a 3rd image close to the center with $\langle\kappa\rangle(\Theta_3) \gg 1$, see e.g. the case of β_2 in Fig. 3.4.
For this 3rd image, the magnification in Eq. 3.19 tends to be very small $\mu \ll 1$ and, in the case of a singular lens (meaning $\lim_{\Theta\to 0}\kappa = \lim_{\Theta\to 0}\langle\kappa\rangle(\Theta) = \infty$), this image disappears completely. In Fig. 3.4, this is plotted for different convergence profiles, each of the curves representing a different convergence profile. Along the curves Eq. 3.20 is fulfilled, meaning that a source at position β is imaged to the image position(s) Θ. For a given source position (e.q. β_3),

---

[2]Since real sources have a finite size, the magnification of such a source will still be finite. Also, the geometrical optics assumption has to be replaced with wave optics in that case, giving finite magnifications(Schneider et al., 2006).

[3]Without loss of generality, we can assume $\beta > 0$ here.

the intersections with the curve representing the lens' convergence profile give the positions of the (multiple) images.
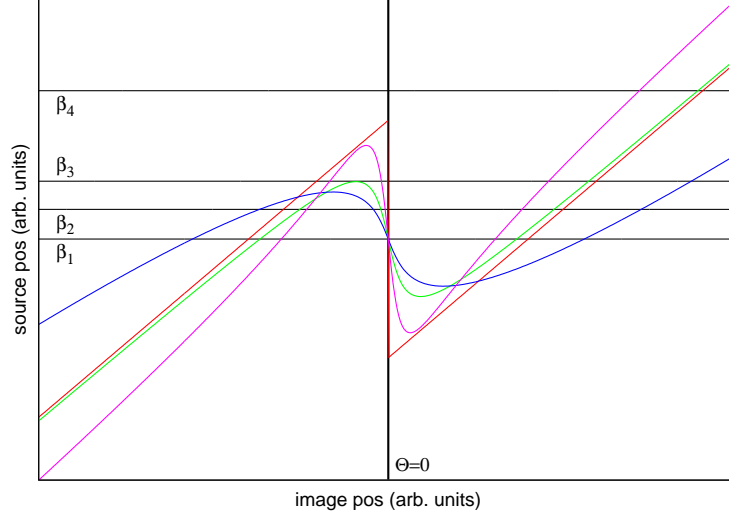
Figure 3.4: Graphical representation of Eq. 3.20. The horizontal lines mark different source positions, each intersection with one of the curves mark a lensed image position of this source position for this lens. The Einstein radius of each profile is defined by the intersection of the curves with the $\beta_1 = 0$ line. All curves have 2D density profiles of the form $\kappa \sim (\Theta^2 + \Theta_c^2)^{-n}$. The red curve represents the case of a singular profile, $\Theta_c = 0$, $n = -0.5$. The red and the green curve share the same n, with $\Theta_c > 0$ for the green curve, while for the blue (purple) curve, $\Theta_c > 0$ and $n > -0.5$ ($n < -0.5$). This form of diagram is also called Young diagram.

As one can see, there exist values of β (e.g. β_2 and the "green" lens) for which we get three solutions, meaning that the same source is imaged three times. We note that the exact image positions for these depend on the properties of the mean convergence $\langle\kappa\rangle(\Theta)$. Furthermore, since only the mean convergence enters the Eq. 3.20, this is the property that one can really measure for axisymmetric lenses.

In Fig. 3.4, two points are of special interest: First the Einstein radius (i.e. the angle Θ to which a source at $\beta_1 = 0$ is lensed to) and, for the non-singular profiles, the radii at which images seem to appear or disappear (e.g. β_3 for the green lens, marking the transition between 3 images for smaller β and 1 image for larger β).

To study the local properties of the lens mapping for an axisymmetric lens, we consider Eq. 3.12. Using Eq. 3.20, we get, see Schneider et al. (2006):

$$A = \begin{pmatrix} 1 - \langle\kappa\rangle(\Theta) & 0 \\ 0 & 1 - \langle\kappa\rangle(\Theta) \end{pmatrix} - \frac{\langle\kappa\rangle'(\Theta)}{\Theta} \begin{pmatrix} \Theta_1^2 & \Theta_1\Theta_2 \\ \Theta_1\Theta_2 & \Theta_2^2 \end{pmatrix} \quad . \tag{3.21}$$

The derivative can be rewritten as

$$\langle\kappa\rangle'(\Theta) = \frac{\mathrm{d}\langle\kappa\rangle(\Theta)}{\mathrm{d}\Theta} = \frac{2(\kappa(\Theta) - \langle\kappa\rangle(\Theta))}{\Theta} \quad . \tag{3.22}$$

This matrix A has the two eigenvalues of

$$\lambda_1 = (1 - \langle\kappa\rangle(\Theta)) \quad \lambda_2 = (1 - \langle\kappa\rangle(\Theta) - \langle\kappa\rangle'(\Theta)\Theta) \quad . \tag{3.23}$$

The determinant of A is zero if one of the eigenvalues is 0. In that case, the magnification grows to infinity and we get a critical line in the image plane. So, in general, there are two

critical lines, since there are 2 eigenvalues. In order to obtain the image behavior at these critical lines, we look at the eigenvectors of this matrix. Without loss of generality, we can set $\Theta_1 = 0$.

We get

$$A = \frac{\partial \vec{\beta}}{\partial \vec{\Theta}} = \begin{pmatrix} 1 - \langle\kappa\rangle(\Theta) & 0 \\ 0 & 1 - \langle\kappa\rangle(\Theta) - \langle\kappa\rangle'(\Theta)\Theta_2 \end{pmatrix} \quad , \tag{3.24}$$

and the eigenvectors

$$v_1 = \begin{pmatrix} 1 \\ 0 \end{pmatrix} \quad v_2 = \begin{pmatrix} 0 \\ 1 \end{pmatrix} \quad . \tag{3.25}$$

A defines the backprojection from the image to the source plane, hence a vanishing eigenvalue means that the image will be stretched in this direction[4]. Since we are on the Θ_2 axis, we get a stretching along the Θ_1 direction for $\lambda_1 = (1 - \langle\kappa\rangle(\Theta)) \to 0$ and therefore term this a tangential critical line (since the stretching is tangential to the line connecting the image position with the lens center). We see that the position of this image is again the Einstein angle.

Likewise we get a stretching along the Θ_2 axis for $\lambda_2 = (1 - \langle\kappa\rangle(\Theta) - \langle\kappa\rangle'(\Theta)\Theta) \to 0$, calling this a radial critical line. This is illustrated in Fig. 3.5, where the relative tangential/radial magnification, defined as the inverse of the respective eigenvalues $|\frac{1}{\lambda_1}|$ / $|\frac{1}{\lambda_2}|$, is plotted. If we remap this tangential / radial critical lines back into the source plane, we get the corresponding caustics. For our spherical example, this could be done using Fig. 3.4 with the high magnification image positions from Fig. 3.5.
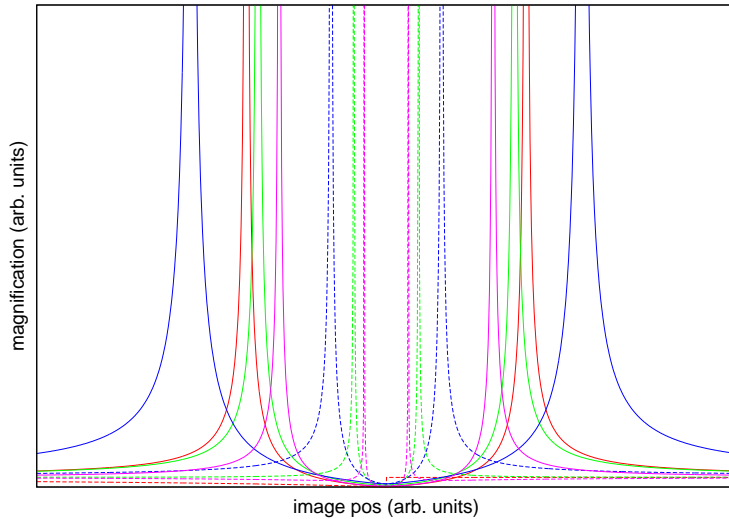
Figure 3.5: Graphical representation of Eq. 3.23. The colors mark the same profiles as in Fig. 3.4 and both plots have the same scale on the horizontal axis. The solid / dashed lines are $|\frac{1}{\lambda_1}|$ and $|\frac{1}{\lambda_2}|$, respectively, i.e. the relative magnifications in tangential and radial direction.

For all the profiles shown, we only get a tangential caustic at $\beta = 0$, meaning that the caustic shrinks to a point in the center behind the lens. As mentioned above, the image appears now

---

[4]A big change of position on the image plane gives only a small change on the source plane, meaning that an extended source gets stretched by a big factor in that direction.

at the Einstein angle Θ_{E}. Since, the source, lens and observer are all aligned on one optical axis, this system is spherical symmetric: The Einstein angle defines a ring of formally infinite magnification. As mentioned before, the magnification of a finite source is still finite. The magnification of a point-source is also not infinite when wave optics are taken into account, see Schneider et al. (2006).

Conversely, the caustic belonging to the radial critical line is circular with a radius which depends on the exact profile of the lens. As mentioned earlier the critical lines mark the lines at which multiple images appear (or disappear) as soon as the source crosses the corresponding caustic moving inward (or outwards).

3.2.2   The case of an elliptical lens

For an elliptical mass profile there is no general analytic solution for the lens equation 3.5. Therefore, for most of the cases, the lens equation for an elliptical mass distribution has to be calculated numerically. However, we can get an analytic description in one special case which is appropriate to most properties of elliptical lenses at least qualitatively. We use a (non-)singular isothermal ellipsoid (NSIE[5]) with a minor to major axis ratio[6] q to discuss the qualitative properties. We take the definition of (Kochanek, 2004):

$$\kappa(\Theta_1, \Theta_2) = \frac{\mathrm{b}}{2\omega(\Theta_1, \Theta_2)}, \quad \omega(\Theta_1, \Theta_2)^2 = \mathrm{q}^2(\Theta_1^2 + \Theta_{\mathrm{c}}^2) + \Theta_2^2 \quad , \tag{3.26}$$

here b denotes some lensing strength, q the minor to major axis ratio and Θ_{c} the core radius. It can be shown (e.g. by differentiation) that the deflection angle of this profile is (Kochanek, 2004):

$$\alpha_1(\Theta_1, \Theta_2) = \frac{\mathrm{b}}{\sqrt{1 - \mathrm{q}^2}} \arctan\left(\frac{\Theta_1 \sqrt{1 - \mathrm{q}^2}}{\omega(\Theta_1, \Theta_2) + \Theta_{\mathrm{c}}}\right) \quad , \tag{3.27a}$$

$$\alpha_2(\Theta_1, \Theta_2) = \frac{\mathrm{b}}{\sqrt{1 - \mathrm{q}^2}} \operatorname{arctanh}\left(\frac{\Theta_2 \sqrt{1 - \mathrm{q}^2}}{\omega(\Theta_1, \Theta_2) + \mathrm{q}^2 \Theta_{\mathrm{c}}}\right) \quad . \tag{3.27b}$$

The resulting right hand side (rhs) of the lens equation in the form

$$0 = \vec{\Theta} - \vec{\alpha}(\vec{\Theta}) - \vec{\beta} \tag{3.28}$$

for two different source positions is plotted in Fig. 3.6. The red and blue surfaces represent the two components of the vector of the rhs. The black surface represents the left hand side(lhs) and is therefore 0, identical for both components. First, we want to consider several source positions so as to understand the imaging properties of this system. We start with a galaxy behind the center of the lens, shown in red in Fig. 3.7. Looking at the lens equation Eq. 3.5 with $\beta_1 = \beta_2 = 0$ and Eq. 3.27, we see that in order to fulfill the lens equation in this case, $0 = \vec{\Theta} - \vec{\alpha}(\vec{\Theta})$ has to be fulfilled at the positions of the multiple images. In Fig. 3.6 the lhs (black) and rhs (red & blue) of Eq. 3.28 are plotted. Therefore, multiple images will occur on the simultaneous intersections of all three surfaces. As can be seen in Fig. 3.6(a), these positions lie along the coordinate axes where either $\Theta_1 = \alpha_1 = 0$ or $\Theta_2 = \alpha_2 = 0$ is true

---

[5]We will discuss some profiles, also including this one, later on in Chapter 4.
[6]The axis ratio is defined for the isodensity contours of the convergence κ.

all along this axis, giving four images. If the profile has a finite core radius, there is also a fifth image in the center of the lens plane. We do not get any more solutions than these five multiple images. This is shown in Fig. 3.6(a): The case of $\alpha_1 - \Theta_1 = 0$ and $\alpha_2 - \Theta_2 = 0$, necessary to fulfill the lensing equation for a source at $\beta_1 = \beta_2 = 0$, is only true at some distinctive positions along the coordinate axes. This explains the red images seen in Fig. 3.7, resulting in five multiple images. A configuration like this also occurs in Fig. 3.8. This object is also called the Einstein cross.

If we move the source off center along one of the coordinate axes (right hand plot in Fig. 3.7) we again get three images along this coordinate axis, similar to the circular case. Along the perpendicular axis (Θ_1 in Fig. 3.7) however, we do not get any solutions, see the green case in Fig. 3.7. The case of $\Theta_1 - \alpha_1 = 0$ and $\Theta_2 - \alpha_2 - \beta_2 = 0$ is only fulfilled simultaneously at distinct positions off the perpendicular axis, see Fig. 3.6(b). This again defines the positions of the five multiple images. Similarly, we can reconstruct the images for all the different source positions seen in Fig. 3.7 and explain its (multiple) image positions.

(a)   (b)
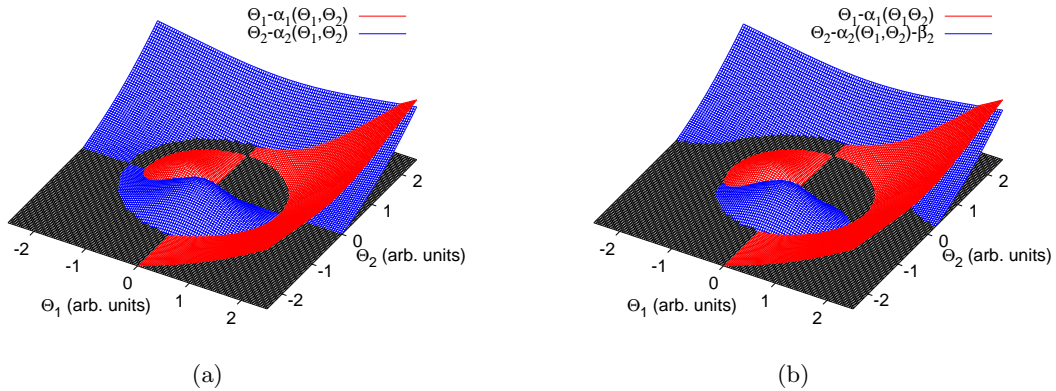
Figure 3.6: These 2 plots represent the lens equation 3.5 for two different source positions. The red and blue areas show the two rhs parts of Eq. 3.28, $\Theta_1 - \alpha_1 - \beta_1$ and $\Theta_2 - \alpha_2 - \beta_2$, respectively. The black area marks the area where the values are 0, the lhs of Eq. 3.28. Therefore, intersections of the red (blue) and black area mark lines where the lens equation is fulfilled for $\Theta_1 - \alpha_1 - \beta_1 = 0$ ($\Theta_2 - \alpha_2 - \beta_2 = 0$). This means that intersection points of the red, blue and black area mark points at which the lens equation 3.5 is fulfilled simultaneously for both dimensions and multiple images occur. The left image shows $\beta_1 = \beta_2 = 0$, the right shows $\beta_1 = 0, \beta_2 > 0$. While on the left image, these multiple images occur along the coordinate axis, the ones along the Θ_2 axis move off this axis if the source has $\beta_2 \neq 0$. For both plots a NSIE model with $\Theta_c = 0.3$ and $q = 0.8$ is used.

To describe the image mapping further, we again want to find the critical lines and corresponding caustics for this elliptical lens. For that, we need the magnification (Kochanek, 2004):

$$\mu(\Theta_1, \Theta_2)^{-1} = 1 - \frac{b}{\omega} - \frac{b^2 \Theta_c}{\omega \left((\omega + \Theta_c)^2 + (1 - q^2) \Theta_1^2 \right)} \quad . \tag{3.29}$$

The radial critical line and its corresponding caustic behaves similar to the circular case, except that they are ellipses instead of circles, as can be seen in Fig. 3.7. The tangential caustic, however changes from being only one point behind the center of the lens in the circular case. Without losing qualitative information, we can set $\Theta_c = 0$. With this simplification, we get for the tangential critical line using $\mu^{-1} = 0$:

(a)   (b)
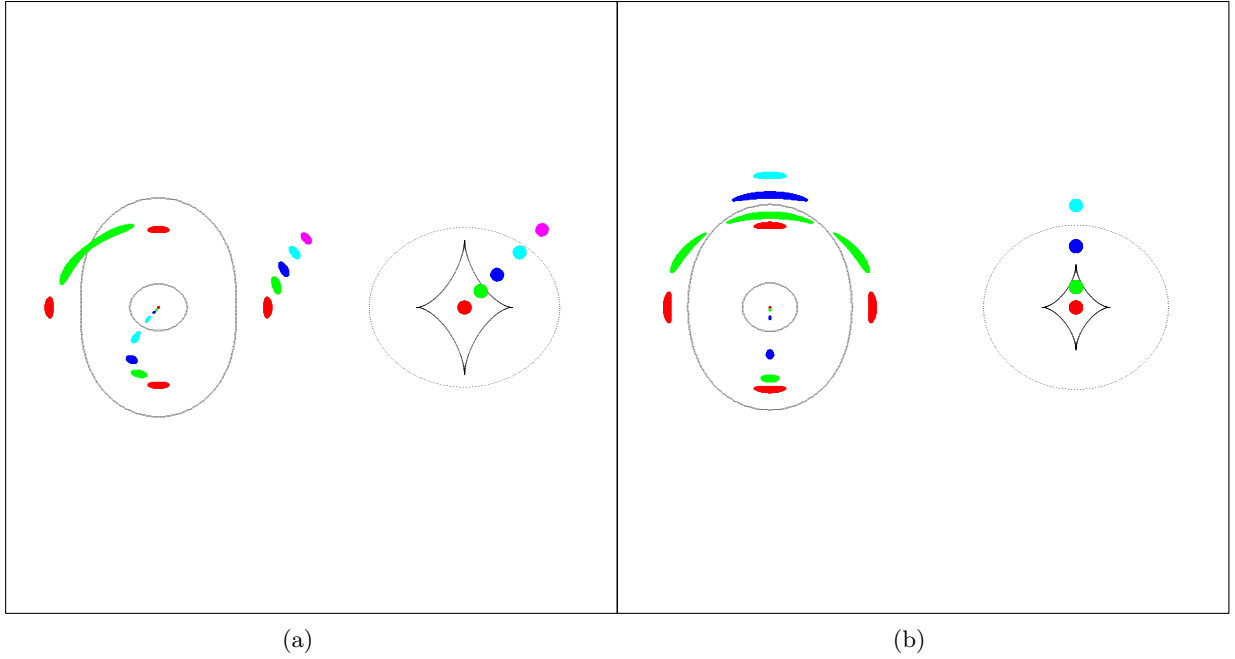
Figure 3.7: These two plots show how a source at different positions in the source plane is mapped into the image plane. In each of the plots 3.7(a) 3.7(b) the lens and source planes are shown on the left and right. Images with the same color originate from the source with the corresponding color in the source plane. Depending on the source position, we get up to five images of the same source with different positions, image distortions and magnifications. Credit: Narayan & Bartelmann (1996).

$$\Theta_2 = \pm\sqrt{b^2 - q^2\Theta_1^2} \quad . \tag{3.30}$$

Inputting this into the lens equation 3.5 and using the deflection angles Eq. 3.27, we get the asteroid shapes seen in Fig. 3.7. Now, putting it all together, we can understand Fig. 3.7, taken from Narayan & Bartelmann (1996). Depending on the source position, we get a different number of multiple images: one image if the source lies outside of the caustics (e.g. the light blue source in Fig. 3.7(b)), three if the source is between both caustics (e.g. the dark blue source in both Figs. 3.7(a) and 3.7(b)) and five if the source is inside both caustics (the green and red sources in Figs. 3.7(a) and 3.7(b)). The images are also distorted, as derived earlier in this chapter. The most prominent cases are the green sources in Fig. 3.7(a) and 3.7(b) as some of the multiple images start to merge and have high magnifications. These configurations give the spectacular giant arcs, as for example seen in Fig. 1.2. Depending on the exact position of the source on the tangential caustic, this is called fold arc (Fig. 3.7(a)) or cusp arc (Fig. 3.7(b)), as the source is close to the fold or cusp of the caustic. Another interesting case is the light blue source in Fig. 3.7(a). In the image plane, the two images close to the radial critical line start to merge, giving a radial arc.
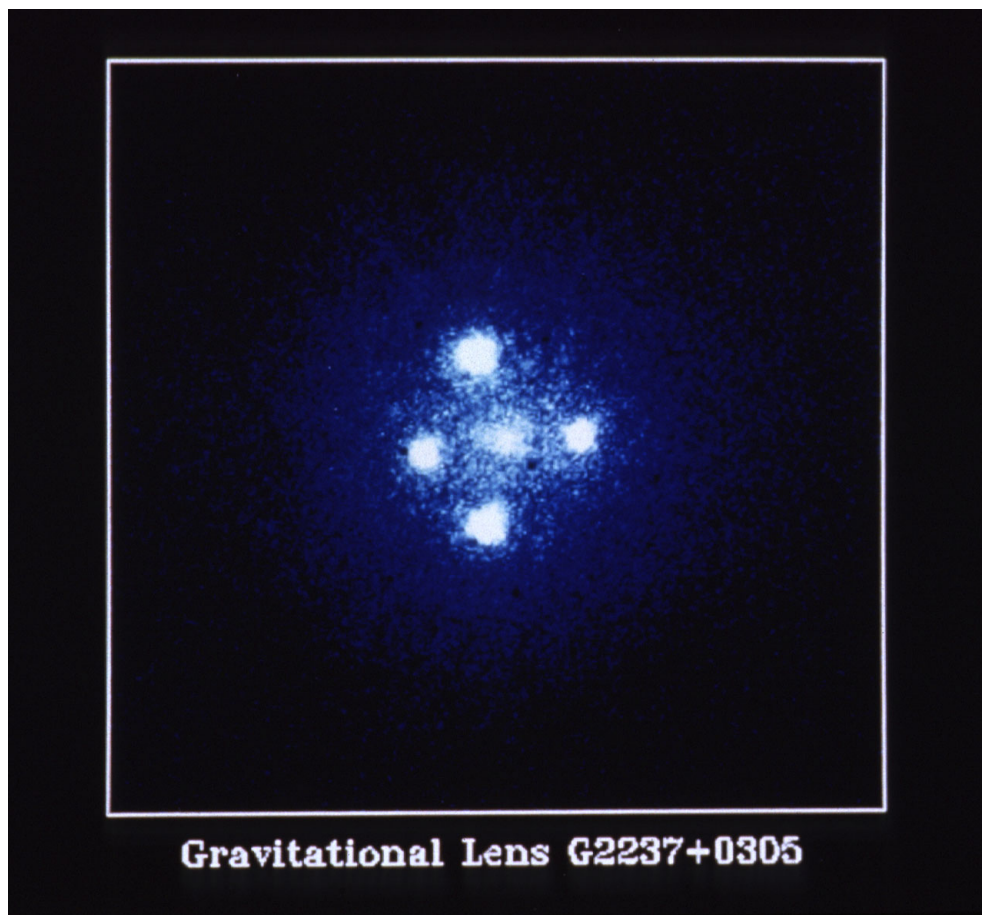
Figure 3.8: The well-known Einstein cross. A distant quasar is lensed into four images almost forming a cross on the sky. The configuration is similar to the red configurations in Fig. 3.7 demonstrating the link between the prediction of multiple image positions and the observed ones. Credit: NASA, ESA and STSci.

Chapter 4

Elliptical galaxies

In his book, Hubble (1936) classified galaxies according to their apparent morphology into mainly three different classes,the famous Hubble sequence: elliptical galaxies, (barred) spiral galaxies and irregular galaxies[1], see Fig. 4.1. At that time, galaxies were considered to evolve from the left to the right along the fork, hence calling elliptical galaxies early–type and spiral galaxies late–type galaxies[2]. In this work, we only concentrate on the left part of the fork, the elliptical galaxies. This galaxies are numbered from E0 to E7, denoting the flattening of their isophotes.
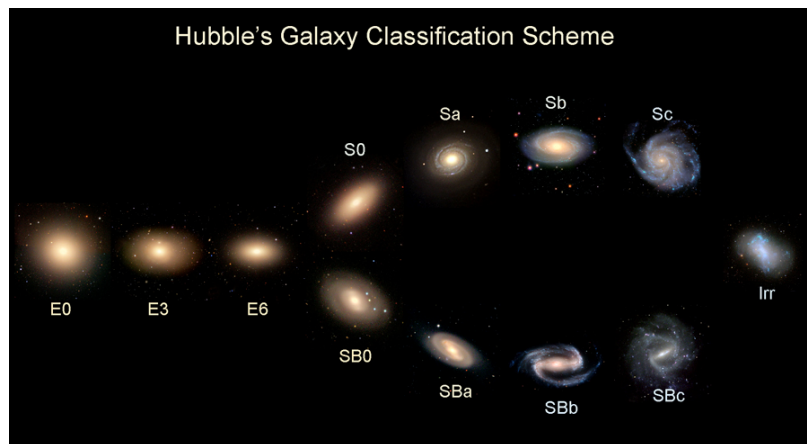
Figure 4.1: The well-known hubble fork. Elliptical galaxies are on the left-hand side, spiral galaxies on the right-hand side. Credit: Galaxy Zoo, http://blog.galaxyzoo.org/2010/05/12/types-of-galaxies/ ©Galaxy Zoo 2007, under the terms of the Creative Commons Attribution-Noncommercial-No Derivative Works Wales License.

4.1   Light distribution

The surface brightness distribution (SFB) I(R) of elliptical galaxies follows the de Vaucouleurs law (de Vaucouleurs, 1948):

---

[1] Actually missing the regime of dwarf galaxies which happen to have the highest number counts.
[2] We now know that galaxies evolve in the other direction, from right to left on the figure.

$$I(R) = I(R_{\text{eff}}) \exp\left(-7.669\left[\left(\frac{R}{R_{\text{eff}}}\right)^{0.25} - 1\right]\right) \quad, \tag{4.1}$$

with R_{eff} denoting the effective radius (the radius of the aperture containing half of the total light). In Fig. 4.2, one example is shown for the surface brightness of an elliptical galaxy which follows this profile.
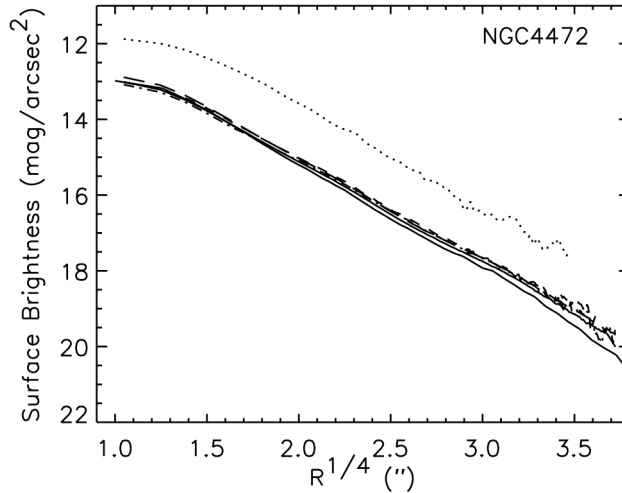
Figure 4.2: This plot shows the surface brightness of the elliptical galaxy NGC4472 in different infrared bands. Shown is the surface brightness versus $R^{1/4}$. Since the surface brightness is given in $\text{mag} \times \text{arcsec}^{-2}$ a straight line in this representation follows Eq. 4.1. As can be seen the light profiles follow Eq. 4.1 well. Credit: Temi et al. (2008). Reproduced by permission of the AAS.

As can be seen, this description fits well with observations. However, there are a few generalizations that should be mentioned here: Firstly, the light profile's steepness in Eq. 4.1 can be generalized to the so-called Sérsic law, see (Sérsic, 1963):

$$I(R) = I(R_{\text{eff}}) \exp\left(-b\left[\left(\frac{R}{R_{\text{eff}}}\right)^{\frac{1}{n}} - 1\right]\right) \quad,$$

with n being the sérsic index. We get the de Vaucouleurs law back for $n = 4$.

Secondly, bright elliptical galaxies tend to have a core radius, meaning that the light profile essentially gets flat within this radius, see e.g. Lauer et al. (2005) for a sample of 77 elliptical galaxies.

Besides the spatial distribution of light, the spectral light distribution of an elliptical galaxy also has some typical features: The visible parts of the spectral energy distribution (SED) of elliptical galaxies are dominated by the redder parts of the spectrum, see Fig. 4.3.

There are no emission features present, which would be typical for short-lived OB type stars. The line spectrum is dominated by many metal absorption lines, further reddening the galaxies' colors. These spectra typically exhibit a break in its fluxes around 4000Å (the so–called 4000Å-break), a coincidence of various metallic absorption lines. Both the spatial and spectral distribution of light traces the properties of the stars emitting this light.
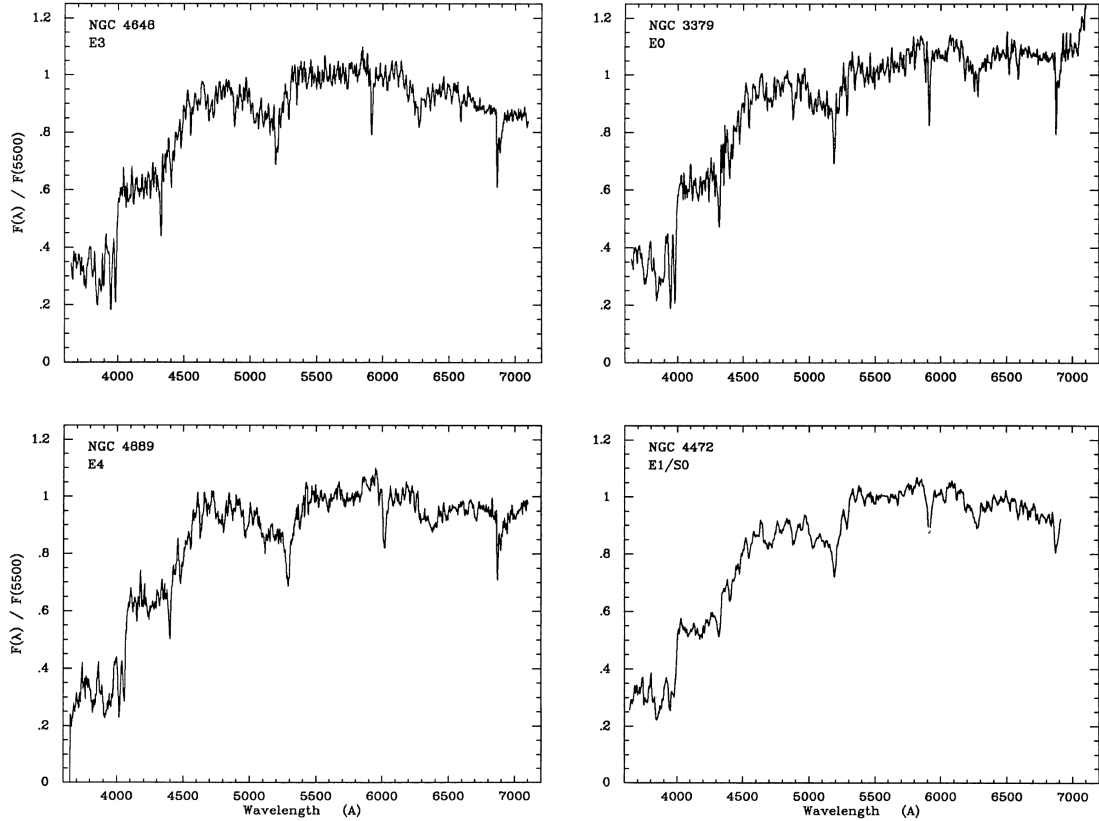
Figure 4.3: The spectra of 4 elliptical galaxies are plotted here. As you can see, there are some features typical for this galaxies: There is the so called $4000\mathring{A}$ break, a flux increase around this wavelength. Also, the spectra a dominated by the redder parts of the visible light, making the galaxies appear red in multi-color images. Credit: Kennicutt (1992). Reproduced by permission of the AAS.

4.1.1   Initial mass function and mass–to–light ratio

The stellar component is characterized by the mixture of stars it consists of: This is given by the so–called initial mass function (IMF). Three main IMFs are used today: Salpeter (Salpeter, 1955), Kroupa (Kroupa, 2001) and Chabrier (Chabrier, 2003). Specifically, the IMF describes the number of stars $N(m)$ initially present within a mass interval $m, m + dm$. Salpeter (1955) obtains a behavior of $N(m) \sim m^{-2.35}$ from star counts in the solar neighborhood. This is a steep function of the star's mass, meaning that a Salpeter IMF predicts few high mass and many low mass stars. Kroupa (2001) and Chabrier (2003) keep the same slope at the high mass end, but weaken the steep power law for less massive stars, e.g. Kroupa (2001) introduces $N(m) \sim m^{-1.3}$ and $N(m) \sim m^{-0.3}$ for stars below $0.5\,\mathrm{M_\odot}$ and $0.08\,\mathrm{M_\odot}$, respectively. Hence for Kroupa (2001) and Chabrier (2003) IMFs fewer low mass stars are present for the same number of high mass stars compared to Salpeter (1955). Since high mass stars are much more luminous per mass than low mass stars, this different IMF behavior at the low mass end directly influences the stellar mass of galaxies: For a Salpeter IMF, there is more mass in stars for the same luminosity than in Chabrier or Kroupa IMF. For example, Grillo et al. (2009) calculate the stellar masses for an ensemble of different strong lensing galaxies and directly observe this trend. However, the question of which IMF is the correct

one is not yet resolved, see e.g. Cappellari et al. (2012b,a) who see different IMFs agreeing
better with the observed dynamical masses depending on the stellar mass of the galaxy. The
actually observed spectral energy distribution (SED), however, is not only depending on the
IMF, but also on the amount of dust present in the galaxy, the stars' metalicity and its for-
mation age. Very briefly, the formation age determines which types of stars are still present
at the time of the light emission, since more massive stars have a bluer color and higher
luminosity, but also a shorter life span. Therefore an older stellar population has a redder
color. Dust present in galaxies also reddens the galaxies' color since it absorbs preferentially
blue light and reemits this at longer (redder) wavelengths. However, the amount of dust in
elliptical galaxies is small ($10^4 - 10^5$ M$_\odot$) (Goudfrooij et al., 1994). The metalicity also makes
stellar spectra redder, since metal–rich stars are cooler than metal–poor stars for the same
mass. Hence, there are several effects shifting the galaxies' light more towards red colors,
making it hard to distinguish these effects.

One important descriptive quantity relating the observed light profile with its mass profile is
the mass–to–light ratio (MtoL) of the galaxy. The stellar (total) MtoL gives the ratio of the
stellar (total) mass of the galaxy and its luminosity (in units of mass to luminosity of the sun).
E.g. Faber & Jackson (1976) get a typical value of the central MtoL of ≈ 10 in the restframe
B-band[3] for elliptical galaxies, measured in that case from velocity dispersions. Cappellari
et al. (2012a) measure MtoLs for the stellar components of early–type galaxies by modeling
the observed dynamics of these galaxies and report values of 2 to 10 for the restframe r-band[4].
While the stellar and central MtoL is one value that describes the galaxy's stars, the total
MtoL also includes some statement about the dark matter component. Since the total mass
and light profiles of galaxies do not follow the same radial behavior, the total MtoL necessarily
changes with radius. If we integrate both the light and total mass of a galaxy, we can give
a total, integrated MtoL. Hoekstra et al. (2004) find a value of $ML_B^{-1} \sim 60 M_\odot L_{\odot,B}^{-1}$ for the
integrated MtoL in the RCS survey using weak lensing. In Fig. 4.4, the stellar MtoL for the
inner parts of different coma galaxies is plotted derived from photometric estimates.
By observing a galaxy's stellar mass or MtoL, e.g. by measuring the dynamics of the stars
or the total enclosed projected mass by lensing, we can infer properties of these elliptical
galaxies, such as the IMFs.

4.1.2 Elliptical galaxies: components, formation and environment

The above summarized characteristics of early–type galaxies are closely connected to the com-
ponents, formation and environment of elliptical galaxies. Some elliptical galaxies observed
in X–ray wavelengths exhibit bright X–ray halos around them. The X–rays are emitted from
hot gas, see e.g. Fabbiano (1989). Hence, elliptical galaxies contain a halo of hot gas. In Fig.
4.5 an example of a measured X–ray profile is shown.
In contrast to the hot gas, little cold gas is observed in elliptical galaxies (Knapp, 1999) im-
plying that almost no recent star formation is occurring in these galaxies, in agreement with
the star formation history presented earlier.
Besides the visible stars and the gas, these galaxies contain large amounts of dark matter,
although this was a matter of debate for a long time (Carollo et al., 1995; Kronawitter et al.,
2000; Dekel et al., 2005). We discuss the most common dark and total matter profiles in

---

[3]B denotes a filter typically centered around $4400\mathring{A}$.
[4]A filter typically centered around $6200\mathring{A}$.
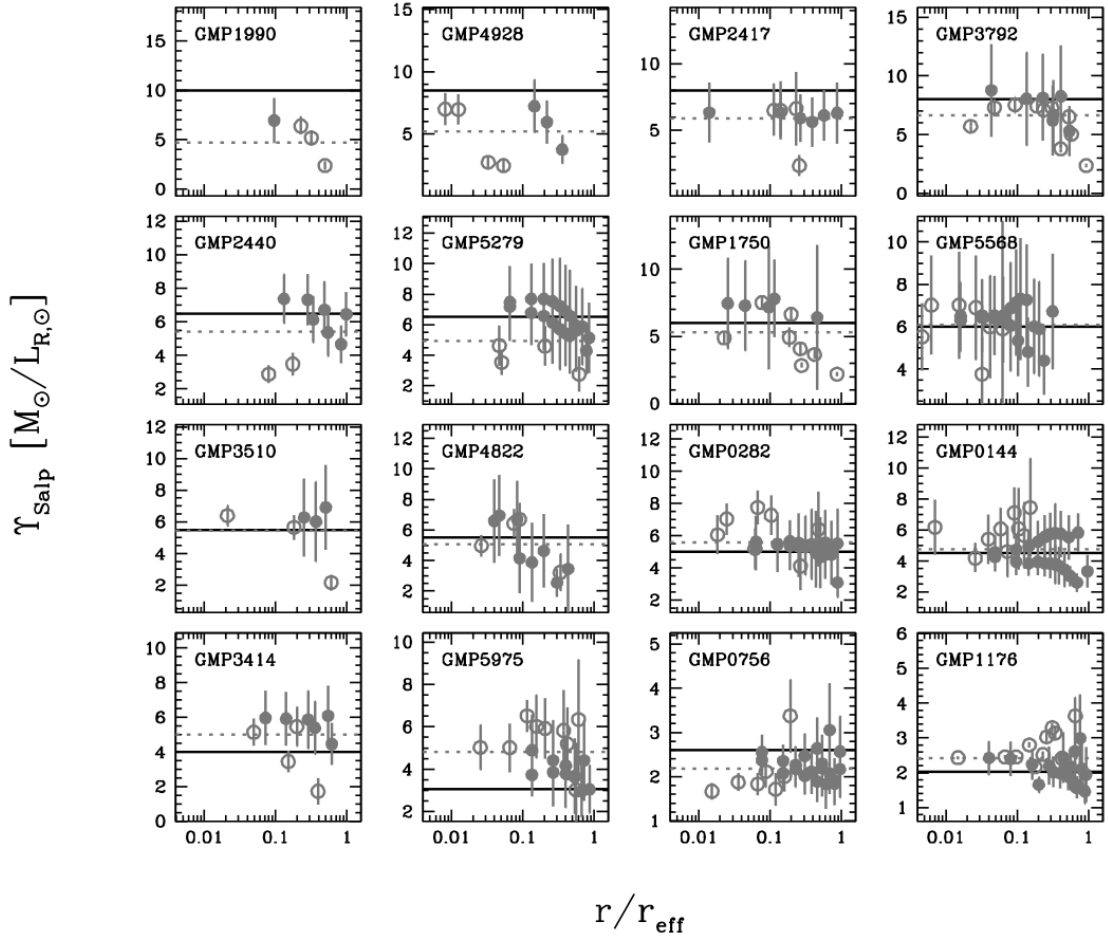
Figure 4.4: This figure shows the radial MtoL ratios for different elliptical galaxies of the Coma cluster. Plotted is the stellar MtoL in R-band assuming a Salpeter IMF at each radius along the major (filled circles) and minor (open circles) axis. The dotted line gives the light-weighted average of the Salpeter MtoL within the effective radius, the solid line represents the MtoL ratio as calculated from dynamical modeling of the shown galaxies. Credit: Thomas, J., Saglia, R. P., Bender, R., Thomas, D., Gebhardt, K., Magorrian, J., Corsini, E. M., Wegner, G., & Seitz, S. 2011: *Dynamical masses of early-type galaxies: a comparison to lensing results and implications for the stellar initial mass function and the distribution of dark matter*, MNRAS, 415, 545. Reproduced by permission of Oxford University Press.

Sec. 4.2.

The environment and formation history of elliptical galaxies are closely connected. As discussed above, the IMF defines which type of stars are formed. The red color and absence of short–lived OB stars show that these galaxies' stellar population is dominated by long–lived, redder and older stars. This implies that significant star formation has not recently taken place, so the formation of these systems' stellar components was completed fairly far in the past, see e.g. Thomas et al. (2005) and their derived star formation history in Fig. 4.6.

We see in Fig. 4.6. that the formation age of an elliptical galaxy also depends on the environment. Elliptical galaxies are dominant in dense environments, see Dressler (1980), i.e. elliptical galaxies reside preferentially in groups or clusters of galaxies. Therefore, it is commonly believed that (massive) elliptical galaxies are products of mergers of smaller galaxies (Lacey & Cole, 1993; Baugh et al., 1996). Toomre & Toomre (1972), Tinsley et al. (1977),
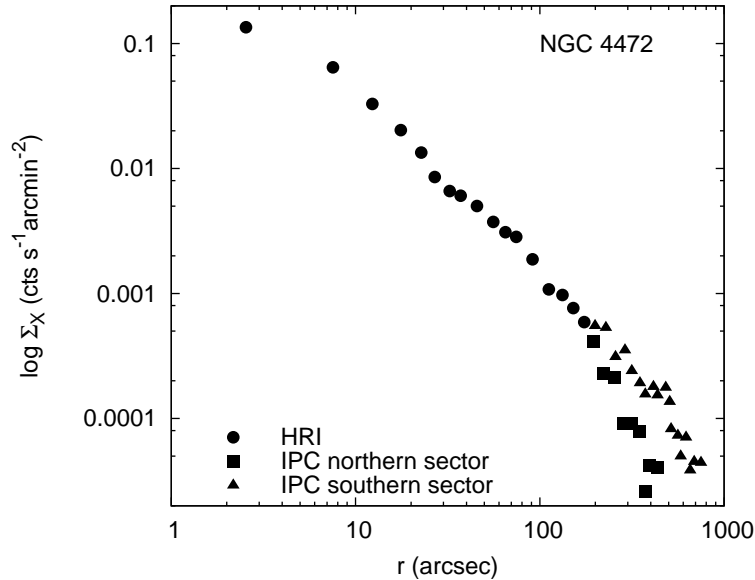
Figure 4.5: The radial X–ray surface brightness for the elliptical galaxy NGC4472. The datapoints for this figure are taken from Fabbiano (1989).

Barnes (1988), Barnes (1989) and Barnes & Hernquist (1992) have shown that elliptical galaxies form from dissipationless merging of progenitor galaxies and, due to the redistribution of angular momentum, turn into the amorphous assemblies that follow the light profiles of ellipticals. During and after such mergers, the star formation in the merger remnant is suppressed if no cold gas is present in the merger process, which gives the elliptical galaxies its red colors mentioned above, see e.g. Springel et al. (2005). Many details of these merger processes are not yet fully understood, such as the preferred mass ratio of the progenitor galaxies. The concept of mergers fits into the ΛCDM structure formation scenario: the structures in the universe are assembled in a hierarchical way, meaning that smaller structures formed earlier than larger ones, see Blumenthal et al. (1984) and the larger structures are assembled from merging of smaller structures.

Since elliptical galaxies exist predominantly in dense environments (clusters and groups of galaxies), they are interacting with their environment. Here, we focus on tidal stripping of dark halos, see e.g. Merritt (1983): Due to the interactions of the galaxies with each other, they lose fractions of their outer halos to the cluster dark matter halo. This effect is stronger the closer a galaxy is to the center of the cluster (Merritt, 1983; Warnick et al., 2008). This effect has been observed several times, see e.g. Natarajan et al. (2002a); Halkola et al. (2007); Limousin et al. (2007a). More details on that topic will be given in Chapter 7.

4.1.3 Clusters of galaxies

As mentioned before, elliptical galaxies reside preferentially in clusters of galaxies and dominate the population of galaxies in a cluster (Dressler, 1980). These clusters are the biggest, gravitationally bound structures in the universe with typical total masses of $10^{14} - 10^{15}\,\mathrm{M_\odot}$. Fig. 1.2 shows a typical image of a rich galaxy cluster. Many elliptical galaxies in a cluster share a tight relation between their color and brightness. This fact is called the red sequence,
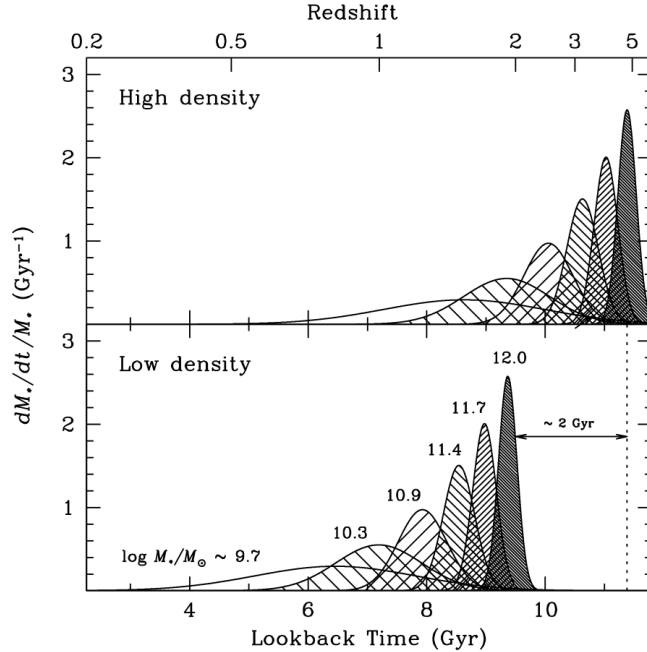
Figure 4.6: Plotted are the star formation histories for early type galaxies of different stellar masses. As can be seen, the star formation for galaxies in high density environments has its peak earlier in time. All elliptical galaxies have its vast majority of star formation far in the past, giving it its red color by evolution of the stellar components. Credit: Thomas et al. (2005). Reproduced by permission of the AAS.

e.g. many of the galaxies visible in Fig. 1.2 appear to have a similar color, forming the red sequence of this cluster. This fact is used to find clusters by looking at spatial clustering of galaxies which follow such a red sequence (e.g. Postman et al. 1996 Gladders & Yee 2000). Typically, in the very center (Lin & Mohr, 2004) of a cluster of galaxies an elliptical galaxy resides, often being the brightest cluster galaxy (BCG), see e.g. Fig. 7.2. This BCG is probably formed through merging processes (Dubinski, 1998). Besides galaxies, a cluster also contains hot, X–ray luminous gas which accounts for $\sim 10\%$ of the total mass of a cluster (Evrard, 1997). This gas can be successfully used to find galaxy clusters (Giacconi et al., 1972), and has already been applied to the whole sky (Böhringer et al., 2000; de Grandi et al., 1999). The most massive component of a galaxy cluster, however, is its dark matter halo. The distribution of the dark matter can be described with the same profile as the galaxy halos (Navarro et al., 1997). Weak gravitational lensing is especially suited for the investigation of the spatial distribution of this component at large radii, e.g. Umetsu et al. (2012).

4.1.4 Elliptical galaxies scaling relations

As seen before, elliptical galaxies show remarkable similarity in some of their properties. Hence, some characteristics of these can be described with simple scaling relations. First, a relation exists between a galaxy's measured stellar velocity dispersion and its luminosity L_x, measured in some filter x. This relation is called Faber-Jackson relation (FJ), as it was first described by Faber & Jackson (1976):

$$\sigma \sim L_x^{\delta} \quad . \tag{4.2}$$

Traditionally, the B-filter has been used for measuring the FJ relation in local galaxies, see Fig. 4.7. The exponent δ has values close to 0.25, although it is subject to change depending on e.g. the mass range, the method and the wavelength considered, see e.g. Rusin et al. (2003a); Matković & Guzmán (2005); Nigoche-Netro et al. (2010). In Fig. 4.7 the first measurement of the Faber-Jackson relation is plotted.
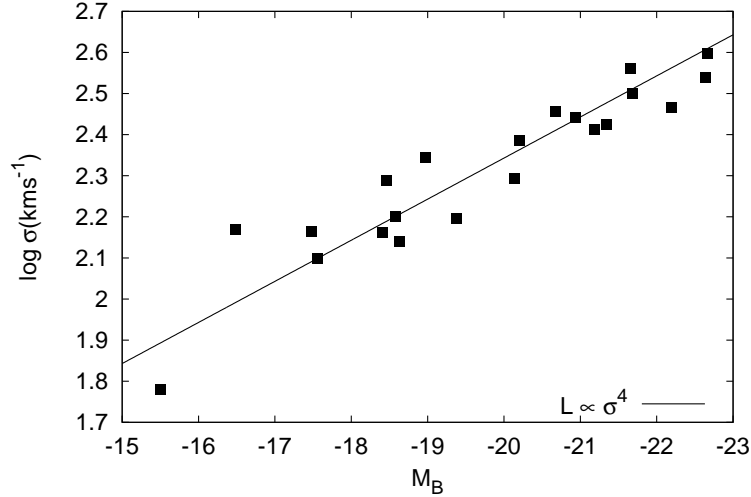
Figure 4.7: This figure shows the Faber-Jackson relation for elliptical galaxies, as published in Faber & Jackson (1976). The logarithm of the line–of–sight velocity dispersion is plotted versus the absolute B-band magnitude. The points mark the measured values for different galaxies, while the line marks the $\delta = 0.25$ reference line. The data for this plot is taken from Faber & Jackson (1976).

Another important scaling relation is the so-called Fundamental Plane (FP) (Djorgovski & Davis, 1987; Bender et al., 1992; Saglia et al., 2010), linking the effective radius R_{eff}, mean surface brightness I_{eff} within this radius and the stellar velocity dispersion σ:

$$\log R_{eff} = a \log \sigma + b \log I_{eff} + c \quad , \tag{4.3}$$

with fit parameters $a \sim 1.5$, $b \sim -0.75$ and $c \sim -8.8$, as taken from Bernardi et al. (2003a) for the g^*, r^*, i^* and z^* filters. Bender et al. (1992) show that this relation can be transformed into a new coordinate system:

$$\kappa_1 = (\log \sigma^2 + \log R_{eff})/\sqrt{2}$$
$$\kappa_2 = (\log \sigma^2 + 2 \log I_{eff} - \log R_{eff})/\sqrt{6} \tag{4.4}$$
$$\kappa_3 = (\log \sigma^2 - \log I_{eff} - \log R_{eff})/\sqrt{3} \quad .$$

A measurement of early-type galaxies in this κ–space is shown in Fig. 4.8.

As can be seen, the galaxies form a tight plane in this representation. This relation holds for local early-type galaxies. Saglia et al. (2010) see some hints that this plane might rotate for higher redshifts ($z \gtrsim 0.7$ for galaxies in clusters).

As stated above the MtoL describes the relation of total / stellar mass to observed luminosity. Considering elliptical galaxies with different luminosity, we see that this MtoL is a function of it:

$$\frac{M_{tot}}{L_x} \sim L_x^\epsilon \quad . \tag{4.5}$$
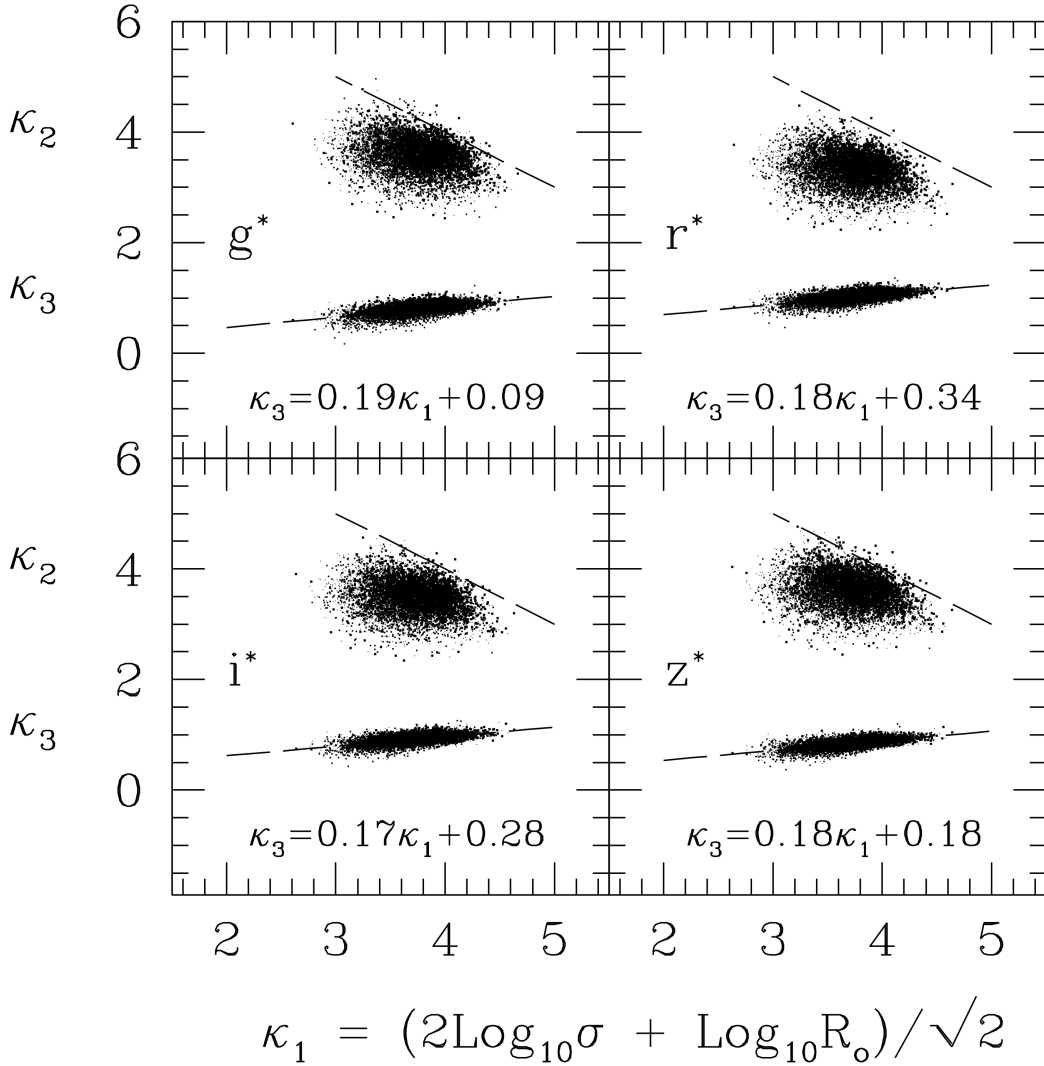
Figure 4.8: This Figure shows the Fundamental Plane of early–type galaxies as observed from the Sloan Digital Sky Survey. Plotted is the κ–space (see Bender et al. 1992) for one of the g^*, r^*, i^* and z^* filters in each of the 4 panels.. As can be seen, the galaxies form a tight plane in this space. Credit: Bernardi et al. (2003a). Reproduced by permission of the AAS.

The value of ϵ is not universal but depends on the filter in which the luminosity is measured and the mass range that is considered, see Barbera et al. (2011). For the fundamental plane stated above, e.g. Bender et al. (1992) get a value $\epsilon \sim 0.2$ in the B–band for the central, dynamical mass.

4.2 Matter profiles

Elliptical galaxies typically have a mass in the range of $10^9 M_\odot$ to $10^{12} M_\odot$ and a luminosity greater than $\approx 3 \times 10^9 L_{\odot,B}$, otherwise, they are counted as dwarf ellipticals (dE), see Sparke & Gallagher (2000). We will briefly summarize the different descriptions for the mass distributions in an elliptical galaxy. To do that, we present common mass profiles for ellipti-

cal galaxies. Since gravitational lensing measures only LOS-projected mass profiles, we only present these. The most common one is the so-called isothermal sphere.

4.2.1   Isothermal profile

This profile is widely used in lensing because the measured velocity dispersions are nearly constant with radius for elliptical galaxies without ordered rotation (see e.g. Bender et al. 1994 and Fig. 4.9).
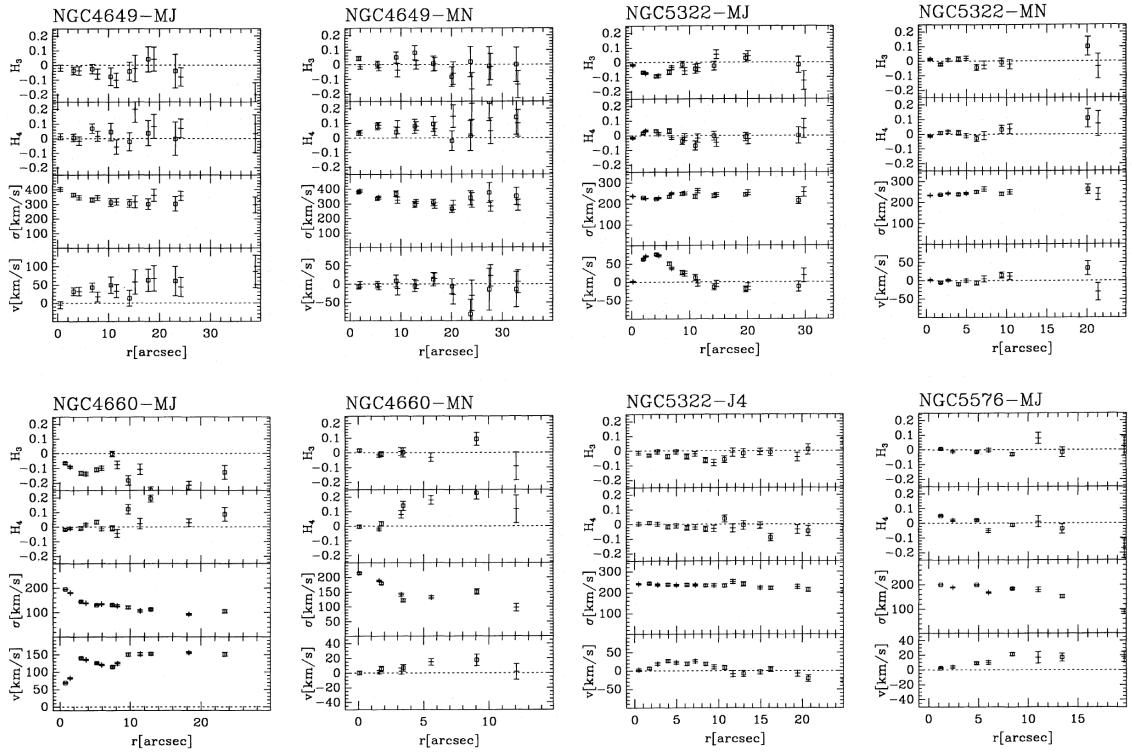
Figure 4.9: For four elliptical galaxies, the velocity dispersion σ and rotation velocity v of stars along the major and minor axis is plotted. H_3 and H_4 mark higher moments of the rotation that we do not consider here. As can be seen, the velocity dispersions are approximately independent of the radius, at least for cases with negligible rotation velocities, justifying the approximation of an isothermal profile. Credit: Bender, R., Saglia, R. P., & Gerhard, O. E. 1994: *Line-of-Sight Velocity Distributions of Elliptical Galaxies*, MNRAS, 269, 785.

Hence we assume a constant velocity dispersion σ_v. We treat the stars in an elliptical galaxy as particles of an ideal gas now, therefore a constant σ_v implies a constant temperature T of that gas. We start with the equation of state for an ideal gas, see e.g. Narayan & Bartelmann (1996):

$$p = \frac{\rho \mathrm{kT}}{\mathrm{m}} \quad , \tag{4.6}$$

with p denoting the pressure, k the Boltzmann constant, T the system's temperature and m the test particle's mass. If we require thermal and hydrostatic equilibrium $\mathrm{m}\sigma_\mathrm{v}^2 = \mathrm{kT}$, $\frac{\mathrm{dp}}{\mathrm{d}r} = -\frac{\mathrm{GM}\rho}{r^2}$ (σ_v denoting the one-dimensional velocity dispersion and M the mass enclosed in radius r), we get for the density:

$$\rho(r) = \frac{\sigma_{\rm v}^2}{2\pi {\rm G} r^2} \quad . \tag{4.7}$$

Projection along the LOS gives for the surface density and convergence:

$$\Sigma(\xi) = \frac{\sigma_{\rm v}^2}{2{\rm G}\xi} \quad , \quad \kappa(\Theta) = \frac{2\pi\sigma_{\rm v}^2}{{\rm c}^2\Theta}\frac{{\rm D}_{\rm ds}}{{\rm D}_{\rm s}} \quad . \tag{4.8}$$

From that, we can calculate the deflection angle via Eq. 3.8:

$$\alpha(\Theta) = \Theta_{\rm E} = \frac{4\pi\sigma_{\rm v}^2}{{\rm c}^2}\frac{{\rm D}_{\rm ds}}{{\rm D}_{\rm s}} \quad . \tag{4.9}$$

As one can see, this implies that the deflection angle is constant for this profile. Since most of the galaxies are not spherical, as we have seen before, for real galaxies we need to extend this to "elliptical models": we can introduce some ellipticity by $\Theta = \sqrt{\Theta_1^2 + \frac{\Theta_2^2}{q^2}}$, where q is the axis ratio of the surface density. Further, to remove the central singularity, we can introduce a core radius $\Theta_{\rm c}$. We then get a convergence of[5]:

$$\kappa(\Theta) = \frac{2\pi\sigma_{\rm v}^2}{{\rm c}^2}\frac{{\rm D}_{\rm ds}}{{\rm D}_{\rm s}}\frac{1}{\left(\Theta_{\rm c}^2 + \Theta_1^2 + \frac{\Theta_2^2}{q^2}\right)^\beta} \quad . \tag{4.10}$$

In Eq. 4.10, we also allowed the actual steepness of the profile to vary by introducing β (in the case of an isothermal model $\beta = 0.5$), and call that a (non–)singular isothermal ellipsoid ((N–)SIE) in the isothermal case or a power–law (PL) model in case of a $\beta \neq 0.5$.

BBS–profile Looking closely at Eq. 4.7, one might notice a flaw in it: the mass enclosed in radius r increases linearly with r. This is problematic since it is nonsensical for objects in the universe to grow to an infinite mass. Therefore, we add a truncation radius $r_{\rm trunc}$ at which the steepness of the profile changes to get a finite mass when integrating out to infinite radius. One way of implementing this was done by Brainerd et al. (1996):

$$\Sigma(\xi) = \frac{\sigma_{\rm v}^2}{2{\rm G}}\left(\frac{1}{\xi} - \frac{1}{\sqrt{\xi^2 + {\rm r}_{\rm trunc}^2}}\right) \quad \kappa(\Theta) = \frac{2\pi\sigma_{\rm v}^2}{{\rm c}^2}\frac{{\rm D}_{\rm ds}}{{\rm D}_{\rm s}}\left(\frac{1}{\Theta} - \frac{1}{\sqrt{\Theta^2 + \Theta_{\rm trunc}^2}}\right) \quad . \tag{4.11}$$

For $\Theta \ll \Theta_{\rm trunc}$, this profile is isothermal, see Eq. 4.8. The other limit $\Theta \gg \Theta_{\rm trunc}$ gives Θ^{-3} as the asymptotic behavior, therefore the integrated mass stays finite.
In Fig. 4.10 some of the above mentioned mass profiles are plotted.
The core radius makes the profile essentially flat within this radius while the profiles follow their singular counterparts on larger radii. We also note that the BBS profile follows its untruncated counterpart well inside the truncation radius, while at larger radii, the density declines faster than the isothermal model.

---

[5]This is only conceptual, actual implementations in lensing modeling codes will have a slightly different appearance for numerical reasons.
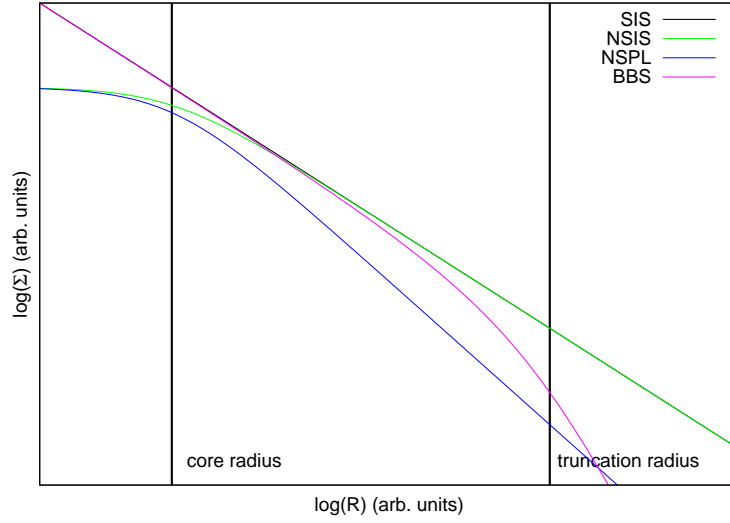
Figure 4.10: This plot shows the different radial isothermal surface density profiles in a log–log scale. We use different kinds of models: A singular isothermal sphere (SIS), Eq. 4.8, two models following its extension Eq. 4.10 for spherical cases (NSIS,NSPL), the BBS model, Eq. 4.11. For both the NSIS and NSPL model, we additionally use the indicated core radius, the NSPL model also has a modified steepness $\beta = 0.7$. For the BBS model, we utilize the indicated truncation radius.

4.2.2 NFW–profile

While the isothermal profile describes the total mass profile, the so called NFW profile Navarro et al. (1997) explicitly describes the cold dark matter halo of a galaxy. In numerical studies of structure formation in a ΛCDM scenario, the halo profiles follow the form

$$\rho(r) = \frac{\delta_{\mathrm{c}} \rho_{\mathrm{c}}}{\frac{r}{r_{\mathrm{s}}} \left(1 + \frac{r}{r_{\mathrm{s}}}\right)^2} \tag{4.12}$$

in the spherical case. ρ_{c} is the critical density of the universe, δ_{c} the characteristic overdensity of the halo and r_{s} is the so–called scale radius which marks a transition in the profile steepness. Most of the time, the NFW-halo is parametrized with a parameter c, called concentration, and r_{200} the radius of the sphere that has an average density of $200\rho_{\mathrm{c}}$:

$$r_{200} = r_{\mathrm{s}} c \quad , \quad \delta_{\mathrm{c}} = \frac{200 c^3}{3 \ln(1 + c) - \frac{c}{1+c}} \quad . \tag{4.13}$$

Wright & Brainerd (2000) investigate the lensing properties of this halo model, so interested readers are referred to their work. For the convergence, they state (R refers to the projected radius on the sky, to avoid ambiguity the speed of light is c_{l} in this case.):
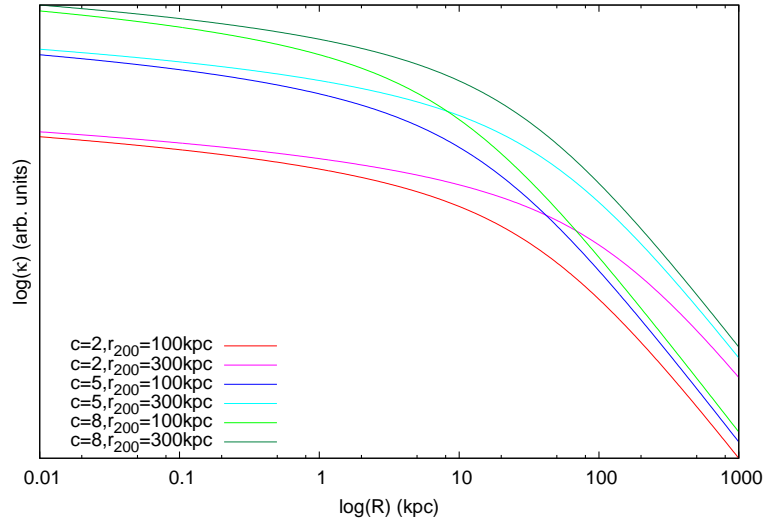
Figure 4.11: Different NFW-like halo convergence maps, the numbers give the concentration c and r_{200} for the plotted curves. As one can see, a higher concentration leads to a higher central density, while a higher r_{200} leads to a higher density on the outskirts of the halo.

$$\kappa(R) = \frac{\Sigma(R)}{\Sigma_{\mathrm{crit}}} = \frac{8\pi G r_s \delta_c \rho_c}{c_l^2} \frac{D_d D_{ds}}{D_s} \begin{cases} \frac{1}{\left(\frac{R}{r_s}\right)^2 - 1}\left[1 - \frac{2}{\sqrt{1-\left(\frac{R}{r_s}\right)^2}}\operatorname{arctanh}\sqrt{\frac{1-\frac{R}{r_s}}{1+\frac{R}{r_s}}}\right] & R < r_s \\ \frac{1}{3} & R = r_s \\ \frac{1}{\left(\frac{R}{r_s}\right)^2 - 1}\left[1 - \frac{2}{\sqrt{\left(\frac{R}{r_s}\right)^2-1}}\arctan\sqrt{\frac{\frac{R}{r_s}-1}{\frac{R}{r_s}+1}}\right] & R > r_s \end{cases} .$$

$$(4.14)$$

This convergence for typical values of the concentration c and r_{200} is plotted in Fig. 4.11.

Golden gravitational lensing systems from the Sloan Lens ACS Survey. I. SDSS J1538+5817: one lens for two sources[12]

C. Grillo[1,2,*], T. Eichner[2], S. Seitz[2,1], R. Bender[2,1], M. Lombardi[3,4], R. Gobat[5], and A. Bauer[2]

[1]Max-Planck-Institut für extraterrestrische Physik, Giessenbachstr., D-85748 Garching bei München, Germany
[2]Universitäts-Sternwarte München, Scheinerstr. 1, D-81679 München, Germany
[3]European Southern Observatory, Karl-Schwarzschild-Str. 2, D-85748 Garching bei München, Germany
[4]University of Milan, Department of Physics, via Celoria 16, I-20133 Milan, Italy
[5]CEA Saclay, DSM/DAPNIA/Service d'Astrophysique, F-91191 Gif-sur-Yvette Cedex, France
[*]cgrillo@usm.lmu.de

5.1 Abstract

We present a gravitational lensing and photometric study of the exceptional strong lensing system SDSS J1538+5817, identified by the Sloan Lens ACS survey. The lens is a luminous elliptical galaxy at redshift $z_l = 0.143$. Using Hubble Space Telescope public images obtained with two different filters, the presence of two background sources lensed, respectively, into an Einstein ring and a double system is ascertained. Our new spectroscopic observations, performed at the Nordic Optical Telescope, reveal unequivocally that the two sources are located at the same redshift $z_s = 0.531$. We investigate the total (luminous and dark) mass

---

[1]Based on observations made with the NASA/ESA Hubble Space Telescope, obtained from the data archive at the Space Telescope Institute. STScI is operated by the association of Universities for Research in Astronomy, Inc. under the NASA contract NAS 5-26555.

[2]Based on observations made with the Nordic Optical Telescope, operated on the island of La Palma jointly by Denmark, Finland, Iceland, Norway, and Sweden, in the Spanish Observatorio del Roque de los Muchachos of the Instituto de Astrofisica de Canarias.

distribution of the lens between 1 and 4 kpc from the galaxy center by means of parametric and non-parametric lensing codes that describe the multiple images as point-like objects. Bootstrapping and Bayesian analyses are performed to determine the uncertainties on the quantities relevant to the lens mass characterization. Several disparate lensing models provide results that are consistent, given the errors, with those obtained from the best-fit model of the lens mass distribution in terms of a singular power law ellipsoid model. In particular, the lensing models agree on: (1) reproducing accurately the observed positions of the images; (2) predicting a nearly axisymmetric total mass distribution, centered and oriented as the light distribution; (3) measuring a value of $8.11^{+0.27}_{-0.59} \times 10^{10}\,M_\odot$ for the total mass projected within the Einstein radius of 2.5 kpc; (4) estimating a total mass density profile slightly steeper than an isothermal one $[\rho(r) \propto r^{-2.33^{+0.43}_{-0.20}}]$. A fit of the Sloan Digital Sky Survey multicolor photometry with composite stellar population models provides a value of $20^{+1}_{-4} \times 10^{10}\,M_\odot$ for the total mass of the galaxy in the form of stars and of $0.9^{+0.1}_{-0.2}$ for the fraction of projected luminous over total mass enclosed inside the Einstein radius. By combining lensing (total) and photometric (luminous) mass measurements, we differentiate the lens mass content in terms of luminous and dark matter components. This two-component modeling, which is viable only in extraordinary systems like SDSS J1538+5817, leads to a description of the global properties of the galaxy dark matter halo. Extending these results to a larger number of lens galaxies would improve considerably our understanding of galaxy formation and evolution processes in the ΛCDM scenario.

galaxies: elliptical and lenticular, cD − galaxies: individual (SDSS J1538+5817) − galaxies: structure − dark matter − gravitational lensing

5.2   Introduction

Early-type galaxies host the majority of the baryonic mass observed in galaxies in the Universe (e.g., Fukugita et al. 1998; Renzini 2006); hence, deciphering the processes that lead to their formation and the mechanisms that rule their subsequent evolution is a key cosmological issue. For instance, it is still debated whether early-type galaxies form at relatively high redshift ($z \lesssim 2$) as a result of a global starburst and then passively evolve to the present (e.g., Eggen et al. 1962; Larson 1974; Arimoto & Yoshii 1987; Bressan et al. 1994) or whether they assemble from mutual disruption of disks in merging events (e.g., Tinsley et al. 1977; White & Rees 1978). Information with which to distinguish these scenarios lies in the characteristics of galaxy dark-matter halos. However, the lack of suitable and easily interpreted kinematical tracers, such as HI in spirals, has made comprehensive studies on the dark matter component in early-type galaxies rather difficult (e.g., Bertin et al. 1992; Saglia et al. 1992; Thomas et al. 2007, 2009).

In the last few years, strong gravitational lensing has allowed astrophysicists to make great progress in the understanding of the internal structure of early-type galaxies. Through lensing, it has become possible to address in detail some fundamental problems related to the mechanisms of formation of early-type galaxies, like the determination of the amount and distribution of dark matter (e.g., Gavazzi et al. 2007; Grillo et al. 2008c, 2009; Barnabè et al. 2009) or the investigation of the total mass density profile and its redshift evolution (e.g., Treu & Koopmans 2004; Koopmans et al. 2006). Several algorithms have been developed in order to fit the observational data of a strong gravitational lens system and, thus, to reconstruct the properties of a lens.

Simplifying, a first difference between codes is the use of a parametric model (e.g., gravlens[3], Keeton 2001c,a; Seitz et al. 1998; Warren & Dye 2003; Halkola et al. 2006; Rzepecki et al. 2007; Grillo et al. 2008c) or a non-parametric model (e.g., PixeLens[4], Saha & Williams 2004; York et al. 2005; Suyu et al. 2009) to describe the mass distribution of a lens. In the former case, the mass distribution of a lens is assumed to be accurately described by an analytical expression; the fundamental scales of the model are determined by comparing the observed and model-predicted properties of the multiple images. In the latter case, a pixelated map or a multipole decomposition of the surface mass density of the lens is usually estimated through a statistical analysis that requires, in addition to the observational information, some extra physically plausible constraints, called priors, on the surface mass density distribution (e.g., positive-definite and smooth) of the lens. On the one hand, parametric models provide a great deal of freedom and complexity, but they do not cover "naturally" all the possible realistic mass distributions (for instance, surface mass density distributions with twisting isodensity contours); on the other hand, even if non-parametric models are more general, their number of degrees of freedom is often much larger than the constraints and this can result in three-dimensional density distributions that are dynamically unrealistic or unstable. A viable solution to obtain physically significant density distributions is to consider a framework where the mass distribution of the lens is reconstructed by combining in a fully self-consistent way both gravitational lensing and stellar dynamics measurements (e.g., Barnabè & Koopmans 2007).
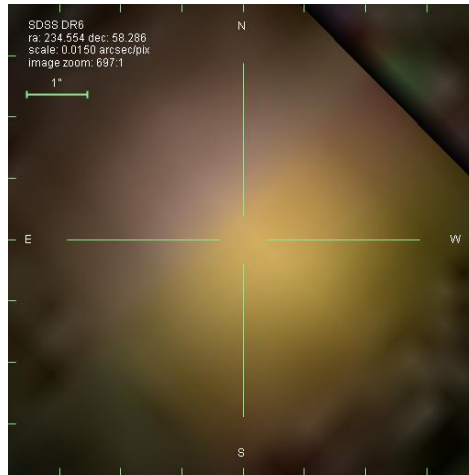
Figure 5.1: SDSS gri image centered on the lens galaxy.

Lensing codes are further distinguished by the fact that the multiple images and the corresponding sources can be modeled as point-like (e.g., gravlens; PixeLens; Seitz et al. 1998; Halkola et al. 2006) or extended (e.g., Warren & Dye 2003; York et al. 2005; Rzepecki et al. 2007; Grillo et al. 2008c; Suyu et al. 2009) objects. In the context of point-like algorithms, the best-fit model is defined as that which minimizes the chi-square between the measured positions of the centroids of the images and the positions reproduced by the model, weighted by the measurement uncertainties. Additional chi-square terms that quantify the agreement between the observed and model-predicted relative fluxes and time delays of the multiple

---

[3]http://redfive.rutgers.edu/~keeton/gravlens/
[4]http://www.qgd.uzh.ch/projects/pixelens/
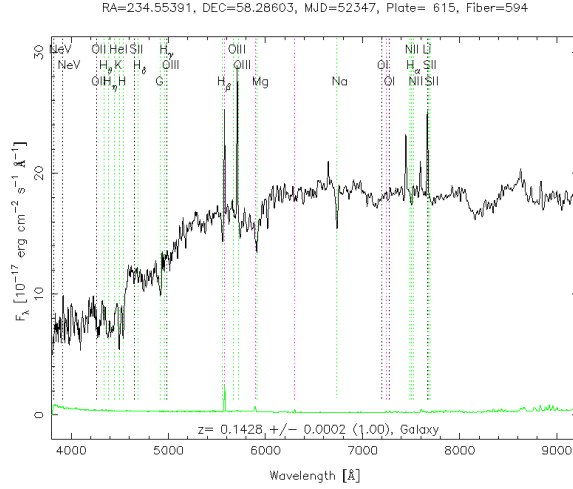
Figure 5.2: SDSS spectrum obtained within an aperture of 3" diameter centered on the lens galaxy.

Table 5.1: The lens galaxy.

RA (J2000)	Dec (J2000)	z_l	$q_{\rm L}$	$\theta_{q_{\rm L}}$ (deg)	θ_e (")	u (mag)	g (mag)	r (mag)	i (mag)	z (mag)
15:38:12.92	+58:17:09.8	0.143	0.82	157.3	1.58	19.50 ± 0.06	18.17 ± 0.01	17.17 ± 0.01	16.74 ± 0.01	16.43 ± 0.01

References – Bolton et al. 2008a.

Notes – Magnitudes are extinction-corrected modelMag (AB) from the SDSS.

images can also be included. For extended algorithms, the goodness of a model is estimated by comparing on a pixelated grid the image surface brightness morphology and distribution which are observed to those which are reproduced by the model (after convolution with the relevant point spread function).

The relative positions of a multiply imaged system can sometimes be measured with an accuracy of a few milli-arcseconds (e.g., Patnaik & Kemball 2001) and these positions represent the most important constraints on the mass distribution of the lens. In fact, although the flux ratios of the multiple images can be easily estimated and offer another important source of information, the sensitivity of the flux measurements to details such as the dark matter substructure of the lens, the extinction in the interstellar medium of the lens, the microlensing effects of the stars present in the lens, and the time variability in the source decrease their potential. Time delays can also help to determine the mass distribution of a lens, but a statistically significant number of measurements of this kind is just starting to become available.

The projected total mass enclosed within a cylinder of radius equal to the Einstein radius of a lensing system can be accurately measured by only fitting the observed positions of the multiple images (e.g., Kochanek 1991; Grillo et al. 2008c), whereas a detailed fit of the possible arcs and rings associated with an extended source is necessary if the interest is in the properties of both lens and source (e.g., Swinbank et al. 2007; Vegetti & Koopmans 2009). By combining lensing and multiband photometric measurements, the amount of mass present in a lens galaxy in the forms of dark and visible matter can be determined (e.g., Grillo et al.
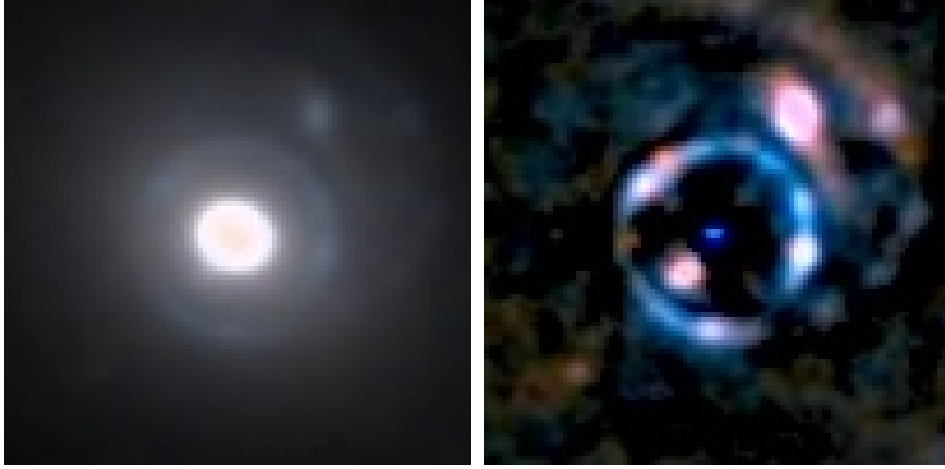
Figure 5.3: Color images of a 5″ × 5″ field around the gravitational lensing system SDSS J1538+5817, before (<u>on the left</u>) and after (<u>on the right</u>) the subtraction of an elliptical model, fitted on the luminosity profile of the lens galaxy. The images are obtained by combining the <u>F606W</u> HST/WFPC2 and the <u>F814W</u> HST/ACS filters.

2008a, 2009).

In addition to projected total mass, lensing analyses allow one to estimate also the total mass density profile of lens galaxies (e.g., Rusin et al. 2003b; Rusin & Kochanek 2005). This can be achieved either by combining in a statistical way lensing and stellar dynamics data in a sample of lens galaxies that are assumed to have a homologous structure (e.g., Koopmans et al. 2006), by performing a joint lensing and extended stellar kinematics study in a single lens galaxy (e.g., Barnabè et al. 2009; Treu & Koopmans 2004), or by using lensing only in exceptional lensing systems that show multiple images of different sources probing wide angular and radial ranges of the lens mass distribution (e.g., Sykes et al. 1998; Nair 1998).

In this paper, we study the lensing system SDSS J1538+5817, discovered by the Sloan Lens ACS (SLACS) survey[5]. This system is particularly interesting because two different sources are lensed, one into an Einstein ring with four luminosity peaks and the other into two images, by an early-type galaxy that has an almost circular projected light distribution. The large number of images at various angular distances from the galaxy center and the nearly perfect axisymmetric lensing configuration of the ring makes this system the ideal laboratory to disentangle the luminous and dark components of the lens mass distribution.

The paper is organized as follows. In Sect. 5.3, we describe the observational data for the complex strong lensing system SDSS J1538+5817. We perform parametric lensing analyses of this system in Sect. 5.4. Then, in Sect. 5.5, we investigate the luminous and dark matter composition of the lens galaxy. In Sect. 5.6, we summarize the results obtained in this study. Finally, in the Appendix, we model the lens mass distribution on a pixelated grid and compare these non-parametric results to those from Sect. 5.4. Throughout this work we assume $H_0 = 70$ km s^{-1} Mpc^{-1}, $\Omega_m = 0.3$, and $\Omega_\Lambda = 0.7$. In this model, 1″ corresponds to a linear size of 2.51 kpc at the lens plane.

Table 5.2: Astrometric and photometric measurements for the multiple images.

	x^{a} (")	y^{a} (")	z_s	$\delta_{x,y}$	f (")	δ_f	d^{a} (")
D_1	0.88	1.31	0.531	0.05	1.00	0.30	1.58
D_2	−0.33	−0.40	0.531	0.05	0.17	0.09	0.52
Q_1	0.96	0.33	0.531	0.05			1.02
Q_2	−0.75	0.60	0.531	0.05			0.96
Q_3	−0.15	−0.98	0.531	0.05			0.99
Q_4	0.95	−0.19	0.531	0.05			0.97

$^{\mathrm{a}}$ With respect to the galaxy center.
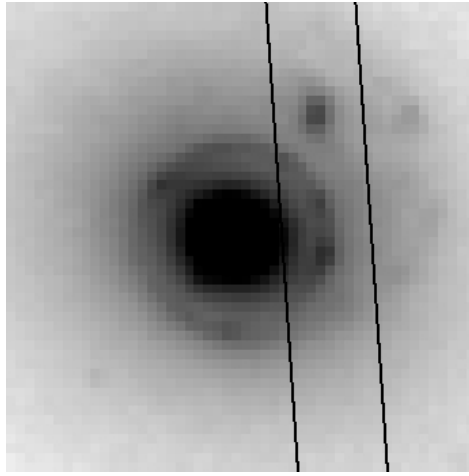
Figure 5.4: Observational configuration for the spectroscopic measurements obtained at the NOT telescope with the ALFOSC instrument: position of the 1" long-slit.
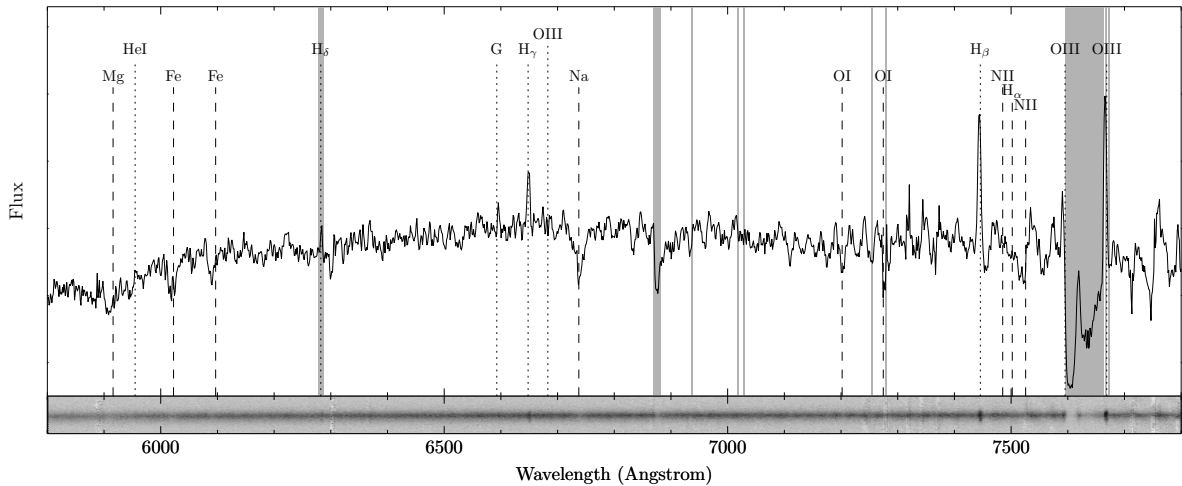
Figure 5.5: The NOT/ALFOSC 1D (on the top) and 2D (on the bottom) spectra of the lensing system SDSS J1538+5817. In the wavelength range shown here, the most prominent spectral features at the redshift of the lens ($z_l = 0.143$) and sources ($z_s = 0.531$) are marked, respectively, with dashed and dotted lines. The shaded regions indicate the principal telluric lines. The flux is given in arbitrary units.
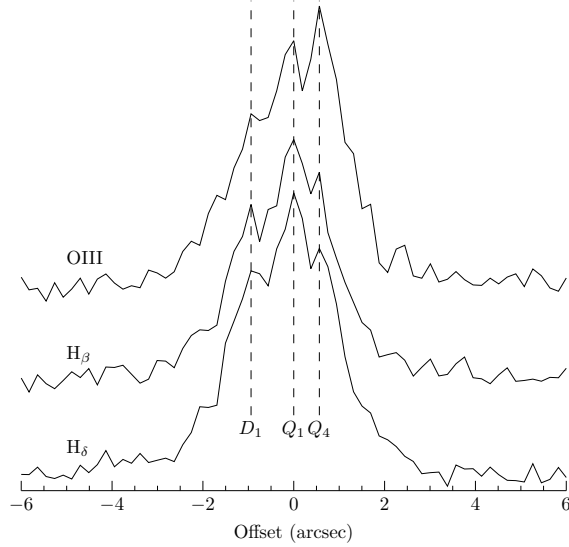
Figure 5.6: Intensity (in arbitrary units) of the three H_δ, H_β, and [OIII] $\lambda 5007$ emission lines along the slit width. The dashed lines mark the positions of three observed peaks that trace closely the geometrical configuration of the D_1, Q_1, and Q_4 images.

5.3 Observations

The SLACS survey was started in 2003 and aims at studying, from a lensing and dynamics perspective, a statistically significant number of galaxies acting as strong lenses and located at redshifts lower than 0.5. The candidate lenses were spectroscopically selected from the Sloan Digital Sky Survey (SDSS)[5] database by identifying those objects that show, in addition to the continuum and absorption lines of a possible lens galaxy at redshift z_l, one or multiple emission lines of a hypothetical source at a higher redshift z_s. The most promising candidates were then observed at least once with the Hubble Space Telescope (HST) Advanced Camera for Survey (ACS) to confirm the lens hypothesis (for further information, see Bolton et al. 2006, 2008a). This procedure resulted in the sample of 63 "grade-A" strong gravitational lensing systems presented in Bolton et al. (2008a). SDSS J1538 + 5817 is one of the lens galaxies discovered by the SLACS survey. The photometric and spectroscopic observations taken by the SDSS are shown in Figs. 5.1 and 5.2. As described above, the redshifts of the lens galaxy and a source ($z_l = 0.143$ and $z_s = 0.531$) were measured from different spectral features.

By making use of the publicly available observations in the F814W and F606W filters of the HST/ACS and Wide Field Planetary Camera 2 (WFPC2) respectively, we model the luminosity distribution of the lens galaxy and subtract the best-fit model from the images. In detail, a model for the lens galaxy is constructed by using an iterative procedure: first, presumable background source images are masked and isophotal contours of the lens galaxy are derived for surface brightness levels separated by 0.1 mag arcsec^{-2}. Then, all isophote contours (even if partially masked) are fitted by ellipses following the method of Bender & Moellenhoff (1987). This provides five parameters (center coordinates, major and minor axis, and position angle) per surface brightness level. The resulting table of these parameters and

associated surface brightnesses is employed to calculate a smooth elliptical model for the lens galaxy. This model is subtracted from the image, leaving as residuals only the images of the background source galaxy. The residuals are used to check and improve the masking of the source galaxy. This procedure is repeated twice until the final model for the lens galaxy is obtained. In addition, images taken in different wavelength bands provide color information for lens and source which is of additional help to identify and separate lens and source components. Color composite images of the strong lensing system and the residuals after the lens galaxy subtraction are shown in Fig. 5.3.

The excellent angular resolution of the HST allows us to identify two systems of multiple images (for labels, see Fig. 5.7): a double (D_1 and D_2) and a quad (Q_1, Q_2, Q_3, and Q_4). The images of the two systems have different colors, but the average distances from the galaxy center of D_1 and D_2 and Q_1, Q_2, Q_3, and Q_4 are consistent within the errors. This fact would imply approximately the same redshift for the two sources, if the lens total mass were close to an isothermal distribution. In addition, the absence in the SDSS spectrum of evident emission lines at a possible third redshift supports the hypothesis that the two sources are at the same distance to the observer.

Since the precise knowledge of the redshift of the two sources plays a crucial role in the determination of the total mass distribution of the lens galaxy, we decided to perform additional spectroscopic measurements to understand whether the emission lines observed in the SDSS spectrum are associated to one or both of the lensed sources. The data were obtained on June 25, 2009 as a Fast-Track Observing Program (P38-428) with the Andalucia Faint Object Spectrograph and Camera (ALFOSC) at the 2.5-m Nordic Optical Telescope (NOT) on La Palma (Spain). We positioned a 1"-wide long-slit centered in Q_1 and passing through D_1 and Q_4, as shown in Fig. 5.4. We used ALFOSC with the 8 grism, that covers a wavelength range between 5825 and 8350 Å with a dispersion of 1.3 Å per pixel. In good atmospheric conditions (seeing between 0.7 and 1") and in the same observational configuration, we obtained six exposures of 24 minutes each, resulting in a total integration time of 2.4 hrs.

In Fig. 5.5, we show the wavelength-calibrated 1D and 2D spectra. We identify several prominent absorption lines at redshift 0.143 and at least six secure emission lines (H_δ, G, H_γ, H_β, [OIII] $\lambda4959$, and [OIII] $\lambda5007$) at redshift 0.531. At the emission line positions, the presence of two intensity peaks, below and above the continuum, is visible in the 2D spectrum. In Fig. 5.6, we plot the intensity of the H_δ, H_β, and [OIII] $\lambda5007$ emission lines as a function of spatial position along the slit's cross-section. This corresponds to a representation of three sections of the 2D spectrum at the emission line abscissas. For these three emission lines, we distinguish three intensity peaks located, with respect to the continuum (lying between Q_1 and Q_4), at angular positions consistent with those of the three images D_1, Q_1, and Q_4. The measurement of the same emission lines at the same observed wavelengths proves in a conclusive way that the two sources D and Q are equally distant from the observer. We remark that the intensity values of the emission lines shown in Fig. 5.6 are differently contaminated by the lens galaxy flux.

In Table 5.1, we summarize the photometric and spectroscopic properties of the lens galaxy: the coordinates (RA, Dec, z_l), the minor to major axis ratio (q_L) and its position angle (θ_{q_L}, degrees east of north), and the SDSS multiband magnitudes (u, g, r, i, z). In Table 5.2, we report the coordinates of the multiple images (x, y, z_s) and the adopted position uncertainty on the first two coordinates ($\delta_{x,y}$), the relative flux of the double system components (f) and the respective error (δ_f), and the distance of the images to the galaxy center (d).

Table 5.3: The best-fit (minimum χ^2) parameters of the different models.

Model	b (")	x_l (")	y_l (")	q	θ_q (deg)	θ_e (")	γ	χ^2	d.o.f.
deV (nf)	1.97	−0.02	0.03	0.782	148.0	1.58		1.02	3
deV (wf)	1.83	−0.02	0.02	0.871	147.9	1.58		2.93	4
SIE (nf)	1.08	−0.03	0.04	0.866	147.5		2.00	1.15	3
SIE (wf)	1.05	−0.02	0.02	0.919	147.6		2.00	3.77	4
PL (nf)	0.82	−0.02	0.03	0.800	147.9		2.33	0.36	2
PL (wf)	0.71	−0.01	0.02	0.820	148.0		2.47	0.99	3

Notes – The notation (wf) and (nf) indicates, respectively, if the flux measurements of the double system are included in the modeling or not.

5.4 Strong gravitational lensing

We address parametric (Sect. 5.4.1) point-like modeling of the strong gravitational lensing system. We focus mainly on projected total mass and total mass density profile measurements. A comparison with the results obtained from non-parametric models is provided in the Appendix.

5.4.1 Parametric models

<u>Gravlens</u> (Keeton 2001c) is a publicly-available lensing software that, starting from the measured observables of a strong lensing system, reconstructs the properties of a lens in terms of an adopted model that is defined by some relevant parameters. By using this code, we perform a parametric analysis in which we describe the total mass distribution of the lens galaxy in terms of either an elliptical de Vaucouleurs model (deV), or a singular isothermal ellipsoid (SIE) model, or a singular power law ellipsoid (PL) model (for further details on the model definitions, see e.g. Keeton 2001a). Both a deV and an SIE model are characterized by five parameters: a length scale $\tilde{b}$ (corresponding to the value of the Einstein angle θ_{Ein} in the circular limit), the two coordinates of the center (x_l, y_l), the minor to major axis ratio q, and its position angle θ_q. For the deV model, we fix the value of the effective angle (θ_e) to that shown in Table 5.1. A PL model is more general than an SIE model. In particular, the former requires as an additional parameter the value of the exponent γ of the three dimensional density distribution $\rho(r) \propto r^{-\gamma}$ (an SIE model is retrieved by setting γ equal to 2). The convergence $\kappa(x, y)$ of a PL model, defined as the surface mass density of the model divided by the critical surface mass density of the studied lensing system (for definitions, see Schneider et al. 1992), depends on the previous parameters as follows

$$\kappa(x, y) \propto \frac{\tilde{b}^{\gamma-1}}{\left(x^2 + \frac{y^2}{q^2}\right)^{\frac{\gamma-1}{2}}} \, . \tag{5.1}$$

Due to the normalization used in the code, <u>gravlens</u> provides values of a length scale b that are related to the values of $\tilde{b}$ by a function $f(\cdot)$ of the axis ratio q:

$$b = \tilde{b}\, f(q) \, . \tag{5.2}$$

Varying the parameters of the two adopted mass models and the positions of the sources $[(x_D, y_D); (x_Q, y_Q)]$, we minimize a chi-square χ^2 function. This function compares first only the observed (see Table 5.2) and predicted positions of the multiple images [deV(nf), SIE (nf), and PL (nf) models] and then also the measured (see Table 5.2) and reconstructed fluxes of the double system [deV (wf), SIE (wf), and PL (wf) models]. In the latter case, the flux of the source imaged twice is an additional free parameter of the models. In our lensing analysis, we decide to neglect the flux constraints relative the quad system because the presence of the Einstein ring prevents us from separating accurately the individual components. For the multiple images, we assume position uncertainties equal to the size of one pixel of ACS ($0.05''$) and flux uncertainties as reported in Table 5.2 and determined by considering the different level of contamination on the flux estimates by the surface brightness of the lens galaxy.

To estimate the statistical errors in the parameters characterizing each model, we perform 2000 χ^2 minimizations on simulated data sets. These are obtained by extracting the image positions and fluxes from Gaussian distributions centered on the measured values and with standard deviations equal to the observational errors reported in Table 5.2. In addition, starting from the sets of optimized parameter values, we estimate the total projected mass $M_{\mathrm{len}}^{\mathrm{tot}}(\leq R_i)$ enclosed within seven different circular apertures of radii R_i. The first three radii are chosen as the projected distances from the lens galaxy center of the inner image of the double system, the "average" Einstein circle, and the outer image of the double system. The remaining four radii are given by the values of the midpoints of the three segments defined by the previous three points and a further point at the same distance from the outer double image as the first point is from the second one [i.e., (0.26, 0.52, 0.75, 0.98, 1.28, 1.58, 1.84)"]. The best-fit (minimum chi-square) parameter and χ^2 values of the different models are summarized in Table 5.3. For all the models, we find that the best-fit χ^2 values are smaller than the corresponding number of degrees of freedom (d.o.f.). This implies that the reconstructed positions of the images are angularly very close to the measured positions of Table 5.2. In this section, we concentrate on the results given by the one-component PL and, as a comparison with the results of previous studies, simpler SIE models and only in the next section we will address the two-component mass decomposition.

In Fig. 5.7, for the best-fit SIE (nf) model we show the reconstructed positions of the sources and the caustics, the observed and reconstructed positions of the images and the critical curves, and the Fermat potential (for definition, see Schneider et al. 1992) with its stationary points. The inclusion of the fluxes of the double system does not change significantly the best-fit parameters of the models. Moreover, the projected total mass estimates, which are presented below, are not particularly sensitive to the flux constraints. For these reasons, in the following we will mainly concentrate on the properties of the models that omit the additional source of information coming from the fluxes of the double system, i.e., the SIE (nf) and PL (nf) models. We note that the best-fit b values are on the order of 1", the typical distance of an image of the quad system from the center of the lens (see Tables 5.2 and 5.3). The best-fit values of the lens center and ellipticity show that the lens mass distribution is well centered and aligned with the galaxy light distribution (see Tables 5.1 and 5.3). In particular, we remark that the total surface mass of the lens is well approximated by an axisymmetric distribution. The best-fit values of the parameter γ of the PL models suggest that the lens total density profile is slightly steeper than an isothermal one. We estimate maximum time delays of approximately 30 and 3 days for the double and quad systems, respectively (see Table 5.4 and Fig. 5.7). Finally, as far as the positions of the sources are concerned, the model predicted angular distance of the two sources is between approximately 0.5 and 0.7"(see Table

5.5), corresponding, respectively, to 3.2 and 4.5 kpc at a redshift of 0.531.

Table 5.4: The model-predicted time delays for the best-fit model parameters given in Table 5.3.

Model	$\Delta t_{D_{2,1}}$ (days)	$\Delta t_{Q_{1,3}}$ (days)	$\Delta t_{Q_{4,3}}$ (days)	$\Delta t_{Q_{2,3}}$ (days)
SIE (nf)	24.8	0.66	0.70	2.88
PL (nf)	33.5	0.82	0.87	3.26
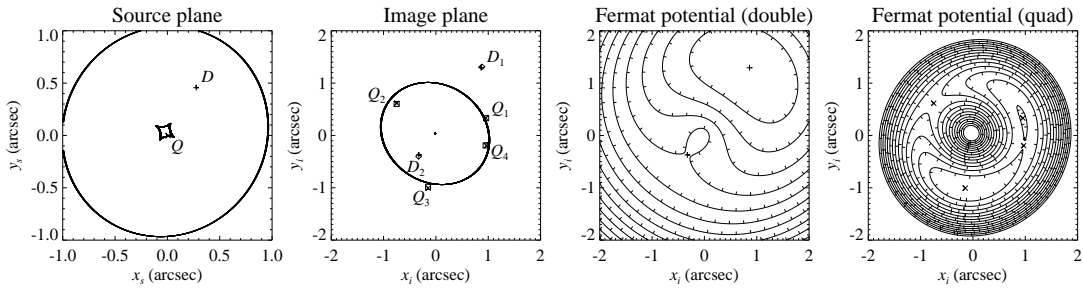
Figure 5.7: Best-fit SIE (nf) model. Left: source plane with caustics. The predicted source positions of the double and quad systems are represented by a plus and a cross symbol, respectively. Left middle: image plane with critical curves. The observed and predicted image positions of the double (diamond and plus symbols, respectively) and quad (square and cross symbols, respectively) systems are shown. Right middle: contour levels of the Fermat potential for the double system. The images are one minimum (D_1) and one saddle point (D_2). Right: contour levels of the Fermat potential for the quad system. The images are two minima (Q_1 and Q_3) and two saddle points (Q_2 and Q_4).

In Figs. 5.8 and 5.9, we plot, respectively, the joint probability distributions of the SIE (nf) and PL (nf) model parameters, with the 68% and 95% confidence regions and the 68% confidence intervals. These intervals are determined by excluding from the 2000 χ^2 minimizations the 320 smallest and the 320 largest values for each model parameter. We have checked that the error estimates determined in this way are unbiased and equivalent to the uncertainties provided by a full Markov chain Monte Carlo analysis. The comparison Figs. 5.8 and 5.9 shows clearly that adding the exponent of the total mass distribution among the parameters increases their degeneracies, hence their error estimates. The probability distribution of the position angle θ_q is bimodal, with a secondary peak located nearly 90° away from the primary one, found at approximately 150°. From the last column of plots in Fig. 5.8, we see that the secondary peak is included only in the 95% CL regions, and, from the last panel of the same figure, we note that the low values of θ_q are associated with almost circular models (i.e., $q \simeq 1$). The bimodal distribution of the values of the lens position angle can then be explained by looking at the source plane of Fig. 5.7. If the axis ratio of a model is close to one, the

Table 5.5: The model-predicted source positions for the best-fit model parameters given in Table 5.3.

Model	(x_D, y_D) (",")	(x_Q, y_Q) (",")	$d_{D,Q}$ (")
SIE (nf)	(0.27,0.46)	(0.00,0.00)	0.53
PL (nf)	(0.39,0.60)	(0.02,−0.01)	0.72
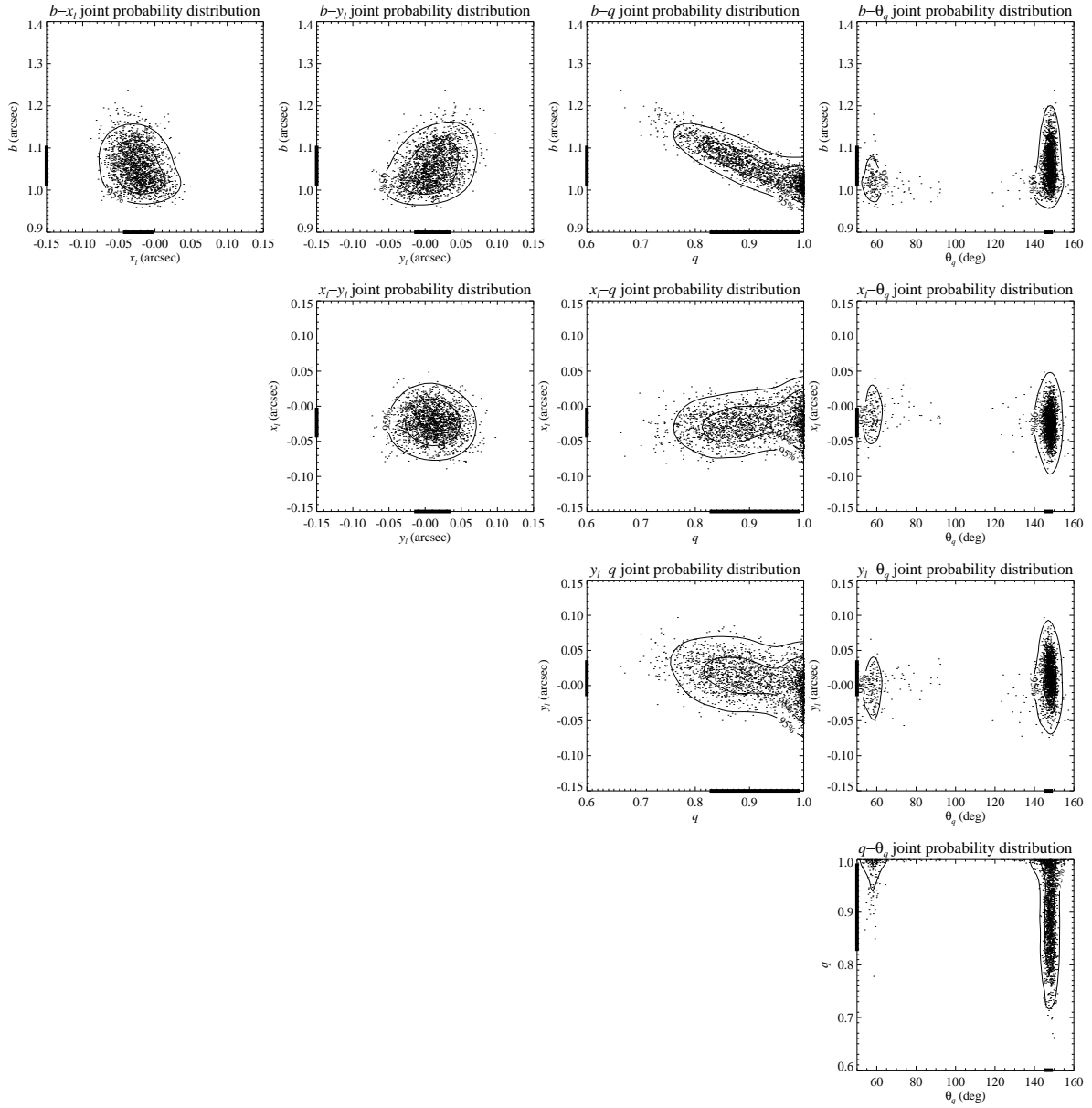
Figure 5.8: Estimates of the errors and correlations in the parameters for an SIE (nf) model. Results of the χ^2 minimizations on 2000 Monte-Carlo simulated data sets. Thick bars on the co-ordinate axes and contour levels on the planes represent, respectively, the 68% confidence intervals and the 68% and 95% confidence regions. For each model parameter, the 68% confidence interval is determined by excluding from the 2000 χ^2 minimizations the 320 smallest and the 320 largest values.
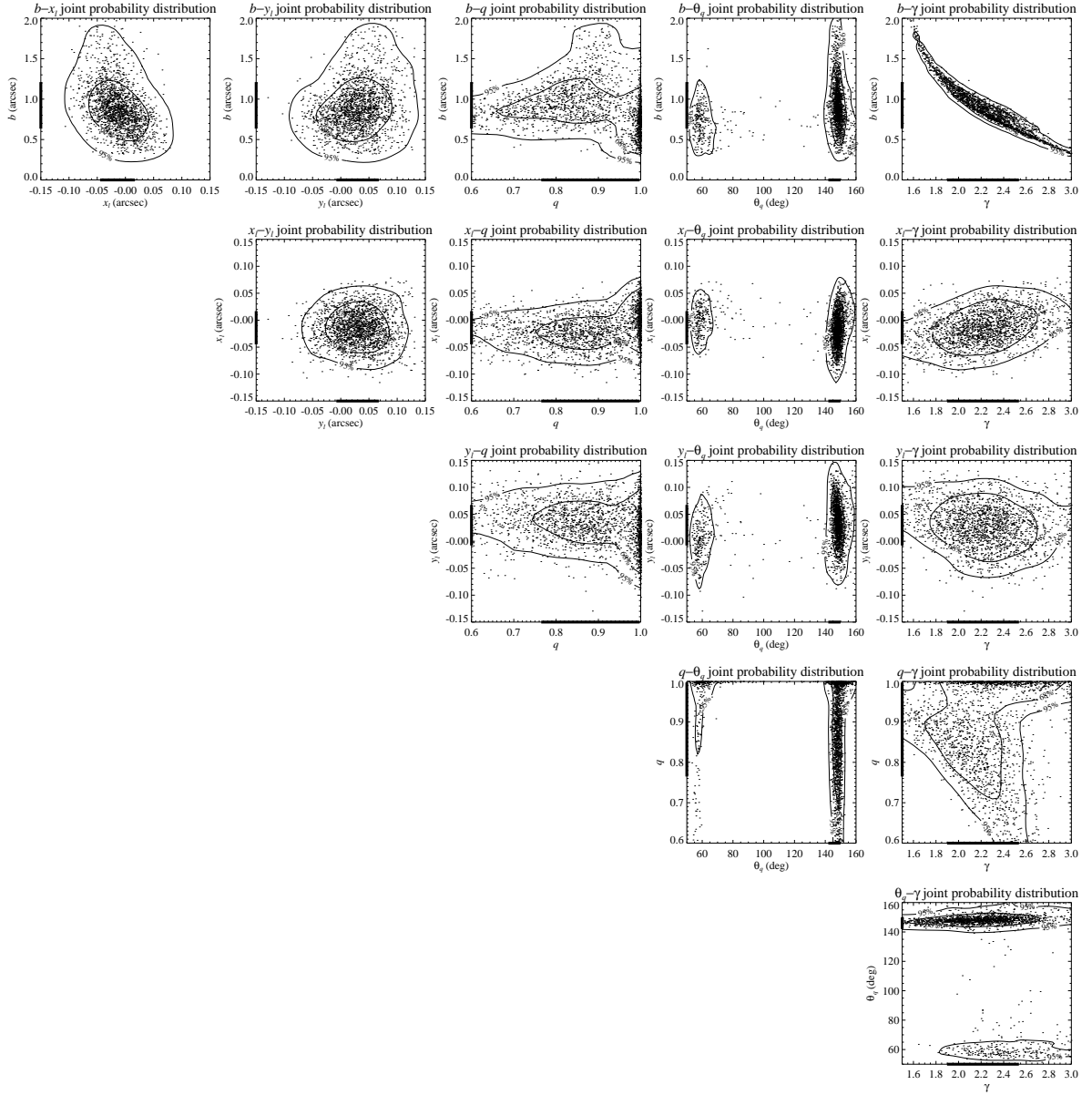
Figure 5.9: Estimates of the errors and correlations in the parameters for a PL (nf) model. Results of the χ^2 minimizations on 2000 Monte-Carlo simulated data sets. Thick bars on the co-ordinate axes and contour levels on the planes represent, respectively, the 68% confidence intervals and the 68% and 95% confidence regions. For each model parameter, the 68% confidence interval is determined by excluding from the 2000 χ^2 minimizations the 320 smallest and the 320 largest values.
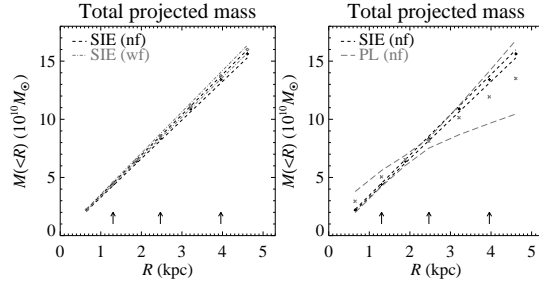
Figure 5.10: Comparison of the projected total mass estimates for the SIE (nf), SIE (wf), and PL (nf) models. For each aperture, the 1σ confidence intervals are determined from 2000 Monte-Carlo simulations by excluding the 320 smallest and the 320 largest mass estimates. The arrows show the projected distances of the observed multiple images from the lens center.

shape of the tangential caustic is approximately symmetric with respect to the center of the lens and the surface enclosed by this caustic is small. In the same limit, the radial caustic is well approximated by a circle centered on the lens center. From these considerations, it follows that the expected positions of the images are almost invariant under a rotation of $90°$ of the lens mass distribution (supposing the positions of the sources are fixed).

The degeneracies between b, q, and γ are connected to their relations defined in Eqs. (5.1) and (5.2). In particular, the strong anti-correlation between the value of the length scale and the steepness (see the fifth panel of Fig. 5.9) is caused by the fact that the Einstein ring of a circular lens model defines a region on the image plane within which the average value of the convergence κ is equal to one. In order for this equality to be approximately valid inside the average circle defined by the positions of our quad system, from Eq. (5.1) and by holding the value of q fixed, it follows that a higher value of b requires a lower value of γ, and vice versa.

The previous considerations on the almost model-independent average value of κ inside the Einstein ring can also be translated in terms of total mass estimates within the same ring. Distinct models, defined by different parameters, that can reproduce well an approximately complete Einstein ring, provide total mass measurements inside this typical aperture that differ by only a few percent. This is shown in Fig. 5.10. There, we plot the median values and the 68% confidence intervals (obtained by excluding from the 2000 χ^2 minimizations the 320 smallest and the 320 largest mass estimates) of the lens projected total mass within the Einstein ring and measure values of $8.35^{+0.20}_{-0.18} \times 10^{10} M_\odot$ for an SIE (nf) model and $8.11^{+0.27}_{-0.59} \times 10^{10} M_\odot$ for a PL (nf) model. We notice that the median values of the 2000 Monte-Carlo cumulative total mass estimates do not necessarily follow a global PL model, but they have in principle more freedom. In fact, even if the total mass values of each of the 2000 models do follow a power law model precisely at all radii, the median values shown in Fig. 5.10 and used in the following for the luminous and dark matter decomposition are more general and do not provide the same value of the steepness γ at each radial position. In general, for the two different models the total mass estimates, that are measured within various apertures (approximately between 1 and 4 kpc from the lens center), are consistent, given the errors. We remark that fixing the exponent of the total mass profile (i.e., γ equal to 2 for the SIE models) result in significant smaller uncertainties in the total mass values. As mentioned above, by modeling also the fluxes of the double system we find total mass measurements that are consistent within 1σ with the estimates obtained by fitting the image positions only.

We generalize our result by emphasizing that the adoption of an isothermal model for strong

lenses often provides a good fit of the observed images, but the errors on the projected mass estimates may be considerably underestimated already at projected distances from the center of the lens that differ from the Einstein radius by half its value. This fact has non-negligible consequences on the inferred properties of a lens dark matter distribution (see below).

We notice that the value of 205 ± 13 km s^{-1} for the central stellar velocity dispersion σ_0, which is determined by rescaling the value of the SDSS spectroscopic stellar velocity dispersion measured inside an aperture of 1.5" $[\sigma = (189 \pm 12)$ km s$^{-1}]$ to an aperture of radius equal to $\theta_e/8$, is consistent, within the errors, with the value of 215 ± 5, which is obtained by converting the total mass estimates shown in Fig. 5.10 for the SIE (nf) model into an effective velocity dispersion σ_{SIE}.

We remark that the best-fit parameters of our SIE point-like models are consistent, given the errors, with the best-fit parameters of the SIE extended model measured by Bolton et al. (2008a). We also note that previous studies (Kochanek 1993, 1994; Treu et al. 2006; Grillo et al. 2008b) agree on finding that the central stellar velocity dispersion of early-type galaxies is a good estimator of the velocity dispersion of a one-component isothermal model.

5.5   Luminous and dark matter

We combine the surface brightness distribution measurement obtained from the HST images (see Sect. 5.3) with the multicolor photometric observations of the SDSS (see Table 5.1) and the projected total mass estimates determined from the lens modeling (see Sect. 5.4) to study the amount and distribution of luminous and dark matter in the lens galaxy.
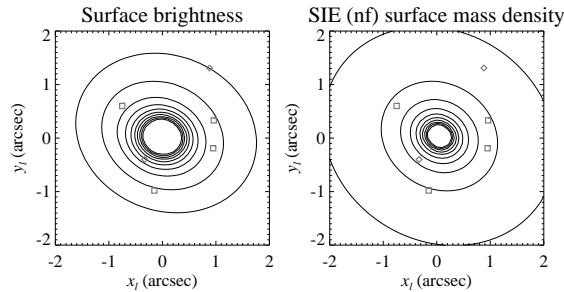
Figure 5.11: Light and mass distributions. Isodensity contours of the best-fit surface brightness (on the left) and parametric (SIE (nf), on the right) total surface mass profiles. The observed image positions of the double (diamond) and quad (square) systems are shown.

First, we compare in Fig. 5.11 the surface brightness and the total surface mass [for the SIE (nf) model] isodensity contours of the best-fit models described in the previous section. We use two images with the same area and pixel size, normalize the images to the sum of the values of all their pixels, and plot the same contour levels in both images. We observe that the distributions of light and total mass from the best-fit SIE (nf) model are nearly axisymmetric, but the former is slightly more concentrated than the latter. This can be inferred by looking at the positions of the inner and outer contour levels. The position angle of the surface brightness and total surface mass distributions are consistent within the errors. Thus, we conclude that the light distribution is approximately circular symmetric in projection and it is a good tracer of the total mass distribution.

Next, we fit the lens spectral energy distribution (SED), consisting of the SDSS ugriz magnitudes (see Table 1), with a three-parameter Bruzual & Charlot composite stellar population
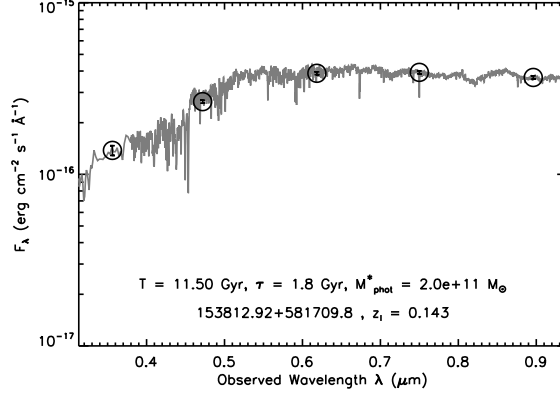
Figure 5.12: SED and best-fit model of the lens galaxy SDSS J1538+5817. The observed total flux densities, measured in the u, g, r, i, and z passbands, and their 1σ errors are represented by circles and error bars. The best-fit is obtained by using Bruzual & Charlot 2003 models. On the bottom, the best-fit values of the age (T), the characteristic time of the SFH (τ), and the luminous mass (M^*_{phot}) are shown.
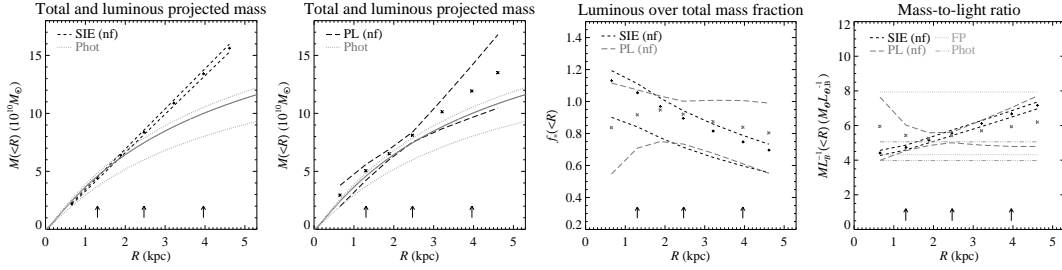
Figure 5.13: Comparison of the projected total mass estimates of the SIE (nf) (left) and PL (nf) (left middle) models with the luminous mass measurements from the best-fit SED model. The fraction of projected mass in the form of stars (right middle) and the total and stellar mass-to-light ratios (right) are obtained by using lensing and photometric information. In each panel, the arrows show the projected distances of the observed multiple images from the lens center and the curves the 1σ confidence intervals.

(CSP) model computed by adopting a Salpeter initial mass function (IMF) and solar metallicity (for further details, see Grillo et al. 2009). The best-fit model, shown in Fig. 5.12, provides a photometric (luminous) mass M^*_{phot} of the lens of $20^{+1}_{-4} \times 10^{10}\,M_\odot$. We then estimate the value of the mass in the form of stars $M^*_{\mathrm{phot}}(\leq R)$, at a projected distance R from the center of the lens, by multiplying M^*_{phot} by an aperture factor $f_{\mathrm{ap}}(\leq R)$, that represents the fraction of light measured within a circular aperture of radius R divided by the total light of the galaxy. The quantities introduced above are explicitly defined as

$$M^*_{\mathrm{phot}}(\leq R) = M^*_{\mathrm{phot}}\, f_{\mathrm{ap}}(\leq R) \tag{5.3}$$

and

$$f_{\mathrm{ap}}(\leq R) = \frac{\int_0^R I(\tilde{R})\tilde{R}\,\mathrm{d}\tilde{R}}{\int_0^\infty I(\tilde{R})\tilde{R}\,\mathrm{d}\tilde{R}}, \tag{5.4}$$

where $I(R)$ is the de Vaucouleurs profile

$$I(R) = I_0 \exp\left[-7.67\left(\frac{R}{R_e}\right)^{\frac{1}{4}}\right], \tag{5.5}$$

with R_e equal to $D_{\rm ol}\theta_e$. As discussed above, the circular symmetry of the light distribution assumed in the previous three equations is a plausible approximation for the lens surface brightness. In Fig. 5.13, we plot at different radii the projected total and luminous mass estimates obtained from the best-fit SIE (nf) and PL (nf) models of Sect. 5.4 and the best-fit SED model.

In the same figure, we show the fraction of projected mass in the form of stars

$$f_*(\leq R) := \frac{M^*_{\rm phot}(\leq R)}{M^{\rm tot}_{\rm lens}(\leq R)} \tag{5.6}$$

and the total mass-to-light ratio

$$\frac{M^{\rm tot}}{L_B}(\leq R) := \frac{M^{\rm tot}_{\rm lens}(\leq R)}{L_B(\leq R)} \tag{5.7}$$

plotted versus the projected radius R. We compare this last quantity with the values of the stellar mass-to-light ratio estimated from the best-fit SED model ($M^*_{\rm phot} L_B^{-1} = 5.0^{+0.1}_{-1.0}\, M_\odot L_{\odot,B}^{-1}$) and the evolution of the Fundamental Plane [$M^*_{\rm FP} L_B^{-1} = (6.1 \pm 1.8)\, M_\odot L_{\odot,B}^{-1}$] (for more information, see Grillo et al. 2009).

The need for a dark component to be added to the luminous one to reproduce the total mass measurements of the SIE (nf) models is suggested by looking at the outer galaxy regions probed by lensing. Due to the larger error bars, the evidence on the presence of dark matter is reduced if the total mass estimates obtained from the PL (nf) models are considered. According to all the lensing models (i.e., deV, SIE, and PL), a value of $0.9^{+0.1}_{-0.2}$ for the fraction of projected mass in the form of stars over total is estimated at a projected distance from the galaxy center of approximately 2.5 kpc, and at 4 kpc from the galaxy center a value of one for the same quantity is excluded by the SIE (nf) models at more than 3σ level. Moreover, at the same distance, the value of the total mass-to-light ratio determined from the SIE (nf) mass measurements is not consistent with the value of the mass-to-light ratio of the luminous component estimated from the galaxy SED modeling. Between 1 and 4 kpc, the same decrease of $f_*(\leq R)$ and deviation of $M^{\rm tot} L_B^{-1}$ from $M^*_{\rm phot} L_B^{-1}$ are also indicated by the values of the PL (nf) mass estimates, but these results are not highly significant because of the large uncertainties.

Finally, by taking advantage of the total mass measurements available at different distances from the center of the lens (not only in the vicinity of the Einstein angle, as in the majority of the known lensing systems), we decide to investigate the dark matter component in greater detail. To make possible a direct comparison of our results with those obtained from dynamical analyses or cosmological simulations, we consider two-component models in which the luminous $\rho_{\rm L}(r)$ and dark $\rho_{\rm D}(r)$ matter density distributions are parametrized by

$$\begin{aligned}
\rho_{\rm L}(r) &= \frac{(3-\gamma_{\rm L})M_{\rm L}r_{\rm L}}{4\pi r^{\gamma_{\rm L}}(r+r_{\rm L})^{4-\gamma_{\rm L}}} \\
\rho_{\rm D}(r) &= \frac{(3-\gamma_{\rm D})M_{\rm D}r_{\rm D}}{4\pi r^{\gamma_{\rm D}}(r+r_{\rm D})^{4-\gamma_{\rm D}}}\ ,
\end{aligned} \tag{5.8}$$

where $M_{\rm L/D}$ is the total mass, $r_{\rm L/D}$ a break radius, and $\gamma_{\rm L/D}$ the inner density slope of the luminous and dark matter distributions. The density profiles of Eq. (5.8) are projected along

the line-of-sight to give the corresponding surface mass density profiles $\Sigma_{L/D}(R)$:

$$
\begin{aligned}
\Sigma_L(R) &= 2 \int_R^\infty \frac{\rho_L(r) r \, dr}{\sqrt{r^2 - R^2}} \\
\Sigma_D(R) &= 2 \int_R^\infty \frac{\rho_D(r) r \, dr}{\sqrt{r^2 - R^2}},
\end{aligned}
\tag{5.9}
$$

which, once integrated, result in the following cumulative mass distributions $M_{L/D}(\leq R)$:

$$
\begin{aligned}
M_L(\leq R) &= \int_0^R \Sigma_L(R) \, 2\pi R \, dR \\
M_D(\leq R) &= \int_0^R \Sigma_D(R) \, 2\pi R \, dR.
\end{aligned}
\tag{5.10}
$$

The total density $\rho_T(r)$, surface mass density $\Sigma_T(R)$, and cumulative mass $M_T(R)$ distributions are defined as the sum of the luminous and dark contributions

$$
\begin{aligned}
\rho_T(r) &= \rho_L(r) + \rho_D(r), \\
\Sigma_T(R) &= \Sigma_L(R) + \Sigma_D(R), \\
M_T(\leq R) &= M_L(\leq R) + M_D(\leq R).
\end{aligned}
\tag{5.11}
$$

We notice again that the circular approximation is plausible for this particular lens.

The luminous quantities introduced in the above equations are completely determined from the photometric observations. In fact, for the luminous component we have estimated the total mass M_L by modeling the SED and, to obtain a surface brightness profile close to a de Vaucoleurs profile, we assume a Hernquist (1990; $\gamma_L = 1$ and $r_L = R_e/1.8153$) or a Jaffe (1983; $\gamma_L = 2$ and $r_L = R_e/0.7447$) density profile. Then, we construct a grid of 13671 models for the dark component. The total mass M_D, the break radius r_D, and the inner density slope γ_D can assume values included between 0.1 and 100 times M_L, 0.1 and 10", and 0.5 and 2.5, respectively. The first two intervals are divided logarithmically into 31 and 21 points respectively, the last one linearly into 21 points. The best-fit dark matter profile is found by minimizing the following chi-square function:

$$
\chi^2(M_D, r_D, \gamma_D) = \sum_{i=2}^6 \left[\frac{M_{\text{lens}}^{\text{tot}}(\leq R_i) - M_T(\leq R_i)}{\sigma_{M_{\text{lens}}^{\text{tot}}(\leq R_i)}} \right]^2.
\tag{5.12}
$$

In order to estimate the errors in the best-fit parameters, we perform 500 Monte-Carlo simulations varying the total mass of the luminous component according to the corresponding measurement errors and the luminous break radius by assuming a realistic 10% uncertainty. In Fig. 5.14, we show the luminous and dark mass decomposition obtained from the best-fit (minimum chi-square) model and in Fig. 5.15 the parameter joint probability distributions. We decide to plot the best-fit dark matter model obtained by assuming a Jaffe profile (no significant differences are present if a Hernquist profile is adopted) for the luminous component and considering the projected total mass estimates coming from the PL (nf) models. The confidence levels on the parameter space of the dark matter component are expressed in terms of the luminous mass fraction $f_L = M_L/(M_L + M_D)$, i.e., the mass in the form of stars to the total mass of the galaxy, the ratio of the dark to luminous break radius r_D/r_L, and γ_D.
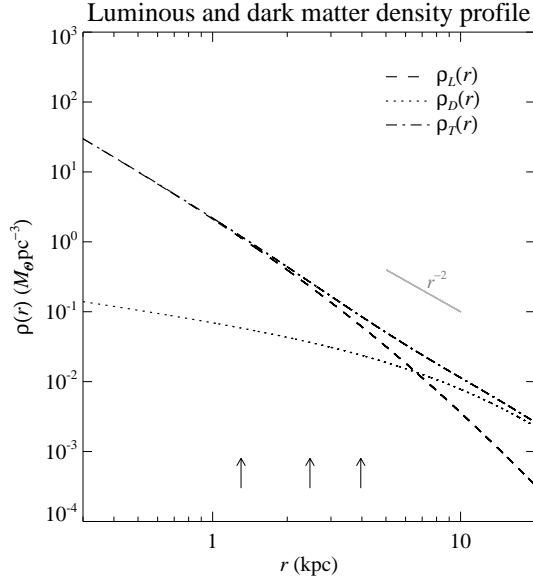
Figure 5.14: Best-fit (minimum chi-square) luminous and dark matter decomposition, determined by assuming a Jaffe profile for the three-dimensional luminous density and projected total mass measurements as estimated from the PL (nf) model. The arrows show the projected distances of the observed multiple images from the lens center.

We find a best-fit χ^2 value of 0.8 with two degrees of freedom (derived from the total mass measurements at the five central radii fitted by three-parametric models). We measure that the values of the dark matter density overcome those of the luminous matter density at radii larger than approximately 1.5 times the effective radius of the galaxy ($R_e = 4.0$ kpc). As in the previous sections, a three-dimensional total density profile close but not exactly equal to a function decreasing as $1/r^2$ (i.e., an isothermal profile) is found. We note that the uncertainties in the dark matter parameters determined by using the projected total mass estimates of the PL (nf) models are significantly larger than those coming from the measurements of the SIE (nf) models. This is a consequence of the different error sizes of the two sets of projected total mass estimates. For the same reason, as already discussed looking at Fig. 5.13, large values of f_L are excluded at a 95% CL only if the lens three dimensional total density profile is fixed to be isothermal. We observe that the dark matter component is in any case more diffused than the luminous one. In fact, r_D/r_L is larger than 2 at more than a 95% CL. Given the assumed parametrization, we also find that the dark matter density profile $\rho_D(r)$ is probably shallow in the inner galactic regions. The value of γ_D is indeed lower than 0.7 at a 68% CL.

5.6 Summary and conclusions

By means of HST/ACS and WFPC2 imaging and NOT/ALFOSC spectroscopy, we have established that SDSS J1538+5817 is a rare lensing system composed of a luminous elliptical galaxy, located at redshift $z_l = 0.143$, that acts as a lens on two distinct and equally-distant ($z_s = 0.531$) sources. The two sources are lensed into a double and a quad (with an almost complete Einstein ring) system, covering rather large angular and radial scales on the lens plane. This exceptional configuration has allowed us to investigate in great detail the lens total mass distribution within the effective radius of the galaxy, through parametric and non-parametric point-like lensing programs and perform a complete statistical study of the errors
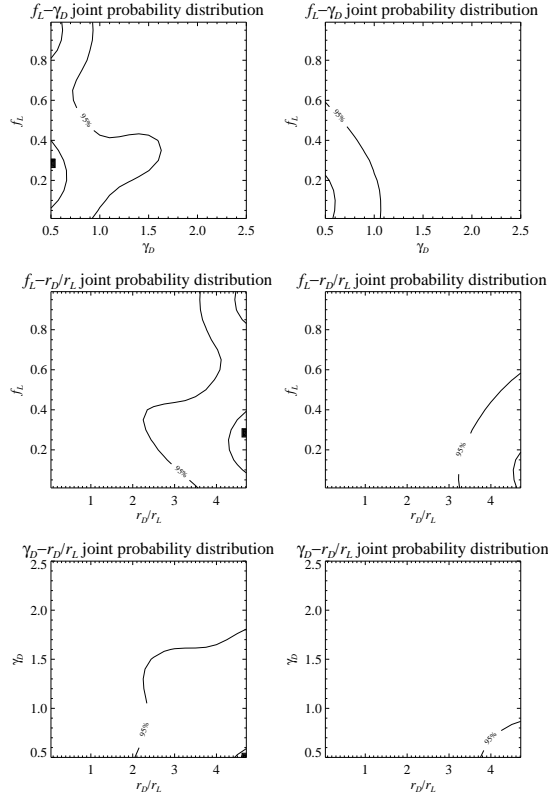
Figure 5.15: Estimates of the errors and correlations in the parameters related to the dark matter component: the luminous mass fraction $f_{\rm L}$, the dark to luminous break radius ratio $r_{\rm D}/r_{\rm L}$, and the dark matter inner density slope $\gamma_{\rm D}$. The projected total mass measurements of the PL (nf) (on the left) and SIE (nf) (on the right) models are used. The small squares on the three left panels show the best-fit parameters corresponding to the dark matter density profile represented in Fig. 5.14.

and correlations on the lens model parameters. Then, by fitting the lens SED with CSP models, we have estimated the luminous mass of the galaxy and combined the lensing and photometric measurements to examine the characteristics of the galaxy dark-matter halo. In detail, our main results can be summarized in the following points:

— Parametric models predict image positions that match closely the observed lensing geometry, and describe lens total mass distributions that are almost circular in projection, moderately steeper than an isothermal profile, and well aligned with the lens light distribution.

— The value of the total mass projected within the Einstein circle of radius 2.5 kpc is slightly larger than $8 \times 10^{10}\, M_\odot$ and approximately 10% of this mass is in the form of dark matter.

— In the inner galactic regions, the galaxy dark-matter density distribution is shallower and more diffuse than the luminous one. The former starts exceeding the latter at a distance of roughly 6 kpc from the galaxy center, corresponding to 1.5 times the value of the luminous effective radius.

We conclude by remarking that strong gravitational lens systems with configurations compa-

rable to or more complex than that of SDSS J1538+5817 are excellent laboratories to study the distribution of luminous and dark matter in early-type galaxies. However, to achieve realistic results on the dark matter component, it is essential to verify the commonly accepted isothermality of the total mass distribution at a higher level than done so far. Strong lensing systems with an Einstein radius significantly larger than the effective radius of the lens galaxy would be invaluable to determine the dark matter properties of the halos of early-type galaxies.

We acknowledge the support of the European DUEL Research Training Network, Transregional Collaborative Research Centre TRR 33, and Cluster of Excellence for Fundamental Physics and the use of data from the accurate SDSS database. We thank Piero Rosati for useful suggestions and the NOT staff for carrying out our observations in service mode. We are grateful to the NOT Scientific Association for awarding some observing time solely on the basis of scientific merit and supporting the NOT Summer School where CG gained some observational experience with the ALFOSC spectroscopic data.

5.7 Appendix: Non-parametric models

PixeLens (Saha & Williams 2004) is a non-parametric lensing program that generates an ensemble of models consistent with the observed data of a lensing system. Each model is composed of a pixelated surface mass density map of the lens, the reconstructed position of the source, and, optionally, an estimate of the value of the Hubble parameter. These results are obtained by using the observed positions of the multiple images (ordered by arrival time, even if time delays are not known), the redshifts of the lens and the source, and some priors based on previous knowledge of general galaxy mass distribution (for further details, see Saha & Williams 1997; Coles 2008). Interestingly, PixeLens has been employed to measure the value of the Hubble parameter from samples of strong lensing systems with measured time delays (e.g., Saha & Williams 2006; Coles 2008).

We model here the surface mass density of the lens on a symmetric circular grid of 2" radius divided into 20 pixels. We consider 400 models with fixed cosmological values and with decreasing total projected mass profiles [i.e., $\Sigma(R) \propto R^{-\alpha}$, where $\alpha > 0$].
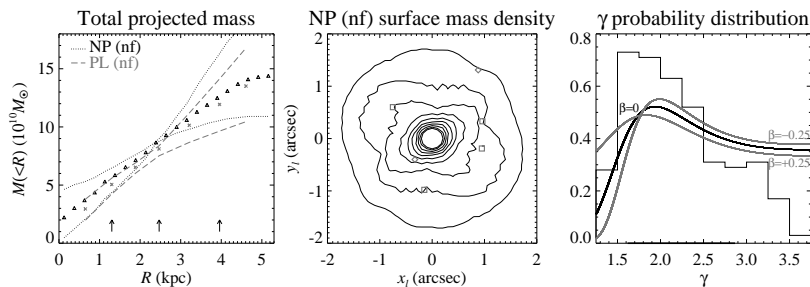
Figure 5.16: <u>Left</u>: Comparison of the total projected mass estimates, with 1σ confidence intervals, from parametric [PL (nf)] and non-parametric [NP (nf)] modeling. The arrows show the projected distances of the observed multiple images from the lens center. <u>Middle</u>: Isodensity contours of the best-fit non-parametric [NP (nf)] total surface mass profile. The observed image positions of the double (diamond) and quad (square) systems are shown. <u>Right</u>: Marginal probability distribution (histogram) of the three-dimensional total density exponent γ from non-parametric modeling. The thick bar on the <u>x</u>-axis shows the 1σ confidence interval. The same probability distribution as obtained by combining strong lensing and stellar dynamics measurements is represented by the smooth curves.

The cumulative total projected mass, the total surface mass density profile of the average

model, and the marginalized probability distribution of the three-dimensional total density exponent γ are shown in Fig. 5.16. We measure a value of the total mass projected within the Einstein radius of $8.59^{+0.13}_{-0.12} \times 10^{10} M_\odot$, at a 68% CL. At the same confidence level, we estimate a value of γ included between 1.62 and 2.87. We observe that the contour levels of the non-parametric total surface mass show non-negligible values of ellipticity in the inner regions. The differences between the surface brightness of Fig. 5.11 and total surface mass of Fig. 5.16 are significant within the area defined by the Einstein radius. This is not surprising since here the total surface mass density distribution is almost completely unconstrained by the lensing observables. This is the equivalent of Gauss' law in gravitational lensing (see Kochanek 2004). We notice that these differences are less evident outside the Einstein ring, where the positions of the multiple images limit the freedom of the non-parametric models in determining the lens total mass distribution. In Fig. 5.16, we also show for comparison the mass estimates obtained in the equivalent parametric modeling [PL (nf)] and the probability distribution of the density exponent that is expected by combining strong lensing and stellar dynamics measurements. In detail, the combined lensing and dynamical probability distribution for γ is obtained by using the following expression

$$\frac{c^2}{4\pi} \frac{\theta_{\mathrm{Ein}}}{\sigma_0^2} \, \tilde{r}(z_l, z_s; \Omega_m, \Omega_\Lambda) = \left(\frac{8\theta_{\mathrm{Ein}}}{\theta_e} \right)^{2-\gamma} g(\gamma, \delta, \beta) \qquad (5.13)$$

that relates through the spherical Jeans equations the values of the central stellar velocity dispersion σ_0, Einstein angle θ_{Ein}, effective angle θ_e, exponent of the three-dimensional luminosity density profile δ, anisotropy parameter of the stellar velocity ellipsoid β, and ratio of angular diameter distances between observer-source and lens-source $\tilde{r}(z_l, z_s; \Omega_m, \Omega_\Lambda)$ $[g(\gamma, \delta, \beta)$ is a numerical factor that depends on the three cited quantities; for definitions and further details, see Koopmans 2006]. In the plots of Fig.5.16, we fix δ equal to 2 and choose two values of β (-0.25 and $+0.25$) representative of small tangential and radial orbit anisotropy. By doubling the size of the grid but keeping the same size of the pixels, we have checked that the choice of a circular grid with a radius of 2" to reconstruct the total surface mass density distribution of our not perfectly circular lens galaxy does not introduce any artificial shear component and does not affect significantly the results.

According to these results and looking at Fig. 5.16, we can conclude that the two independent parametric and non-parametric analyses are in general consistent, within the errors, as far as total projected mass and three-dimensional total density exponent measurements are concerned, but small differences and some considerations are worth noticing.

The projected total mass estimates obtained with PixeLens are systematically larger than those obtained with gravlens. This can be caused by a combination of the mass-sheet degeneracy (see Falco et al. 1985; Schneider & Seitz 1995) and the prior on the positive definiteness of every pixel of the grid of the total surface mass density. Among all the arbitrary constants that can be added to the convergence κ, leaving though the image positions unchanged, those which provide a negative value of κ somewhere on the grid are excluded, a priori, from the non-parametric lensing analysis. This fact may bias the projected total mass measurements to slightly larger values.

As far as γ is concerned, the larger uncertainty coming from the non-parametric reconstruction with respect to the parametric one is probably just a consequence of the more general allowed models. A bias towards small values of γ may be associated to the prior present in PixeLens that constrains the value of κ on one pixel of the grid to be lower than twice the average value

of the neighboring pixels. For large values of γ, two adjacent pixels located in the central region of the lens may have very different values of κ, hence these models may not be included in the statistical ensemble.

Finally, we remark on the overall agreement between the lensing only and lensing plus dynamics probability distributions of γ. We notice, though, that lensing alone does not reach the precision needed to distinguish among models with different values of the stellar anisotropy parameter β.

Chapter 6

Golden gravitational lensing systems from the Sloan Lens ACS Survey. II. SDSS J1430+4105: A precise inner total mass profile from lensing alone

Thomas Eichner[1,2] [1], Stella Seitz[1,2], Anne Bauer[1,3]

[1] Universitäts-Sternwarte München, Scheinerstr. 1, 81679 Muenchen, Germany

[2] Max-Planck-Institut für extraterrestrische Physik, Giessenbachstraße, 85748 Garching, Germany

[3] Institut de Ciències de l'Espai, CSIC/IEEC, F. de Ciències, Torre C5 par-2, Barcelona 08193, Spain

6.1 Abstract

We study the Sloan Lens ACS survey (SLACS) strong lensing system SDSS J1430+4105 at $z_l = 0.285$. The lensed source ($z_s = 0.575$) of this system has a complex morphology with several subcomponents. Its subcomponents span a radial range from $4\,\mathrm{kpc}$ to $10\,\mathrm{kpc}$ in the plane of the lens. Therefore we can constrain the slope of the total projected mass profile around the Einstein radius from lensing alone. We measure a density profile that is slightly but not significantly shallower than isothermal at the Einstein radius. We decompose the mass of the lensing galaxy into a de Vaucouleurs component to trace the stars and an additional dark component. The spread of multiple image components over a large radial range also allows us to determine the amplitude of the de Vaucouleurs and dark matter components separately. We get a mass to light ratio of $\frac{M_{\mathrm{deVauc}}}{L_B} \approx (5.5 \pm 1.5)\,\frac{M_\odot}{L_{\odot,B}}$ and a dark matter fraction within the Einstein radius of $\approx 20\%$ to 40%. Modelling the star formation history assuming composite stellar populations at solar metallicity to the galaxy's photometry yields

a mass to light ratio of $\frac{M_{\star,salp}}{L_B} \approx 4.0^{+0.6}_{-1.3} \frac{M_\odot}{L_{\odot,B}}$ and $\frac{M_{\star,chab}}{L_B} \approx 2.3^{+0.3}_{-0.8} \frac{M_\odot}{L_{\odot,B}}$ for Salpeter and Chabrier IMFs, respectively. Hence, the mass to light ratio derived from lensing is more Salpeter-like, in agreement with results for massive Coma galaxies and other nearby massive early type galaxies. We examine the consequences of the galaxy group in which the lensing galaxy is embedded, showing that it has little influence on the mass to light ratio obtained for the de Vaucouleurs component of the lensing galaxy. Finally, we decompose the projected, azimuthally averaged 2D density distribution of the de Vaucouleurs and dark matter component of the lensing signal into spherically averaged 3D density profiles. We can show that the 3D dark and luminous matter density within the Einstein radius ($R_{Ein} \approx 0.6 R_{eff}$) of this SLACS galaxy is similar to the values of Coma galaxies with the same velocity dispersions.
gravitational lensing: strong − galaxies: elliptical and lenticular, cD − galaxies: haloes − galaxies: individual: SDSSJ 1430+4105

6.2   Introduction

Early-type galaxies contain a large fraction of the total stellar mass observed in the Universe (e.g., Fukugita et al. 1998; Bell et al. 2003). Studying the internal structure of early-type galaxies is crucial for understanding the baryonic physics that plays a key role in the formation and evolution of these objects. Several studies have shown that the stars assembled in early-type galaxies are embedded in massive dark matter haloes (e.g.,Gavazzi et al. 2008; Lagattuta et al. 2010; Weijmans et al. 2008), but the precise amount of dark matter contained in the galaxies' inner regions is still under debate.

Dark matter only simulations have found indications of a universal density profile for dark matter haloes, present also in galaxies (the so called NFW profile; Navarro et al. 1997). Nevertheless, more recent and realistic simulations that include also the physics of baryons (e.g., Gnedin et al. 2004; Duffy et al. 2010; El-Zant et al. 2001; Bertin et al. 2003; Ma & Boylan-Kolchin 2004; Blumenthal et al. 1986; Jesseit et al. 2002), like radiative cooling and supernova and black hole feedback, have suggested that the inner profile of the dark matter component can be significantly affected by the interactions between baryonic and dark matter.

The internal structure of nearby early-type galaxies has been for decades the object of intense dynamical analyses (e.g., Saglia et al. 1992; Gerhard et al. 2001; Thomas et al. 2007; Thomas et al. 2009; Thomas et al. 2011; Pu et al. 2010). One focus of these studies is to compare stellar with dynamical mass to light ratios. The dynamical studies, e.g. Gerhard et al. (2001), Thomas et al. (2011) find ratios for nearby elliptical galaxies of $M/L_B \approx 4$ to 10. Similar values are also found by Cappellari et al. (2006). Only in the last few years has gravitational lensing also contributed significantly to our understanding of the luminous and dark matter composition of early-type galaxies beyond the local Universe (Barnabè et al. 2009; Grillo et al. 2010; Barnabè et al. 2010). Strong gravitational lensing in early-type galaxies has also proved to be a powerful cosmological tool to probe the geometry of the universe independently from other diagnostics (e.g., Grillo et al. 2008b; Suyu et al. 2009, 2010b).

By combining strong gravitational lensing and stellar dynamics in a sample of first 15, then 58 early-type galaxies, Koopmans et al. (2006) and Koopmans et al. (2009) have found that the average total (luminous and dark) mass density distribution within the effective radius – the radius of the isophote containing half of the total light of the galaxy – is well represented by an isothermal distribution ($\rho \propto r^{-2}$), although significant deviations from this result can be observed in individual galaxies. Only rare systems where an extended or several distinct

sources are gravitationally lensed over an extended radial area on the lens plane can be used to determine the total mass density profile of the lens galaxy over a wide radial range through lensing only (e.g. Grillo et al. 2008c, 2010; Fadely et al. 2010). Moreover, combining lensing total mass measurements with photometric stellar mass estimates in these systems offers a unique way to disentangle their luminous and dark matter components.

In this paper, we study the gravitational lensing system SDSS J1430+4105 that is composed of a massive early-type galaxy acting as a lens for an irregular background source. This galaxy was part of the SLACS survey[2] and has been studied as part of their lens sample, especially in Bolton et al. (2008a), Auger et al. (2009) and Auger et al. (2010): Bolton et al. (2008a) fit a singular isothermal lens model to the observed multiple images, while Auger et al. (2009) and Auger et al. (2010) combine the measured Einstein radii and masses with photometric and dynamical data. The surface brightness distribution of the lensed source shows several peaks that extend from 4 to 10 kpc from the lens galaxy centre. This fact provides the opportunity to investigate the lens galaxy mass distribution on radial ranges larger than those explored in similar analyses of other gravitational lensing systems (e.g., Xanthopoulos et al. 1998, Cohn et al. 2001,Grillo et al. 2010).

The paper is organised as follows: Section 2 gives an overview of the observations and data used in this work and introduces the environment of SDSSJ 1430+4105; Section 3 describes the details of the strong lensing models. Section 4 states the implications for the total mass and the mass profile. In Section 5 the mass to light ratio for the de Vaucouleurs component is constrained, in Section 6 the results are discussed. Appendix A contains further variants of strong lensing models. Appendix B gives further details of the environment implementation. The cosmological model adopted in this paper is parametrized by $\Omega_{\mathrm{m}} = 0.3, \Omega_{\Lambda} = 0.7, H_0 = 70 \, \mathrm{km \, s^{-1} \, Mpc^{-1}}$. In the cosmology assumed, 1 arcsec in the lens ($z_{\mathrm{l}} = 0.285$) and source ($z_{\mathrm{s}} = 0.575$) plane corresponds to 4.30 and 6.55 kpc.

6.3   Observations

The SLACS Survey aimed at finding strong gravitational lenses among the galaxies observed in the SDSS. The lens detection strategy is presented in Bolton et al. (2004) and is based on the examination of the SDSS galaxy spectra, taken with a 3 "diameter fibre, to identify emission lines not associated with the primary target galaxy but with an additional source, aligned with the first galaxy and located at a higher redshift. The lens candidates are then ranked in terms of their probability of being lensing systems and are consequently observed with the HST/ACS and WFPC2.

Up to now, 85 confirmed (grade-A) lenses (Bolton et al. 2006, Auger et al. 2009) were discovered in this way, and SDSSJ 1430+4105 is one of these. In Fig. 6.1 we show the SDSS spectrum, from which lens and source redshifts of $z_{\mathrm{l}} = 0.285$ and $z_{\mathrm{s}} = 0.575$ are measured, together with the lens aperture velocity dispersion of $\sigma_{\mathrm{SDSS}} = (322 \pm 32) \, \mathrm{km \, s^{-1}}$.

6.3.1   Galaxy light profile and lensing observables

The basic photometric and spectroscopic properties of SDSSJ 1430+4105, taken from Bolton et al. (2008a), are stated in Table 6.1.

---

[2]http://www.slacs.org

Figure 6.1: The SDSSJ 1430+4105 spectrum as observed by the SDSS 3 "diameter fibre. On the bottom, the observed wavelength is stated, while on the top, this is converted into the restframe wavelength of the lens ($z = 0.285$). The dotted vertical lines give the SDSS emission / absorption line sample at the redshift of the lens. The dashed vertical lines give some prominent emission lines at the redshift of the source. Overplotted in the lower part of the figure is the flux uncertainty given again by SDSS. The spectrum shows several absorption lines typical of an early type galaxy at $z = 0.285$ and some additional emission lines at redshift $z = 0.575$ (e.g. the lines at 5872Å, 7661Å and 7813Å, which can be identified as the redshifted [OII]3728, Hβ and [OIII]4960 lines respectively). Data taken from from www.sdss.org, York et al. (2000)

Table 6.1: Photometric and spectroscopic quantities of the lens system

RA (J2000)	Dec (J2000)	z_l	z_s	q_L ($\frac{b}{a}$)	$\Theta_{q,L}$ (°)	Θ_{eff} (")	σ_{SDSS} (km s^{-1})
14:30:04.10	+41:05:57.1	0.285	0.575	0.79	-12.8[1]	2.55	322 ± 32

Given are the position of the galaxy(RA, Dec), the redshifts of galaxy and source (z_l z_s), the axis ratio(q_L), the orientation ($\Theta_{q,L}$), the effective radius (Θ_{eff}) of the lens' light distribution and the velocity dispersion σ_{SDSS}. Values are taken from Bolton et al. (2008a)

[1]This angle is equivalent to $-59.3°$ in the WCS coordinate system, defined as (-E) over N.

For these, Bolton et al. (2008a) fitted a de Vaucouleurs (de Vaucouleurs, 1948) profile with elliptical isophotes to the galaxy's surface brightness distribution. They obtained an effective radius of $\Theta_{eff} = 2.55'' = 10.96$ kpc, a minor to major axis ratio of $q_L = 0.79$, and a major axis angle of $\Theta_{q,L} = -12.8°$. The angles are transformed to the adopted local reference frame shown in Fig. 6.2, and measured counterclockwise with the y-axis equals to $0°$.

We retrieve the public HST images from the Hubble Space Telescope archive at ESO[3]. Three filters were available for this system: HST/WFPC2 F606W with a total integration time of 4400s (ua1l4501m, ua1l4502m, ua1l4503m, ua1l4504m), HST/ACS F814W with a total integration time of 2128s (j9op36010) and HST/WFC3 F160W with a total integration time of 2497s. For the lensing analysis we use the ACS F814W filter observations, since the PSF of the ACS camera is smaller than the one of the WFPC2 and WFC3. First, we subtract the lensing galaxy's light contribution with GALFIT (Peng et al. 2002) by using a de Vaucouleurs profile, with the parameters of Table 6.1. Then, in order to refine the lens galaxy subtraction and especially remove the residuals still present in the central region, an additional Sersic

---

[3]http://archive.eso.org/archive/hst/

Figure 6.2: The multiple image systems that are identified after the lens galaxy subtraction and used as input for the lensing analysis. The labels A1 to E2 mark the positions used for the strong lensing analysis. The same letters correspond to images coming from the same source feature, the labelling is done according to Table 6.2. The cross marks the centre of the subtracted lens galaxy light. Also indicated are the derived shear direction from Sec. 6.9.1 and the direction of galaxy I. For orientation north is given as well. Angles are measured in the local coordinate system counterclockwise as (-x) over y if not otherwise stated. The image is rotated relative to the WCS J2000 by $47.21°$.

profile (Sérsic 1963) with index 1.2 is subsequently subtracted.

Fig. 6.2 shows the final galaxy subtracted image. The lensed source has a complex surface brightness distribution, with 5 surface brightness maxima which are imaged 2 times each. We mark and label the 5×2 multiple image positions, identified as the brightest pixels, in Fig. 6.2. Their coordinates are reported in Table 6.2 together with approximate error estimates. We assume in the following that all subcomponents A-E are at the same redshift and not unlikely line-of-sight projections at different redshifts. The distances of the multiple images from the centre of the lens galaxy light distribution span a range from $0.93''$ to $2.32''$. In the rest of the paper, if not otherwise stated, we adopt the coordinate system introduced in Fig. 6.2 which is rotated relative to the WCS J2000 (world coordinate system) by $47.21°$.

6.3.2 Observed environment

SDSSJ 1430+4105 is not an isolated galaxy. It coincides in redshift and location with a galaxy group at $z = 0.287$, listed in the maxBCG cluster catalogue, (Koester et al., 2007). Therefore, we should consider the light deflection by the lens' environment when we model this lens. We show the environment of SDSSJ 1430+4105 (labelled as A) in Fig. 6.3.

The galaxy labelled as I was proposed to be the brightest cluster galaxy (BCG) of this group found in Koester et al. (2007). The photometric redshift of the group GI is estimated to be $z = 0.287$ with a typical redshift error in the maxBCG catalogue of 0.01. Within this error the photometric redshift of the group is identical to the spectroscopic redshift (0.28496) of the lensing galaxy. The group consists of 12 members within the R_{200} of this group, $N_{(gal,200)} = 12$. At this richness level, the maxBCG cluster is typically more than 90% pure and complete, based on tests with mock catalogues. We now estimate the group members

Table 6.2: Observed positions of the multiple image systems

ID	$\Theta_1{}^1$	$\Theta_2{}^1$	z_s	δ_Θ	d^1
	($''$)	($''$)		($''$)	($''$)
A1	-1.99	-0.32	0.575	0.05	2.02
A2	0.69	0.62	0.575	0.05	0.93
B1	-2.08	0.47	0.575	0.05	2.13
B2	1.08	0.08	0.575	0.05	1.08
C1	-2.28	0.42	0.575	0.05	2.32
C2	0.93	0.03	0.575	0.05	0.93
D1	-1.84	0.27	0.575	0.05	1.86
D2	0.84	0.80	0.575	0.05	1.35
E1	0.39	-1.21	0.575	0.05	1.27
E2	-1.64	1.11	0.575	0.05	1.98

[1]relative to the centre of the galaxy light distribution

based on astrometric and photometric data from SDSS DR7 (Abazajian et al. 2009). We consider each galaxy within 10 from the main lens of SDSS J1430+4105. We allow for galaxies which have at least one of the photometric redshift estimates (template based (Template-z) (Adelman-McCarthy et al. 2007) or neural network based (CC2 z and D1 z) (Oyaizu et al. 2008)) consistent within one standard deviation with the spectroscopic redshift value of SDSS J1430+4105 and the photometric redshift of the group GI. The neighbours which pass these requirements are listed in Table 6.3.

This table shows that for our definition the galaxy A is a group member from both its photometric and spectroscopic redshift. The magnitudes of the galaxies A and I in the ugriz filters are 20.43, 19.02, 17.74, 17.12, 16.87 and 22.54, 19.44, 17.92, 17.35, 17.00 for A and I respectively, and thus A is formally the brightest galaxy ('BCG') of this group. Since the group membership and group redshift estimate of the maxBCG catalogue (Koester et al., 2007) is mostly based on the g-r colour, the contaminated g-r colour of A due to lensing has likely led to A not being considered as a group member and therefore as the BCG. Using the same definition for the r_{200} as stated in Koester et al. (2007) we find 11 group members from Table 6.3.
From Johnston et al. (2007), who tested the maxBCG cluster finder on simulated groups and clusters of galaxies, we derive the probability that a group of the richness given in the maxBCG catalogue $N_{(gal,200)} = 12$ is centred on the correct BCG in the maxBCG cluster catalogue to be $p_c(N_{200} = 12) = 0.63$. Therefore both A or I could be the true mass centre of the group GI. Finally, the Koester et al. (2007) group catalogues could also contain false positive detections. Song et al. (2012) have shown that the false detection rate of such groups can be as large as 40%. This motivates why we will consider lens models with and without an external group contribution. We will show that including a galaxy group centred on galaxy I has only minor influence on the lens parameters.

Table 6.3: Observed environment of SDSSJ 1430+4105

Obj	RA (J2000)	Dec (J2000)	mag$_i$	σ_i	Template z	Error	NN CC2 z	Error	NN D1 z	Error	Spectro-z	Error
A	217.51704	41.0992	17.216	0.006	0.228	0.033	0.231	0.027	0.234	0.026	0.28496	2.13E-4
B	217.44551	41.0456	18.729	0.018	0.202	0.015	0.216	0.073	0.260	0.067		
C	217.45406	41.0460	18.495	0.020	0.262	0.019	0.287	0.045	0.316	0.048		
D	217.45941	41.0625	18.657	0.019	0.179	0.032	0.312	0.055	0.309	0.064		
E	217.46178	41.1010	18.870	0.016	0.266	0.019	0.287	0.055	0.343	0.073		
F	217.46445	41.0738	19.134	0.020	0.286	0.082	0.309	0.096	0.344	0.073		
G	217.47010	41.1054	18.708	0.013	0.224	0.011	0.228	0.073	0.267	0.063		
H	217.49009	41.0825	19.356	0.024	0.200	0.024	0.259	0.070	0.339	0.060		
I	217.49493	41.1044	17.348	0.008	0.273	0.019	0.272	0.020	0.272	0.016		
J	217.50190	41.0995	18.697	0.018	0.251	0.021	0.293	0.062	0.326	0.063		
K	217.50545	41.0779	18.283	0.015	0.263	0.020	0.267	0.037	0.293	0.032		
L	217.51212	41.0655	18.008	0.0100	0.268	0.015	0.273	0.022	0.279	0.023		
M	217.52402	41.1253	19.358	0.026	0.298	0.084	0.451	0.042	0.424	0.042		
N	217.54462	41.1407	18.947	0.026	0.275	0.063	0.284	0.057	0.296	0.048		
O	217.54641	41.0450	18.500	0.016	0.169	0.056	0.210	0.043	0.236	0.057		
P	217.58642	41.0746	19.373	0.027	0.371	0.088	0.401	0.059	0.403	0.064		

Properties of the galaxies considered as part of the environment of J1430+4105. Given in the rows are the object name (Obj), the position (RA, Dec), its i band magnitude mag$_i$ and its error σ_i, and its various photometric redshift estimates together with its errors: first the template method and its error, summarised in Adelman-McCarthy et al. (2007), followed by the neural network based methods CC2 and its error and D1 and its error (Oyaizu et al. 2008).
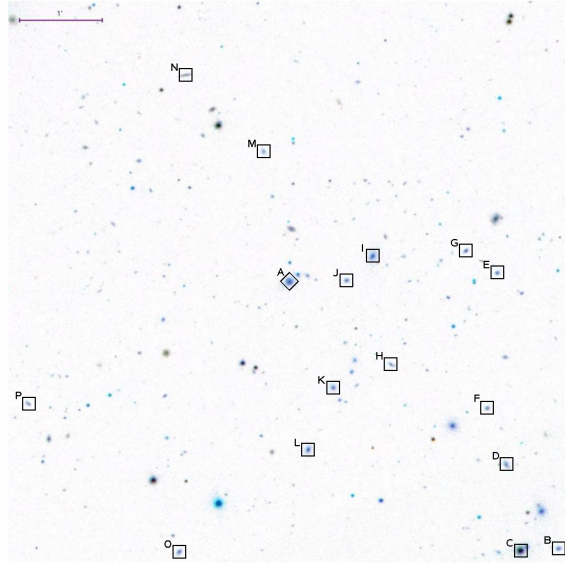
Figure 6.3: The observed environment of J1430+4105, taken from SDSS. All galaxies with a photometric redshift consistent with the spectroscopic redshift of SDSSJ 1430+4105 (labelled with A and marked with a diamond) within 1 standard deviation are marked by squares. The galaxy marked as I is the BCG for the group identified by Koester et al. (2007). In the image, north is up and east is left. This image is rotated relative to Fig. 6.2 by $47.21°$. The size is 7.5×7.5. For the properties of the galaxies, see Table 6.3.

6.4 Strong gravitational lensing

In this section we model the lens mass distribution with the public GRAVLENS (Keeton (2001b)) code (Sec. 6.4.1) assuming point sources and with the LENSVIEW (Wayth & Webster (2006)) code (Sec. 6.4.3) using the 2–dimensional surface brightness distribution of the same system. Both approaches give consistent results. We give a description of the influence of the environment on the lens model of SDSSJ 1430+4105 in Sec. 6.4.2.

6.4.1 Parametric modelling using GRAVLENS

GRAVLENS[4] is a public code that uses parametric lens models to reconstruct the properties of an observed lensing system. The lens-modelling we implement here is similar to the one of Grillo et al. (2010) where the reader can find more details. In this subsection, we use peaks in the surface brightness distribution of the lensed images as point-like position constraints for the lens model (see Table 6.2 and Fig. 6.2). Since the complex surface brightness distribution of the lensed galaxy makes it difficult to associate reliably a flux measurement to each multiple image, we neglect flux constraints. In GRAVLENS the convergence κ for a (non–)singular isothermal ellipsoid ((N–)SIE) or an ellipsoidal powerlaw (PL) is parametrized as

$$\kappa(\Theta_1, \Theta_2) = \frac{b^{\beta-1}}{2(1-\epsilon)^{\frac{\beta-1}{2}} \left(\frac{\Theta_c^2}{1-\epsilon} + \Theta_1^2 + \frac{\Theta_2^2}{q^2} \right)^{\frac{\beta-1}{2}}} \tag{6.1}$$

---

[4]see http://redfive.rutgers.edu/~keeton/gravlens

with

$$\epsilon = \frac{1 - q^2}{1 + q^2} \quad,$$

where b is the lensing strength, β denotes the steepness of the density profile ($\beta = 2$ in the case of an isothermal profile), Θ_1 and Θ_2 are the coordinates on the plane of the sky relative to the centre of mass of the lens, Θ_c is the core radius and q is the axis ratio of the isocontours of the convergence (q = 1 for a circular mass model). In the special case of a circular lens without core radius, b equals the Einstein radius Θ_{Ein} of the lens defined as $\overline{\kappa}(\Theta \leq \Theta_{\mathrm{Ein}}) = 1$. Further we use a de Vaucouleurs Model (de Vaucouleurs, 1948) parametrized as

$$I(R) = I_e e^{-7.67\left[(\frac{R}{R_{\mathrm{eff}}})^{1/4} - 1\right]} \quad, \tag{6.2}$$

with R_{eff} being the effective radius (the radius which contains half the light) and I_e the surface density at this radius. In GRAVLENS this is implemented as

$$\kappa = b_{\mathrm{deV}} e^{-7.67\left[\frac{(\Theta_1^2 + \Theta_2^2/q^2)^{1/2}}{\Theta_{\mathrm{eff}}}\right]^{1/4}} \quad. \tag{6.3}$$

In this parametrisation, b_{deV} is the value of the central convergence. The Einstein radius, however, depends also on Θ_{eff} and q. Also a Navarro, Frenk and White (NFW) profile (Navarro et al., 1997) is used, defined as

$$\rho(r) = \frac{\delta_c \rho_c}{r/r_s(1 + r/r_s)^2} \quad, \tag{6.4}$$

with ρ_c denoting the critical density of the universe at the redshift of the lens, and r_s and δ_c are characteristic properties of the individual halo. For an overview of its lensing properties, see Wright & Brainerd (2000).

The relation for the LOS projected surface mass density Σ of the lens and lensing convergence κ is

$$\kappa = \frac{\Sigma}{\Sigma_{\mathrm{crit}}} \quad \text{with} \quad \Sigma_{\mathrm{crit}}^{-1} = \frac{4\pi G}{c^2} \frac{D_d D_{ds}}{D_s} \quad,$$

where D_d, D_s and D_{ds} are the angular diameter distances from the observer to the lens, the source and from the lens to the source, respectively. The goodness of a model is judged by the χ^2:

$$\chi_{\mathrm{lens}}^2 = \sum_i \frac{\parallel \boldsymbol{\Theta}_i - \boldsymbol{\Theta}_{0,i} \parallel^2}{\delta_{\Theta_i}^2} \quad, \tag{6.5}$$

where $\boldsymbol{\Theta}_i$ denote the model-predicted positions of the i-th images, $\boldsymbol{\Theta}_{0,i}$ is its observed position, and δ_{Θ_i} its observed positional uncertainty.

Any priors described in the text are added to this χ^2 in GRAVLENS via

$$\chi_{\mathrm{tot}}^2 = \chi_{\mathrm{lens}}^2 + \chi_{\mathrm{prior}}^2$$

with

$$\chi_{\mathrm{prior}}^2 = \frac{(p - p_{\mathrm{prior}})^2}{\sigma_{\mathrm{prior}}^2} \quad,$$

Table 6.4: Minimum-χ^2 values and parameter estimates derived with GRAVLENS for the isothermal and powerlaw models

		b ($''$)	q	Θ_{q} ($°$)	β	χ^2	d.o.f.	$\frac{\chi^2}{\text{d.o.f}}$
Model I	SIE	1.49	0.71	-21.6	2.00^1	11.5	7	1.6
		$1.47 - 1.51$	$0.69 - 0.73$	-24.1 − -19.3				
Model II	PL	2.76	0.86	-21.9	1.59	10.1	6	1.7
		$1.60 - 2.72$	$0.74 - 0.85$	-24.7 − -20.1	$1.60 - 1.94$			

[1]fixed value

where p is the used parameter value, p_{prior} its prior and σ_{prior} its 1σ error. Results give best-fitting parameters and their 1σ errors. The likelihood of a parameter set is given by $L \propto \mathrm{e}^{-\chi^2_{\mathrm{tot}}/2}$. In almost all cases, the best-fitting values are within the 68% error interval of the marginalised distributions.

The values of the parameters for the minimum χ^2 models are given in Tables 6.4 and 6.5. There, we give the model number, type, the best-fitting parameters of the model together with the resultant χ^2, the number of degrees of freedom (d.o.f.) and the reduced $\chi^2_{\mathrm{red}} = \frac{\chi^2}{\text{d.o.f.}}$ of each model. Also, the 1σ error intervals are given. These error estimates of the parameters are carried out using Monte Carlo Markov Chains (MCMC) methods with several thousand steps each. For each model, 10 chains are calculated with different starting points. Convergence is reached by comparing the variance of the point distribution of each of this chains with its combined distribution, see Fadely et al. (2010), Gelman et al. (1995). From the final chains, the 2nd half of each chain is combined to the final MCMC point distribution. The acceptance rate typically lies between 0.25 and 0.3. We explore potential parameter correlations from these and derive 68% confidence intervals[5] on the parameters by exclusion of the lowest and highest 16 % of the MCMC points' distribution; the central value is given by the median value of the MCMC points' distribution, since there are only small deviations between the median and the average values of the 68% and 90% error intervals.

We describe the most important different models without the lens' environment in the following: To check for the basic properties of the system, we model the lens as one component SIE (Model I) and PL (Model II) model. To derive the de Vaucouleurs masses in this lens, we combine a de Vaucouleurs component with a dark matter halo model (Model III) and show that this result is not significantly affected by also taking the environment into account (Models IV, V).

Model I The lens is modelled as a SIE (Eq. 6.1 with $\beta = 2$); the environment of the lens is ignored. The free parameters of this model are the lensing strength b, the axis ratio q, and its position angle Θ_{q}. The best-fitting model is shown in Fig. 6.4.

The results of the MCMC are shown in Fig. 6.5.

The density contours describe the probability density for the parameter values, whereas the best-fitting model is marked with a cross. The reason for the apparent correlation of q and b in Fig. 6.5 lies in the definition of κ in Eq. 6.1. The marginalised 68% confidence errors are:

---

[5]all given errors in this section are the 68% confidence values of the marginalised distributions, unless otherwise stated

Table 6.5: Minimum-χ^2 values and parameter estimates derived with GRAVLENS for the two component de Vaucouleurs plus dark matter models

		M ($10^{11} M_\odot$)	q_d	$\Theta_{q,d}$ (°)	c_d (″)	r_{200}	b_{group}	χ^2	d.o.f.	$\frac{\chi^2}{d.o.f}$
Model III	deVauc+NFW	7.4	0.79	-26.1	1.7	514		7.9	5	1.6
		$6.9 - 10.1$	$0.62 - 0.82$	$-28.3 - -23.3$	$1.4 - 2.8$	$277 - 534$				
Model IV	deVauc+GI	13.5					8.0	18.9	8	2.4
		$13.3 - 13.7$					$7.3 - 8.7$			
Model V	deVauc+NFW+GI	9.5	0.79	-24.6	2.2	280	3.7	7.8	4	2.0
		$8.7 - 11.8$	$0.68 - 0.90$	$-27.1 - -12.8$	$1.0 - 2.6$	$168 - 463$	$3.2 - 6.5$			
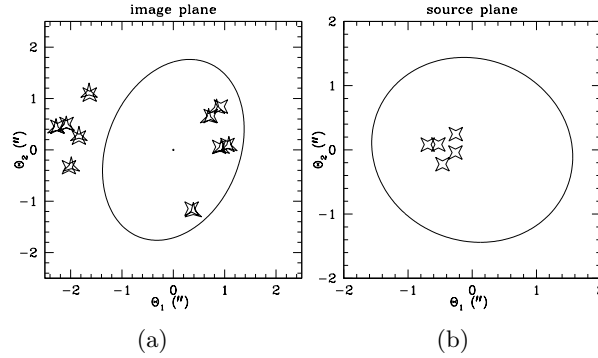
Figure 6.4: The best-fitting model derived with GRAVLENS for the SIE case (Model I) (see Table 6.4), both the image plane and the source plane are plotted. On the image plane triangles mark the input positions, while crosses mark the best-fitting model positions. On the source plane, the predicted source positions are plotted. Further, the respective critical lines (caustics) on the image (source) plane are plotted.

$b = (1.49^{+0.02}_{-0.02})''$, $q = (0.71^{+0.02}_{-0.02})$ and $\Theta_q = (-21.8^{+2.5}_{-2.3})°$. These values are in very good ($\approx 1\sigma$) agreement with the values derived by Bolton et al. (2008a) using a similar parameterisation for the lens total mass distribution.

Model II   Model II follows a power law (PL) (Eq. 6.1 with arbitrary β within the limits $[1, 2.7]$), and thus has one more free parameter relative to Model I. The values for the parameter distributions are shown in Fig. 6.6.
The marginalised distributions change to $b = (2.12^{+0.60}_{-0.52})''$, $q = (0.81^{+0.04}_{-0.07})$, $\Theta_q = (-22.2^{+2.1}_{-2.5})°$ and $\beta = (1.73^{+0.21}_{-0.13})$. We observe again (see Fig. 6.6) that the parameters b, q and β are correlated with each other. This is entailed by the definition of the convergence κ in Eq. 6.1. The steepness parameter β is constrained to a value shallower than isothermal on a 1.3σ level. The orientation Θ_q stays at the same angle as in the SIE case, while its axis ratio moves towards rounder solutions, now being comparable to the axis ratio of the light distribution.

Model III   In the following, we split the mass distribution into different components. We use a de Vaucouleurs like component as traced by the stellar component and add dark matter with different profiles if needed. Since the de Vaucouleurs component for galaxy A alone does not provide a good model, see Appendix 6.8, we add a dark matter component centred at galaxy A. We add an elliptical NFW-like component to the de Vaucouleurs profile. This composition resembles the common picture of galaxy mass distribution. For the dark matter halo, we impose a prior on the axis ratio based on the Bolton et al. (2008b) work of $q_{dark,prior} = (0.79 \pm 0.12)$. Also we set the limit of the scale radius to values $< 500''$, approximately 10 times the value we find from Sec 6.9.2 for the scale radius. The total mass of the de Vaucouleurs component is $M_{deV} = (8.8^{+1.3}_{-1.9}) \times 10^{11} M_\odot$ while the parameters of the dark matter halo are, see Fig. 6.7: $q_d = (0.72^{+0.1}_{-0.1})$, $\Theta_q = (-26.0^{+2.7}_{-2.3})°$, $c_d = (1.8^{+1.0}_{-0.4})$ and $r_{200} = (406^{+128}_{-129})''$.
We note that there is some degeneracy between the concentration c and r_{200}. Further we have no constraints on r_{200} from the data, since we do not have observables outside $2.32''$. Using a NSIE-like dark matter component yields similar results, as described in Appendix 6.8, Model IIIb.
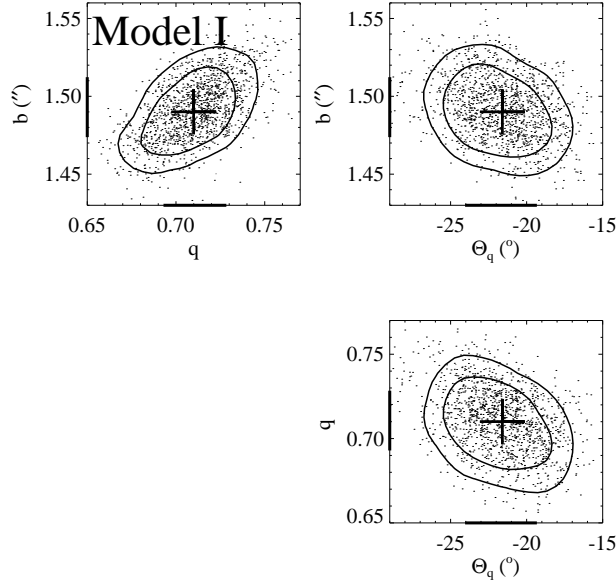
Figure 6.5: Error estimates of the MCMC for the SIE case (Model I), plotted are the individual points of the MCMC together with the 68 and 90 % confidence regions of the distribution, indicated by the density contours. The crosses mark the minimum-χ^2 value from Table 6.4. The bars on the axes mark the respective 68 % marginalised error intervals.

6.4.2 Lens modelling of the environment

As mentioned before, this galaxy is not an isolated field galaxy, hence we investigate the possible impact on the derived lens parameters by taking the environment into account. In the following, we centre a smooth group contribution at galaxy I and calculate its convergence and shear at the position of SDSSJ 1430+4105. Further modelling of the group contribution by summing up the contributions of the individual members ("clumpy group"), and by centreing it at galaxy A itself is discussed in Appendix 6.9.

Smooth group mass distribution centred at galaxy I

According to Rozo et al. (2009), we can transform the group richness into a group mass of $M_{500} = (0.72 \pm 0.29) \times 10^{14} M_\odot$ within 1σ. This mass can be converted into a velocity dispersion of $\sigma_{\mathrm{group}} = 519 \pm 107 \mathrm{km \, s^{-1}}$, using the critical density of the universe $500\rho_{\mathrm{c}}(z) = \frac{3M_{500}}{4\pi r_{500}^3}$ and the singular isothermal sphere equation: $M_{500} = M(r_{500}) =: \frac{2\sigma_{\mathrm{group}}^2 r_{500}}{G}$. There $\rho_{\mathrm{c}}(z)$ denotes the critical density of the universe at redshift z and σ_{group} the velocity dispersion of the group. Subsequently this gives an Einstein radius of $\Theta_{\mathrm{Ein}} = 3.6 \pm 1.5''$, using again a SIS assumption (see Sec. 6.4.1 for details). This results in a convergence of and shear of

$$
\begin{aligned}
\kappa_{\mathrm{A}}^{\mathrm{SIS \, group}} &= 0.029 \quad , \\
\gamma_{\mathrm{A}}^{\mathrm{SIS \, group}} &= 0.029
\end{aligned}
\tag{6.6}
$$

at galaxy A if galaxy I is assumed to be the group centre.
Alternatively, we model the smooth group as a 'typical' richness 12 galaxy group NFW (Navarro et al. (1997)) halo with concentration c = 4.22 and $r_{200} = 848 \, \mathrm{kpc}$ from Johnston
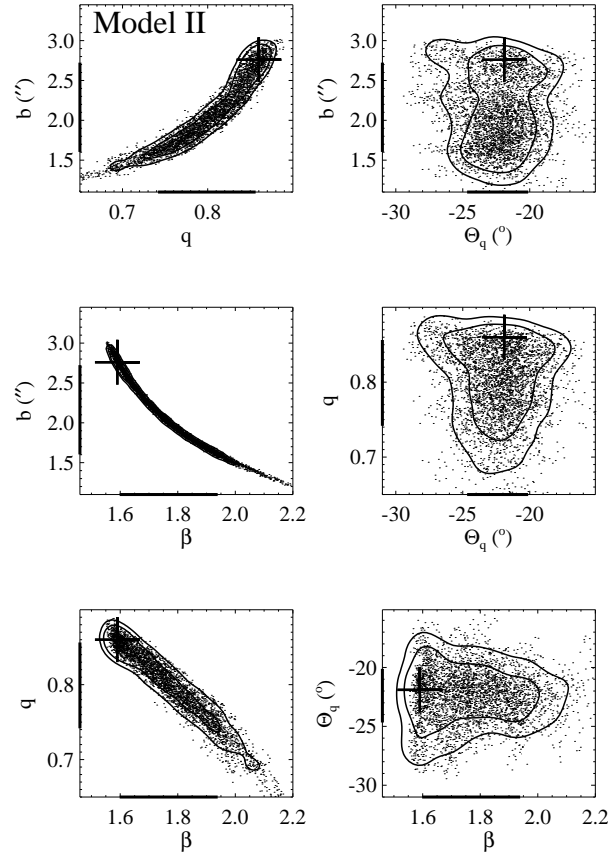
Figure 6.6: Error estimates of the MCMC for the PL case (Model II), plotted are the individual points of the MCMC together with the 68 and 90 % confidence regions of the distribution. The crosses mark the minimum-χ^2 value from Table 6.4. The bars on the axes mark the respective 68 % marginalised error intervals.

et al. (2007). We obtain a convergence and shear of

$$
\begin{aligned}
\kappa_{\mathrm{A}}^{\mathrm{NFW\,group}} &= 0.025 \quad , \\
\gamma_{\mathrm{A}}^{\mathrm{NFW\,group}} &= 0.026 \quad .
\end{aligned}
\tag{6.7}
$$

Further, we note that the angle of A towards I is $-26°$, therefore forming an angle of $16°$ with the external shear value derived in Sec. 6.9.1. We examine the HST and SDSS frames which cover galaxy I and its vincinity for group–scale multiple images to further constrain the group mass distribution but do not find any sign for strong lensing.

Model IV From Section 6.3.2 we expect that there is some environment dark matter present in this galaxy. We check whether using this group dark matter contribution with a de Vaucouleurs component for galaxy A is sufficient to explain the observations, even though modelling this system with a pure de Vaucouleurs component fails, see Appendix 6.8. Therefore, in this model, we combine the de Vaucouleurs profile with a group halo centred at galaxy I. To account for the environment, we include the galaxy group explicitly as a SIS profile centred at galaxy I in Table 6.3. We use a prior on the group Einstein radius of $b_{\mathrm{group,prior}} = (3.6 \pm 1.5)''$. The de Vaucouleurs component has shape parameters as stated in Table 6.1. The group acts
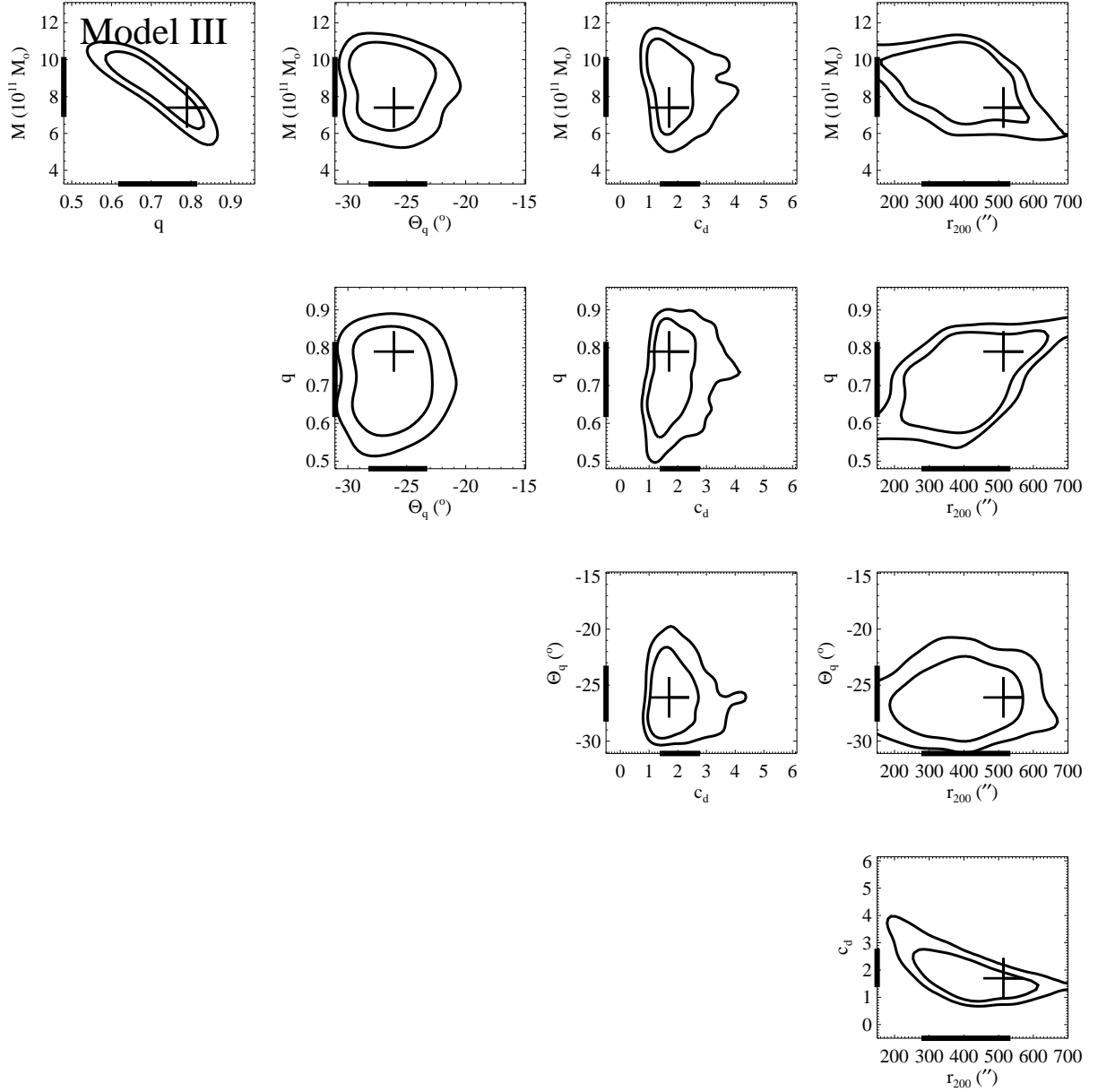
Figure 6.7: Error estimates of the MCMC for the NFW+de Vaucouleurs model (Model III), plotted are the 68 and 90 % confidence regions of the distribution. The crosses mark the minimum-χ^2 value from Table 6.5. The bars on the axes mark the respective 68 % marginalised error intervals. The individual points of the MCMC are omitted for clarity.

almost as a mass sheet. We get a $\chi^2 = 18.9$ for the best-fitting model. We get parameter estimates of $M_{\mathrm{deV}} = (13.5^{+0.2}_{-0.2}) \times 10^{11} M_\odot$ and $b_{\mathrm{group}} = (8.0^{+0.7}_{-0.7})''$ as can be seen in Fig. 6.8.
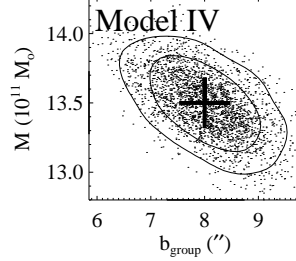

Figure 6.8: Error estimates of the MCMC for the de Vaucouleurs+GI model (Model IV), plotted are the individual points of the MCMC together with the 68 and 90 % confidence regions of the distribution, indicated by the density contours. The crosses mark the minimum-χ^2 value from Table 6.5. The bars on the axes mark the respective 68 % marginalised error intervals.

Besides being a worse fit than most of the other models, this model also needs a much more massive group present than what is likely from the observations. Therefore, dark matter that is distributed almost uniformly within Θ_{Ein} of the galaxy does not provide a good model for the system.

Model V This model adds environmental effects to Model III. Therefore we add the group GI explicitly as above, yielding 3 components: the group GI, the dark matter associated with the galaxy as an elliptical NFW profile and a stellar component modelled as a de Vaucouleurs profile. We use the same constraints as for Model III. We get the following parameters, see also Fig. 6.9: $M_{\mathrm{deV}} = (10.4^{+1.4}_{-1.7}) \times 10^{11} M_\odot$, $q_d = (0.79^{+0.11}_{-0.11})$, $\Theta_q = (-21.6^{+8.8}_{-5.4})°$, $c_d = (1.4^{+1.2}_{-0.4})$, $r_{200} = (321^{+141}_{-153})''$, and for the galaxy group $b_{\mathrm{group}} = (4.9^{+1.6}_{-1.7})''$.
We note that these parameter estimates do not significantly change compared to Model III, therefore the inclusion of group GI has only a small influence on the estimated galaxy parameters; the M_{deV} for the de Vaucouleurs component is slightly increased. Again, we are not able to constrain the concentration c or r_{200} of the dark matter halo. Models Va and Vb in Appendix 6.8 employ a NSIE-like galaxy dark matter halo (Model Va) and an external shear contribution instead of a explicit group contribution (Model Vb) and again give results very similar to Model V regarding the parameters for the lensing galaxy.

6.4.3   Full surface brightness distribution using LENSVIEW

We also use LENSVIEW (Wayth & Webster (2006)) to derive models and mass estimates for SDSSJ 1430+4105 and to reproduce the full surface distribution of the lensed galaxy and its unlensed source. LENSVIEW is a publicly available program that fits parametric lens models to image data and uses the best-fitting lens model to reconstruct the source and image. The code uses the image data, a corresponding noise map, and an image mask to minimise $\chi^2 - \lambda S$, where χ^2 is the chi square difference between the reconstructed image and the data, S is the entropy in the source, and λ is internally adjusted such that χ^2 approaches its target value. If the data are well fit by the model, the entropy term serves to smooth the source. Because the flux of each unmasked data pixel is used in the fit, LENSVIEW is well-suited to systems with extended flux like SDSS J1430+4105. The profile used here is defined, following Barkana (1998), as
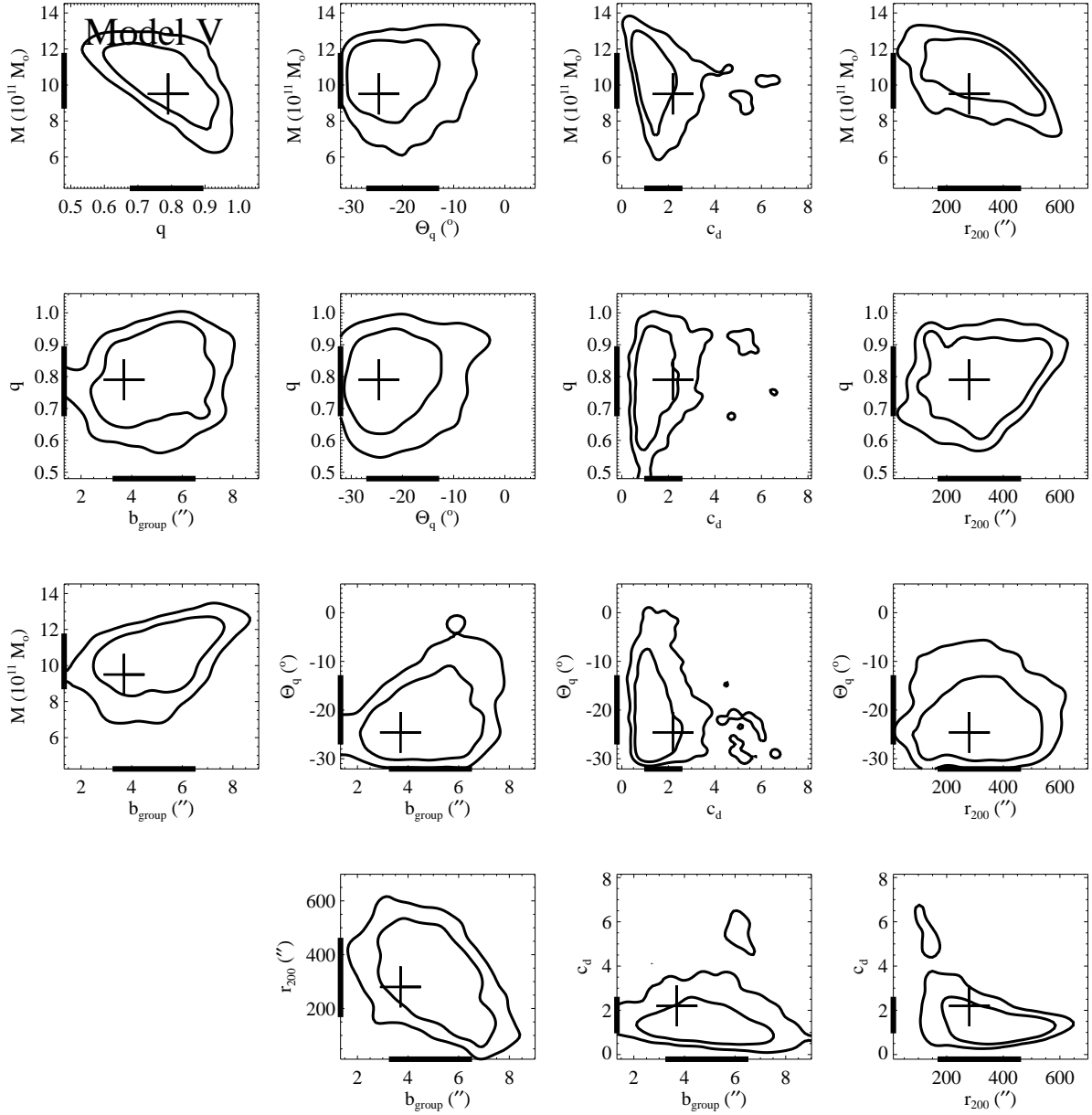
Figure 6.9: Error estimates of the MCMC for the de Vaucouleurs+NFW model (Model V), plotted are the 68 and 90 % confidence regions of the distribution. The crosses mark the minimum-χ^2 value from Table 6.5. The bars on the axes mark the respective 68 % marginalised error intervals. The individual points of the MCMC are omitted for clarity.

Table 6.6: Minimum-χ^2 values derived with LENSVIEW

	b	q	Θ_q	γ^1	Θ_γ	β	χ^2_{red}
	($''$)		($°$)				
SIE	1.49	0.69	-19.5	0^2	0^2	2.00^2	1.4
SIE+ES	1.45	0.80	-23.0	0.046	-105	2.00^2	1.02
PL	1.53	0.77	-20.2	0^2	0^2	1.83	1.02
PL+ES	1.50	0.85	-22	0.047	-106	1.89	0.99

[1]The external shear at the position of the galaxy A

[2]fixed value

$$\kappa(\Theta_1, \Theta_2) = \frac{b'}{2} \left(\frac{3 - \beta}{q} \right)^{\frac{\beta - 1}{2}} (\Theta_1^2 + \frac{\Theta_2^2}{q^2})^{\frac{1 - \beta}{2}} , \tag{6.8}$$

where b' gives the Einstein radius, q the axis ratio and β again the power law exponent of the profile. We note that the normalisation of the profiles is different from Eq. 6.1, resulting in different values for the Einstein radius in both approaches.

The minimum-χ^2 results are stated in Table 6.6.

The SIE best-fitting parameter values derived here agree with those found in Sec. 6.4.1, when directly compared to Model I in Table 6.4. For the PL model, we see a consistency of the different models from GRAVLENS and LENSVIEW within the stated errors for q, Θ_q and β. Since, as mentioned before, the normalisation of the convergence profiles is different, the b / b' values do not compare directly to each other. For the models including the environment, the direct comparison of the SIE+ES model with Model Ia shows again a consistency within the errors derived in Appendix 6.8 for the lens parameters. However, the external shear angle shows a discrepancy, the angle is offset relative to the expected value derived in Sec. 6.3.2. Since the external shear contributes no mass, this will not have a significant effect on the mass estimates in Sec. 6.5. The same is true for the PL+ES case, the comparison with Model IIa gives an agreement within the given errors in all parameters besides Θ_γ. The best–fitting SIE model, residual and source are shown in Fig. 6.10.

(a)   (b)   (c)
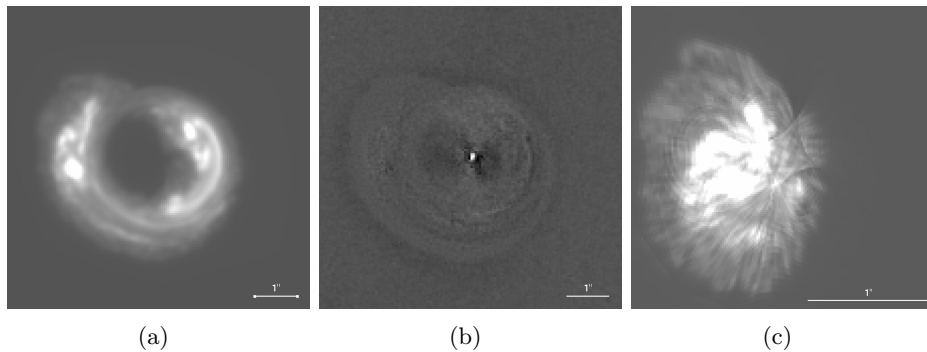
Figure 6.10: best-fitting model for the SIE case 6.10(a), its residuals 6.10(b) and the corresponding source 6.10(c). For the images 6.10(a) and 6.10(b), the pixel size is the same as in Fig. 6.2; the source has a 3 times smaller pixel size. The same flux scaling has been used on all images.

6.4.4 Tests on the strong lensing assumptions

For all but the single, pure de Vaucouleurs model, the centre of the light and mass distribution do not necessarily have to coincide. To address possible systematic effects of the assumption that the mass model profiles are centred on the centre of light, we use Model I with a free centre with priors on the centre position of uncertainty $\sigma_{\Theta_{1,l}} = \sigma_{\Theta_{2,l}} = 0.2''$. In this case, we find: $b = (1.51^{+0.02}_{-0.02})''$, $q = (0.69^{+0.06}_{-0.04})$ and $\Theta_q = (-26.1^{+2.3}_{-2.4})°$. The lens total mass centre moves to $\Theta_{1,l} = (-0.02^{+0.05}_{-0.07})''$ and $\Theta_{2,l} = (-0.11^{+0.04}_{-0.04})''$. The lensing strength b and the axis ratio q agree within the errors with the values derived for Model I, but the uncertainty on q increases. While the lens position $\Theta_{1,l}$ is still consistent with 0, there is a dependency of $\Theta_{2,l}$ and Θ_q. This has no effect on the mass profiles $M(< R)$, so we conclude that we can fix the lens total mass centre to its centre of light without inducing systematic effects on the derived masses.

In the previous sections we restricted the smooth mass model of the group GI to be spherically symmetric. We alter the shape of group GI to an elliptical isothermal profile (SIE) and study the changes on the best-fitting SIE lens models. This model is analogous to Model Ia, but combines a SIE lens with a SIE instead of a SIS galaxy group centred on galaxy I. Therefore, we create 2000 random representations of group GI as a SIE. For each of these representations, the axis ratio is randomly chosen between $q_{GI} = [0.6, 1]$ with a random orientation. The centre of this SIE group model is taken from a gaussian distribution, centred on galaxy I, with a width of $\sigma_{x,GI} = \sigma_{y,GI} = 1.5''$. We recalculate the best-fitting parameters for each of these SIE+GI(SIE) models and evaluate the scatter of the best-fitting parameters to estimate the systematic uncertainties emerging from the assumption of a simple SIS group halo. This results in 68% c.l. distributions of the best-fitting parameters for this modified Model Ia: $b_{lens} = [1.44, 1.46]''$, $q_{lens} = [0.79, 0.82]$, $\Theta_q = [-18.4, -16.2]°$ and $b_{group} = [4.27, 4.42]''$. These intervals are small compared to the statistical uncertainties for Model Ia derived from the MCMC sampling. We conclude that the details of the group model representation do not change the results for the lensing galaxy significantly, therefore including the most simple SIS model for group GI is sufficient.

6.5 Results for the galaxy mass profile

The total masses $M(< R)$ within a cylinder of radius R and their derivatives obtained from the lensing analysis for Models I to V are shown in Figs. 6.11 and 6.13. We have calculated these values within several concentric apertures with radii ([0.46 0.92 1.26 1.59 1.95 2.32 2.78] $''$), chosen to lie in the radial regions covered by the lensed images plus extrapolations towards smaller / larger radii. For the Models I to V of Secs. 6.4.1 and 6.4.2, the masses are estimated by randomly taking 1000 MCMC points and creating convergence maps for each one of these 1000 models. The 68 % (90 %) errors are estimated by taking the central 680 (900) models at each radius.

6.5.1 Mass profiles for the single component isothermal and powerlaw models

First we focus on the masses derived for Models I and II in Table 6.4. The Einstein radii are defined as the radii within which the mean convergence equals 1. For this, we calculate

the mean convergence around the Einstein radius in $0.03''$ distance bins. The results of this calculation are stated in Table 6.7.

Since all models agree on an Einstein radius of $\Theta_{\text{Ein}} = 1.51'' \stackrel{\wedge}{=} 6.48\,\text{kpc} = R_{\text{E}}$, we adopt this value as "the" Einstein radius of this lens with an uncertainty of $0.03'' \stackrel{\wedge}{=} 0.13\text{kpc}$. We get a mean Einstein mass of $(5.37 \pm 0.06) \times 10^{11} M_\odot$ for the Models I and II with a fixed Einstein radius of $\Theta_{\text{Ein}} = 1.51''$. This values are in good agreement with the ones stated by Auger et al. (2009) for this system also based on strong lensing.

We also extrapolate the models to the effective radius $r_{\text{eff}} = 2.55'' \stackrel{\wedge}{=} 10.96\,\text{kpc}$ of the galaxy, and calculate the mass and its derivative. We find an enclosed mass between $M_{\text{tot,enc}} = 8.9 \times 10^{11} M_\odot$ and $M_{\text{tot,enc}} = 11.3 \times 10^{11} M_\odot$ on a 1σ level, depending on the model used. The azimuthally averaged results of the included masses are plotted in Fig. 6.11.
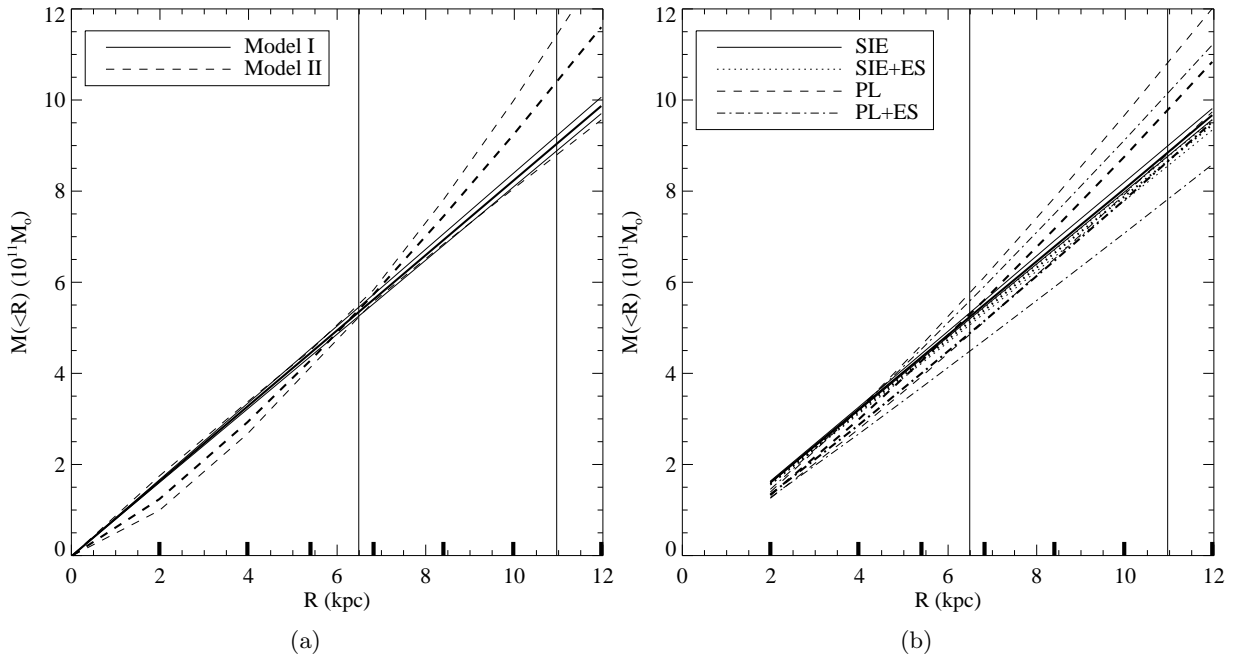
Figure 6.11: The mass within radius R, $M(< R)$, from the models I and II, analysed in Sec. 6.4 is plotted in Fig. 6.11(a). For each model, 1000 random entries from the MCMC are used to calculate the errors. Each time, the means and 90 % errors are shown, with the respective means in bold lines. The bars at the bottom mark the radii of the apertures used to calculate the enclosed projected masses. The masses are in units of $10^{11} M_\odot$, the radii are stated in kpc in the lens plane. The mass estimates for the Models I and II are shown as solid (I) and dashed (II) lines. Vertical lines indicate the Einstein and effective radius in both plots. Fig. 6.11(b) shows the same as Fig. 6.11(a) but for the LENSVIEW derived masses. The errors are estimated by an increase of the reduced χ^2 of the extended model by 1. As can be seen, the masses agree with each other in terms of derived masses within the errors.

For an SIE model, the mass included within radius r grows linearly with the radius, so the derivative of it is expected to be independent of the radius. This is the case for the singular isothermal model (Model I) in Table 6.4. If we allow the steepness to vary (Model II) the mass profile tends to be steeper at the Einstein and effective radius. For the radial mass derivative at the Einstein radius, we calculate values between $\frac{\text{d}M_{\text{tot,enc}}}{\text{d}R} = 0.8 \times 10^{11} M_\odot \text{kpc}^{-1}$ and $\frac{\text{d}M_{\text{tot,enc}}}{\text{d}R} = 1.2 \times 10^{11} M_\odot \text{kpc}^{-1}$. The extrapolation to the effective radius ranges from $\frac{\text{d}M_{\text{tot,enc}}}{\text{d}R} = 0.8 \times 10^{11} M_\odot \text{kpc}^{-1}$ for Model I to $\frac{\text{d}M_{\text{tot,enc}}}{\text{d}R} = 1.6 \times 10^{11} M_\odot \text{kpc}^{-1}$ for Model II. This values are plotted in Fig. 6.12. Here and in Table 6.4 we state the 68 % c.l. errors.

Table 6.7: The masses and mass derivatives at the Einstein radius, the globally adopted Einstein radius and the effective radius for the different models. Given are the projected, enclosed masses and its derivatives

Model	Θ_{Ein} ($''$)	$\mathrm{M}_{\mathrm{Ein}}$ $10^{11} M_\odot$	$\frac{dM}{d\Theta}(\Theta_{\mathrm{Ein}})$ $10^{11} M_\odot/''$	κ_{Ein}	$\mathrm{M}(<1.51'')$ $10^{11} M_\odot$	$\frac{dM}{d\Theta}(\Theta=1.51'')$ $10^{11} M_\odot/''$	$\mathrm{M}(<2.55'')$ $10^{11} M_\odot$	$\frac{dM}{d\Theta}(\Theta=2.55'')$ $10^{11} M_\odot/''$
Model I	1.51 ± 0.03	$5.35^{+0.07}_{-0.06}$	3.55 ± 0.04	$0.497^{+0.006}_{-0.005}$	$5.35^{+0.07}_{-0.06}$	3.55 ± 0.04	$9.04^{+0.11}_{-0.10}$	3.55 ± 0.04
Model II	1.54 ± 0.03	$5.54^{+0.06}_{-0.05}$	$4.5^{+0.6}_{-0.8}$	$0.68^{+0.08}_{-0.10}$	$5.40^{+0.04}_{-0.05}$	$4.5^{+0.6}_{-0.7}$	$10.4^{+0.9}_{-1.1}$	$5.1^{+1.1}_{-1.3}$

[1] galaxy part only, mass contribution of GI is ignored
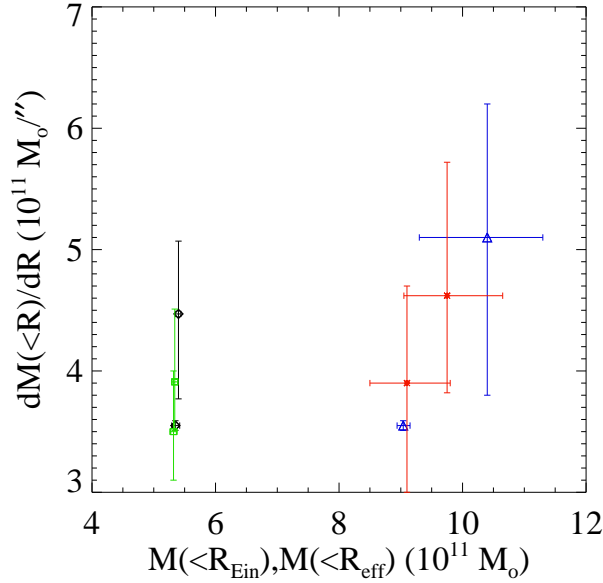
Figure 6.12: The masses and radial derivatives for the Models stated in Table 6.7 and Table 6.8. Plotted are the mean values together with its 1 σ error bars. For Models I and II, the black asterixes mark the values at the Einstein radius (fixed to $1.51''$), while the blue triangles mark the extrapolations to the effective radius of the galaxy. For the de Vaucouleurs like models III and V, the green squares are the values at the Einstein radius, the red crosses are the ones at the effective radius. While the total mass within the Einstein radius is tightly constrained independent of the model used, the mass within the effective radius depends on the mass model used.

6.5.2 Mass profiles for the de Vaucouleurs plus dark matter halo models

From the single component lens analyses in Sec. 6.5.1, we conclude that the total projected mass density profile is isothermal or slightly shallower than isothermal. The de Vaucouleurs mass density drops faster with radius than the isothermal profile. Therefore, we expect the pure de Vaucouleurs profile to be a poor description of this lens' mass profile (as seen in Model IV in Sec. 6.4.2 and Model IVa in Appendix 6.8) and expect that we need to add some component which follows a shallower than isothermal density profile. In principle a constant mass sheet, like a nearby group halo would approximately provide, could do this, given that it provides enough mass at the position of the lens. In Model IV, we see that this model is a poor fit to the data. Therefore a (dark) matter component centred at the position of the lens is necessary. We model this in Models III, IIIa and IIIb in Sec. 6.4.1 and Appendix 6.8 with different types of dark matter halo profiles. A SIE-like dark matter component (Model IIIa) suppresses the de Vaucouleurs part of the matter profile, effectively yielding a single component model. Because the light distribution is well-fit by a de Vaucouleurs profile, we require a non-zero de Vaucouleurs component for this 2 component fit, hence we do not consider Model IIIa in the following. The Models IIIb, Va and Vb in Appendix 6.8 give similar results to Models III and V in Sec. 6.4.1. Therefore, in the following, we mostly consider Models III and V, which model the lens using an NFW profile for the dark matter component.

Besides the stars and the dark matter, an elliptical galaxy or a galaxy group also contains some amount of gas. Since we do not model this component individually, this gas needs to be incorporated in either the dark matter or the de Vaucouleurs component, effectively limiting the accuracy of our mass estimates to the gas mass fraction in elliptical galaxies and groups

of galaxies. Young et al. (2011) get typical molecular gas masses of early-type galaxies in the ATLAS^{3D} project of $M(H_2) \leq 10^9 M_\odot$, less than 1% of the total galaxy masses derived here. The hot gas component in an elliptical galaxy or a group of galaxies can contribute up to 10% of the total mass in the centre of the galaxy or group of galaxies, see e.g. Sanderson et al. (2003). Hence the uncertainty of our mass estimates due to the neglected gas is $\approx 10\%$.

We again adopt $\Theta_{\text{Ein}} = 1.51''$ for the Einstein radius. First we focus on the masses within this radius, see Table 6.8.

For the total masses within the Einstein radius of the models III and V, we measure $M_{\text{tot,Ein}} = (5.33 \pm 0.04) \times 10^{11} M_\odot$ The radial mass derivative is $\frac{dM_{\text{tot,enc}}}{dR} = 0.86^{+0.09}_{-0.07} \times 10^{11} M_\odot \text{kpc}^{-1}$. The extrapolations to the effective radius give $M_{\text{tot,eff}} = 9.5^{+0.6}_{-0.5} \times 10^{11} M_\odot$ for the mass and $\frac{dM_{\text{tot,enc}}}{dR} = 1.00^{+0.16}_{-0.14} \times 10^{11} M_\odot \text{kpc}^{-1}$ for its derivative. This values are plotted in Fig. 6.12. As can be seen, the enclosed masses and its derivatives at the Einstein radius and the effective radius agree with each other throughout Models I, II, III and V. We state the de Vaucouleurs mass within the Einstein and effective radius of Model III as Component IIIA in Table 6.8. We get a mass of $M_{\text{deV,Ein}} = (3.2^{+0.5}_{-0.7}) \times 10^{11} M_\odot$, meaning that $\frac{M_{\text{deV,Ein}}}{M_{\text{deV,tot}}} \approx 35\%$ of the total de Vaucouleurs mass is concentrated within the Einstein radius for this lens. For Model V, we get similar values for the de Vaucouleurs component, see Component VA in Table 6.8. In Fig. 6.13 and Fig. 6.20 in Appendix 6.8, the projected, enclosed lens masses and their derivatives are plotted versus radius for the different 2 component strong lensing models.

The measurements are done using circular apertures, so all of these values are azimuthally averaged. As one can see, including an explicit group halo GI (Model V) has only a minor influence on the mass estimates and their derivatives. The total masses agree very well with the one component estimates in Fig. 6.11. Also, all models agree very well on the total masses and their radial derivatives, tending to give a shallower than isothermal mass profile in the centre. For the Models III and V in Fig. 6.13, the dark matter haloes modelled as NFW-haloes agree very well with each other, meaning that the environment has only minor influence on the mass estimates. This is also true for the de Vaucouleurs component. We note that the uncertainties on the individual components are larger than the uncertainties on the total masses and derivatives, giving a well-constrained total mass.

6.5.3 3d spherical reconstruction

Further, we also reconstruct the 3d matter densities from the 2d data for Model III. For this, we employ the inverse Abel-transform:

$$\rho(r) = -\frac{1}{\pi} \int_r^\infty \frac{d\Sigma}{dR} \frac{dR}{\sqrt{R^2 - r^2}} \quad , \tag{6.9}$$

transforming a 2d circular density function Σ into a 3d sperical density function ρ. Since this only transforms circular to spherical profiles and vice versa, we start from the mass measurements within a cylinder in Fig 6.13(a) for the azimuthally averaged profile. In Eq. 6.9 the integration extends to infinity, which is not possible due to our limited range of reliable data. To estimate the radial range at which we can use Eq. 6.9 only integrating up to our last data bin we test it on a SIS toy model. For a SIS toy model, we know both the spherical and the projected circular density. We then consider this radial range reliable where the deviation of the reconstructed 3d density from the analytical SIS density does not exceed $2 \times 10^7 M_\odot \text{kpc}^{-3}$. From this comparison, we conclude that this inverse Abel transformation

Table 6.8: Same as Table 6.7 for the 2 component models.

Model	Θ_{Ein} ($''$)	$\mathrm{M}_{\mathrm{Ein}}$ $10^{11}M_\odot$	$\frac{d\mathrm{M}}{d\Theta}(\Theta_{\mathrm{Ein}})$ $10^{11}M_\odot/''$	κ_{Ein}	$\mathrm{M}(<1.51'')$ $10^{11}M_\odot$	$\frac{d\mathrm{M}}{d\Theta}(\Theta=1.51'')$ $10^{11}M_\odot/''$	$\mathrm{M}(<2.55'')$ $10^{11}M_\odot$	$\frac{d\mathrm{M}}{d\Theta}(\Theta=2.55'')$ $10^{11}M_\odot/''$
Model III	1.51 ± 0.03	5.34 ± 0.05	$3.9^{+0.6}_{-0.4}$	$0.55^{+0.08}_{-0.06}$	5.34 ± 0.05	$3.9^{+0.6}_{-0.6}$	$9.8^{+0.9}_{-0.9}$	$4.6^{+1.1}_{-0.8}$
Component IIIA[1]					$3.2^{+0.5}_{-0.7}$	$1.4^{+0.2}_{-0.3}$	$4.4^{+0.7}_{-1.0}$	$0.90^{+0.15}_{-0.20}$
Model V	1.48 ± 0.03	5.21 ± 0.06	3.5 ± 0.4	0.50 ± 0.06	5.32 ± 0.06	$3.5^{+0.5}_{-0.5}$	$9.1^{+0.7}_{-0.7}$	$3.9^{+0.8}_{-0.9}$
Component VA[1]					$3.8^{+0.5}_{-0.6}$	$1.6^{+0.2}_{-0.3}$	$5.2^{+0.7}_{-0.8}$	$1.06^{+0.15}_{-0.17}$
Component VB[2]	1.45 ± 0.03	$4.91^{+0.09}_{-0.08}$	$3.2^{+0.5}_{-0.4}$	$0.47^{+0.07}_{-0.06}$	$5.11^{+0.10}_{-0.09}$	3.2 ± 0.5	$8.5^{+0.8}_{-0.7}$	$3.3^{+1.1}_{-0.8}$

[1] de Vacouleurs like part only, dark matter contribution is ignored
[2] galaxy part only, mass contribution of GI is ignored
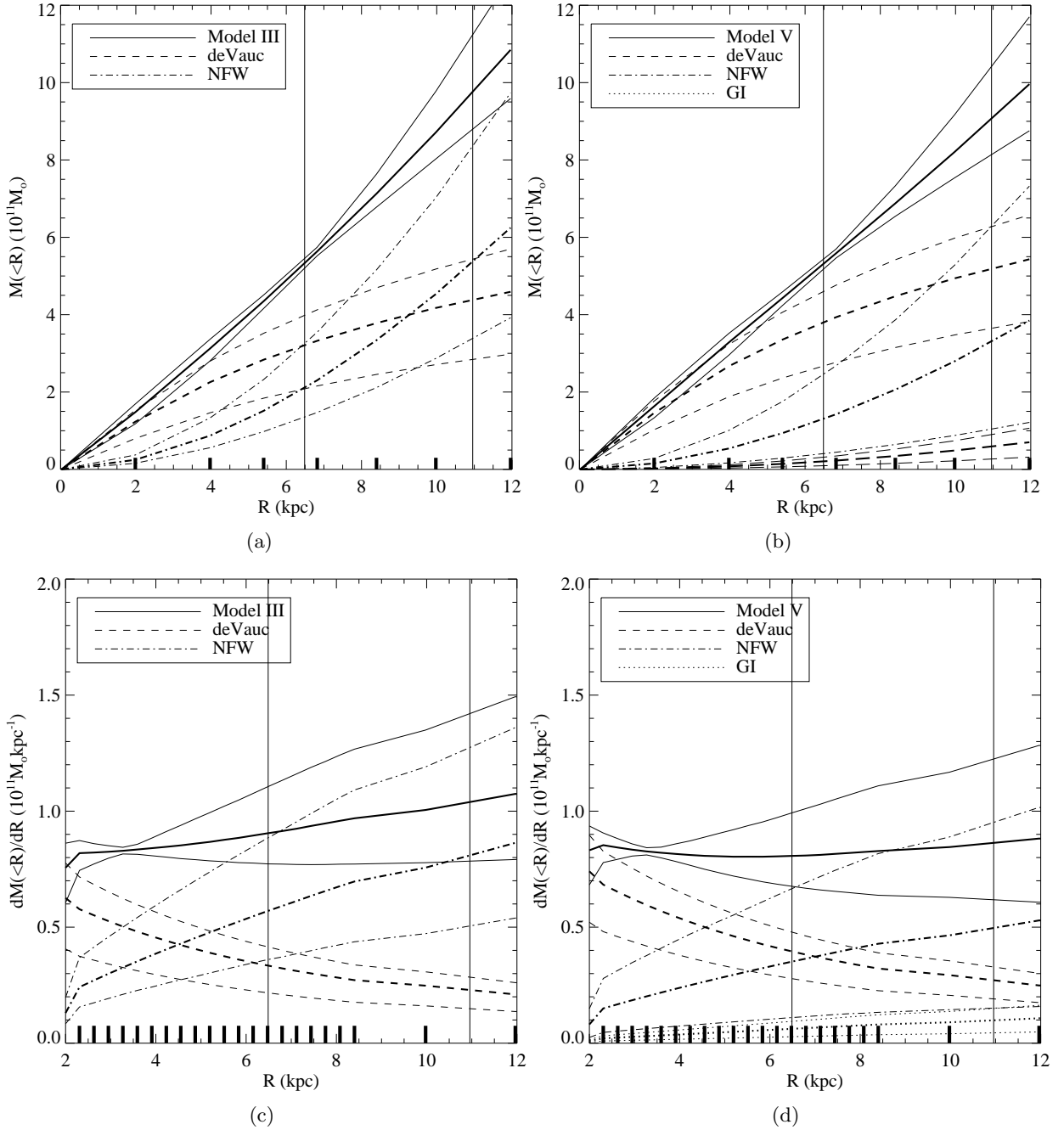
Figure 6.13: The mass within radius R, $M(< R)$ from the Models III and V analysed in Sec. 6.4. For each model, 1000 random entries from the MCMC chains are used to calculate the errors. All errors plotted are the 90 % error intervals with the respective means in bold symbols. The bars at the bottom mark the radii of the apertures used to calculate the enclosed projected masses or its derivatives. The masses are in units of $10^{11} M_\odot$, the radii are stated in kpc in the lens plane. In 6.13(a), the mass estimates of Model III for the de Vaucouleurs (dashed line), NFW (dot–dashed line) and its sum (solid line) are plotted. While the sum of these two is fairly well constrained, the errors on the individual parts are bigger. In 6.13(b), the same mass estimates are plotted for Model V, together with its 90 % error intervals, splitted in de Vaucouleurs (dashed line), NFW (dot–dashed line) and GI (dotted line) parts and its total sum (solid line). The radial mass derivatives are plotted in 6.13(c) for Model III and 6.13(d) for Model V, keeping the line coding. Plotted is the change in enclosed mass with radius. This can also be interpreted as the mass in a thin ring with width dR at radius R, $M(R)$. Again, vertical lines indicate the Einstein and effective radius in both plots.

is only reliable up to ≈ 6.5 kpc with a systematic error smaller than 30%, given our limited radial range of data. The reconstructed 3d profile is shown in Fig. 6.14.
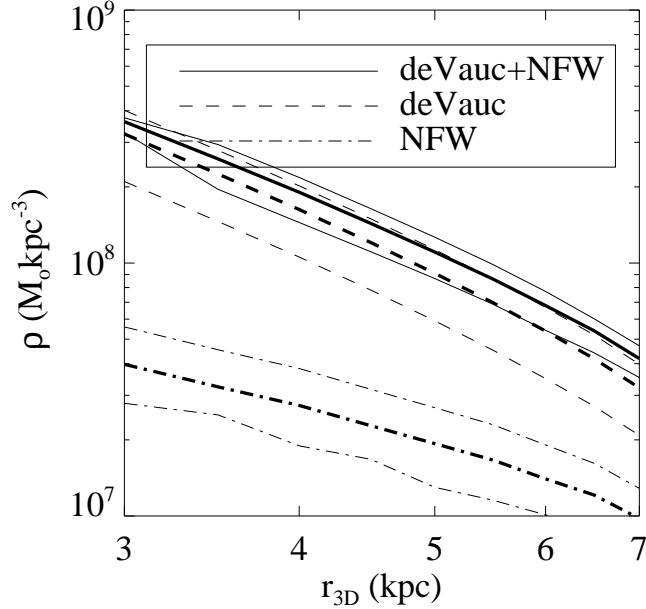
Figure 6.14: The 3d densities for the stellar (dashed) and the dark (dash-dotted) component, as well as the total matter (solid) For this, the data of Model III is used. Plotted are the median (thick) and the 90 % c.l. intervals. Spherical symmetry is assumed for this reconstruction.

The errors plotted are only statistical, not taking any systematic effects into account. The dark matter accounts for only a minor fraction of the total mass in the 3d centre of the galaxy. We now turn to Fig. 7 in Thomas et al. (2011). In the lower part of Fig. 7 they have displayed the ratios of the mean dark matter density and mean total density within the Einstein radius of Coma galaxies as a function of their velocity dispersion. (For the definition of the synthetic Einstein radius for Coma galaxies, see Thomas et al. 2011). To see whether there are structural differences for the Coma and the higher redshift SLACS sample one would like to enter the corresponding deprojected values for SLACS galaxies in these figures as well. These were not available until now because the dark to total matter fractions were only calculated for the line of sight projected densities within the Einstein radii (i.e. cylindrical averages) by gravitational lensing. The corresponding projected values are shown for SLACS (and Coma) galaxies in the upper part of Fig. 7 of Thomas et al. (2011). The projected and deprojected values differ, since the projection along the line of sight mixes scales: parts of the matter that have a large physical distance from the centre of the galaxy but lie on the line of sight are taken into account when calculating the projected dark matter fractions. Due to the monotonic increase of the dark to total matter density ratios as a function of radius, the projected ratios displayed in the upper part of Fig. 7 of Thomas et al. (2011) are upper limits to the central, 3–dimensional density ratios at the Einstein radius. With the analysis described in this work we are able to measure the 3–dimensional densities of the (spherically averaged) dark matter and de Vaucouleurs components of the lensing galaxy separately from gravitational lensing alone due to the large radial coverage of multiple images in the image plane by one source. Since the source is only one background object, we do not need to take the systematic uncertainties into account that arise in systems with multiple image systems

from sources at different redshifts like e.g Gavazzi et al. (2008). At the Einstein radius we obtain (using Fig. 6.14, displaying Model III (de Vaucouleurs+NFW)) a dark to total density ratio of 22 per cent for the dark to total density. Doing the same for the Model V where SDSSJ 1430+4105 (consisting of de Vaucouleurs and dark matter component) is embedded in a DM halo centred on galaxy I we find that the ratio of dark to total matter density at the Einstein radius is about 14%. Since the dark matter fraction increases towards the outskirts, these ratios of densities at the Einstein radius are upper limits for the mean dark matter to total matter density ratios of galaxy SDSSJ 1430+4105 within the same Einstein radius. On a (90 per cent c.l.) basis, the density ratios at the Einstein radius are larger than 15 per cent (Model III) and 5 per cent (Model V) for the dark to total matter density.

6.6 Mass to light ratios for the de Vaucouleurs component and dark to total mass ratio

Since we calculated the de Vaucouleurs masses for this galaxy, we now want to estimate the rest–frame mass–to–light ratios of this galaxy. Further, we evolve these mass–to–light ratios to present–day values in order to compare it with those of Coma galaxies. First, we calculate the dark matter fractions within the Einstein radius. In Fig. 6.15, we plot the dark over total enclosed mass fraction within the Einstein radius.
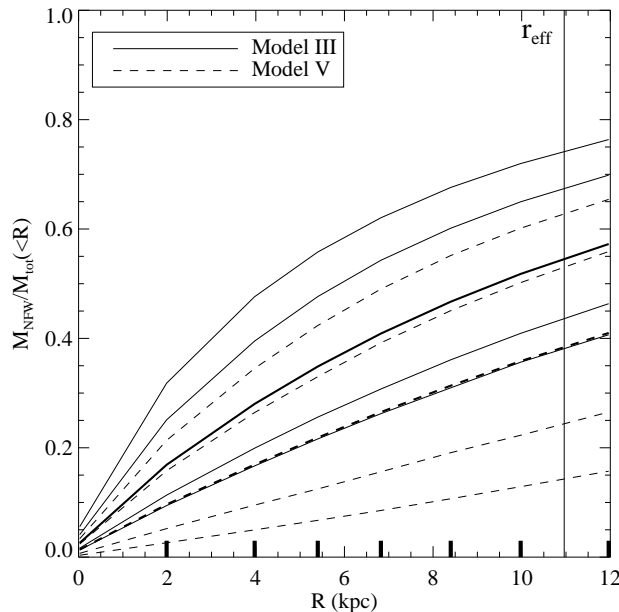
Figure 6.15: Dark over total enclosed mass ratio for this galaxy. Shown are Models III (solid) and V (dashed). For Model V the group contribution is ignored, meaning that we only consider the dark matter associated with the galaxy itself as dark matter and only the sum of de Vaucouleurs and dark matter as the total matter. The vertical line indicates the effective radius of the galaxy. As one can see, both models predict dark matter contributions in the centre of this galaxy, with changing amounts depending on the modelling details. Plotted are the 68 % and 90 % errors, respectively.

The error bars are estimated as before from the central 68 and 90 per cent entries of the random sample drawn from the MCMC for Models III and V, respectively. The fractions for Model III and V are: $\frac{M_{NFW}}{M_{tot}} = (0.40^{+0.13}_{-0.09})$ and $\frac{M_{NFW}}{M_{tot}} = (0.27^{+0.12}_{-0.11})$. These fractions indicate

Table 6.9: Galaxy luminosity evolution factors for the different IMF and metallicity models

	$(B - R)_{\rm rf}$ ABmag	T Gyrs	τ Gyrs	$\frac{L_{\rm B,rf}}{L_{\rm B,z=0}}$	$\frac{L_{\rm R,rf}}{L_{\rm R,z=0}}$	$M_\star$ $(10^{11} M_\odot)$
A	0.77	8	2	1.77	1.48	6.7
B	0.85	8	2	1.92	1.55	4.4
C	0.81	9	2	1.66	1.42	4.0

a substantial amount of dark matter within the Einstein radius of this lens. As can be seen, this picture is not significantly altered by locating the group at I in Model V. Although the actual numbers change, we still need dark matter associated with the lens in the centre of the galaxy. Since we ignore the dark matter contribution associated with the group GI in Model V for the total mass, we get a lower dark matter fraction for Model V compared to Model III.

For the Models III and V, we calculate the mass to light ratios for the de Vaucouleurs component at the redshift of the lens. We use the masses from lensing and the light (in rest frame B and R) as obtained from photometric data. To compare the mass to light ratios with present day galaxies, we also need the luminosity evolution to redshift zero in these bands. We take the observed griz SDSS photometry for this system which covers the rest frame B and R filters to calculate the B-R rest frame colour.[6] We calculate a colour of $(B - R) = (0.80 \pm 0.03)$ and luminosities of $L_{\rm B,rf} = (1.66 \pm 0.03) \times 10^{11} L_{\odot,\rm B}$ and $L_{\rm R,rf} = (1.92 \pm 0.02) \times 10^{11} L_{\odot,\rm R}$ from the absolute rest frame magnitudes. To estimate the luminosity evolution until today, we fit 3 extinction-free BC (Bruzual & Charlot, 2003) composite stellar population (CSP) models to the observed griz SDSS photometry: A Salpeter initial mass function (IMF) (Salpeter, 1955) with solar metallicity (Model A) and 2 models with Chabrier IMF (Chabrier, 2003) and solar / super–solar metallicity (Models B,C), respectively, see Drory et al. (2001, 2004). The best-fitting results are stated in Table 6.9 together with the luminosity evolutions in B and R bands and the best-fitting stellar masses, which agree with Grillo et al. (2009).

From the best-fitting star formation histories (SFH) to the spectral energy distribution (SED) we obtain a stellar age of typically 8 Gyrs and a B-R colour of 0.8. Therefore, this galaxy has a formation redshift of approximately 2 to 3 which is a typical value for elliptical galaxies. If we divide the de Vaucouleurs masses derived by lensing in Sec. 6.4 by the luminosities derived from the SDSS photometry we obtain the mass to light ratios (MtoL) for the de Vaucouleurs component of this galaxy. For Models III and V, we find a MtoL of $\frac{M_{\rm deV}}{L_{\rm B}} = (5.3^{+0.8}_{-1.1}) \frac{M_\odot}{L_{\odot,\rm B}}$ and $\frac{M_{\rm deV}}{L_{\rm B}} = (6.2^{+0.9}_{-1.0}) \frac{M_\odot}{L_{\odot,\rm B}}$ in the B-band rest frame at the redshift of the lens. These two Models give the same MtoL within the errors, although including the group GI explicitly increases the most-likely MtoL. We compare this with the total light of the galaxy and the stellar mass derived in Grillo et al. (2009), who use composite stellar population models with a Salpeter or Chabrier IMF, a delayed exponential star formation history, and solar metallicity to model the SDSS multi band photometry. First, we compare in the rest frame B band. In Fig. 6.16 we plot the cumulative distribution function for the stellar mass to light ratios derived from the respective de Vaucouleurs parts of the Models III and V and Models IIIb and Va from Appendix 6.8.

---

[6] All magnitudes are given in AB.
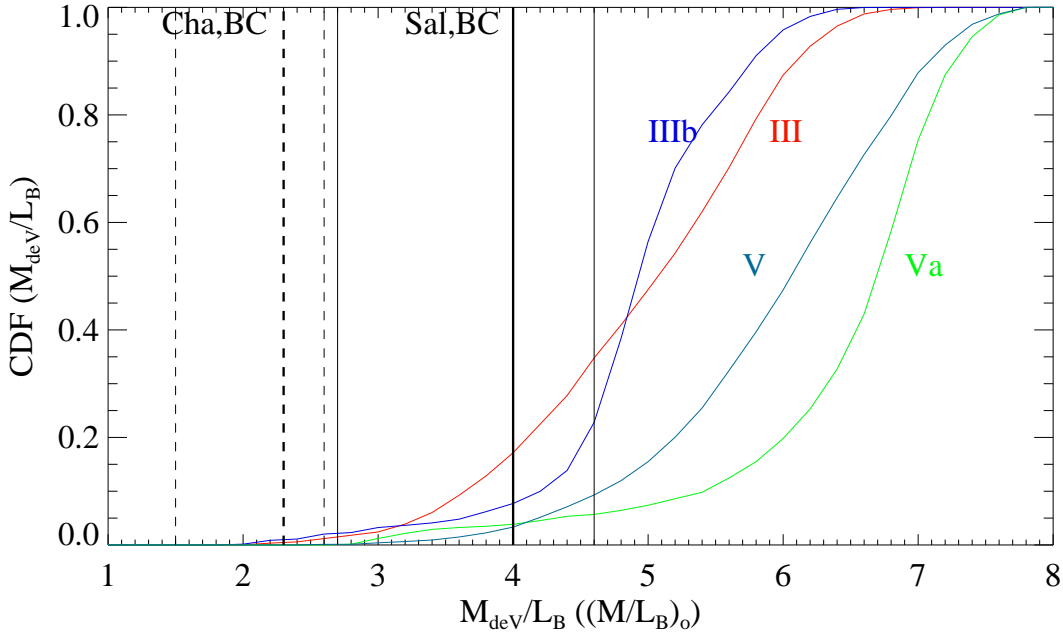
Figure 6.16: Cumulative probability distribution functions of the mass to light ratios for the de Vaucouleurs components of the models III and V. Models III, IIIb, V and Va are marked by red, blue, turquoise and green. The vertical lines mark the derived stellar mass to light ratios with its 1 σ errors from Grillo et al. (2009) for this system fitting SFH to broad band SDSS photometry using a Salpeter IMF (solid line) and Chabrier IMF (dashed line). The mass to light ratios are as observed at $z = 0.285$ and not corrected for luminosity evolution to redshift zero.

We overplot the stellar MtoL ratios derived in Grillo et al. (2009) for this system and get the best agreement for a NFW like halo and a Salpeter IMF.

In the R-band, we get a MtoL for Models III and V of $\frac{M_{deV}}{L_R} = (4.6^{+0.8}_{-1.1})\frac{M_\odot}{L_{\odot,R}}$ and $\frac{M_{deV}}{L_R} = (5.4^{+0.7}_{-0.9})\frac{M_\odot}{L_{\odot,R}}$. To compare the lensing galaxy SDSSJ 1430+4105 with present day Coma galaxies (Thomas et al., 2011) we have to account for the luminosity evolution between redshift 0.285 and now. We use the average evolution factor from the SFH models stated in Table 6.9, derived from the extrapolations of the fitted SFH models to redshift 0, which increases the MtoL in the R band by a factor of 1.48 for z=0, giving $(\frac{M_{deV}}{L_R})_{pres} = (6.8^{+1.2}_{-1.6})\frac{M_\odot}{L_{\odot,R}}$ and $(\frac{M_{deV}}{L_R})_{pres} = (8.0^{+1.1}_{-1.3})\frac{M_\odot}{L_{\odot,R}}$ for Models III and V, respectively. In Fig. 6.17, we plot this R-band de Vaucouleurs mass to light ratio at redshift zero against the present day R-band mass to light ratio for a Kroupa-IMF (Kroupa 2001), obtained again from the SFH fit of Grillo et al. (2009), translated to R-band and evolved to redshift zero.

We added the results from a dynamical study of Coma galaxies by Thomas et al. (2011). This allows us to conclude that SDSSJ 1430+4105 evolves into a galaxy with mass to light ratio similar as the Coma galaxies, and shows the same conflict with respect to a Kroupa IMF as they do. This conflict to a Kroupa IMF would be resolved if, for example, the de Vaucouleurs component is not made of stars only but contains dark matter as well.

6.7 Discussion and conclusions

In this paper, we studied the lensing properties of SDSS J1430+4105. From the complex source, we identified 5 double image systems, spanning a radial range from below $0.9''$ to
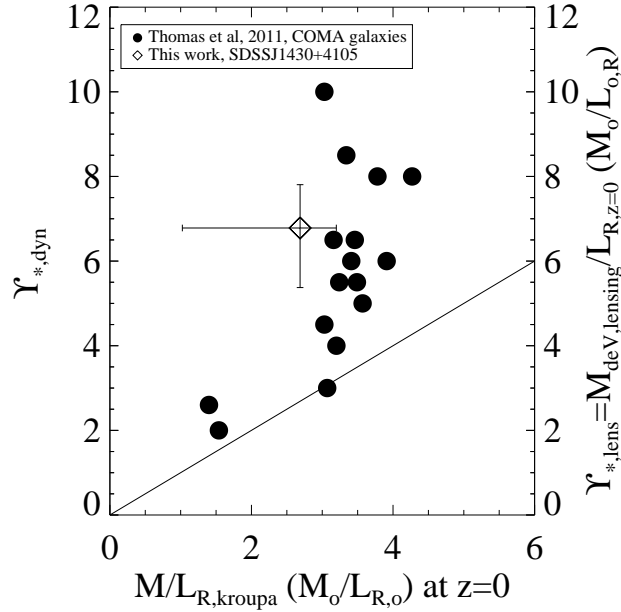
Figure 6.17: Mass–to–light in R from lensing versus stellar mass using a Kroupa IMF (see Grillo et al. 2009). Both values are evolved passively to the redshift 0. The lensing estimate is taken from Model III. The black points show the mass to light ratios derived from stellar dynamics analysis of the COMA cluster galaxies versus their stellar mass–to–light ratio derived from photometry for a Kroupa IMF, taken from Thomas et al. (2011). The solid line marks the one–to–one correspondence.

almost $2.1''$. The source is spectroscopically confirmed at a redshift of 0.575. Parametric models can match the observed image positions well with an average scatter in the position comparable to the pixel size of the ACS camera input image, which is $0.05''$. Our results are:

I) The best-fitting reconstruction of the profile favours a profile slope shallower than isothermal for the best-fitting model. However, profiles with free slope for the density steepness are consistent with an isothermal profile at 90% c.l.. This is also true when combining an explicit model for the de Vaucouleurs-like light distribution with a NFW-like dark matter component. Auger et al. (2010) found a steepness for the 3d density profile for this system of $\rho \sim r^{-(2.06\pm0.18)}$ by using the location of the Einstein radius only and combining this with stellar dynamics, in agreement with our results for the one component powerlaw total mass distribution of $\rho \sim r^{-(1.73^{+0.21}_{-0.13})}$ within the errors.

II) The galaxy is part of a group of galaxies listed in the maxBCG cluster catalogue. Using a lens mass component following the stellar light, we can not model the strong lensing signal for this galaxy if we use this component alone or combine it with a dark matter halo not centred on SDSS J1430+4105, called galaxy A. Therefore, this leads to two possibilities: Either A is indeed the centre of the galaxy group, or the galaxy A is a satellite of this group, residing in its own dark matter halo. Since we cannot distinguish between these 2 cases, neither from the lensing signal nor from external data, we model both scenarios and show that these lead to similar results regarding the mass distribution of the galaxy. We show that the dark matter halo of galaxy A must not be singular and isothermal at the same time, since this would suppress the de Vaucouleurs component. Both a non-singular, isothermal halo and a NFW-like halo

for the dark matter halo of galaxy A fit the data well. We find agreeing dark matter fractions and distributions for both cases. From the lensing data, we cannot distinguish whether the dark matter halo follows a NFW or NSIE profile in the centre, since we cannot constrain the concentration c and r_{200} – or Θ_c for a NSIE dark matter halo – of the dark matter component well. From the models taking explicitly the environment into account we conclude that the dark matter and the light of the galaxy have the same axis ratio and are likely coaligned.

III) We estimate the rest frame B-band mass to light ratios for the lensing galaxy from the de Vaucouleurs lensing component. For the case of a deVauc+NFW mass model, we obtain a total mass of $M_{deV,tot} = (8.8^{+1.3}_{-1.9}) \times 10^{11} M_\odot$ for the de Vaucouleurs component. Grillo et al. (2009) have obtained stellar mass estimates for the luminous component using the ugriz broad band SDSS photometry and SFH fits. They assumed solar metallicity composite stellar populations with a delayed exponential SFH, and examined the Salpeter IMF (with BC and MAR (Maraston, 2005) single stellar populations (SSP)), and the Chabrier and Kroupa IMF (based on BC-SSPs). They obtained stellar masses of $M_\star = (5.6^{+0.8}_{-1.8}) \times 10^{11} M_\odot$, $M_\star = (3.9^{+1.6}_{-2.2}) \times 10^{11} M_\odot$, $M_\star = (3.2^{+0.4}_{-1.1}) \times 10^{11} M_\odot$, and $M_\star = (2.9^{+0.6}_{-1.8}) \times 10^{11} M_\odot$ for these four cases. The stellar mass agrees best with the mass of the de Vaucouleurs component obtained from lensing if we assume a Salpeter IMF. In principle, the mass to light ratios also depend on the age of the galaxy and its metallicity. According to De Lucia et al. (2006), solar metallicity and a formation redshift of 3 to 5 as used in Grillo et al. (2009) are good assumptions for a galaxy of the measured stellar mass. Thus, the IMF must not be Chabrier or Kroupa like unless a fraction of the de Vaucouleurs component is not of stellar origin, i.e. part of the dark matter follows the light distribution. We measure a mass to light ratio for the stellar component of $\frac{M_{deV}}{L_B} = (5.3^{+0.8}_{-1.1}) \frac{M_\odot}{L_{\odot,B}}$ using gravitational lensing and assuming a NFW-like dark matter halo. If we allow for a group halo at galaxy I, we obtain $\frac{M_{deV}}{L_B} = (6.2^{+0.8}_{-1.0}) \frac{M_\odot}{L_{\odot,B}}$. These results again favor a Salpeter IMF, and are in agreement with the Fundamental Plane results $\frac{M}{L_B} = (4.8 \pm 1.4) \frac{M_\odot}{L_{\odot,B}}$ for this galaxy from Grillo et al. (2009). These results hold as long as the metallicity is approximately solar. We compare the mass to light ratio, passively evolved to z=0, to those of Coma galaxies analysed in Thomas et al. (2011). We confirm their trend towards a Salpeter IMF, again disfavouring a Kroupa-IMF. This trend also is seen in Cappellari et al. (2012a) for the most massive galaxies. Their data indicate a more Salpeter-like IMF for high velocity dispersion galaxies. The dark to total mass fraction of SDSSJ 1430+4105 rises from the centre outwards, giving a value of $\frac{M_{dark}}{M_{tot}} = (0.4^{+0.14}_{-0.10})$ at the Einstein radius. In this galaxy, we need a significant amount of dark matter in its projected centre to explain the observations.

IV) We compare the 3d densities of total, dark and luminous dark matter with to those of Coma galaxies analysed by Thomas et al. (2007), based on dynamical modelling, especially their Figure 5. Our galaxy has an effective radius of 10.96kpc and a velocity dispersion of $322 \pm 32 \text{kms}^{-1}$. Concerning the effective radius it is most similar to the Coma galaxies GMP 0144, GMP 4928 and GMP 2921, a cD galaxy, which have effective radii of 8.94 kpc, 14.31 kpc and 16.43 kpc (Thomas et al. 2007) and effective velocity dispersions of $211.8 \pm 0.4 \, \text{kms}^{-1}$ and $314.8 \pm 2.9 \, \text{kms}^{-1}$ and $\approx 400 \, \text{kms}^{-1}$ (Thomas et al. 2007, Corsini et al. 2008). Since our 3 dimensional matter densities are reliably known only between 3 kpc and about 6.5 kpc we decide to compare the matter densities at 3

kpc. At this radius the matter density values of Thomas et al. (2007) are reliable as well. At the same time this radius is within the core radius (r_c in Table 2 of Thomas et al. 2007) for all 3 GMP galaxies and thus the densities at this radius define the central dark matter densities in these galaxies. We read off dark matter and total densities of $6 \times 10^{-2} \mathrm{Mpc}^{-3}$ and $3 \times 10^{-1} \mathrm{Mpc}^{-3}$ for GMP 0144, of $1.5 \times 10^{-2} \mathrm{Mpc}^{-3}$ and $2 \times 10^{-1} \mathrm{Mpc}^{-3}$ for GMP 4928 and $1 \times 10^{-1} \mathrm{Mpc}^{-3}$ and $3 \times 10^{-1} \mathrm{Mpc}^{-3}$ for GMP 2921. For SDSSJ 1430+4105 these numbers are $4 \times 10^{-2} \mathrm{Mpc}^{-3}$ and $3.5 \times 10^{-1} \mathrm{Mpc}^{-3}$ for the dark matter and the total density at 3 kpc with fractional errors of about 25%. This means that the dark matter and total densities at 3 kpc for our galaxy and the 3 Coma galaxies are comparable, and that the ratio of dark to total matter density of about 1:10 is consistent within the error with the ratios of 1:5 and 1:13 for the non-central Coma galaxies.

6.8   Appendix: Additional strong lensing models

To check for the robustness of the previously derived lensing results, we also examine some different strong lensing models to the ones presented in Secs. 6.4.1 and 6.4.2. These models confirm the previous results without adding new implications for the results, therefore we add these models in this appendix. The minimum χ^2 values and parameter estimates of the models are shown in Tables 6.10 and 6.11.

Model Ia   To account for the environment, we include the galaxy group explicitly as a SIS profile centred at galaxy I in Tab. 6.3. We use a prior on the group Einstein radius of $b_{group,prior} = (3.6 \pm 1.5)''$, as derived in Sec. 6.4.2. The results and 68 % c.l. marginalised errors of this SIE+GI (Model Ia) case are: $b = (1.45^{+0.02}_{-0.02})''$, $q = (0.81^{+0.04}_{-0.04})$, $\Theta_q = (-17.4^{+3.9}_{-4.0})°$ and $b_{group} = (4.6^{+1.6}_{-1.4})''$, see Fig. 6.18 for the derived parameter errors.
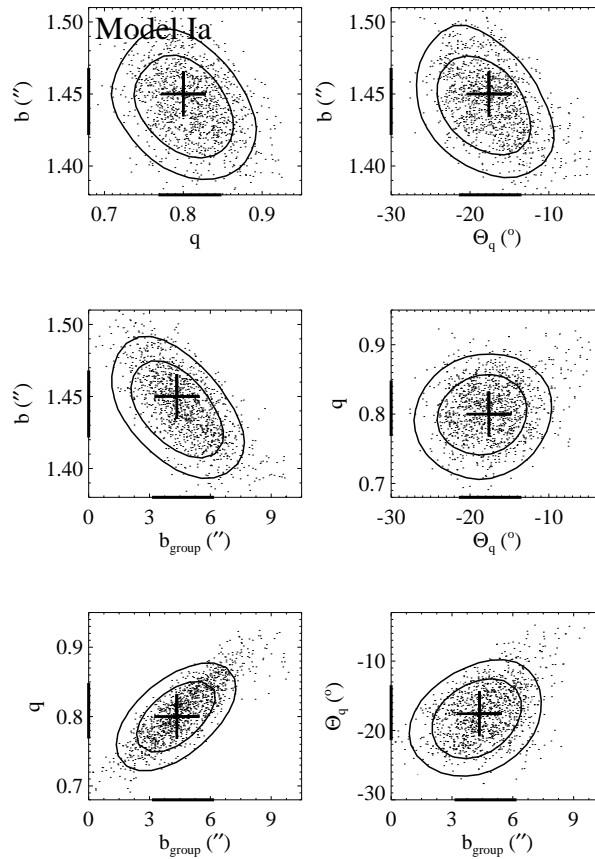
Figure 6.18: Error estimates of the MCMC for the SIE case with GI (Model Ia), plotted are the individual points of the MCMC together with the 68 and 90 % confidence regions of the distribution. The crosses mark the minimum-χ^2 value from Table 6.4. The bars on the axes mark the respective 68 % marginalised error intervals.

This plot shows an anti-correlation of b and b_{group}. This is expected since the total convergence needed at the position of the main lens can either be provided by the main lens or by the mass associated with GI. We also include the environment as external shear, as calculated in Sec 6.9.1, see Model Ib in Appendix 6.8. This has only small effects on the derived parameter values.

Table 6.10: Minimum-χ^2 values and parameter estimates, derived with GRAVLENS for the one component isothermal and powerlaw models

		b ($''$)	q	Θ_q ($°$)	β	Θ_c ($''$)	b_{group} ($''$)	χ^2	d.o.f.	$\frac{\chi^2}{d.o.f}$
Model Ia	SIE+GI	1.45	0.80	-17.6	2.00^1		4.4	8.7	6	1.5
		$1.43 - 1.47$	$0.77 - 0.85$	$-21.4 - -13.5$			$3.2 - 6.2$			
Model Ib	SIE+es	1.50	0.82	-7.2	2.00^1			9.1	5	1.8
		$1.48 - 1.52$	$0.74 - 0.89$	$-22.1 - -0.9$						
Model IIa	PL+GI	2.53	0.93	-13.0	1.60		4.3	7.6	5	1.5
		$1.40 - 2.89$	$0.80 - 0.96$	$-20.9 - -5.1$	$1.58 - 2.04$		$3.0 - 6.0$			
Model IIb	NSIE	1.49	0.71	-21.6	$2.00\ ^1$	3.8×10^{-5}		11.5	6	1.9
		$1.53 - 1.80$	$0.72 - 0.78$	$-23.8 - -19.5$		$0.035 - 0.24$				

[1] fixed value

Model Ib Model Ib is for a SIE with external shear γ, hence it has 1 more free parameter relative to Model Ia. The external shear priors are based on the environment models derived in Sec. 6.3.2 and Appendix 6.9: We use $\gamma_{\text{prior}} = (0.012 \pm 0.031)$ and $\Theta_{\gamma,\text{prior}} = (-10 \pm 25)°$. The marginalised errors are: b = $(1.50^{+0.02}_{-0.02})''$, q = $(0.81^{+0.08}_{-0.07})$, $\Theta_q = (-13.4^{+12.5}_{-8.7})°$, $\gamma = (0.050^{+0.025}_{-0.025})$ and $\Theta_\gamma = (-29.6^{+7.9}_{-15.8})°$. There is a correlation present between the axis ratio q and the external shear γ, reflecting the fact that the shear and the ellipticity can compensate each other in its effects on the deflection angle, since both are pointing in the same direction within $\approx 16°$.

Model IIa If we add the group GI, we obtain a marginalised steepness value of $\beta = (1.71^{+0.33}_{-0.13})$ together with b = $(2.09^{+0.80}_{-0.69})''$, q = $(0.91^{+0.05}_{-0.11})$, $\Theta_q = (-15.3^{+10.2}_{-5.6})°$ and $b_{\text{group}} = (4.5^{+1.5}_{-1.5})''$. Since there is no correlation between β and b_{group}, the details of the environment implementation have no systematic influence on the derived steepness of the lens mass profile. The shear and convergence provided by the group are $\gamma_{\text{GI}} = \kappa_{\text{GI}} = 0.037$ in agreement with our expectations.

Model IIb A mass density profile which is flatter than isothermal at the Einstein radius can also be achieved by an isothermal mass distribution with a finite core radius. Therefore, Model IIb is for an isothermal ellipsoid with a core radius (NSIE) with $\beta = 2$ and arbitrary value for the core radius Θ_c. For such a model one expects to also find a demagnified third image, which is not observed. We assume that the demagnified third image in the centre produced by a non-singular mass profile could be detected if its flux exceeds 3σ of the sky+object noise in the image for the brightest source pixel. We exclude a region of $0.2''$ in the centre due to residuals of the galaxy subtraction, where we have no limits on the image fluxes at all. We then get the following marginalised errors: b = $(1.63^{+0.17}_{-0.10})''$, q = $(0.75^{+0.03}_{-0.03})$, $\Theta_q = (-21.5^{+2.0}_{-2.3})°$ and a core radius of $\Theta_c = (0.11^{+0.13}_{-0.075})''$. However, the best-fitting model is identical to Model I, i.e. purely isothermal. There is a linear dependency between b and Θ_c due to the definition of the non-singular profile: A larger core radius needs to be compensated by a larger lensing strength b to get the same enclosed mass within the Einstein radius.

Model IIIa In Model IIIa we allow for a dark matter component that is centred on the lensing galaxy. Here, we test if we can improve the modelling by combining the de Vaucouleurs profile with a SIE halo. For the dark matter SIE halo, we impose a prior on the axis ratio based on the Bolton et al. (2008b) work of $q_{\text{dark,prior}} = (0.79 \pm 0.12)$. For the errors, we get b = $(1.43^{+0.05}_{-0.08})$, $q_d = (0.71^{+0.02}_{-0.02})$, $\Theta_{q,d} = (-21.9^{+2.1}_{-2.6})°$ and $M_{\text{deV}} = (0.6^{+0.7}_{-0.4}) \times 10^{11} M_\odot$. Since the best-fitting model has a $\chi^2 = 11.8$ and almost zero de Vaucouleurs mass, this implies that a de Vaucouleurs like mass model for the light plus a purely isothermal density profile for the dark matter are not compatible with the data. The Einstein radius of the SIE component and the de Vaucouleurs mass are anticorrelated, forcing the total projected mass within the Einstein radius to be constant.

Model IIIb Instead of the NFW component, we can also model the dark matter component with a NSIE. We limit the core radius of this component to be between 0 and $50''$, and use the same prior on the axis ratio as before. For the mass of the de Vaucouleurs component, we get: $M_{\text{deV}} = (8.5^{+1.1}_{-0.7}) \times 10^{11} M_\odot$. For the other parameters, we get (see Fig. 6.19): $q_d = (0.78^{+0.05}_{-0.08})$, $\Theta_q = (-26.0^{+2.6}_{-2.4})°$, $b_d = (19.2^{+13.0}_{-10.1})''$ and $\Theta_c = (24.7^{+15.5}_{-12.9})''$.
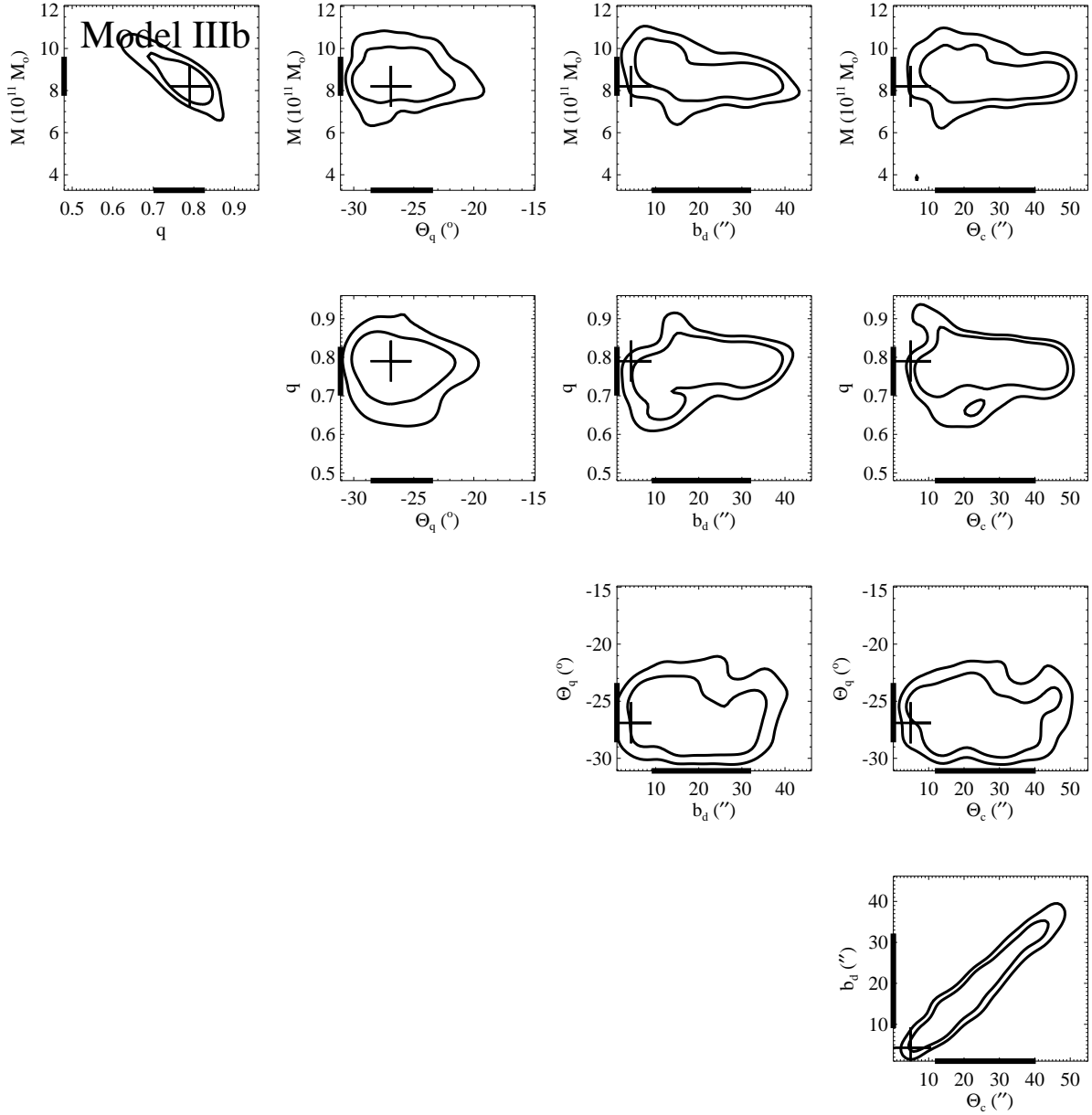
Figure 6.19: Error estimates of the MCMC for the de Vaucouleurs+NSIE model (Model IIIb), plotted are the individual points of the MCMC together with the 68 and 90 % confidence regions of the distribution. The crosses mark the minimum-χ^2 value from Table 6.5. The bars on the axes mark the respective 68 % marginalised error intervals. The individual points of the MCMC are omitted for clarity.

Again, we note that there is a degeneracy between b_d and Θ_c, emerging from the profile definition. Since there are no observed images for radii larger than $2.32''$, this leaves the upper limit of the core radius Θ_c totally unconstrained. Large Θ_c make this dark matter distribution flat at the Einstein radius, with b_d giving its density value. The radial mass estimates and their derivatives are plotted in Fig. 6.20

Model IVa We model the mass distribution by a de Vaucouleurs model with the shape parameters following the light profile as stated in Table 6.1 Therefore, the mass of the de Vaucouleurs component is the only free parameter in this model. The best-fitting light model (Model IVa) in Table 6.11 has a $\chi^2 = 118$, meaning that a pure de Vaucouleurs profile is a bad fit to the observations.
The de Vaucouleurs mass in this case is $M_{deV} = (15.0^{+0.2}_{-0.2}) \times 10^{11} M_\odot$. This badness of the fit implies that there must be a (dark) mass component not following a de Vaucouleurs profile.

Model Va Here we do the same as in the Model V before: We combine the 2 component model (Model IIIb) with an explicit description for the galaxy group GI. For the de Vaucouleurs component, we get: $M_{deV} = (11.5^{+0.7}_{-1.5}) \times 10^{11} M_\odot$. For the other parameters, we get $q_d = 0.74^{+0.11}_{-0.10}$, $\Theta_q = (-21.8^{+6.7}_{-5.3})°$, $b_d = (5.5^{+4.1}_{-3.0})''$, $\Theta_c = (16.4^{+12.1}_{-9.1})''$, and for group GI $b_{group} = (5.1^{+1.3}_{-1.6})''$. As one can see, again there is no significant difference between this model's parameters and the one of Model IIIb. As for the NFW-like dark matter halo, the M_{deV} is increased relative to Model IIIb by introducing the group halo GI. Again, the radial mass estimates and their derivatives are plotted in Fig. 6.20

Model Vb Model Vb is motivated by the fact that for the preceding models (Models III and V), the axis of the dark matter halo is always offset from that of the light by about $-10°$, which is statistically significant on a more than 3σ level for Models III and IIIb, see Figs. 6.7 and 6.19. At the same time, the axis ratio of the dark matter haloes are consistent with the axis ratio of the stellar component, see Table 6.1. This could be mimicked by a non accounted external shear which is present if galaxy A is not the centre of the group. From the results for Models Ia, IIa, V and Va, we conclude that if we include the group explicitly as centred on galaxy I the matter gets more aligned with the light. Looking at Model Ib we see that using an external shear instead of GI changes the best-fitting orientation of the total mass distribution more towards the observed light's angle. So, in this Model, we combine Model IIIb with the external shear of Model Ib. In numbers, we get here: $M_{deV} = (9.9^{+2.1}_{-2.7}) \times 10^{11} M_\odot$, $q_d = (0.77^{+0.10}_{-0.10})$, $\Theta_q = (-14.2^{+13.0}_{-11.2})°$, $c_d = (4.1^{+4.1}_{-1.7})$, $r_{200} = (166^{+61}_{-55})''$, and for the external shear $\gamma = (0.038^{+0.023}_{-0.021})$ and $\Theta_\gamma = (-35.2^{+9.2}_{-15.2})°$. We also note that with this improvement, the dark matter profile becomes more concentrated, at a level expected for galaxies.

6.9 Appendix: Alternative descriptions for the lens environment

In this Appendix, we discuss 2 alternative scenarios for the environment, firstly a scenario in which the group is only consisting of its members ("clumpy group") without a reference to a group halo, secondly a scenario where the group is a typical group with 12 members, but centred on galaxy A instead of galaxy I.

Table 6.11: Minimum-χ^2 values and parameter estimates, derived with GRAVLENS for the two component de Vaucouleurs plus dark matter models

		M $(10^{11} M_\odot)$	q_d	$\Theta_{q,d}$ (°)	b_d (″)	Θ_c (″)	b_{group} (″)	χ^2	d.o.f.	$\frac{\chi^2}{\text{d.o.f}}$
Model IVa	deVauc	15.0 $14.8 - 15.2$						118	9	13.1
Model IIIa	deVauc+SIE	0.0004 $0.2 - 1.3$	0.72 $0.69 - 0.73$	-21.5 $-24.5 - -19.8$	1.50 $1.38 - 1.48$			11.8	6	2.0
Model IIIb	deVauc+NSIE	8.2 $7.8 - 9.6$	0.79 $0.70 - 0.83$	-26.9 $-28.4 - -23.4$	4.3 $9.1 - 32.2$	4.9 $11.8 - 40.2$		7.6	5	1.5
Model Va	deVauc+NSIE+GI	10.0 $10.0 - 12.2$	0.79 $0.64 - 0.86$	-25.5 $-27.1 - -15.1$	2.1 $2.5 - 9.6$	3.6 $7.3 - 28.5$	3.6 $3.5 - 6.4$	7.6	4	1.9
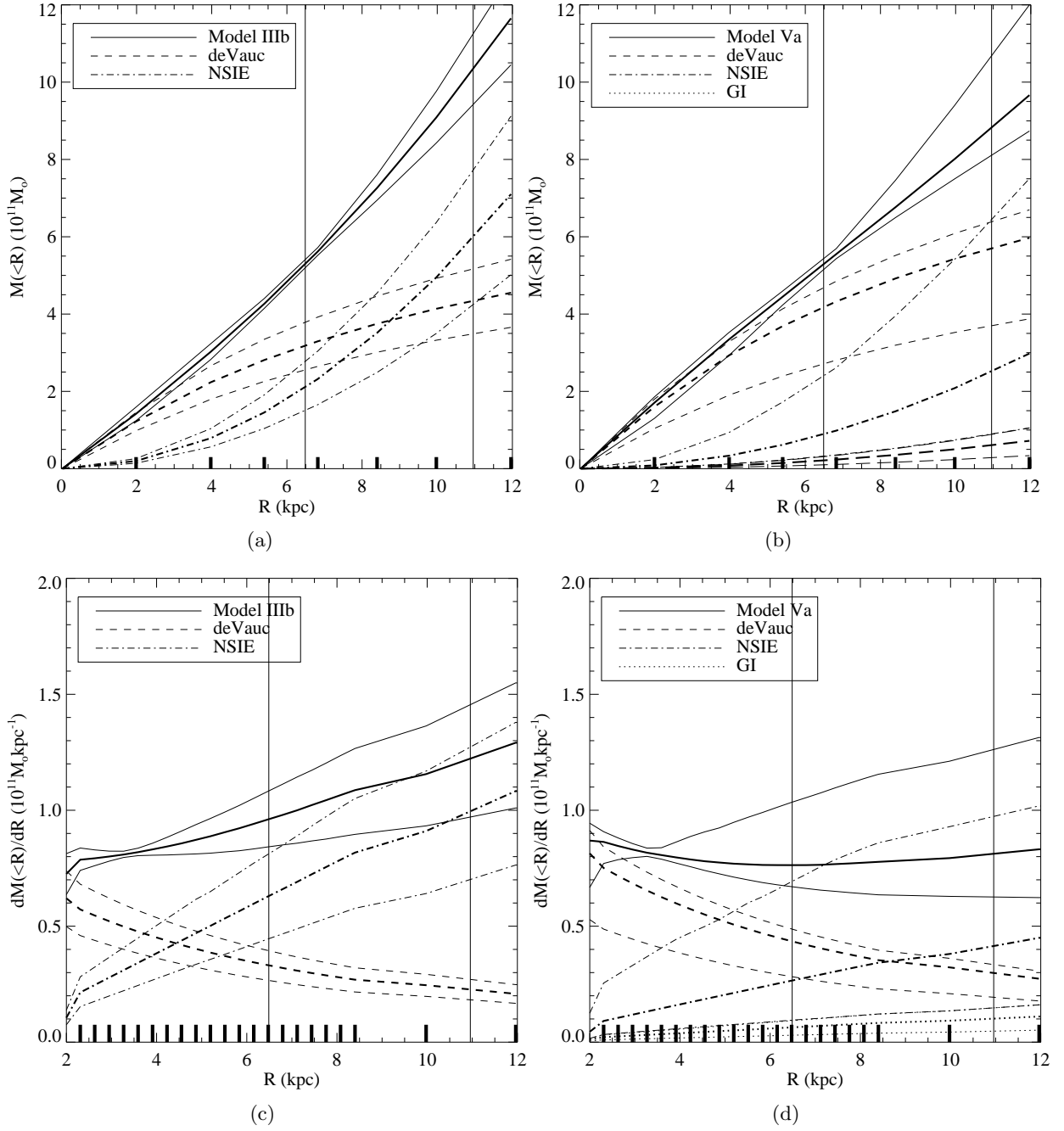
Figure 6.20: The same as Fig. 6.13, only for Models IIIb and Va.

6.9.1 Clumpy group

A clumpy group model is obtained if all group mass is considered to be associated to the group galaxies. We describe the galaxies as singular isothermal spheres (SIS) without truncation of their mass profiles and obtain at the position of the lens:

$$
\begin{aligned}
\kappa_{\mathrm{A}}^{\text{clumpy group}} &= \sum_{\mathrm{n}} \kappa_{\mathrm{SIS,n}} \quad , \\
\gamma_{\mathrm{A}}^{\text{clumpy group}} &= \sum_{\mathrm{n}} \gamma_{\mathrm{SIS,n}} \quad .
\end{aligned}
\tag{6.10}
$$

In this model, the shear and surface density at the location of the lens depends on the 2-dimensional galaxy distribution and not at all on the centre of mass of the group. The galaxies themselves are parametrized only by their positions and velocity dispersions σ_{n}. The value of the velocity dispersion σ_{A} for SDSS J1430+4105 is taken from the central velocity dispersion measured by the SDSS. The estimates σ_{n} for the neighbouring galaxies are obtained from the Faber-Jackson relation (Faber & Jackson 1976),

$$
\sigma_{\mathrm{n}} = \sigma_{\mathrm{A}} \left(\frac{i_{\mathrm{n}}}{i_{\mathrm{A}}} \right)^{0.25} \quad ,
$$

where i is the SDSS i band flux of the neighbours and i_{A} the flux of the lens galaxy A. The shear $\gamma_{\mathrm{n}}(d_{\mathrm{n}})$ and convergence $\kappa(d_{\mathrm{n}})$ for a SIS at a projected angular distance d_{n} from its centre are

$$
\kappa(d_{\mathrm{n}}) = \gamma_{\mathrm{n}}(d_{\mathrm{n}}) = \frac{2\pi\sigma_{\mathrm{n}}^2}{c^2 d_{\mathrm{n}}} \left(\frac{D_{\mathrm{ds}}}{D_{\mathrm{s}}} \right) \quad ,
$$

with c denoting the speed of light and D_{ds} and D_{s} mark the angular diameter distances from the lens to the source and from the observer to the source, respectively. The proper (vector) addition of these convergence and shear values yields a prediction of

$$
\begin{aligned}
\gamma_{\mathrm{A}}^{\text{clumpy group}} &= 0.012 \quad , \\
\kappa_{\mathrm{A}}^{\text{clumpy group}} &= 0.023 \quad .
\end{aligned}
\tag{6.11}
$$

The angle of the shear is $-10°$ in the local coordinate system. The fact that we model the galaxies as SISs, ignoring the finite halo sizes which would keep the mass associated to galaxies limited, is not relevant, since finite halo sizes can only lead to lower estimates for the convergence and shear at the position of galaxy A. Therefore, we get an upper limit of the clumpy group estimates using this assumption. As we see in Sec. 6.4.2, the parameters of the lensing galaxy only mildly depend on the assumptions about the group as long as it is centred on galaxy I. To calculate the mass of this clumpy group, we first need the r_{200}. We adopt the definition of Koester et al. (2007) of r_{200} as a function of number of group members. We sum up all mass contributions of member galaxies in Table 6.3 within this $r_{200} = 3.8$ centred on A or I, respectively and calculate the total projected mass of the group within its r_{200}: $\mathrm{M}_{200} = 5.5 \times 10^{14}\,\mathrm{M}_{\odot}$. This value gives an upper limit of the mass associated with the group, since SIS profiles for its members overestimate the densities of each member at large radii.

6.9.2 Smooth group mass distribution centred at galaxy A

In principle, the assumption of the group being located at A could already be in conflict with the lensing observables. The most secure strong lensing estimate is the observed critical mass

$\pi R_{\mathrm{Ein}}^2 \Sigma_{\mathrm{crit}} = 5.43^{+0.15}_{-0.16} \times 10^{11} M_{\odot}$ within the Einstein radius, obtained from all models in Sec. 6.5 consistently. We now can model the group – located at A as an NFW or SIS (see Sec. 6.4.1 for details) profile and estimate its projected mass within the observed Einstein radius. If this halo mass estimate exceeds the observed critical mass, the assumption of this group being a typical group with 12 members and with galaxy A as its centre is already in conflict with the lensing observables.

In Fig. 6.21 we show the c-r_{200} diagram for a NFW profile.
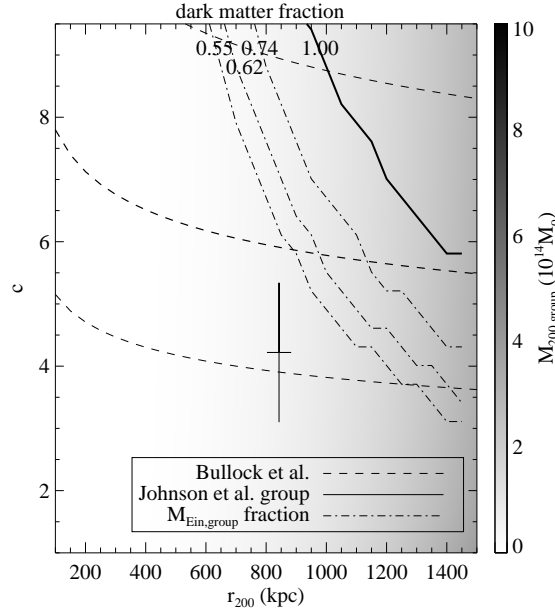
Figure 6.21: This figure shows the concentration c - r_{200} properties for a NFW halo profile. The levels of grey show the virial masses of the dark matter haloes. Overplotted are several different lines: The dashed lines are the Bullock et al. (2001) c-r_{200} relation with its 1σ error. This marks the area typically populated by galaxy groups. Further we overplot the c-r_{200} values for a typical richness N=12 group halo as found by Johnston et al. (2007) with its errorbars. This shows where we expect the group halo to lie approximately in this plane. The dash-dotted lines mark the transition above which more than 55, 62 and 74 % of the observed critical mass within the observed Einstein radius would be made up by the dark matter halo of the group. All group haloes above this dash-dotted line in this c-r_{200} plane overpredict the observed total mass within the Einstein radius, therefore this lines mark regions with excluded group haloes. Since the typical Johnston et al. (2007) group halo lies below this lines, the observed critical mass within the Einstein radius does not exclude A as the group centre. The thick, solid 1.00 line marks the transition where the dark matter group halo alone would provide the observed critical mass within the Einstein radius. Hence along this line no baryons (or dark matter) in the lensing galaxy A would be required at all.

The levels of grey indicate the virial M_{200} mass of a group with parameter values c and r_{200}. The thick solid line marks the transition where the NFW group halo mass within the observed Einstein radius alone (without baryons and dark matter of the galaxy A) exceeds the critical mass, predicting a bigger than the observed Einstein radius. Therefore all groups that lie above this line would – from its group halo mass alone – overpredict the observed total projected mass within the Einstein radius and cannot be centred at galaxy A.

In reality, some of the observed mass within the Einstein radius has to be contributed by the stars, giving an even smaller upper limit for the dark matter mass within the Einstein radius. Hence, we plot the analogous curves for the case where the dark matter makes up only a fraction of the total critical mass within the Einstein radius. The dark to total matter fractions shown also in Fig. 6.21 as dash-dotted lines are $f_{\mathrm{dark}} = 0.55, 0.62, 0.74$. To obtain

these numbers, we subtract the stellar mass measurements within the Einstein radius done in Grillo et al. (2009) from the derived lensing mass within the Einstein radius in this work. If we attribute the missing mass to the group dark matter halo, we get again upper limits for the possible group halo mass contribution within the Einstein radius, allowing us to exclude all groups that would exceed this upper mass limits. Grillo et al. (2009) fit composite stellar population models to the SDSS photometry of this galaxy to derive its stellar mass within the observed Einstein radius. We use the Salpeter IMF stellar masses of Grillo et al. (2009), since these give the highest mass in stars. Now we plot the model group with richness 12 in Fig. 6.21 to see where it resides. From Johnston et al. (2007), we obtain c-r$_{200}$ values of 4.22 and 848 kpc for a richness 12 group. Since this group therefore does not fall into the excluded regions of Fig. 6.21, we cannot exclude A as the group centre from the lensing observables. This conclusion also holds in the picture where the group is modelled as SIS. If the group follows a SIS matter profile it has an Einstein radius of $\Theta_{\rm Ein} = 3.6 \pm 1.5''$, see Sec. 6.4.2. This is consistent within the errors with the value derived from the strong lensing models in Sec. 6.5. Therefore a typical group with richness 12, as seen in the vicinity of SDSSJ 1430+4105, does not violate the observed critical mass within the Einstein radius, nor the Einstein radius itself. Hence, galaxy A could also be the group centre without violating the lensing observables for a typical group of this richness.

Galaxy halo truncation from Giant Arc Surface Brightness Reconstruction in the Cluster MACSJ1206.2-0847

Thomas Eichner[1,2,*], Stella Seitz[1,2], Sherry H. Suyu[3,4], Aleksi Halkola[5], Keiichi Umetsu[6], Adi Zitrin[7], Dan Coe[8], Anna Monna[2,1], Piero Rosati[9], Claudio Grillo[10], Italo Balestra[2], Marc Postman[8], Anton Koekemoer[8], Wei Zheng[11], Ole Høst[10], Doron Lemze[11], Tom Broadhurst[13], Leonidas Moustakas[14], Larry Bradley[8], Alberto Molino[15], Mario Nonino[16], Amata Mercurio[17], Marco Scodeggio[18], Matthias Bartelmann[7], Narciso Benitez[15], Rychard Bouwens[19], Megan Donahue[20], Leopoldo Infante[21], Stephanie Jouvel[12,22], Daniel Kelson[23], Ofer Lahav[12], Elinor Medezinski[11], Peter Melchior[24], Julian Merten[14], Adam Riess[8,11]

[1]Universitäts-Sternwarte München, Scheinerstr. 1, 81679 München, Germany [2]Max-Planck-Institut für extraterrestrische Physik, Giessenbachstraße, 85748 Garching, Germany [3]Department of Physics, University of California, Santa Barbara, CA 93106, USA [4]Kavli Institute for Particle Astrophysics and Cosmology, Stanford University, 452 Lomita Mall, Stanford, CA 94035, USA [5]Institute of Medical Engineering, University of Lübeck, Ratzeburger Allee 160 23562 Lübeck, Germany [6]Institute of Astronomy and Astrophysics, Academia Sinica, P. O. Box 23-141, Taipei 10617, Taiwan [7]Institut für Theoretische Astrophysik, ZAH, Albert-Ueberle-Stra e 2, 69120 Heidelberg, Germany [8]Space Telescope Science Institute, 3700 San Martin Drive, Baltimore, MD 21208, USA. [9]ESO-European Southern Observatory, D-85748 Garching bei München, Germany [10]Dark Cosmology Centre, Niels Bohr Institute, University of Copenhagen, Juliane Maries Vej 30, 2100 Copenhagen, Denmark [11]Department of Physics and Astronomy, The Johns Hopkins University, 3400 North Charles Street, Baltimore, MD 21218, USA [12]Department of Physics Astronomy. University College London, Gower Street, London WCIE 6 BT, UK [13]Department of Theoretical Physics, University of the Basque

Country, P. O. Box 644, 48080 Bilbao, Spain [14]Jet Propulsion Laboratory, California Institute of Technology, MS 169-327, Pasadena, CA 91109, USA [15]Instituto de Astrofísica de Andalucía (CSIC), C/Camino Bajo de Huétor 24, Granada 18008, Spain [16]INAF-Osservatorio Astronomico di Trieste, via G.B. Tiepolo 11, 40131 Trieste, Italy [17]INAF-Osservatorio Astronomico di Capodimonte, via Moiariello 16, I-80131 Napoli, Italy [18]INAF-IASF Milano, Via Bassini 15, I-20133, Milano, Italy [19]Leiden Observatory, Leiden University, P. O. Box 9513,2300 RA Leiden, The Netherlands [20]Department of Physics and Astronomy, Michigan State University, East Lansing, MI 48824, USA [21]Departamento de Astronoía y Astrofísica, Pontificia Universidad Católica de Chile, V. Mackenna 4860, Santiago 22, Chile [22]Institut de Cincies de l'Espai (IEEC-CSIC), Bellaterra (Barcelona), Spain [23]Observatories of the Carnegie Institution of Washington, Pasadena, CA 91 101, USA [24]Center for Cosmology and Astro-Particle Physics, & Department of Physics; The Ohio State University, 191 W. Woodruff Ave., Columbus, Ohio 43210, USA
[*]eichner@usm.lmu.de

7.1 Abstract

In this work we analyze the mass distribution of MACSJ1206.2-0847, especially focusing on the halo properties of its cluster members. This cluster appears already relaxed in Xray data, but its huge amount of not yet centrally diffuse intra cluster light is a sign of its recent built up enforcing cluster galaxy halo stripping and tidal disruption. The cluster lenses 12 background galaxies into multiple images and one galaxy at $z = 1.033$ into a giant arc and its counterimage. The multiple image positions and the surface brightness distribution (SFB) of the arc which is bent around several cluster members are sensitive to the cluster galaxy halo properties. We model the cluster mass distribution with a NFW profile and the galaxy halos with two parameters for the mass normalization and extent of a reference halo assuming scalings with their observed NIR–light. We match the multiple image positions at an r.m.s. level of $0.85''$ and can reconstruct the SFB distribution of the arc in several filters to a remarkable accuracy based on this cluster model. The length scale where the enclosed galaxy halo mass is best constrained is about 5 effective radii – a scale in between those accessible to dynamical and field strong lensing mass estimates on one hand and galaxy galaxy weak lensing results on the other hand. The velocity dispersion and halo size of a galaxy with $m_{160W,AB} = 19.2$ or $M_{B,Vega} = -20.7$ are $\sigma = 150 kms^{-1}$ and $r \approx 26 \pm 6 kpc$. We also reconstruct the unlensed source (which is smaller by a factor of ~ 5.8 in area), demonstrating the increase of morphological information due to lensing and conclude that this galaxy has likely star–forming spiral arms with a red (older) central component.
Galaxies:clusters:individual:MACSJ1206.2-0847 Galaxies:halos Galaxies:elliptical and lenticular, cD Galaxies:interactions Gravitational lensing:strong

7.2 Introduction

For elliptical galaxies the half light radii, central velocity dispersions and surface brightness within their half light radii form a fundamental plane (Bender et al., 1992). This fundamental plane relation is very similar for field and cluster galaxies at the same redshift (Andreon, 1996; Saglia et al., 2010). The redshift evolution of the ellipticals' mass to light ratio is independent of the cluster velocity dispersion; it is compatible with passive evolution of the

stellar population (Bender et al., 1998; van Dokkum & van der Marel, 2007; Saglia et al., 2010) and slightly stronger for field galaxies. The effective radii and velocity dispersion of ellipticals evolve with time, but not depending significantly on the galaxy environment.

Studying elliptical dark matter halos with stellar dynamics, Thomas et al. (2005) & Thomas et al. (2009) have shown that (1) the stars of ellipticals form at high redshift (z=3-5), (2) the dark matter halos of (Coma) ellipticals formed earlier than spiral galaxies of same brightness and environment and (3) the halos of ellipticals mostly formed at least as early as their stars (see Fig. 13 of Wegner et al. (2012))

In general, however, galaxy environment plays a major role for the formation of galaxies and the transforming of galaxy types according to the morphology-density relation of Dressler (1980) and their evolution with redshift (Dressler et al., 1997). Dressler et al. (1997) conclude that "the formation of elliptical galaxies predates the formation of rich clusters, and occurs instead in the loose-group phase or even earlier".

Wilman & Erwin (2012) confirmed this picture in a quantitative way: According to their interpretation ellipticals are centrals or they are satellites which have been centrals in halos before they have been accreted; Taken together this implies that the central stellar dynamics and the stellar population content of elliptical galaxies depend on the present day environment on a minor level. Elliptical galaxies stay elliptical galaxies when larger scale halos like groups and clusters form, but depending on whether they become central or satellite galaxies their dark matter halos undergo growth or stripping.

The stripping of dark matter halos embedded in group and cluster halos by tidal fields is theoretically expected (Merritt (1983), Merritt (1984)) and gets stronger the denser the environment is. Stripping has also been studied in N–body dark matter simulations (Ghigna et al., 1998; Limousin et al., 2009). Gao et al. (2004) have shown that on average 90 percent of mass associated with halos accreted at z=1 are removed from the accreted halos and contribute to the smooth host halo at z=0. Highest mass accreted halos reach the centers more quickly, due to dynamical friction, and thus become stripped most quickly. Diemand et al. (2007) have shown that subhalo mass is removed from outside, in agreement with the observations that any changes of fundamental plane (FP) relation with environment can be explained by slight age differences of the stellar populations, i.e. that the structural parameters of ellipticals do not change during the build up of groups and clusters. Warnick et al. (2008) have shown, that on average surviving subhalos lose about 30 percent of their mass per orbit in group and cluster halos (this excludes tidally disrupted halos), where halos with radial orbits may lose 80 per cent or even more per orbit. Their Fig.4 illustrates the subhalo mass loss sorted as a function of subhalo distance to the halo center, for different central halo masses. Within 10 percent of the virial radius the majority of subhalos has lost more than 50 percent of its original mass. Limousin et al. (2009) have studied galaxy dark matter halo truncation in high density environments with hydrodynamical N–body simulations. They predict half light radii of galaxies in a Coma and Virgo like cluster as a function of 3D and 2D projected separation to the cluster center, finding a measurable effect in both, at a level stronger than that of Ghigna et al. (1998). According to their work the total mass of galaxy halos is a few times larger than its stellar mass in the center and up to about 200 (50) times larger in the outskirts of the cluster at z=0.7 (z=0).

Galaxy halo stripping in clusters has been measured with planetary nebula kinematics in local galaxies (Ventimiglia et al. (2011) and references therein). Pu et al. (2010) have analyzed the stellar kinematics of massive local ellipticals and measured halo sizes of orders of 60 kpc based on the Mgb absoprtion line strength vs escape velocity relation. These methods for

analysis of individual galaxy halos do not work for large samples and larger distances yet. Galaxy halo sizes can be also measured with weak galaxy galaxy lensing for field galaxies (Schneider & Rix, 1997; Hoekstra et al., 2004) and also for cluster galaxies using statistical methods and large samples. In clusters the effect is stronger per galaxy since the signal is boosted by the matter of the cluster itself (Geiger & Schneider, 1999), but this imposes also a degeneracy in measuring the galaxy halos (Geiger & Schneider, 1999). Nevertheless halo truncation has been measured with weak galaxy galaxy lensing (Narayan (1998), Geiger & Schneider (1999), Natarajan et al. (2002a), Natarajan et al. (2002b), Limousin et al. (2007a)) and truncations in half mass radii by a factor of 4 to field galaxies or more have been reported. Halkola et al. (2007) have worked out a different idea: Using strong gravitational lensing, they described the mass distribution in the massive strong lensing cluster Abell 1689 with a smooth dark matter component and a smaller scale component traced by the cluster galaxies. The combined 'granular' mass distribution maps multiply imaged galaxies differently than the best fitting pure smooth cluster component. Making use of the fundamental plane and Faber Jackson scaling relations for the cluster galaxies the properties of a reference halo could be measured. This method finds the statistically best fitting reference galaxy halo mass distribution to reproduce the astrometry of multiply imaged sources best. It relies on a very precise global mass model (Broadhurst et al. (2005), Halkola et al. (2006), Limousin et al. (2007b), see also Diego et al. (2005), Coe et al. (2010)) constrained by a huge number of multiple images (in this case 32 background galaxies mapped into 107 images) spread over the Einstein radii corresponding to the various source redshifts.

Studying the impact of substructure in the lens with multiple images positions does not make use of the full information, since this just makes use of the differences of deflection angles between multiply imaged sources and not of higher order or local derivatives of the deflection angle. This can be done when mapping the full surface brightness distribution of the images and adjusting the model such that for every image system of a reproduced source the SFBs match the observations. Colley et al. (1996) were the first to measure the unlensed surface brightness distribution of the 5 image system in Cl0024 and thereby helping to constrain the mass distribution of the cluster. Seitz et al. (1998) analyzed the lensing effect of the cluster MS1512 using several multiply imaged systems and obtained the surface brightness distribution of the highly magnified galaxy cB58 to a unprecedented spatial resolution. In this analysis it was important to account for the mass distribution of a galaxy perturbing the cB58arc such that it was bent away from the cluster center – although measuring galaxy halos was not the aim of this work. Later on Suyu & Halkola (2010) analyzed the surface brightness distribution of a source multiply imaged by a galaxy with a satellite as perturber and could indeed measure the satellite halo size in this way, showing that the sensitivity of this method can be extended to (still massive) satellites in favorable lensing systems. On cluster lens scale Donnarumma et al. (2011) used a method similar to Halkola et al. (2007), to constrain halo sizes in another cluster. In this case one of the sources is mapped into a giant arc system, of which they used several corresponding surface brightness knots for lens modeling, thus partially making use of the surface brightness distribution of the arc in this cluster.

In this work we will study galaxy halo truncation in the cluster MACSJ1206.2, since this is an ideal target for several reasons: MACSJ1206.2 is a massive cluster at redshift $z = 0.439$ (for a summary on properties and lensing, Xray and SZE results see Umetsu et al. 2012, Zitrin et al. 2012b). This cluster shows still signs of its recent assembly, since there is a 'trail' of intra cluster light along its major axis (in mass and light), indicating previous tidal strippings

down to the core of galaxies or tidal disruption of galaxies. On the other hand its central galaxy is almost at rest relative to the center of mass (as obtained from cluster members' velocities),see Biviano et al. in preparation. Further, this cluster appears relaxed from its Xray contours (Ebeling et al., 2009; Umetsu et al., 2012). This means that cluster members orbited each other for at least a significant fraction of the crossing time, were exposed to the dense cluster environment and had the necessary (and short) time to become tidally stripped. Due to its deep multi-band HST photometry this cluster has many multiple image systems (Zitrin et al. (2012b)) and furthermore has a giant arc, which is bent around several cluster members, making the light deflection of galaxy halos already visible to the eye. Using the SFB distribution of the arcs and the multiple images positions, this cluster thus offers the opportunity to provide very strong constraints on halo sizes.

This paper is organized as follows: In Section 2 we give an overview of the data used, in Sect. 3 we present the models for the mass distribution of the cluster and the halos traced by cluster galaxies, in Sect. 4 we introduce the scaling relations connecting galaxy luminosity and dark matter halo properties. In Sect. 5 we obtain a strong lensing model using only point source constraints from multiple images and the giant arc. Section 6 then also includes the full surface brightness distribution of the arc and its counterimage in the analysis. In Sect. 7 we will discuss our results concerning the scaling of cluster galaxies' luminosity with their velocity dispersion and halo sizes and the properties of the unlensed source of the arc's counterimage. We use WMAP7[1] (Komatsu et al., 2011) cosmology throughout the paper. This gives a scale of $5.662\,\mathrm{kpc}/''$ at the redshift of the cluster, $z = 0.439$. Einstein radii, convergence and shear values are given in units of the ratio of the angular diameter distances from the lens to the source ($\mathrm{D_{ds}}$) and the observer to the source ($\mathrm{D_s}$), $\mathrm{D_{ds}D_s^{-1}}$ if not otherwise stated.[2] All angles are defined as N over (-E).

7.3 Data

The data used in this work are described in Postman et al. (2012), Zitrin et al. (2012b) and Ebeling et al. (2009). All raw and reduced HST imaging data taken by CLASH are public. We obtain position and shapes of cluster galaxies with SEXTRACTOR (Bertin & Arnouts, 1996) from the F606W filter data. The F435W, the F606W and the F814W filter data are used to extract the surface brightness distribution of the arc and its counterimage for the lens modeling. We need a r.m.s.-noise estimate for each pixel of the giant gravitational arc and its counterimage for the surface brightness reconstruction. We obtain the pre-reduced, publicly available *FLT* images for the F435W, F606W and F814W filters, respectively. The pre-reduction, done by *calacs*, includes overscan and bias correction as well as flat-fielding of the single images. Afterwards, *Multidrizzle* has been used for the alignment, background subtraction, cosmic–ray rejection and weighted coaddition of the individual frames and the r.m.s.–noise estimate. The weighting scheme used is the *ERR*–scheme, where the weighting is done by the inverse variance of each pixel. From this inverse variance, we calculate the r.m.s.–noise estimate for each pixel. For these frames, we choose a pixel scale of $0.05''$ resembling the natural pixel scale of the ACS camera in these filters. We verify that the corresponding star positions in the different filters are accurate to $\approx 0.5\mathrm{pix}$.

---

[1] $\mathrm{H_0 = 71 kms^{-1}Mpc^{-1}}$, $\Omega_\mathrm{M} = 0.267$, $\Omega_\Lambda = 0.734$
[2] Another interpretation would be $\mathrm{D_{ds}D_s^{-1}} = 1$, which is theoretically ill–defined.

7.4 Modeling the cluster and its galaxy component

Since we want to measure the parameter values for halo truncation, we use parametric lens models. The main cluster component is modeled by a NFW (Navarro et al., 1997) halo. Its lensing properties are described in Wright & Brainerd (2000) and Golse & Kneib (2002):

$$\Sigma(X) = 2r_{\mathrm{s}}\delta_{\mathrm{c}}\rho_{\mathrm{c}} \times \times \begin{cases} \frac{1}{X^2-1}\left[1 - \frac{2}{\sqrt{1-X^2}}\mathrm{arctanh}\sqrt{\frac{1-X}{1+X}}\right] & X < 1 \\ \frac{1}{3} & X = 1 \\ \frac{1}{X^2-1}\left[1 - \frac{2}{\sqrt{X^2-1}}\arctan\sqrt{\frac{X-1}{1+X}}\right] & X > 1 \,. \end{cases} \tag{7.1}$$

Here r_{s}, δ_{c} and ρ_{c} are the scale radius and the characteristic overdensity of the halo and the critical density of the universe for closure at the redshift of the halo. For the spherical case, $X = \frac{R}{r_{\mathrm{s}}}$ denotes the dimensionless distance in the image plane. Following Golse & Kneib (2002); Halkola et al. (2006), we introduce elliptical isopotential contours by introducing the axis ratio q = ba^{-1} with major and minor axes a and b, respectively. $X = \sqrt{x_1^2/q + x_2^2 q}$ then denotes the non–spherical extension of the spherical case above, with x_1 and x_2 being the Cartesian coordinates in the major axis coordinate system. In the following we will only consider the elliptical case, calling that the NFW profile.

We model the cluster galaxies as Brainerd et al. (1996) with their so called BBS: The density profile is an isothermal sphere with a "velocity dispersion" σ and a truncation radius r_t:

$$\rho(r) = \frac{\sigma^2}{2\pi\mathrm{G}r^2}\frac{r_{\mathrm{t}}^2}{r^2 + r_{\mathrm{t}}^2} \,. \tag{7.2}$$

The projected surface mass density is:

$$\Sigma(R) = \frac{\sigma^2}{2\mathrm{G}R}\left[1 - \left(1 + \frac{r_{\mathrm{t}}^2}{R^2}\right)^{-0.5}\right] \,. \tag{7.3}$$

This gives an enclosed mass within a cylinder of radius R of

$$M(< R) = \frac{\pi\sigma^2}{\mathrm{G}}\left[R + r_{\mathrm{t}} - \sqrt{R^2 + r_{\mathrm{t}}^2}\right] \,, \tag{7.4}$$

and a total mass of

$$M_{\mathrm{tot}} = \frac{\pi\sigma^2 r_{\mathrm{t}}}{\mathrm{G}} \,, \tag{7.5}$$

where G is the gravitational constant and R the 2D-radius. For its exact lensing properties, see Brainerd et al. (1996). Following Halkola et al. (2006), ellipticity is again introduced in the potential in the same way as in the NFW case. The truncation radius r_{t} marks the transition region from a density slope $\rho \sim r^{-2}$ to a slope of $\rho \sim r^{-4}$. At r_{t} the projected density is half the value of the SIS model with the same σ. For the 3D density the truncation radius is equal to the half-mass radius of the profile, see Elíasdóttir et al. (2007); Limousin et al. (2009). For the 2D projected density the 2D half mass radius is smaller, $r_{1/2,2D} = 0.75r_{\mathrm{t}}$.

7.5 Galaxy scaling relations

We are likely not able to constrain galaxy halos individually. Therefore we use scaling relations between the different galaxy halos based on the luminosity of the individual galaxies. As in

Table 7.1: The scaling parameters for different values of δ, ϵ and α.

Field galaxies				Stripped galaxies			
δ	ϵ	$\frac{\alpha}{\delta}$	α	δ	$\frac{\alpha}{\delta}$	α	$\epsilon_{\text{stripped}}$
0.3	0.2	2	0.6	0.30	1	0.30	-0.10
0.25	0.0	2	0.5	0.25	1	0.25	-0.25
0.25	0.2	2.8	0.7	0.233	1	0.233	-0.30
0.3	0.0	4/3	0.4				

Halkola et al. (2006, 2007); Limousin et al. (2007a) we make use of the Faber-Jackson (Faber & Jackson, 1976) relation connecting the luminosity (L) of early type galaxies with their central stellar velocity dispersion σ_{star} and halo velocity dispersion σ:

$$\sigma = \sigma^{\star} \left(\frac{L}{L^{\star}} \right)^{\delta} \quad . \tag{7.6}$$

The truncation radius is assumed to scale with luminosity as

$$r_{\text{t}} = r_{\text{t}}^{\star} \left(\frac{L}{L^{\star}} \right)^{\alpha} = r_{\text{t}}^{\star} \left(\frac{\sigma}{\sigma^{\star}} \right)^{\alpha/\delta} \quad . \tag{7.7}$$

Here, $\sigma^{\star}$, $L^{\star}$ and $r_{\text{t}}^{\star}$ are the parameter values for a galaxy halo with reference luminosity $L^{\star}$. With $M_{\text{tot}} \propto \sigma^2 r_{\text{t}}$ (Eq.7.5), we obtain for the mass luminosity relation

$$\frac{M_{\text{tot}}}{L} \propto L^{\epsilon} \propto \sigma^{2+\alpha/\delta-1/\delta} = \sigma^{\epsilon/\delta} \tag{7.8}$$

and for the relation of the power law indices we obtain

$$\frac{\alpha}{\delta} = \frac{\epsilon}{\delta} - 2 + \frac{1}{\delta} \quad . \tag{7.9}$$

For elliptical galaxies the scaling relations between dark matter halo mass and light, $M_{\text{tot}}/L \propto L^{\epsilon}$, has a slope of about $\epsilon \approx 0.2$ (see e.g. Grillo et al. (2009); Auger et al. (2010), who measure the central M_{tot}/L from strong gravitational lensing of early-type galaxies). The ratio for their central dynamical mass and their light is very similar $M_{\text{dyn}}/L \propto L^{\epsilon_{FP}}$, with a fundamental plane slope of $\epsilon_{FP} \approx 0.2$ (Bender et al., 1992). The exact value depend also on the filter used to measure the luminosity, see Barbera et al. (2011). If $\epsilon = 0$ then the total mass to light ratio is independent of luminosity and mass.

The values for the Faber-Jackson slope δ quoted in literature depend on the wavelength range used for the luminosity measurement and on the considered magnitude range (Nigoche-Netro et al., 2011; Focardi & Malavasi, 2012). For the B-band relation we will in the following consider slopes between $\delta = 0.3$ (Ziegler & Bender (1997)) and $\delta = 0.25$ (see also Fritz et al. (2009), Kormendy & Bender (2012) and Focardi & Malavasi (2012)). Therefore the scaling between truncation radius and velocity dispersion varies between power law indices of one and three, and the scaling between truncation radius and luminosity varies between a power law index of 0.4 and 0.7 as can been seen from Table 7.1.

For halos in a dense environment, however, we expect the stripping radius to be (Merritt, 1983)

$$r_{\text{t}} \propto M_{\text{tot}}^{1/3} \tag{7.10}$$

and with $M_{\text{tot}} \propto \sigma^2 r_{\text{t}}$ we obtain $\alpha/\delta = 1$. The mass velocity relation is $M_{\text{tot}} \propto \sigma^3$. This gives for the mass to light ratio using Eq. 7.6:

$$\frac{M_{\text{tot,stripped}}}{L} \propto L^{\epsilon_{\text{stripped}}} \propto \sigma^{3-\delta^{-1}} \tag{7.11}$$

and thus

$$\epsilon_{\text{stripped}} = 3\delta - 1 = 3\alpha - 1 \quad . \tag{7.12}$$

Thus, as expected for stripped halos, the power law index for the mass to light ratio as function of light is negative and of order $\epsilon_{\text{stripped}} = -0.1$ to $\epsilon_{\text{stripped}} = -0.3$, depending on the value of δ, see Table 7.1.

As we will see later, we cannot distinguish the different exponents of the truncation law with this work, but only the truncation scale. Hence we fix the values of ϵ and δ. On the one hand, the galaxy cluster MACSJ1206.2-0847 represents a dense environment, on the other hand, since galaxy clusters are relatively young objects, the halo stripping might not be entirely complete. Therefore, we choose values somewhat in between field and cluster galaxies; we take $\epsilon = 0$ as an intermediate value for the mass-to-light ratio evolution with luminosity. For δ, e.g. Bernardi et al. (2003b) find empirically a value of $\delta = 0.25$ from the Sloan Digital Sky Survey. There are, however indications for an increase in δ for fainter elliptical galaxies (see e.g Matković & Guzmán (2005) and references therein). To take that increase into account, we take $\delta = 0.3$, as empirically derived in Rusin et al. (2003a) from gravitational lensing of field elliptical galaxies and get the following equation for the truncation scaling:

$$r_{\text{t}} = r_{\text{t}}^{\star} \left(\frac{\sigma}{\sigma^{\star}}\right)^{\frac{4}{3}} \quad . \tag{7.13}$$

This scaling relation between the velocity dispersion and truncation radius is the one adopted in most parts of the paper. Therefore, one aim of the paper is to measure $\sigma^{\star}$ and $r_{\text{t}}^{\star}$.

7.6   Strong lensing model for point-like sources

A first strong lensing model for cluster MACSJ1206.2-0847 was published by Ebeling et al. (2009), based on 2 surface brightness peaks multiply mapped into knots on the giant arc and its counterimage. The CLASH data allowed Zitrin et al. (2012b) to identify 12 multiply imaged systems lensed into 52 multiple images. Distances for the lensed galaxies were inferred from spectroscopic redshifts if available or precise photometric redshifts. In the following, we use a parametric strong lensing model for the dark matter and we also model the cluster members close to the strong lensing area. We describe the model input first, followed by the results.

7.6.1   Model ingredients

For the point-like strong lensing analysis, we need two ingredients: The point-like multiple image positions and models for the cluster scale mass distribution and the substructure as traced by the cluster galaxies.

Multiple image systems

We start with similar sources as Zitrin et al. (2012b), Table 1, but modify this selection. In Table 7.2 we present our multiple image identifications; their positions are given in Fig 7.2. The differences to (Zitrin et al., 2012b) are as follows: First, we keep the systems 2,3,4,5,6,7,8,12,13 unchanged. We split the Arc system 1 into 3 subsystems at the same redshift, labeled "1a", "1b" and "1c", using corresponding surface brightness peaks, see also Fig. 7.13. Since systems 2 and 3 are two brightness peaks in the same source, we replace these systems by numbers 2b and 2c. For the systems 9 and 10, Zitrin et al. (2012b) state an ambiguity of images 9.3, 9.4, 10.3 and 10.4. We implement these images as 10.3 and 10.4 only: First, the surface brightness distribution of 10.3 and 10.4 looks more similar to 10.1 and 10.2 than 9.1 and 9.2 and second, also the best-fit model gives a significantly better fit to this identification of the observations than 9.3 and 9.4. Also, for these systems, we neglect the only probable counterimages 9.5 and 10.5 of Zitrin et al. (2012b). For system 11, we also neglect the candidate images 11.1 and 11.2, keeping 11.3 to 11.5 as a triple imaged system only. Our best fit model does indeed not predict the multiple images 11.1 and 11.2 and gives model positions 9.5 and 10.5 $6.2''$ and $9.5''$ away from the positions given in Zitrin et al. (2012b), respectively. However there is no certain identification possible for these images.

We use the spectroscopic redshift of image systems measured as part of the VIMOS campaign at the VLT where these are available. Otherwise, we combine the available photometric redshifts in Zitrin et al. (2012b) into an error weighted mean redshift and mean error for each multiple image system belonging to the same source. The mean redshift becomes the central value for a Gaussian shaped redshift prior, and the mean redshift error becomes the 1σ width of this prior. This gives an approximate, more conservative estimate for the uncertainties of the redshifts than the r.m.s.–error of the mean. Any systematic uncertainty in the photometric redshift estimate is equally present in the estimate of each multiple image, since they have the same color. Therefore a pure statistical error would underestimate the true uncertainty of the photometric redshift. These photometric redshifts constraints of the multiple image systems are used as priors in the model optimization.

For the positional uncertainty of the multiple images, we adopt a value of $0.5''$. This value is driven by line–of–sight (LOS) structure and substructure not accounted for in the lens modeling, since the measurement error of the positions of the multiple images is usually only a fraction of a pixel. Jullo et al. (2010) estimate the LOS structure to produce an r.m.s. image position scatter of $\approx 1''$ for a cluster like A1689. Host (2012) estimates a relative LOS structure deflection angle depending on the distance from the cluster center and the redshift of the source to be $0.5''$ to $2.5''$ for typical strong lensing situations.

Cluster galaxies tracing dark matter substructure

We use the BPZ Photometric redshifts (Benítez, 2000; Benítez et al., 2004; Coe et al., 2006) as described in Postman et al. (2012) and spectroscopic information for this cluster (Rosati et al, 2012, in prep), wherever available for the cluster member selection. For simplicity, we consider as cluster members galaxies with spectroscopic redshifts between z=0.43 and 0.45; all other galaxies with different spectroscopic redshifts are excluded.

For galaxies lacking spectroscopic redshifts we use the photometric redshift estimates and consider all galaxies with a photometric redshift estimate between 0.39 and 0.49 and a 95 % confidence interval width smaller than 0.5 (i.e. $c.l.(95\%)_{max} - c.l.(95\%)_{min} < 0.5$) as cluster

Table 7.2: Multiple image positions

Obj id	$\Theta_1{}^1$ ($''$)	$\Theta_2{}^1$ ($''$)	z_{input}	z_{model}
1a.1	12.85	19.73	1.033^2	1.033^2
1a.2	20.76	3.46	1.033^2	1.033^2
1a.3	19.56	-6.79	1.033^2	1.033^2
1b.1	13.72	18.91	1.033^2	1.033^2
1b.2	20.71	4.96	1.033^2	1.033^2
1b.3	19.71	-7.54	1.033^2	1.033^2
1c.1	12.46	20.26	1.033^2	1.033^2
1c.2	19.56	-5.84	1.033^2	1.033^2
2a.1	-35.30	-28.95	3.03^2	3.03^2
2a.2	-42.15	-14.20	3.03^2	3.03^2
2a.3	-42.65	15.40	3.03^2	3.03^2
2b.1	-33.60	-30.95	3.03^2	3.03^2
2b.2	-42.15	-12.85	3.03^2	3.03^2
2b.3	-42.30	14.65	3.03^2	3.03^2
2c.1	-34.00	-30.45	3.03^2	3.03^2
2c.2	-42.11	-13.15	3.03^2	3.03^2
2c.3	-42.30	14.85	3.03^2	3.03^2
4.1	14.37	12.57	2.54^2	2.54^2
4.2	-6.43	21.42	2.54^2	2.54^2
4.3	-15.10	2.74	2.54^2	2.54^2
4.4	0.62	3.63	2.54^2	2.54^2
4.5	6.36	-39.21	2.54^2	2.54^2
5.1	-21.60	17.60	1.73 ± 0.17^3	1.59
5.2	-22.30	-2.80	1.73 ± 0.17^3	1.59
5.3	-6.50	-30.45	1.73 ± 0.17^3	1.59
6.1	13.95	28.15	2.73 ± 0.15^3	1.86
6.2	22.36	-23.50	2.73 ± 0.15^3	1.86
6.3	26.25	11.30	2.73 ± 0.15^3	1.86
7.1	-56.30	-15.10	3.82 ± 0.3^3	2.90
7.2	-55.60	-19.30	3.82 ± 0.3^3	2.90
7.3	-53.10	-24.30	3.82 ± 0.3^3	2.90
7.4	-56.29	-13.62	3.82 ± 0.3^3	2.90
7.5	-56.61	-12.68	3.82 ± 0.3^3	2.90
8.1	-2.67	34.72	5.46 ± 0.29^3	5.03
8.2	23.27	13.86	5.46 ± 0.29^3	5.03
8.3	-16.33	-0.46	5.46 ± 0.29^3	5.03
8.4	13.01	-40.68	5.46 ± 0.29^3	5.03
9.1	8.95	14.05	1.73 ± 0.23^3	1.64
9.2	2.40	16.55	1.73 ± 0.23^3	1.64
10.1	0.35	18.95	1.34 ± 0.26^3	1.69
10.2	12.30	10.70	1.34 ± 0.26^3	1.69
10.3	-5.55	2.00	1.34 ± 0.26^3	1.69
10.4	-2.45	2.25	1.34 ± 0.26^3	1.69
11.3	-10.79	19.02	1.35 ± 0.44^3	1.44
11.4	-13.87	-0.56	1.35 ± 0.44^3	1.44
11.5	2.38	-28.57	1.35 ± 0.44^3	1.44
12.1	-19.04	33.42	3.84 ± 0.52^3	3.28
12.2	-24.78	-7.58	3.84 ± 0.52^3	3.28
12.3	-3.95	-36.07	3.84 ± 0.52^3	3.28
13.1	-10.99	-37.61	3.18 ± 0.99^3	2.34
13.2	-29.83	-1.72	3.18 ± 0.99^3	2.34
13.3	-28.73	17.18	3.18 ± 0.99^3	2.34

[1]relative to the center of the BCG at 12:06:12.134 RA (J2000) -08:48:03.35 DEC (J2000)
[2]spectroscopic redshift, fixed [3]photometric redshift estimate, weighted mean and error

members as well. From these cluster galaxies, we use only a subsample which fulfill 2 criteria: First, we only use those within a 3×3-sized box centered on the BCG. Second, these galaxies have to trace a sufficiently massive halo to be relevant for the lens modeling: From the galaxy sample we pick the second brightest galaxy of this cluster, located at 12:06:15.647 RA (J2000), -08:48:21.88 DEC (J2000) as the reference galaxy (called hereafter GR), see Fig. 7.2.

We use the F160W fluxes of the cluster members in units of GR and use Eq. 7.6 to scale the velocity dispersions relative to GR. We convert the velocity dispersions in a "cosmology-free" Einstein radius by

$$\Theta_{\mathrm{E}} = \frac{4\pi\sigma^2}{\mathrm{c}^2} \tag{7.14}$$

with c being the vacuum speed of light. We explicitly model only those cluster galaxies which have an Einstein radius larger than 3% of the Einstein radius of GR. An Einstein radius of $1''$ corresponds to a velocity dispersion $\sigma = 186 \mathrm{kms}^{-1}$. Looking at Eq. 7.13 we note that we need to measure 2 values to fully determine the halo properties: $\sigma^\star$ and $r_t^\star$. We use 2 different sets of parameters: $r_{t,1''}$, for a reference $\sigma = 186 \mathrm{kms}^{-1}$ which gives the value for a galaxy with an Einstein radius of $1\Theta_{\mathrm{E}}''$, and $r_{t,\mathrm{GR}}$, which gives the truncation radius for galaxy GR itself.

With this procedure, we obtain 92 galaxies. We take their positions, orientations and ellipticities from a SEXTRACTOR (Bertin & Arnouts, 1996) run on the HST/ACS F606W band. A list of all cluster galaxies in our model is stated in Table 7.9. A comparison with the HST/ACS F814W shows consistent values for the orientations and ellipticities of the cluster members.
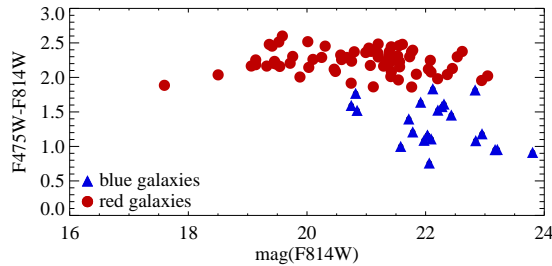
Figure 7.1: The color-magnitude diagram of the selected cluster galaxy lenses. Plotted is the F475W-F814W color against the F814W magnitude of the galaxies. We mostly select red galaxies with similar color. Since we do not select by galaxy color but by photometric and spectroscopic redshift, we also identify some bluer galaxies as cluster members, which would not have been possible based on a pure red sequence cut. The typical error on the magnitude and color is smaller than the symbol size. The color indicates the SED type of galaxies, separated in red and blue galaxies.

With Eqs. 7.6 and 7.13 we now have a complete description of all cluster galaxy lenses with only 2 free parameters, the normalizations of equations 7.6 and 7.13. Since we take L* for GR, the only free parameters in our galaxy model are σ_{GR}, thus fully determining Eq. 7.6 and $r_{t,\mathrm{GR}}$ fully determining Eq. 7.13 for σ_{GR}.[3] We will attribute these two parameters to the reference galaxy GR, but we should however keep in mind that the derived parameters of GR are due to the combined signal of all the galaxies and that it is irrelevant which galaxy was chosen as reference. For this reference galaxy, we measure an effective radius R_{eff} of

---

[3]However, we can equivalently use $r_{t,1''}$ with $\sigma = 186 \mathrm{kms}^{-1}$ as the full determination of Eq. 7.13.

Table 7.3: Model lens input parameters and priors. Stated are the parameter, its prior type, the minimal and maximal allowed value and the most likely and its 95 % CL error.

parameter	prior	min	max	model result(95% c.l.)
γ	uniform	0	0.4	$0.20^{+0.03}_{-0.03}$
Θ_γ	uniform	$-90°$	$90°$	$25.7^{+3.0}_{-2.5}°$
x_{NFW}[1]	uniform	$-8''$	$8''$	$0.19^{+0.44}_{-0.47}''$
y_{NFW}[1]	uniform	$-8''$	$8''$	$0.78^{+0.23}_{-0.23}''$
q_{NFW}	uniform	0.35	1	$0.686^{+0.014}_{-0.016}$
Θ_{NFW}	uniform	$-20°$	$44°$	$19.0^{+1.2}_{-1.0}°$
$\Theta_{\mathrm{E,NFW}}$	uniform	$25''$	$200''$	$43.8^{+1.2}_{-1.4}''$
$r_{\mathrm{s,NFW}}$	uniform	$50''$	$650''$	$175^{+23}_{-20}''$
$r_{\mathrm{t,1''}}$	uniform	11kpc	142kpc	31^{+36}_{-14}kpc
σ_{GR}	uniform	$59\mathrm{kms}^{-1}$	$395\mathrm{kms}^{-1}$	$236^{+29}_{-32}\mathrm{kms}^{-1}$

[1]relative to the center of the BCG at 12:06:12.134 RA (J2000) -08:48:03.35 DEC (J2000)

5kpc to 6kpc from a Sérsic, (Sérsic, 1963), a de Vaucouleurs (de Vaucouleurs, 1948) and a de Vaucouleurs+exponential disc in the F160W and F814W filters consistently using GALFIT (Peng et al., 2010). This effective radius agrees well with measurements (in the HST-F814W and VLT-FORS-I-band filters) of other elliptical galaxies in various clusters of similar redshift, see Figure 10 in Saglia et al. (2010).

Modeling of the cluster component

We model the cluster as a NFW (Navarro et al., 1997) halo. We have also used a non singular isothermal elliptical (NSIE) profile for the halo, but this results in worse fits to the positions of the multiple image systems. The best fit χ^2 for the NFW is $\chi^2_{\mathrm{NFW}} = 227$, while a NSIE cluster scale halo with the same number of free parameters gives a $\chi^2_{\mathrm{NSIE}} = 434$, for the full model using point–like images. A similar difference for a NSIE vs NFW model has been reported already for the stacked weak lensing signal of clusters and groups of galaxies in the SDSS (Mandelbaum et al., 2006).

We also add external shear as a free parameter to allow for a contribution of the large scale environment in the vicinity of the cluster.

This gives in total 6 free parameters for the NFW halo, 2 for the external shear, 2 for the galaxy lenses, 9 for the source redshifts and 32 free parameters for the (RA,DEC) source positions of the 16 sources. The lens model parameters and its priors are posted in Table 7.3. We use flat priors with defined minimum and maximum values for each of the parameters. From the multiple images, we get 104 constrains, leaving this model with 53 d.o.f.

7.6.2 Results of the point-like modeling

Putting all together, we can now reconstruct the lensing signal for this cluster. We use the strong lensing code GLEE, a lens modeling software developed by S. H. Suyu and A. Halkola (Suyu & Halkola, 2010; Suyu et al., 2012). This method does not only yield the best fitting model (using either source plane or image plane minimization) but in addition
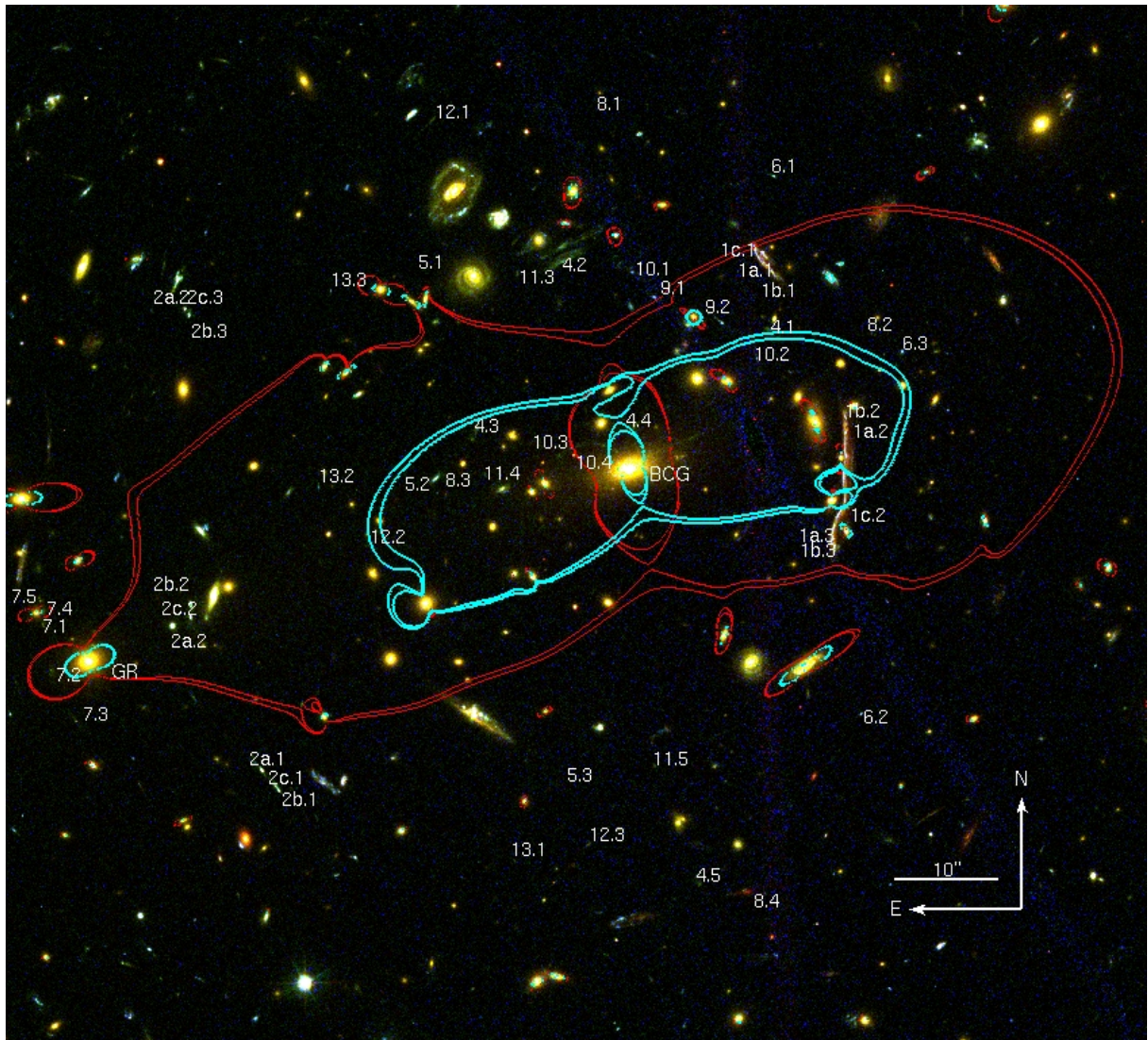
Figure 7.2: A $110'' \times 100''$ cutout of the cluster center. The multiple image systems are labeled according to Tab 7.2. We have added the critical lines for a source at the redshift of the arc ($z = 1.03$) in cyan and for a source at $z = 2.54$ in red. The critical lines are calculated from a pixelated magnification map, enclosing the high magnification areas of the image. The BCG and the reference galaxy GR are marked in the image. North is up and east is left. This color composite image is made from the F435W, F606W and F814W HST/ACS filter data.

includes a Monte Carlo Markov Chain (MCMC) sampler yielding the most likely parameters with their confidence limits. We obtain the best–fitting cluster model by maximizing the posterior probability distribution function. For that, the likelihood is multiplied with the priors, see Halkola et al. (2006, 2008); Suyu & Halkola (2010). The likelihood is proportional to $\sim \exp(-\chi^2/2)$. The χ^2 is calculated from the difference between the observed and the model predicted image position:

$$\chi^2 = \sum_i \frac{\parallel \mathbf{\Theta}_i - \mathbf{\Theta}_{0,i} \parallel^2}{\delta^2_{\Theta_i}} \quad,$$

where $\mathbf{\Theta}_i$ and $\mathbf{\Theta}_{0,i}$ mark the model predicted and observed position of multiple image i and δ_{Θ_i} its input uncertainty. The MCMC sampling procedure is described in Dunkley et al. (2005) and Suyu & Halkola (2010). We get acceptance rates of typically ~ 0.25 for the MCMC, the covariance matrix between parameters is derived from a previous run of the MCMC procedure for the same model parameters. Convergence is achieved based on the power spectrum test given in Dunkley et al. (2005).

Results for the cluster–scale model

For the best-fit values[4], we get: $r_{t,1''} = 23.7$kpc, $\sigma_{GR} = 246$kms^{-1}, $\gamma = 0.19$, $\Theta_\gamma = 26°$, $x_{NFW} = 0.15''$, $y_{NFW} = 0.74''$, $b/a_{NFW} = 0.69$, $\Theta_{NFW} = 19°$, $\Theta_{E,NFW} = 44.1''$ and $r_{s,NFW} = 174''$. As explained already the external shear and the Einstein radius are given in units of $D_{ds}D_s^{-1}$. The redshift estimates of the best-fit model are given in Table 7.2. Most of the redshifts agree with their photometric estimates within the errors, only system 6 is a clear outlier. The critical lines for the arc redshift and a redshift of z = 2.54 are plotted in Fig. 7.2.
In Fig. 7.3, we show the differences of the input and model output positions for our best-fit model.
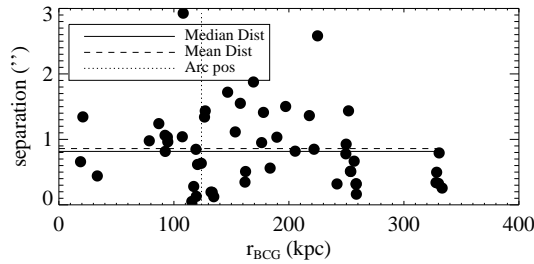
Figure 7.3: The radial error dependence for the best fit model is shown in this plot. Plotted is the distance between observed and model predicted multiple image position on the y-axis against its distance from the center of the BCG. Overplotted are the respective median and mean of the images. The vertical dotted line marks the mean distance of the giant arc and its counterimage to the center of the BCG. There is no radial dependence of the error visible in this Model.

As one can see, the mean and median differences are $0.86''$ and $0.82''$. This justifies the used input uncertainty of $0.5''$, since this is a good estimate of the reconstruction uncertainty.
The MCMC sampling provides us with estimates for the parameter uncertainties. The probability densities for the parameter estimates are shown in Fig. 7.4.

---

[4]The error erstimates from the MCMC sample will be discussed below
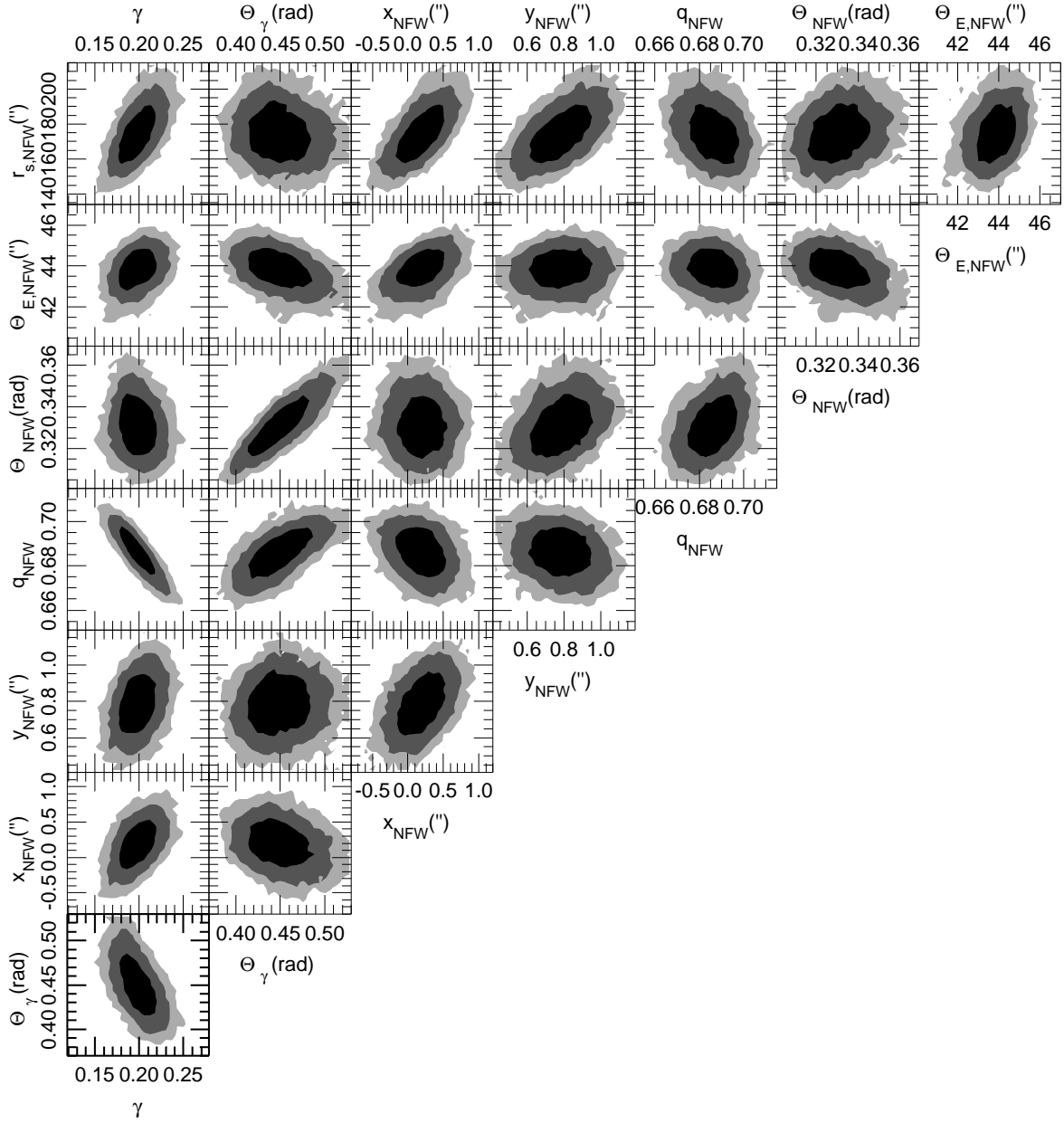
Figure 7.4: Parameter estimates from the MCMC sampling of the parameter space. The shaded regions give the 68.3% 95.5 % and 99.7 % uncertainty areas, from dark to light gray, respectively.

We want to discuss some of the parameters here, quoting the 95 % confidence intervals: First, the external shear values are: $\gamma = 0.20^{+0.03}_{-0.03}$ and $\Theta_\gamma = 25.7^{+3.0}_{-2.5}{}^\circ$. This shear can originate from external structure present in the vicinity of the cluster or from substructure present in the cluster, but not accounted for in the model. Indeed, the cluster mass reconstruction map of Umetsu et al. (2012) (see their Fig. 8) shows two additional structures, one in the southeast one in the northwest of the cluster center. We take the 2D mass reconstruction map of Umetsu et al. (2012), and subtract the surface mass density of the their best–fitting cluster NFW-profile, leaving us with the residual mass map. We calculate the shear that these additional masses cause in the cluster center, and obtain a values of $\gamma \lessapprox 0.13$ for $D_{ds}D_s^{-1} = 1$. This thus explains a part of the shear present in the model. In addition there is a faint, bar like intra–cluster–light structure in the center of MACSJ1206.2-0847, visible mostly in the NIR, see Fig. 7.5.
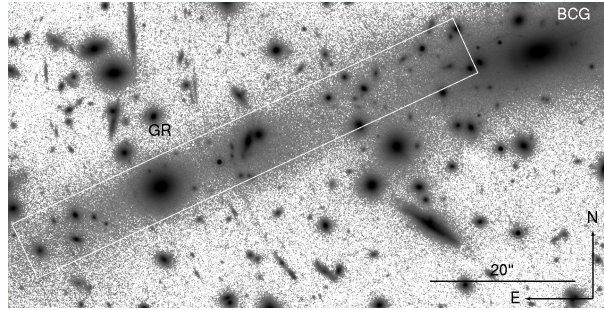
Figure 7.5: The center of the cluster MACSJ1206.2-0847 as observed with the F160W HST/WFC3 filter. The faint, bar-like structure in the intra-cluster light is marked with a white box. It extends ~ 1.5 radially outwards from the BCG to the SE. The mass associated with this ICL acts as further substructure. We use logarithmic scaling for the fluxes in this image.

The mass associated with this light causes an additional shear. To verify this, we model this bar as an isothermal, highly elliptical mass profile ($q_{bar} < 0.4$) with similar values for the core and truncation radii. A best–fit total bar mass of a few times $10^{12} M_\odot$ is sufficient to lower the required external shear values down to the expectation[5] from the environment and, at the same time, further improve the overall fit quality of the model significantly. We check that including this intra–cluster–light bar does not change the $r_{t,1''}$ significantly and ignore it for the rest of this work. A detailed study of the mass associated to the intra cluster light is beyond the scope of this paper.

Second, the cluster–scale NFW halo has the following most likely parameter estimates: $x_{NFW} = 0.19^{+0.44}_{-0.47}''$, $y_{NFW} = 0.78^{+0.23}_{-0.23}''$, $q_{NFW} = b/a_{NFW} = 0.686^{+0.014}_{-0.016}$, $\Theta_{NFW} = 19.0^{+1.2}_{-1.0}{}^\circ$, $\Theta_{E,NFW} = 43.8^{+1.2}_{-1.4}''$, $r_{s,NFW} = 175^{+23}_{-20}''$. The results regarding the cluster-scale dark matter halo are within our expectations:

- The halo center's position follows the same trend as the X-ray center in Ebeling et al. (2009), i.e., the center has a slight tendency to move towards positive values of x and y relative to the BCG center. In total, the center of mass is shifted by approximately $(0.8 \pm 0.3)''$. Ebeling et al. (2009) report a displacement of the X-ray center from the BCG center of $(1.7 \pm 0.4)''$ in approximately the same direction implying that these displacements agree on a 2σ level. The level of displacement between the BCG and the dark matter halo center is comparable to Zitrin et al. (2012a).

---

[5]For the bar model, we get an external shear value of $\gamma = 0.13^{+0.04}_{-0.04}$.

- The orientation of the NFW-major axis follows the major axis of the BCG within $\approx 5°$

- There is some degeneracy between the orientation of the cluster halo and the external shear, since both can compensate each other partially. The same is true for the axis ratio of the halo and the value of the external shear.

- For the Einstein and scale radius of the NFW halo, we get: $\Theta_{\rm E,NFW} = 43.8^{+1.2}_{-1.4}{''}$, $r_{\rm s,NFW} = 175^{+23}_{-20}{''}$. The total mass included within a cylinder of radius R is shown in Fig. 7.6.
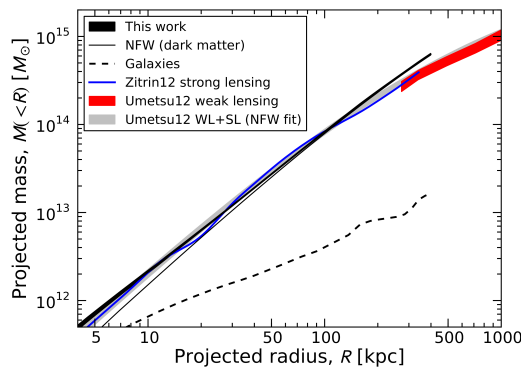
Figure 7.6: The projected mass estimates within circular apertures are shown in this figure. The black area shows the 68 % confidence interval for the combined mass, the black solid and dashed lines show the mass contributions for the NFW halo alone and the galaxies for the best-fit model, respectively. The small uncertainty for the mass estimate comes from the fact that we use a parametric model, which needs to reproduce the correct Einstein radius, therefore giving too small errors in the intermediate radii. We overplot the mass estimates from Umetsu et al. (2012), more explicitly their NFW fit to the weak and strong lensing data in gray, their weak lensing mass estimates alone (red area), and the Zitrin et al. (2012b) strong lensing estimate in blue. The mass estimate in this work agrees in the range of $\sim 4\mathrm{kpc}$ to $\sim 150\mathrm{kpc}$ with our previous work.

Comparisons with Zitrin et al. (2012b) and Umetsu et al. (2012) show that we derive the same mass estimates within 68 % c.l. in the range up to $\approx 150\mathrm{kpc}$. Our errors on the measured masses are derived from the mass distribution of 200 random cluster models from the MCMC points. Since we use a parametric model for the lens, we only measure the uncertainty within this parametric model, not taking into account that different parameterizations could give similar good fits with a slightly different mass profile, hence underestimating the true error on the radial mass profile.

- We fit a circular NFW[6] halo to the total azimuthally averaged mass in Fig. 7.6 to estimate the concentration c_{200} and $r_{\rm s,NFW}$ from the total included mass with a least square fit. We get a concentration of $c_{200} = 3.7 \pm 0.2$ and a scale radius of $r_{\rm s,NFW} = 677 \pm 48\mathrm{kpc}$. When we exclude the central 70kpc from the fit, we get $c_{200} \approx 3.2$ and $r_{\rm s,NFW} = 827\mathrm{kpc}$. Our radially averaged mass distribution agrees with the results of Umetsu et al. (2012) in the center. Our scale radius value is an extrapolation beyond the scales of strong lensing datapoints. Since Umetsu et al. (2012) do a combined

---

[6]We give the values for an overdensity of $\Delta = 200$. The conversion to Umetsu et al. (2012), who use $\Delta = 132$, is $c_{132} \sim 1.2 c_{200}$.

strong and weak lensing analysis constraining the profile on a much larger scale than our work can do, confidence intervals for these two parameters are smaller than ours and their conclusions are much more firm. Regarding results of MACSJ1206.2-0847's mass–concentration relation we therefore refer the reader to the work of Umetsu et al. (2012).

Results for galaxy halos tracing the cluster–substructure

Using the F160W flux of the galaxies and scaling relations, the mass distribution of the galaxies is described as a function of the two (free) parameters, the velocity dispersion of GR σ_{GR}, and the normalization of the truncation radius scaling $r_{\mathrm{t},1''}$. This truncation scale $r_{\mathrm{t},1''}$ is not to be confused with $r_{\mathrm{t,GR}}$, which gives the truncation radius for galaxy GR and is shown in Fig. 7.7.
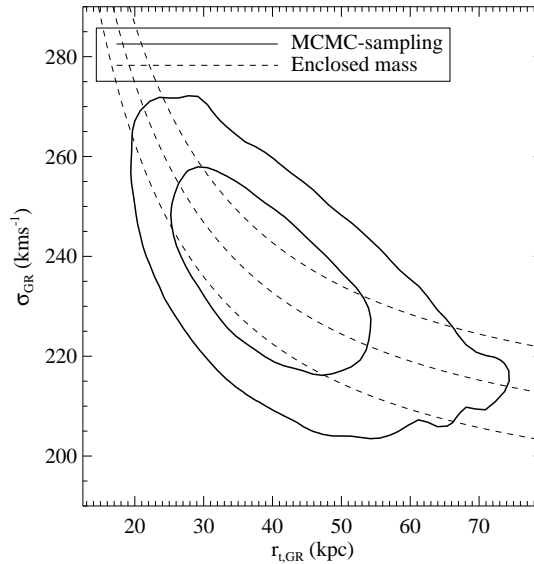
Figure 7.7: Here we show the probability contours for the 2 parameters governing the profile of the GR for the point source modeling: The truncation radius $r_{t,GR} = r_{\mathrm{t},1''}(\sigma_{\mathrm{E,GR}}(186\mathrm{kms}^{-1})^{-1})^{1.333}$ and the velocity dispersion of the GR $\sigma_{\mathrm{E,GR}}$. We also show the best fit for the enclosed mass within an effective radius as dashed lines, which gives a radius of $\mathrm{R_{mass,eff}} = 26.6\mathrm{kpc}$ and a enclosed mass of $M(< R_{\mathrm{mass,eff}}) = 7.3 \pm 0.6 \times 10^{11}M_{\odot}$ for the GR.

For these 2 values, we get the most likely values of: $r_{\mathrm{t,GR}} = 41^{+34}_{-18}\mathrm{kpc}$ and $\sigma_{\mathrm{GR}} = 236^{+29}_{-32}\mathrm{kms}^{-1}$. We apply the Faber-Jackson relation and show the velocity dispersions for all cluster members galaxies as a histogram in Fig. 7.8.

Since the lenses' impacts scale like $\propto \sigma^2$, most of the low velocity dispersion galaxies have a minor influence on the lensing signal. There is however a secondary effect, i.e. that the deflection angle that a galaxy can impose on the LOS to a multiple image position depends also on the transverse distance to it. We therefore now weight each cluster galaxy by its deflection angle (it imposes on all multiple images) and obtain the effective velocity dispersion histogram for the cluster members. It shows that the major impact is caused by galaxies with velocity dispersion between $100\mathrm{kms}^{-1}$ and $200\mathrm{kms}^{-1}$ (55% of cluster galaxies light deflection for multiple images) or $250\mathrm{kms}^{-1}$ (60%).
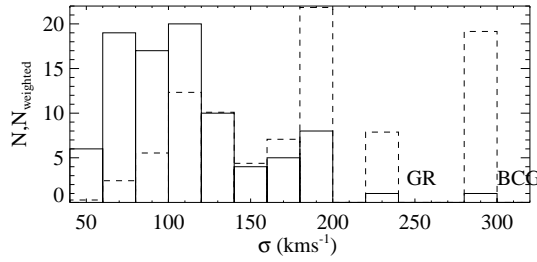
Figure 7.8: The velocity dispersion distribution for the galaxy cluster MACSJ1206.2-0847 is shown here for the best fit. Marked are the brightest cluster galaxy (BCG) and the second brightest galaxy (GR) which is used as a reference for the Einstein radius scaling in this work. For the same galaxies, the dashed histogram gives the weighted velocity dispersion distribution. As a weight, the mean deflection angle of a galaxy on all multiple images is used. As can be seen, the galaxies with lower velocity dispersions get down-weighted, meaning that they contribute on a minor level to the summed galaxies' lensing signal. The BCG has a velocity dispersion of $\sim 290 \mathrm{kms}^{-1}$ from the best fit scaling law. This agrees with Sand et al. (2004) who measure a stellar velocity dispersion of $\sigma \sim 250 \pm 50 \mathrm{kms}^{-1}$ in the central $\sim 1.5''$ of the BCG.

For the galaxies, we get the following scaling law on a 95% CL basis:

$$r_{\mathrm{t},1''} = 31^{+36}_{-14}\mathrm{kpc} \left(\frac{\sigma}{186\mathrm{kms}^{-1}} \right)^{\frac{4}{3}} \quad . \tag{7.15}$$

We translate the output of the MCMC sampling for the truncation radius of a galaxy with $1''$ cosmology free Einstein radius into (1σ and 2σ) confidence contours for σ_{GR} and $r_{t,\mathrm{GR}}$ and show them in Fig. 7.7. If we would be able to constrain only the mass $M(< R_{\mathrm{m}})$ within one scale R_{m} (as it is the case for strong lensing analysis of galaxies with one multiple image or one Einstein radius only) then the contours would extend to infinite truncation radius and also smaller minimum value, given by Eq. 7.4 as

$$\sigma^2 = \frac{GM(< R_{\mathrm{mass,p}})}{\pi} \left[R_{\mathrm{mass,p}} + r_{\mathrm{t}} - \sqrt{R_{\mathrm{mass,p}}^2 + r_{\mathrm{t}}^2} \right]^{-1} \quad . \tag{7.16}$$

Hence the contours in Fig. 7.7 demonstrate that the degeneracy between the two free parameters is broken (albeit not yet completely). This implies that not only the enclosed mass at some radius but also the gradient of the mass profile at this radius must be constrained by the observables, i.e. there must exist a scale $R_{\mathrm{mass,p}}$, where the profile is best determined, i.e where the enclosed mass is most equal for all σ_{GR} and $r_{t,\mathrm{GR}}$ pairs of the Chain output. We use Eq. 7.4 for all MCMC sample output pairs and find this scale to be $R_{\mathrm{mass,p}} = 4.7''\widehat{=}26.6\,\mathrm{kpc}$. The enclosed mass at this scale becomes $M(< R_{\mathrm{mass,p}}) = 7.3 \times 10^{11}M_{\odot}$ for the most likely σ_{GR} and $t_{t,\mathrm{GR}}$ pair. The curve of this constant enclosed mass is added as thick dashed line in Fig. 7.7. As expected it traces the degeneracy in the σ_{GR} and $r_{t,\mathrm{GR}}$ parameter space.
We then use Eq. 7.4 at this fixed enclosed mass radius and calculate the mass within $R_{\mathrm{mass,p}} = 4.7''$ for each pair in the MCMC sample. From this distribution of enclosed masses, we take the central 68 % as the error interval and get an enclosed mass of $M(< R_{\mathrm{mass,p}}) = 7.3 \pm 0.6 \times 10^{11}M_{\odot}$ at the fixed enclosed mass radius of $R_{\mathrm{mass,p}} = 4.7''$. These 68% upper and lower confidence values are plotted as dashed lines in Fig. 7.7.
Thus we conclude that our lens model is indeed not only sensitive to the total mass associated with galaxies but also to the size of the galaxy dark matter halos. There remains a degeneracy between halo velocity dispersion and truncation radius at a level of a factor of 2

for the truncation radius. For the reference halo within radius $R_{mass,p} = 4.7'' \widehat{=} 26.6 \, kpc$ the enclosed mass is $M(< R_{mass,p}) = 7.3 \pm 0.6 \times 10^{11} M_\odot$

For galaxies with different luminosity and thus velocity dispersion and truncation radius the radius where the mass is best known and the mass within this radius scales like $R_{mass,p} \propto r_t/r_{tGR}$ and $M(< R_{mass,p}) \propto \sigma^2 r_t/(\sigma_{GR}^2 r_{tGR})$.

To constrain the truncation scaling even further, we need to trace the lensing signal at various galaxy distances more densely. This is achieved with the pixel by pixel image reconstruction of the giant arc since every pixel has a different distance to the several centers of the surrounding galaxies.

7.7 Strong lensing modeling of the full surface brightness of the giant arc and its counterimage

We aim to further constrain the scaling relation for the truncation radius in this section. For that, we take a different approach, reproducing the full surface brightness of the giant arc and its counterimage. The full surface brightness not only contains information about the deflection angle, but also about its derivative, making it a good tool to explore galactic halo truncation in this system.

We use data from the F435W, F606W and F814W bands for the extended image reconstruction. We take different filters to minimize effects of light pollution of the surrounding galaxies. The cluster galaxies are significantly dimmer in the F435W filter, therefore minimizing possibility of galaxy light disturbing the arc light. Since the arc is already faint in this filter (The average signal–to–noise ratio in the used cluster area is ~ 0.5), we do not consider even bluer bands. We also include a redder filter (F606W) in which the arc but also the surrounding galaxies become brighter. We add the F814W filter with an even brighter arc. In this filter the systematic uncertainty from the subtraction of the surrounding galaxies' light gets comparable to the noise in the arc region, hence we refrain from investigating even redder bands. We apply GALFIT from Peng et al. (2010) to subtract the light of the surrounding galaxies G1 to G5, see Fig. 7.9. For the F435W and F606W-filter data, we fit a de Vaucouleurs profile (de Vaucouleurs, 1948) as a light model to the data and subtract it. For these 2 filters, the subtracted fluxes at the position of the arc are small compared to the intrinsic noise of the images for these pixels, so the impact of the exact details of the subtracted galaxy's light model are small. This is not the case for the F814W filter, therefore we create a best-fit de Vaucouleurs, a best-fit Sérsic (Sérsic, 1963) and a best-fit King profile for galaxies G1 to G5. From these 3 light models, we create a mean model and subtract that from the observed image. To account for the systematic error introduced by the light subtraction in this filter, we add the difference of the maximum and minimum value in each pixel for this 3 models to the error image derived before. We limit the analysis to a small region around the arc and its counterimage for computational reasons. This masked region is shown in Fig. 7.9.

The region is chosen by eye based on the arc visible in the F814W filter and used in all 3 bands.

As a systematic test, we choose the region to be reconstructed also by a signal–to–noise larger than 2 cut on the F814W frame. Before the modeled area is selected, the signal–to–noise map is block–smoothed with a length of 7 pixels. This leads to a slightly different selection of the modeled region. The changes introduced on the truncation law by changing the mask however are small, as described below.

(a) (b)
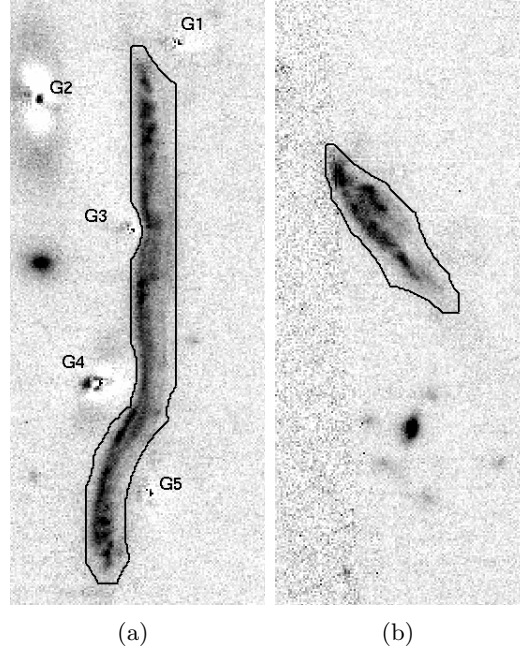
Figure 7.9: This frame shows the used region around the giant arc 7.9(a) and its counterimage 7.9(b) in this galaxy cluster. The mask is outlined in black. The underlying image is the F814W observed image for this cluster. The galaxies marked with G1 to G5 in Fig. 7.9(a) have been subtracted to minimize possible contamination of the arc light from the galaxies. One pixel corresponds to $0.05''$. North is up and east is left.

For the source reconstruction, we use a 9×9 pixel grid with a free pixel scale and source plane position, therefore the physical size of the reconstructed source is unrestricted by the number of source pixels. We compare different numbers of source pixels later on. For details of the extended surface brightness reconstruction, see Suyu et al. (2006); Suyu & Halkola (2010). It uses a linear inversion method (Warren & Dye, 2003) with curvature regularized source in a Bayesian framework (Suyu et al., 2006). We search for the most probable solution of the nonlinear lens mass parameters by maximizing the posterior in reconstructing the source (see, Eq. 11 of Suyu & Halkola 2010). The lens parameter space is sampled by MCMC methods. We tried both the curvature and gradient forms of regularization, and find that the resulting lens parameters are insensitive to the choice of regularization.

We now concentrate on the galaxies G1 to G5 around the arc which are already subtracted in Fig. 7.9. We fix all parameters (shear, cluster halo, source redshifts, galaxy parameters) to its best-fit values from Sec. 7.6.2, and now only model galaxies G1 to G5. For the galaxies G1, G2, G4, and G5, we allow each galaxy its own orientation and Einstein radius, keeping a joint truncation scaling law following Eq. 7.13 for these galaxies. The values derived in Secs. 7.6.1 and 7.6.2, used as starting values, are stated in Table 7.4.

We do not enforce the scaling law on G3, since it is doubtable whether it is a cluster member or not (it has a different photometric redshift and is formally not in our cluster member catalog). Therefore G3 is modeled with 3 free parameters: its orientation, Einstein radius and truncation radius. We obtain a best fit model using this 12 free parameters, optimizing the F435W, F606W and F814W filter data simultaneously.

The best-fit data, model and residuals for each of the 3 filters are shown in Figs. 7.10, 7.11

Table 7.4: Galaxies G1 to G5; results from the point-like model in Sec. 7.6.2

	z	$\Theta_1{}^1$	$\Theta_2{}^1$	q	$\Theta_{\rm pt}$	$\sigma_{\rm pt}$	$r_{\rm t,pt}$	M_B
		($''$)	($''$)		($°$)	(kms^{-1})	(kpc)	
G1	0.4449^2	21.592	5.996	0.79	18.5	121^{+16}_{-15}	13^{+15}_{-6}	-19.46
G2	0.46 ± 0.06^3	17.846	4.499	0.68	-47.3	190^{+26}_{-25}	24^{+28}_{-11}	-21.06
G3	0.53 ± 0.04^3	20.365	1.021	0.91	-68.9	143^{+19}_{-20}	16^{+19}_{-8}	-
G4	0.4380^2	19.473	-3.083	0.80	25.5	139^{+19}_{-19}	16^{+18}_{-7}	-19.94
G5	0.4446^2	20.862	-6.007	0.71	-74.9	104^{+14}_{-14}	11^{+12}_{-5}	-18.94

The errors give 95%c.l., derived from the respective errors in Sec. 7.6.2. M_B is measured independently from the HST photometry, assuming a galaxy redshift of z=0.44 [1]relative to the center of the BCG at 12:06:12.134 RA (J2000) -08:48:03.35 DEC (J2000) [2]spectroscopic redshift [3]photometric redshift estimate, 95% confidence

Table 7.5: most likely values and errors for the full surface brightness model of the arc and its counterimage

	$r_{\rm t,1''}$	Θ	σ	$r_t{}^1$
	(kpc)	($°$)	(kms^{-1})	(kpc)
G1	$4{*}34.2^{+1.2}_{-1.2}$	$-1.5^{+3.3}_{-3.7}$	130^{+10}_{-11}	21^{+4}_{-4}
G2		$-49.9^{+0.8}_{-0.8}$	165^{+2}_{-2}	29^{+2}_{-2}
G4		$-1.4^{+2.3}_{-2.3}$	$143.1^{+1.2}_{-1.2}$	$24.1^{+1.5}_{-1.5}$
G5		$-41.2^{+2.5}_{-2.7}$	$114.9^{+1.5}_{-1.5}$	$17.9^{+1.5}_{-1.5}$

Given are the 95% c.l. errors. The best fit cluster model from Sec. 7.6.2 is used as the cluster model. [1]calculated for the galaxies from the scaling law

and 7.12.

The statistical error is estimated again using a MCMC sampling of the parameter space. The most likely values and the errors for $r_{\rm t,1''}$ and the truncation radius for each of the galaxies can be seen in Table 7.5.

The truncation for the individual galaxies is still following Eq. 7.13 with $\sigma^\star = 186 {\rm kms}^{-1}$. For every galaxy we give its most likely values and the 95% c.l. errors. The truncation uncertainties for each of the galaxies are derived from the uncertainties on the Einstein radii and the truncation scaling law. Especially by comparing Tables 7.4 and 7.5, we note that the truncation scaling amplitude and the Einstein radii for the galaxies agree within the errors, but giving tighter constraints from the extended image reconstruction. The orientations of the galaxies in Tables 7.4 and 7.5 change by ≈ 20 to $30°$, meaning that there is a misalignment between light and total mass for these galaxies. This misalignment value is slightly higher than the $\approx 18°$ found by Bolton et al. (2008b) on isolated early type strong lensing galaxies. Suyu & Halkola (2010) quote a misalignment of their satellite light and dark matter major axis of about $50°$. Knebe et al. (2008) show from N–body simulations that satellite halos as a whole prefer to be radially aligned with respect to the centers of their host halos, but not the satellites' inner parts (which predominantly trace the light distribution). This leads to a misalignment between light and dark matter of satellite galaxies. Our misalignment is not as high, but nevertheless it would be worth to study how tidal effects can alter the major axis of dark matter halos.

In Fig. 7.13 the observed arc (Fig. 7.13(a)) and its counterimage (Fig. 7.13(b)) are shown in the left column and the top row of the middle column; alongside with this, the same is

$$(a) \qquad (b) \qquad (c)$$
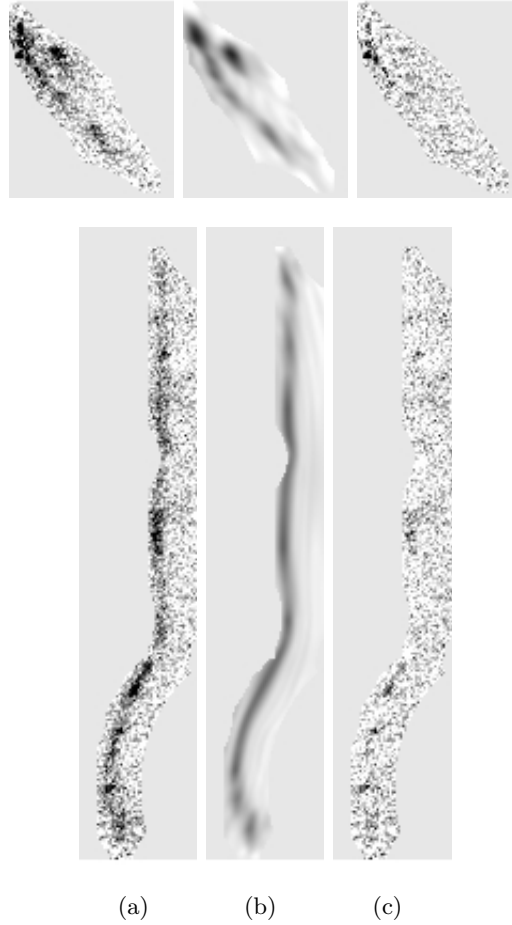
Figure 7.10: The arc and its counterimage reconstruction in the F435W filter, from left to right are shown the data, the model and the residuals. The top row shows the counterimage, the bottom row shows the giant arc. The levels of gray are the same in each image. For this figure, a source size of 20×20 pixels is used.

shown for a replacement of the arc and its counterimages with its full surface brightness reconstruction from its best-fit models in the left column (Fig. 7.13(f)) and the bottom row of the middle column (Fig. 7.13(e)). The angular scales are given in the figures. The reconstructed source can also be seen in this Figure as the two panels in the middle column (Figs. 7.13(c) and 7.13(d)). It is fully lensed into the counterimage and only partly lensed into the arc itself. There are 2 versions of the source, one with 50×50 pixels, giving a resolution superior to HST/ACS and a 25×25 pixels source, giving the same source as it would be observed at approximate HST/ACS resolution. Both sources show the same field of view of $0.94''$ in x and $1.42''$ in y direction, respectively.

To estimate the magnification of the counterimage, we map the masked area in Fig. 7.9(b) ($A_{\mathrm{CI}} = 6.3\mathrm{arcsec}^2$) back into the source plane and get an area of $A_{\mathrm{sr}} = 1.1\mathrm{arcsec}^2$. Therefore, the magnification of the counterimage is $\mu_{\mathrm{counterimage}} = 5.8$. We repeat this with the signal-to-noise based mask mentioned above ($A_{\mathrm{CI}} = 5.2\mathrm{arcsec}^2, A_{\mathrm{sr}} = 0.9\mathrm{arcsec}^2$) and get the same value for the magnification. Also, a direct calculation of the Jacobian matrix at the position of the counterimage gives a similar value.

While the above statements are made for the best fit cluster model we now marginalize

(a)   (b)   (c)
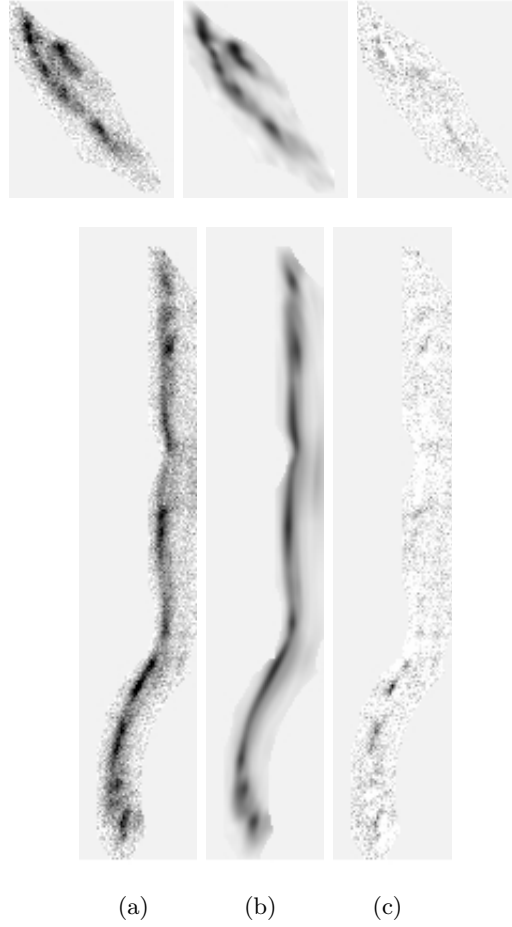
Figure 7.11: same as Figure 7.10, this time for the F606W filter.

over the variety of cluster distributions compatible with the observations. To estimate the uncertainty related with the cluster model, we repeat the extended model analysis for 30 random cluster representations. These representations are taken from the MCMC sampling calculated in Sec. 7.6.2 to estimate the error. The results are presented in Table 7.6.

We see that the errors on the parameter estimates are increased compared to Table 7.5 by taking the uncertainties from the cluster model into account. For the truncation, we still get tighter constrains than the point-like model described in Eq. 7.15 in Sec. 7.6.2. We get:

$$r_{\rm t} = 35 \pm 8 {\rm kpc} \times \left(\frac{\sigma}{186 {\rm kms}^{-1}} \right)^{\frac{4}{3}} \quad .$$

The velocity dispersions and truncation radii for galaxies G1, G2, G4 and G5 for the different clusters are plotted in Fig. 7.14.

Tests for systematic errors

The statistical error for the truncation scaling scale in this galaxy cluster is on the order of 25%, making this method in principle a good tool to study truncation of galaxies.

We now investigate the robustness of the truncation and Einstein radii results derived in

(a)   (b)   (c)
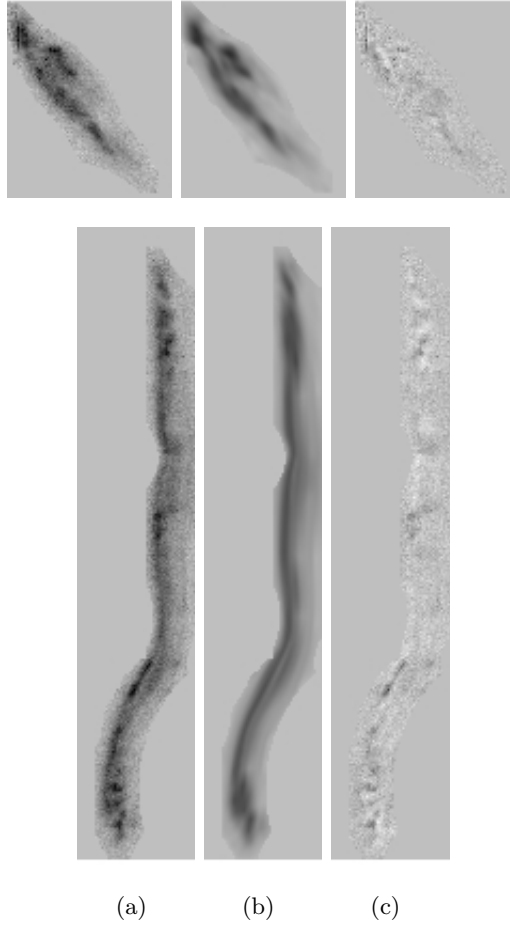
Figure 7.12: same as Figure 7.10, this time for the F814W filter.

Sec. 7.7 against possible sources of systematic errors. Possible systematic effects might stem from the treatment of the data of the filters or the frames itself, the analyzed arc region, the number of source pixels or the forced scaling law. First, we repeat the analysis in each of the filters individually. The results for the different filters are summarized in Table 7.7: All values agree with each other within the 95% c.l. intervals, implying that the surface brightness distribution in different filters gives consistent results regarding the halo truncation. Since the F435W band data have lower signal to noise for the arc than the data in the two redder filters considered in this work, the best fit parameters for the the model using all 3 filter data simultaneously are driven by the two redder bands.

Next, we change the investigated region around the arc based on a 2σ cut of a smoothed signal to noise map in the F814W filter. We again use the data of all three filters at the same time. For the mask based on the signal to noise level we get slightly different but consistent values for the truncation scale and the individual Einstein radii, see Table 7.7("mask2").

Next we use different numbers of source pixels. For the analysis, we use only the F814W filter and the standard mask. Starting from a 8×8 pixel grid and going up to a 13×13 grid, we calculate the best fit for each model. The results are again given in Table 7.7("sr pix"). We get a systematic uncertainty from the source pixel size comparable to the statistic
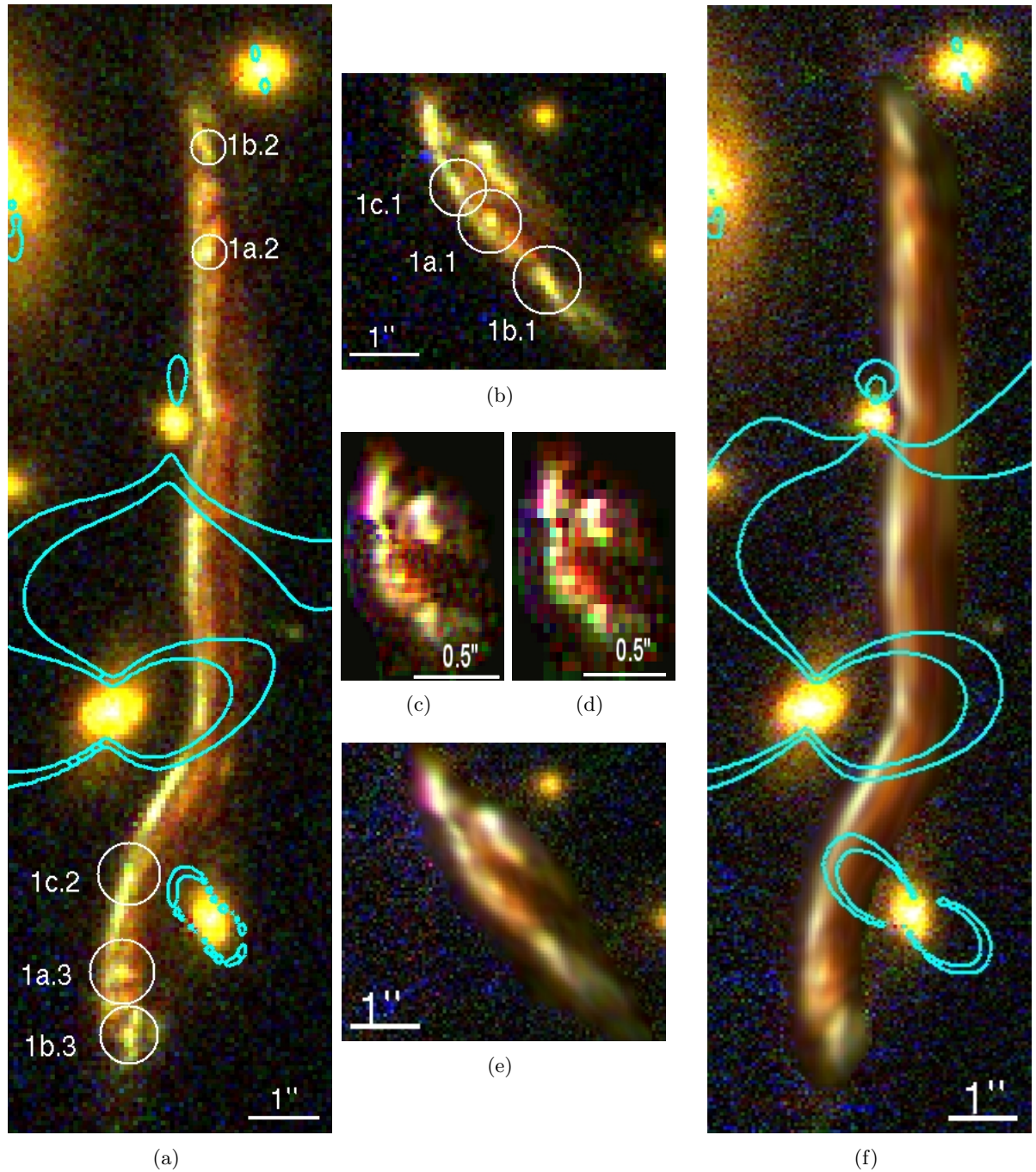
Figure 7.13: This figure shows, from left to right: The observed arc on the left. In the middle, from top to bottom: The observed counterimage, the reconstructed source with different resolutions and the model counterimage. On the right: The model arc. All images are combinations of the F435W, F606W and F814W bands, respectively. On the left, the numbers mark the multiple image input positions on the arc for the point-like model. We overplot the critical line structure in cyan on the left for the point-like model, on the right for full surface brightness reconstruction, respectively. The critical lines are calculated from a pixelated magnification map, the lines define regions above a absolute magnification value of 100, not taking parity into account. For the sources, the left source (7.13(c)) shows the source galaxy at a 50 pixel grid, giving a better than HST resolution, the right hand source (7.13(d)) shows the same source at approximate HST resolution.

Table 7.6: most likely values and errors for the full surface brightness model of the arc and its counterimage, taking different cluster models into account

	$r_{t,1''}$ (kpc)	Θ (°)	σ (kms^{-1})	r_t (kpc)
G1	4*35 ± 8	1.2 ± 20.6	128 ± 18	22 ± 7
G2		−47.0 ± 6.1	165 ± 6	30 ± 6
G4		9.3 ± 17.6	140 ± 6	24 ± 6
G5		−45.3 ± 19.1	124 ± 13	20 ± 4

From the MCMChain used to calculate the errors in Sec. 7.6.2, 30 random cluster representations are drawn. The analysis outlined for the best-fit cluster model is repeated for each of the random cluster models. The errors give the r.m.s errors on the parameters from this different cluster models.

uncertainties for the best fit cluster model when we fix the cluster potential. We verify that this is also true for much different numbers of source pixels. Using a 25×25 and 30×30 pixel grid and get values consistent with the ones stated in Table 7.6. Recent spectroscopic results indicate that G3 could be a member of the galaxy cluster. Hence we repeat the above outlined analysis including G3 as a cluster member allowing for a free central velocity dispersion and orientation. Doing this, there is no change in the truncation scaling or a decrease of the errorbars.

Finally we investigate how the truncation results depend on the assumed Faber-Jackson index δ. We use $\delta = 0.25$ instead of $\delta = 0.3$, still keeping $\epsilon = 0$. We restart the modeling for the point-like images, fixing the global parameters and then turn again to the extended image modeling. The corresponding truncation radii are shown in the last column of Table 7.7("FJ,$\delta = 0.25$"). Here, the truncation law gets:

$$r_{\mathrm{t}} = 41.8\mathrm{kpc} \times \left(\frac{\sigma}{186 \mathrm{kms}^{-1}} \right)^2 \quad .$$

The individual velocity dispersions and derived truncation radii, however agree with the ones derived before within the errors, see Tables 7.6 and 7.7. This means, there is no indication for the preferred exponent of the scaling law in this work since both scaling laws give similarly good fits.

Our tests show that the systematic errors are smaller than the ones from the uncertainty of the cluster potential, making our estimates robust with respect to systematic effects. Summarizing we conclude that if we vary the weighting of the extended image input data (SFB in different filters), the masking regions or modeling details as the assumed Faber Jackson index then these changes the estimated halo sizes less than our "statistical errors" due to different global halo models from the MCMC sample.

7.8 Discussion & conclusion

7.8.1 Lens modeling and cluster mass distribution

Using positions of multiply imaged galaxies we measured the mass distribution in the center of MACSJ1206.2-0847 based on a parameterized model, where the smooth dark matter was described with an elliptical NFW-profile and the matter traced by cluster galaxies was
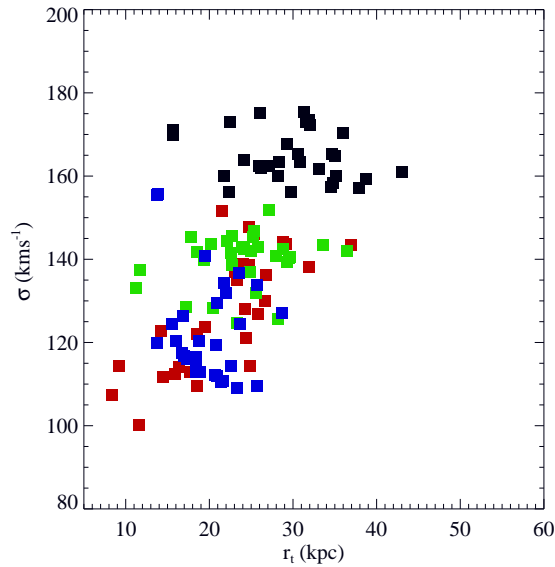
Figure 7.14: The velocity dispersions and calculated truncation radii for the galaxies G1, G2, G4 and G5 for the different cluster realizations. Each cluster representation has one entry for each galaxy. The color coding is the following: red: G1, black: G2, green: G4, blue: G5.

described with elliptical truncated isothermal spheres. Using scaling relations between luminosity and velocity dispersion and between luminosity and truncation radius, the essential halo parameters (velocity dispersions and truncation radii) of all dark matter halos are modeled with just 2 free parameters. The best fit model reproduces the observed multiple image positions with a mean accuracy of $0.86''$. The level of the positional mismatch is in agreement with expectations from unaccounted substructure or LOS contamination. For the same cluster Zitrin et al. (2012b) get a slightly higher value of $\approx 1.3''$ for the average image–plane reproduction uncertainty per image.

In general the match of multiple image position seems to depend on the number of multiple images that have been identified (Zitrin et al., 2011; Richard et al., 2010b; Limousin et al., 2008; Halkola et al., 2006). Given the number of multiple image systems a mean image plane distance below $1''$ is a rather good value.

Finally we found out that the model becomes better and requires a more reasonable value for the external shear if we account for the intra-cluster light which has an almost rectangular shape and a major axis in the direction of the major cluster axis, indicating stripped stars. This offers prospects to constrain the properties (e.g.. mass) of the intra cluster light component, which is however beyond the scope of this work.

Our total mass profile agrees with that from the previous work of Zitrin et al. (2012b) and Umetsu et al. (2012). Regarding values for concentration and scale radius for the total cluster mass distribution we refer the reader to the work of Umetsu et al. (2012) since in this work the mass profile has been constrained on much larger scale (using strong- and weak-lensing shear and magnification information).

In addition to previous work we pay special attention to match the extended surface brightness distribution of the giant arc and its counterimage as observed in the F435W-, the F606W- and the F814W-filters. This helps us to constrain the velocity dispersion and truncation

Table 7.7: Parameter estimates, systematic tests of the full surface reconstruction

		F435W[1]	F606W[1]	F814W[1]	mask2	sr pix[2]	FJ,$\delta = 0.25$
$r_{t,1''}$	(kpc)	$35.1^{+6.3}_{-4.7}$	$36.0^{+2.1}_{-2.0}$	$36.9^{+2.2}_{-2.0}$	35.6	34.9 ± 0.9	41.8
$\frac{\alpha}{\delta}$		$\frac{4}{3}$	$\frac{4}{3}$	$\frac{4}{3}$	$\frac{4}{3}$	$\frac{4}{3}$	2.00
σ_{G1}	(kms^{-1})	115^{+5}_{-6}	$126.4^{+1.4}_{-1.4}$	$129.1^{+1.3}_{-1.4}$	124	124 ± 8	133
$r_{t,G1}$	(kpc)	18.2	22.6	21.6	20.1	20.2 ± 1.6	21.5
σ_{G2}	(kms^{-1})	161^{+6}_{-7}	161^{+2}_{-2}	166^{+2}_{-2}	164	162 ± 3	165
$r_{t,G2}$	(kpc)	28.4	31.1	30.1	29.3	29.0 ± 0.8	32.5
σ_{G4}	(kms^{-1})	132^{+4}_{-5}	$140.7^{+2.4}_{-2.5}$	$141.9^{+1.2}_{-1.2}$	139	140.7 ± 1.8	143
$r_{t,G4}$	(kpc)	21.9	25.9	24.6	23.7	24.1 ± 0.6	24.7
σ_{G5}	(kms^{-1})	$117.9^{+1.5}_{-1.5}$	$117.9^{+1.5}_{-1.5}$	$113.4^{+1.5}_{-1.5}$	119	117.9 ± 3.5	116
$r_{t,G5}$	(kpc)	19.3	20.8	18.0	19.3	19.0 ± 0.8	16.2

[1]The errors given are the 95 % c.l. on the input parameters
[2]given are the r.m.s. errors We omit errors for the truncation radii of the individual galaxies since these can be derived from the truncation law for the individual filters. We omit all errors for the mask2 and FJ,$\delta = 0.25$ models since these are similar to the ones stated in Table 7.5.

parameters of cluster galaxy halos considerably beyond the result obtained from our point source modeling alone. We ensured that the results are robust regarding modeling details and regarding the exact information used from the extended light distribution of the arc.

7.8.2 Halo velocity dispersion versus Faber-Jackson relation

The amplitudes for the luminosity vs velocity dispersion scaling law (and the luminosity vs truncation radius scaling law) were constrained without any reference to optical galaxy properties. We obtain for the relation between the apparent AB-magnitude in the $F160W$-filter and the halo velocity dispersion

$$m_{160,AB} = -8.333 \log(\sigma[\text{kms}^{-1}]) + 37.39 \quad . \tag{7.17}$$

In the above relation the value for the slope was assumed and the zeropoint determined. On the other hand it is known from field elliptical strong lenses that multiple image systems can be well reproduced assuming an isothermal total mass profile with an amplitude given by the central stellar velocity dispersion. This isothermality is measured out to two Einstein radii (Koopmans et al. (2006); Grillo et al. (2010); Eichner et al. (2012)). However, since Einstein radii of elliptical galaxies are typically of the order of the effective radius, the mass distribution is only measured out to one effective radius with strong lensing of field elliptical galaxies. This is the scale where the stellar mass is still dominating or at most the dark matter and luminous matter are of the same order. The lensing derived velocity dispersion in this work agrees also with measured stellar velocity dispersion for the BCG. Recent measurements also indicates an agreement of the lensing derived and measured velocity dispersion for GR.
We have shown in Sec. 7.6.2 that we constrain the mass profile of our cluster galaxies most strongly at a scale of ~ 5 effective radii. This is where dark matter dominates and thus we now can compare the halo velocity dispersion derived from lensing with the stellar velocity dispersion amplitude. An estimate for the stellar velocity dispersion amplitude can be obtained from the Faber-Jackson relation (Faber & Jackson, 1976) or the Fundamental Plane

(Bender et al., 1992).

Using the FJ-relation we proceed as follows: For all galaxies in our cluster member catalog we fit the spectral energy distribution (SED) using their full 16-filter photometry (see Fig. 10 of Postman et al. 2012) and assuming that they are at $z = 0.44$. We in this way obtain for each cluster member the SED-type and an estimate for the restframe absolute magnitude in the Bessel B-band, M_B (in the Vega system). We then use redshift evolution of the ellipticals fundamental planes mass to light ratio, which we then assume to be due to aging of stellar population (luminosity evolution). Saglia et al. (2010) measured this in the EDISC sample with cluster (and field) ellipticals and obtained an evolution of the mass to light ratio of cluster ellipticals of $\Delta \log M/LB = -1.6 * (1 + z)$ which gives a flux dimming by a factor of 1.8 from $z = 0.44$ to $z = 0$. We plot the luminosity evolved absolute B-band magnitudes of red cluster members versus their halo velocity dispersion in Fig. 7.15.
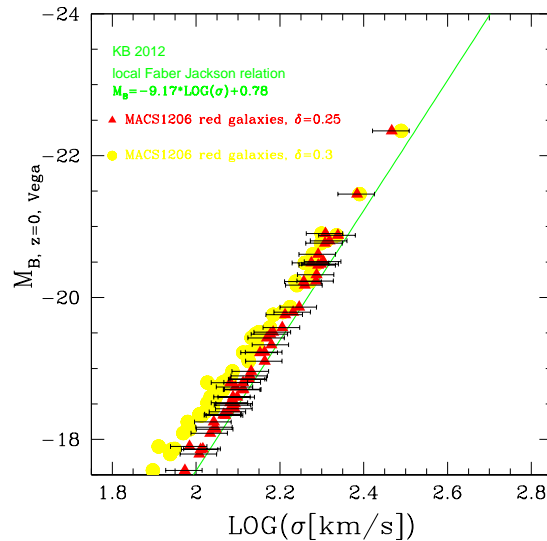
Figure 7.15: This Figure shows with a green line the local Faber-Jackson relation in absolute Vega B-Magnitudes vs the central stellar velocity dispersion from Kormendy & Bender (2012). The red triangles show the absolute B-magnitude of MACSJ1206.2 red cluster members corrected for the luminosity evolution to redshift zero by a factor of 1.8 versus the halo velocity dispersion obtained from the lens modeling. Note that we do not model each galaxy separately but only the amplitude of the relation for the assumed scaling law (in this case $\delta = 0.25$). The filled yellow circles show the same galaxies for the assumed scaling law of $\delta = 0.30$. The scatter around the $\delta = 0.25$-slope is due to the fact that the luminosity-σ scaling was applied using the NIR F160W-data and not the restframe B-magnitude obtained from the SED-fitting. The small scatter demonstrates that the SEDs of the red galaxies are fairly uniform.

(The velocity dispersion results for the $\delta = 0.3$ case are shown in yellow, and those for the $\delta = 0.25$ case in red). We do not change the halo velocity dispersion when evolving the cluster ellipticals to redshift zero, since at fixed stellar mass there is hardly any evolution of the stellar velocity dispersion from redshift 0.44 to zero according to the Fig. 22 of Saglia et al. (2010) and we assume the same to hold also for the halo velocity dispersion. We also draw errors of 10 % for the velocity dispersion to guide the eye, since this is the accuracy at which we can determine the amplitude of the luminosity versus velocity dispersion scaling. In the same Figure we added the local Faber-Jackson relation from Kormendy & Bender (2012)

as a green line. Its slope (in our notation) is $\delta_{FJ} = 0.273$ and thus in between our assumed $\delta = 0.25$ (red triangles) and $\delta = 0.3$ (yellow circles) cases. Both results agree within their errors with the Faber-Jackson relation, although the $\delta = 0.3$ case is shifted to lower velocity dispersions at the faint end. Stars in elliptical galaxies are dynamically colder than their dark matter halo (see Gerhard et al. (2001)) and their velocity dispersion is linked to the maximum circular halo velocity as $\sigma_{\text{stars}} = 0.66 v_{\text{circ}}^{\text{max}}$ (at least for the sample of ellipticals investigated in Gerhard et al. (2001), see their Eq. (2)). Therefore we would expect the halo velocity dispersion to be $\sigma_{\text{halo}} = 1.07 \sigma_{\text{stars}}$. Our best fit halo velocity dispersions are slightly smaller than those of the stars according to the FJ relation, but the approximate 10 percent error in measuring the velocity dispersion amplitude makes it also compatible that the halo velocity dispersion is a few percent larger than the stellar velocity dispersion. We would need a more precise global cluster (to decrease the error on the halo velocity dispersions) and spectroscopic stellar velocity dispersions for the red cluster members to measure the relation between halo and stellar velocity dispersion more precisely.

7.8.3   Halo truncation and stripped mass fraction

The truncation radius vs velocity dispersion relation for the halo of cluster members is

$$r_{\text{t}} = (35 \pm 8\text{kpc}) \left(\frac{\sigma}{186\text{kms}^{-1}} \right)^{\frac{4}{3}} \quad , \tag{7.18}$$

from the full surface brightness reconstruction of the extended arc and its counterimage, based on 4 nearby cluster galaxies. We get a very similar relation for the point-like modeling, which includes all cluster members statistically. We have shown in Fig. 7.8 that the galaxies contributing most strongly to our point-like halo truncation measurement have velocity dispersions between 100kms^{-1} and 200kms^{-1}. In the Eq. 7.18 the exponent $\frac{4}{3}$ is assumed to be known and the amplitude is determined. As can be seen in Fig. 7.16 the errorbars on this relation in the range of 100kms^{-1} and 200kms^{-1} are quite large, hence different exponents for the truncation vs velocity dispersion law fit the multiple image positions equally well, as long similar values for the actual truncation radii of the most relevant individual galaxies are predicted. If the exponent was changed to 2 the results are still very similar for the majority of galaxies and we get a similar fit quality. Our velocity dispersion vs truncation radius relation is shown in Fig. 7.16 where the error intervals obtained from the point like modeling are in red and the smaller errors for the extended SFB modeling are in blue.
Since the halo velocity dispersion is not a direct observable a more practical relation than Eq. 7.18 is to rephrase the upper equation as a function of apparent $m_{AB,160}$ magnitude,

$$\log r_t = \log(35 \pm 8) - 0.16 m_{AB,160} + 2.96 \quad , \tag{7.19}$$

such that it gives a recipe to model the galaxy halos also for other clusters at the same redshift. To obtain a redshift independent relation we transform Eq. 7.19 to relate the truncation radius of each galaxy directly to its absolute B-band magnitude (in Vega). We obtain:

$$\log r_{\text{t}} = \log(35 \pm 8) - 0.16 M_B - 3.372 \quad , \tag{7.20}$$

This equation holds for the red galaxies in Fig. 7.1. We now compare our results with previous work on the truncation of galaxies halos in clusters of galaxies: Halkola et al. (2007) do a
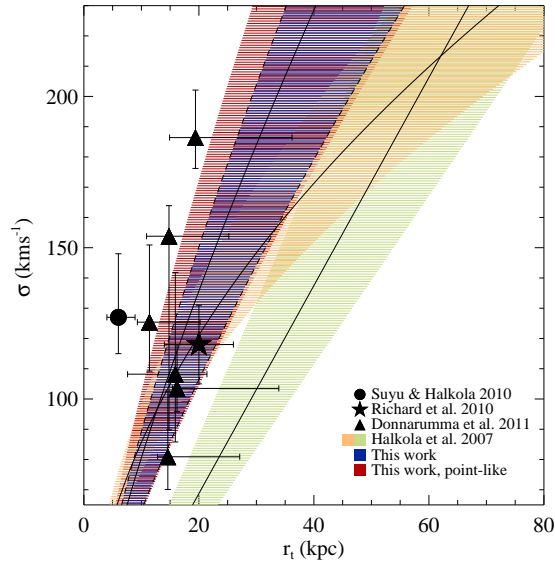
Figure 7.16: This figure shows our results for the halo truncation radius vs velocity dispersion for the point source modeling (red region marks the 68% confidence interval) and the SFB-modeling of the arc (best fit is the black line, and the 1 sigma confidence region is shown in blue). The triangles mark constraints (and their 1 sigma errors) for individual galaxies obtained by Donnarumma et al. (2011), the star marks the result for one galaxy from Richard et al. (2010a), the point is taken from Suyu & Halkola (2010). The light green and light orange marks the 1σ confidence intervals obtained from halkola for two different scaling relations, $r_\mathrm{t} \sim \sigma$ and $r_\mathrm{t} \sim \sigma^2$, analyzed in their work.

statistical analysis of all galaxies in the strong lensing regime of the cluster A1689. Although they include galaxies in the modeling with (Fundamental plane and Faber-Jackson) velocity dispersion estimates from about $300\mathrm{kms}^{-1}$ down to about $20\mathrm{kms}^{-1}$ (see Fig. 5 Halkola et al. 2006) in their sample it seems that their sensitivity for halo truncation is mostly due to massive galaxies with a velocity dispersion of $220\mathrm{kms}^{-1}$. This can be seen in Fig. 7.16 which shows that the halo truncation size for the two parameterizations ($s \propto \sigma$ and and $s \propto \sigma^2$) agrees for $\sigma = 220\mathrm{km/s}$ galaxies where the halo size then is equal to about 65kpc with a one sigma error of about $15\mathrm{kpc} - 20\mathrm{kpc}$. Besides this their Fig. 1 shows that their χ^2 starts to rise steeply only for halo sizes smaller than 30kpc. This implies that their result is in agreement with ours.

The work of Richard et al. (2010a) and Donnarumma et al. (2011) allows a more direct comparison to our results since they analyze a situation more similar to ours. Their cluster galaxies have mostly low velocity dispersion (triangle and stars in Fig. 7.16) and they typically have a projected distance to the cluster center of the order of $\approx 10''$.

Our median "lensing-weighted" cluster galaxy distance to the cluster center is $\sim 26''$ (the 4 cluster members close to the arc have a distance of $\sim 20''$ which is 6% of the virial radius of this cluster by Umetsu et al. (2012)). This means that our galaxy sample and that of Richard et al. (2010a) and Donnarumma et al. (2011) is likely to have undergone a similar amount of stripping (assuming that the central cluster density and the collapse state of their clusters is similar to ours). The results of Richard et al. (2010a) and Donnarumma et al. (2011) are inserted into Fig. 7.16 and are in agreement with ours.

Suyu & Halkola (2010) measure the individual truncation of a satellite halo embedded in a

group (for which we estimate a velocity dispersion of about 400kms^{-1} to 500kms^{-1} based on their lensing model) where the satellite is only $\sim 26 \text{kpc}$ away in projection from the group center. They estimate the velocity dispersion of the satellite galaxy to be around 120km/s and have a truncation radius of only $4 - 9 \text{kpc}$ at 95% c.l.. Their result shows that indeed halo truncation can be severe close to centers of groups (and thus even more for clusters).

With a different method, Limousin et al. (2007a) measure the truncation of cluster galaxies with weak lensing for 5 different clusters and get similar results within the errors. Pu et al. (2010) investigate 3 nearby group members using dynamical modeling. They use a common cutoff-radius for all three galaxies with velocity dispersions between $\sigma \approx 200 \text{kms}^{-1}$ and $\sigma \approx 300 \text{kms}^{-1}$, somewhat higher than our sample. Their best-fit value is $R_c = 60 \text{kpc}$ which would agree with our measurement if we extrapolate to higher velocity dispersions.

We compare our value for the truncation radius with the half mass radius derived in Limousin et al. (2009) from simulations of halo stripping in 2 numerically simulated clusters, one with a similar virial mass as MACSJ1206.2-0847. Our galaxy G4 in Table 7.6 has a truncation radius of $24 \pm 6 \text{kpc}$ and a R-band rest-frame luminosity of $L_{R,rf} \approx 3 * 10^{11} L_{R,\odot}$. At this luminosity, Limousin et al. (2009) get a half mass radius of $r_{1/2} \approx 20 \text{kpc}$ for a galaxy close to cluster center in projection, which agrees well with our result.

We can infer the amount of stripped dark matter for cluster galaxies if we compare their truncation radii with the truncation radii of the corresponding galaxies in the field. Brimioulle et al. (2013) measure a truncation radius of $s = 245^{+64}_{-52} h_{100}^{-1} \text{kpc}$ for a reference galaxy with $\sigma = 144 \text{kms}^{-1}$, with red SED and in underdense environments. For the same velocity dispersion our cluster galaxies have a truncation radius of $r_t = 25 \pm 6 \text{kpc}$. Consequently the ratio for the total halo mass in the field and in the cluster for this kind of galaxy are $M_{\text{tot,field}}/M_{\text{tot,cluster}} = 13.9^{+4.9}_{-4.4}$. In the last step we have assumed that "the velocity dispersion" (i.e. kinematics of stars and central dark matter particles) of a halo does not change when it is stripped during cluster infall. Models of massive galaxies Pu et al. (2010) indeed suggest that a change in the halo truncation radius (as long as it happens beyond $\sim 5 R_{\text{eff}}$) has no detectable influence on the stellar kinematics inside $\sim 5 R_{\text{eff}}$. (J. Thomas, private communication). The truncation radius for GR is ~ 5 times higher than the effective radius of this galaxy. Romanishin (1986) give a relation for the absolute B-band magnitude $M_B \sim -2.06 \log R_{\text{eff}}$. This means that R_{eff} drops faster with fainter M_B than r_t in Eq. 7.20, implying that the r_t/R_{eff} rises for smaller fluxes and hence stripping of the galaxies does also not affect the kinematics of the lower luminosity galaxies.

The large mass loss of the cluster galaxies (close in projection to the cluster center) agrees with results from numerical modeling of the stripping (see also introduction), which shows that mass losses up to 90% are common for cluster galaxies close to the cluster center (Warnick et al. (2008)).

If we assume that all cluster galaxies considered in our model have halo masses of only 10% of their infall mass then the total stripped mass amounts $M_{\text{stripped}} = 5.1^{+1.8}_{-1.5} \times 10^{13} M_{\odot}$ out to a projected radius of $\approx 100 \text{kpc}$. The total mass estimate at the same radius is $7.11^{+0.04}_{-0.03} \times 10^{13} M_{\odot}$. Within a projected radius of $\approx 400 \text{kpc}$, the ratio of stripped to total cluster mass gives values of 25 to 50%. This will be an upper value, since the fractional stripped galaxy halo masses will be smaller in the outskirts. Nevertheless it implies that a significant fraction of the smooth dark matter component in the cluster core originates from cluster members stripped during the formation and relaxation of the cluster.

Table 7.8: apparent magnitudes of the counterimage (CI) and modeled source (SR)in AB

Filter	F435W	F475W	F606W	F625W	F775W	F814W	F850LP	F105W	F110W	F125W	F140W	F160W
CI	22.20	22.14	21.73	21.52	20.92	20.76	20.39	20.25	20.06	19.93	19.81	19.72
SR	24.11	24.05	23.64	23.43	22.83	22.67	22.30	22.16	21.97	21.84	21.72	21.63

7.8.4   The SFB-distribution of the source of the giant arc

Since not all of the arc source is lensed into the giant arc – basically, all parts above image 1c.1 on the counterimage are outside of the caustic and therefore only imaged one time in the counterimage and not in the arc – only the observed counterimage can be used to obtain the source properties. The observed counterimage and the best-fit source model can be seen in Fig. 7.13, both at HST resolution and better than HST resolution. Comparing the observed counterimage and the source at HST resolution, the increase in the level of detail due to lensing in this case can be seen. The observed counterimage (Fig. 7.13(b)) and the high resolution delensed counterimage (Fig. 7.13(c)) reveal the magnification of the source due to lensing. The magnification is approximately equal to ~ 5.8, this corresponds to a flux brightening by about 2 magnitudes.

A three color representation of the counterimage in the F775W, F125W and F160W filters and an approximately delensed version of it is shown in Fig. 7.17. The filters are chosen to be equal to the restframe B, R and I band filters. The color image suggests that the source is a fairly inclined, spiral star-forming galaxy with a core hosting more evolved stars. Comparing with CANDLES results (Fig.2 of Wuyts et al. 2012) we conclude that the lensed galaxy is a fairly normal redshift one galaxy. Results of the 3D-HST project indicate that about half of the $1 < z < 1.5$ galaxies have H_α emission lines width with rest-frame equivalent widths for the detected galaxies within a $10\mathring{A}$ to $130\mathring{A}$ (van Dokkum et al. (2011)) and that star formation occurs inside out with H_α-emission lines in the outskirts of galaxies and continuum emission from their centers, Nelson et al. (2012). Thus it is likely that our source has emission lines, too. This makes the galaxy an ideal target for measuring the 2D kinematics with the ground based NIR IFUs of KMOS at the VLT.

In Table 7.8, the magnitudes of the counterimage and the source are stated. The increase in brightness due to the lensing effect makes this galaxy at $z = 1.036$ much easier to observe than the unlensed source would be.

(a)   (b)

Figure 7.17: Color images using the F775W, F125W and F160W frames, corresponding to approximate BRI restframe colors, left is the HST observation of the counterimage; right is the unlensed source at a pixel size observed by HST for the unlensed source. The unlensed source is convolved with a Gaussian function in each filter representing the approximate PSF. In the source plane $1''$ corresponds to 8.13kpc, we gain an increase in spatial resolution by the gravitational telescope of $\sim \sqrt{5.8}$. The images are false color images from the F775W, F125W and F160W frames, respectively

7.9 Galaxy lenses list

In this appendix, we present the list of derived galaxy lenses used for the strong lensing model in Table 7.9. We show the position relative to the BCG, the ellipticity and orientation and the best fit Einstein and truncation radius from the best-fit model presented in Sec. 7.6.2. The positions are again given relative to the BCG.

Table 7.9: Derived galaxy lenses

x^1 ($''$)	y^1 ($''$)	q	Θ_q ($°$)	σ (kms^{-1})	r_t (kpc)
0.000	0.000	0.59	14.6	296.3	57.8
-51.961	-18.520	0.85	28.2	235.7	42.6
52.028	-23.567	0.87	-47.1	196.6	33.4
70.454	-24.260	0.42	-78.3	191.3	32.2
79.369	-16.726	0.49	62.4	188.9	31.7
-75.133	-19.806	0.56	36.5	185.7	31.0
17.846	4.499	0.68	-47.3	182.3	30.2
16.918	-18.981	0.37	36.7	182.3	30.2
-19.523	-12.957	0.92	89.3	181.9	30.2
-58.427	-2.920	0.66	8.6	180.5	29.8
36.181	44.994	0.83	57.2	179.8	29.7
-27.249	52.149	0.53	58.0	174.4	28.5
-25.792	57.782	0.75	56.9	167.0	26.9
60.244	-20.431	0.77	28.4	165.9	26.7
65.420	45.366	0.24	-70.9	159.9	25.4

x^1	y^1	q	Θ_q	σ	r_t
-8.492	75.149	0.76	31.2	154.6	24.3
56.269	39.858	0.67	-88.2	147.2	22.7
-78.600	-29.236	0.81	62.5	146.7	22.6
-5.413	26.620	0.86	59.3	144.0	22.1
9.396	8.386	0.69	-10.1	135.6	20.4
19.473	-3.083	0.80	25.5	133.9	20.0
93.544	-8.950	0.61	-29.5	133.3	19.9
-8.863	-49.294	0.82	39.6	133.0	19.9
17.747	51.281	0.31	-6.5	130.1	19.3
-23.885	17.186	0.84	-8.0	128.2	18.9
-6.973	-48.796	0.55	-13.6	128.1	18.9
-1.892	7.503	0.67	34.0	124.3	18.2
10.517	-52.862	0.91	44.5	121.7	17.6
22.649	-53.029	0.94	-7.4	120.6	17.4
9.135	-16.001	0.56	67.1	117.3	16.8
-8.101	-1.448	0.77	-41.9	116.4	16.6
6.194	14.554	0.75	-37.1	116.4	16.6
21.592	5.996	0.79	18.5	115.7	16.5
59.033	14.592	0.76	54.0	114.5	16.3
-29.284	9.803	0.63	61.5	111.5	15.7
-9.271	-10.396	0.81	-52.7	111.5	15.7
67.743	5.471	0.48	-81.6	111.2	15.6
46.041	-9.524	0.75	83.3	110.8	15.6
-13.786	79.453	0.95	13.8	109.3	15.3
-52.979	-8.875	0.83	60.4	106.9	14.8
-66.483	-38.795	0.87	38.7	105.6	14.6
52.678	-9.056	0.82	-35.2	105.4	14.6
-9.375	-2.275	0.82	-17.6	105.2	14.5
-10.290	-55.387	0.57	-2.6	104.3	14.4
-72.341	-21.512	0.71	13.0	104.0	14.3
-27.184	9.263	0.46	39.5	102.2	14.0
-1.316	22.373	0.92	4.4	102.2	14.0
33.113	-24.055	0.78	27.2	100.8	13.7
-56.983	-13.861	0.79	19.6	100.5	13.7
20.862	-6.007	0.71	-74.9	98.9	13.4
77.397	-10.026	0.74	-76.1	97.9	13.2
-64.503	18.440	0.74	-66.3	97.6	13.1
-20.902	16.033	0.53	-34.5	96.0	12.9
-21.888	-34.820	0.86	16.5	93.7	12.4
-29.310	-23.851	0.82	-68.7	92.7	12.3
3.169	25.294	0.68	-1.7	92.3	12.2
-19.579	16.272	0.44	77.8	91.7	12.1
34.186	-5.002	0.54	-82.8	91.2	12.0
84.412	-3.159	0.90	67.9	89.5	11.7
-10.054	-32.007	0.92	76.0	85.3	11.0

Continued on next page

x^1	y^1	q	Θ_q	σ	r_t
-51.558	-28.504	0.63	-35.0	85.1	10.9
-11.110	-10.114	0.56	28.8	85.0	10.9
-56.052	-46.963	0.82	-29.5	84.0	10.8
-58.147	16.382	0.91	89.8	83.3	10.6
19.309	18.352	0.54	-55.4	82.6	10.5
-62.885	19.793	0.59	59.2	81.9	10.4
44.739	40.229	0.71	-82.0	78.1	9.8
-6.185	23.563	0.69	-4.0	77.7	9.7
-47.318	20.110	0.42	5.7	77.3	9.6
-42.827	-33.806	0.61	21.9	77.2	9.6
18.023	-83.677	0.58	65.9	76.0	9.4
44.578	-39.135	0.80	-89.8	75.7	9.4
45.326	-39.482	0.76	-40.3	75.7	9.4
-54.643	12.139	0.70	-40.9	75.7	9.4
-68.528	12.943	0.95	38.1	75.3	9.3
-8.039	-23.346	0.70	11.6	74.7	9.2
-63.008	9.546	0.18	-37.4	74.0	9.1
-20.924	34.030	0.37	41.5	71.6	8.7
-54.231	-35.225	0.82	-35.1	70.5	8.5
-25.998	7.123	0.54	33.7	68.1	8.1
-34.878	-43.036	0.49	71.2	67.7	8.1
55.964	-49.356	0.58	-83.0	64.8	7.6
28.577	28.456	0.82	0.9	64.7	7.6
26.103	-30.477	0.97	5.7	64.4	7.5
41.714	41.585	0.67	40.0	62.5	7.3
43.372	-11.300	0.70	-73.7	58.1	6.6
20.281	19.628	0.77	-9.3	57.2	6.5
0.946	32.097	0.77	11.2	53.1	5.8
-58.728	33.022	0.61	80.6	51.4	5.6
44.865	52.272	0.60	-11.5	45.3	4.7
55.581	-41.990	0.60	-87.2	42.8	4.4

---

[1]relative to the center of the BCG at 12:06:12.134 RA (J2000) -08:48:03.35 DEC (J2000)

Chapter 8

Summary & outlook

Summary

I used gravitational lensing to measure properties of the studied elliptical galaxies – especially regarding their dark matter properties.
For the inner mass profile, we study two exceptional gravitational lenses, SDSS J1538+5817 and SDSS J1430+4105. In both cases, the lensed background sources span a large radial range in the lens plane, allowing us to trace the total mass distribution over 3 and 6 kpc, respectively. For the inner mass profiles of SDSS J1538+5817 and SDSS J1430+4105 we adopt one component singular isothermal and power–law elliptical mass profiles and calculate best–fitting parameters and error intervals. We compare these one component mass profiles with other reconstructed mass profiles. For SDSS J1538+5817 we employ a non–parametric reconstruction of the inner mass profile, showing good agreement with the parametric profile. We reconstruct the inner mass profile of SDSS J1430+4105 using the full surface brightness of the lensed image, again giving consistent results. Furthermore, both galaxies allow us to disentangle luminous and dark matter from gravitational lensing alone, since the two matter components follow different, well–motivated radial profiles. For SDSS J1538+5817 we do this based on the observed total mass profile, and for SDSS J1430+4105 by a direct decomposition of the observed lensing signal. Specifically, we find the following:

- In both cases the observed multiple images can be reproduced well by simple parametric mass models for the lensing galaxy. The distance of the image positions predicted by the model and the input image positions is on the order of the pixel scale of the input frames, $0.05''$.

- For SDSS J1538+5817 well–constrained values are achieved for the Einstein radius of $R_{Ein} \sim 2.5\,\mathrm{kpc}$ and an enclosed total mass within this radius of $M_{Ein} \sim 8.2 \times 10^{10} M_\odot$. For SDSS J1430+4105 the values are: $R_{Ein} \sim 6.5\,\mathrm{kpc}$ and $M_{Ein} \sim 5.4 \times 10^{11} M_\odot$.

- We derive for SDSS J1430+4105 a total stellar mass of $M_{deV} = 8.8^{+1.3}_{-1.9} \times 10^{11} M_\odot$. From Bruzual & Charlot composite stellar population models with Salpeter initial mass function and stellar metalicity, we get a stellar mass of $M_\star = 5.6^{+0.8}_{-1.8} \times 10^{11} M_\odot$, meaning that the de Vaucouleurs mass agrees with a Salpeter IMF at solar metalicity. Using the same assumption as before we get for SDSS J1538+5817 a photometric mass of $M_{\star,Ein} = 7.6^{+0.4}_{-1.5} \times 10^{10} M_\odot$ within the Einstein radius. This agrees with the lensing derived total mass within the same radius.

- The projected dark matter fractions within the Einstein radius are $\frac{M_{tot}-M_{phot}}{M_{tot}} = 0.1^{+0.2}_{-0.1}$ and $\frac{M_{tot}-M_{deV}}{M_{tot}} = 0.40^{+0.14}_{-0.10}$ for SDSS J1538+5817 and SDSS J1430+4105, respectively.

- The 3D densities for the dark matter have similar values of $\rho_{dark} \sim 4 \times 10^7 M_\odot kpc^{-3}$ in the center for both galaxies at radii of $\approx 3\,kpc$. At the same radius, however, the luminous matter densities are $\rho_{lum} \sim 1.5 \times 10^8 M_\odot kpc^{-3}$ and $\rho_{lum} \sim 3.5 \times 10^8 M_\odot kpc^{-3}$ for SDSS J1538+5817 and SDSS J1430+4105. These values agree with values measured for member galaxies of the local Coma cluster with dynamical methods by Thomas et al. (2011).

- The stellar mass to light ratios of both SDSS J1538+5117 and SDSS J1430+4105 are determined by composite stellar population fits to the SDSS photometry. The comparison with lensing observed masses, combined with the observed luminosities, shows agreement with Salpeter IMF in both cases, disfavoring a Chabrier or Kroupa IMF.

In conclusion, systems such as the ones studied in this work are ideal candidates for the study of lensing derived enclosed masses and mass profiles. These mass profiles can be split into approximate luminous and dark matter components, using well-motivated models for both components. The direct decomposition of the lensing signal allows these components to be measured for distant galaxies. A comparison of the mass of the luminous component with the mass derived from stellar population fits to the observed photometry allows some constraints on the IMF.

Measurements of the dark matter halo sizes of distant galaxies are rare, since dynamical methods are not yet sensitive enough to achieve this. Hence, we rely on the gravitational lensing signal to study truncation of elliptical galaxies in a galaxy cluster. To measure the galaxy halo truncation in MACSJ1206.2-0847, we first build a model for the cluster mass distribution based on the observed multiple image systems using 12 image systems with 52 multiple images recently found in this cluster. We model the sizes of the cluster galaxies employing scaling laws based on the NIR fluxes. We can then derive the average truncation of the galaxy halos by optimization of these scaling laws. Based on that, we reconstruct the full surface brightness distribution of the giant arc and its counterimage in this cluster. We model the truncation of the cluster galaxies surrounding the arc separately, giving agreeing results for both approaches. In detail, we find:

- We get a mean distance of the model predicted multiple image positions from its input positions of $\sim 0.85''$. Considering the number of multiple images, this is a good value.

- The central, projected mass profile of MACSJ1206.2-0847 can be determined using strong gravitational lensing. We derive a mass of $M_{tot} \sim 7 \times 10^{13} M_\odot$ within a radius of 100kpc, which is in good agreement with other studies of this cluster.

- We reconstruct mass profiles for the individual galaxies assuming scaling relations with the F160W band flux of each galaxy, and keeping the normalizations of these scaling laws as free parameters. We refer these normalizations to one reference galaxy and calculate values of $r_{t,GR} = 41^{+34}_{-18} kpc$ and $\sigma_{GR} = 236^{+29}_{-32} kms^{-1}$. We constrain the mass distribution of cluster galaxies best at ~ 5 effective radii. Assuming passive luminosity evolution for the absolute B-band luminosity of the cluster galaxies, we show that our lensing derived velocity dispersions agree well with values given in Kormendy & Bender

(2012) for local elliptical galaxies.

- We reconstruct the full surface brightness of the giant arc and its counterimage by individually modeling the 4 cluster galaxies closest to it. For these 4 galaxies, we calculated values for the individual velocity dispersions that agree with those previously derived from the scaling relation. The truncation law also has a similar normalization with slightly smaller errorbars. We derive the following truncation law for cluster members when reconstructing the full surface brightness distribution of the arc:

$$r_t = (35 \pm 8\mathrm{kpc}) \left(\frac{\sigma}{186\mathrm{kms}^{-1}} \right)^{\frac{4}{3}}.$$

  This truncation law agrees with predictions from simulations and with other measurements carried out in dense environments. Testing different exponents of the truncation law gives agreeing results for the sizes of the individual galaxies within the error ranges, meaning that we cannot distinguish between different exponents.

- The above stated truncation law means that large fractions of the dark matter halos of the cluster galaxies in this cluster have been stripped from their galaxies when compared to field galaxies of the same velocity dispersion. Again, this agrees with expectations from simulations.

In summary, the investigated galaxies in MACSJ1206.2-0847 have shrunk significantly and consistently, derived from both point-like modeling of all multiple image systems as well as from the full surface brightness of the arc and its counterimage. This truncation mostly affects the dark matter halos, since it occurs several effective radii away from the galaxies' centers. In particular, the results for the sizes of the galaxies in the center of this cluster at z = 0.44 agree with results derived for other clusters at lower redshifts, e.g. Abell 1689 or the Coma cluster, indicating that truncation of cluster galaxies is already present at this redshift.

Outlook

The analyses carried out in this thesis are only performed on selected individual objects, thus giving only limited statistical significance. Applying the performed analyses on other galaxies and galaxy clusters with similar properties to increase the number of objects studied will be the natural next step for this work.

For the investigation of the central matter profile, three candidates have already been detected and preliminarily analyzed by Weidinger (2010). These candidates are: SDSS J0728+3835, SDSS J1250+0523 and SDSS J1630+4520. The multiple images span ranges of $0.6''$ to $1.6''$, and in the case of SDSS J1630+4520 up to $2.5''$, meaning that physical ranges of $\approx 2\,\mathrm{kpc}$ to $\approx 6\,\mathrm{kpc}$ are covered, and in the case of SDSS J1630+4520 even up to $\approx 10\,\mathrm{kpc}$. Hence, an analysis similar to the one carried out in Chapter 6 can be performed with these galaxies, estimating the dark and luminous matter distributions in the centers of these galaxies.

For the examination of the truncation of galaxies in galaxy clusters, again further candidates have to be found. Ideal candidates would be well–known, well–studied clusters with tight constraints on the cluster potential. These constraints could stem from an abundance of multiple image systems with known redshifts. We can expect the CLASH survey to fulfill these requirements due to its many photometric bands and large spectroscopic follow-up. Hence, systems similar to MACSJ1206.2-0847 can be searched for in other clusters observed by CLASH.

(a)   (b)
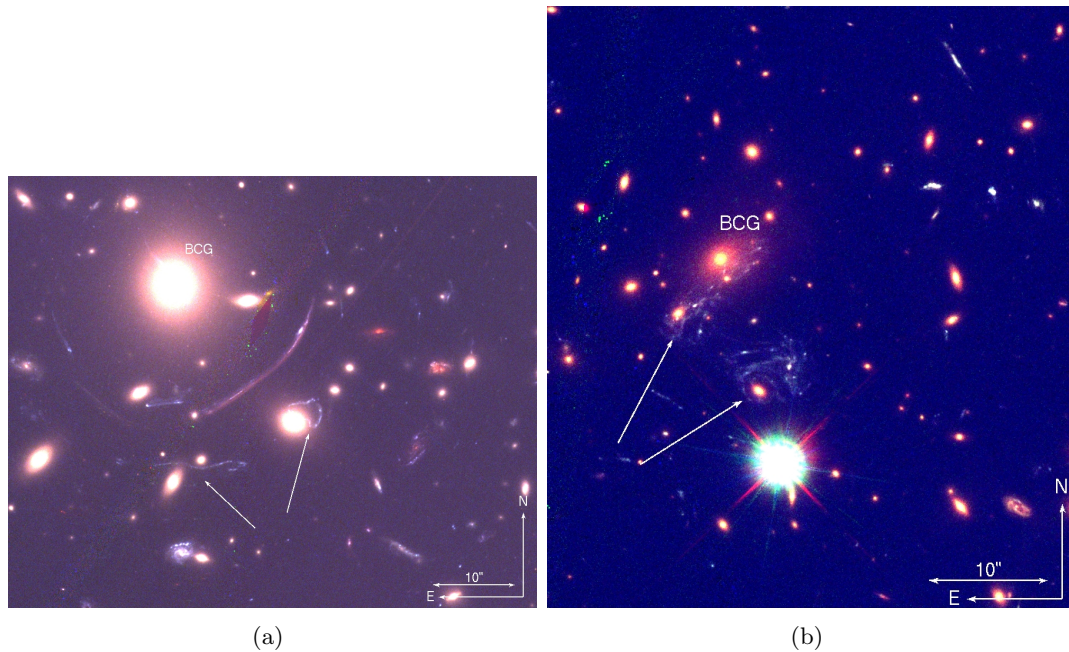
Figure 8.1: Abell 383 and MACSJ1149.6+2223: two candidates for truncation studies. On Abell 383, 8.1(a), two arcs are adjacent to cluster galaxies(marked with arrows) and can be investigated for their truncation similar to the work shown in this thesis. For MACSJ1149.6+2223 8.1(b) the situation appears even more promising, since two of the cluster galaxies(marked with arrows) are completely surrounded by the multiple imaged background galaxy.

Indeed two candidates emerge when inspecting the observed clusters: MACSJ1149.6+2223 and Abell 383, see Fig. 8.1. In MACSJ1149.6+2223, a background face on spiral galaxy at z=1.491 is lensed multiple times (Smith et al., 2009; Zitrin & Broadhurst, 2009), enclosing some cluster galaxies. These enclosed cluster galaxies are ideal candidates for studies similar to that of Chapter 7. The other candidate is Abell 383, a well-studied cluster (e.g. Zitrin et al. (2011)) with a similar situation to the cluster studied here, but with a less pronounced arc.

Bibliography

Abazajian, K. N., Adelman-McCarthy, J. K., Agüeros, M. A., Allam, S. S., Allende Prieto, C., An, D., Anderson, K. S. J., Anderson, S. F., Annis, J., Bahcall, N. A., & et al. 2009: *The Seventh Data Release of the Sloan Digital Sky Survey*, ApJS, 182, 543

Adelman-McCarthy, J. K., Agüeros, M. A., Allam, S. S., Anderson, K. S. J., Anderson, S. F., Annis, J., Bahcall, N. A., Bailer-Jones, C. A. L., Baldry, I. K., Barentine, J. C., Beers, T. C., et al. 2007: *The Fifth Data Release of the Sloan Digital Sky Survey*, ApJS, 172, 634

Alcock, C., Allsman, R. A., Alves, D. R., Axelrod, T. S., Becker, A. C., Bennett, D. P., Cook, K. H., Dalal, N., Drake, A. J., Freeman, K. C., Geha, M., et al. 2000: *The MACHO Project: Microlensing Results from 5.7 Years of Large Magellanic Cloud Observations*, ApJ, 542, 281

Andreon, S. 1996: *The morphological segregation of galaxies in clusters. II. The properties of galaxies in the Coma cluster.*, A&A, 314, 763

Arimoto, N. & Yoshii, Y. 1987: *Chemical and photometric properties of a galactic wind model for elliptical galaxies*, A&A, 173, 23

Auger, M. W., Treu, T., Bolton, A. S., Gavazzi, R., Koopmans, L. V. E., Marshall, P. J., Bundy, K., & Moustakas, L. A. 2009: *The Sloan Lens ACS Survey. IX. Colors, Lensing, and Stellar Masses of Early-Type Galaxies*, ApJ, 705, 1099

Auger, M. W., Treu, T., Bolton, A. S., Gavazzi, R., Koopmans, L. V. E., Marshall, P. J., Moustakas, L. A., & Burles, S. 2010: *The Sloan Lens ACS Survey. X. Stellar, Dynamical, and Total Mass Correlations of Massive Early-type Galaxies*, ApJ, 724, 511

Bacon, R., Copin, Y., Monnet, G., Miller, B. W., Allington-Smith, J. R., Bureau, M., Carollo, C. M., Davies, R. L., Emsellem, E., Kuntschner, H., Peletier, R. F., et al. 2001: *The SAURON project - I. The panoramic integral-field spectrograph*, MNRAS, 326, 23

Bamford, S. P., Nichol, R. C., Baldry, I. K., Land, K., Lintott, C. J., Schawinski, K., Slosar, A., Szalay, A. S., Thomas, D., Torki, M., Andreescu, D., et al. 2009: *Galaxy Zoo: the dependence of morphology and colour on environment*, MNRAS, 393, 1324

Barbera, F. L., Lopes, P. A. A., & de Carvalho, R. R. 2011, The Fundamental Plane of Early-Type Galaxies: Environmental Dependence from g Through K, ed. I. Ferreras & A. Pasquali, 79

Barkana, R. 1998: *Fast Calculation of a Family of Elliptical Mass Gravitational Lens Models*, ApJ, 502, 531

Barnabè, M., Auger, M. W., Treu, T., Koopmans, L. V. E., Bolton, A. S., Czoske, O., & Gavazzi, R. 2010: *The non-evolving internal structure of early-type galaxies: the case study SDSSJ0728+3835 at z = 0.206*, MNRAS, 406, 2339

Barnabè, M., Czoske, O., Koopmans, L. V. E., Treu, T., Bolton, A. S., & Gavazzi, R. 2009: *Two-dimensional kinematics of SLACS lenses - II. Combined lensing and dynamics analysis of early-type galaxies at z = 0.08-0.33*, MNRAS, 399, 21

Barnabè, M. & Koopmans, L. V. E. 2007: *A Unifying Framework for Self-consistent Gravitational Lensing and Stellar Dynamics Analyses of Early-Type Galaxies*, ApJ, 666, 726

Barnes, J. E. 1988: *Encounters of disk/halo galaxies*, ApJ, 331, 699

Barnes, J. E. 1989: *Evolution of compact groups and the formation of elliptical galaxies*, Nat, 338, 123

Barnes, J. E. & Hernquist, L. 1992: *Dynamics of interacting galaxies*, ARA&A, 30, 705

Baugh, C. M., Cole, S., & Frenk, C. S. 1996: *Evolution of the Hubble sequence in hierarchical models for galaxy formation*, MNRAS, 283, 1361

Bell, E. F., McIntosh, D. H., Katz, N., & Weinberg, M. D. 2003: *A First Estimate of the Baryonic Mass Function of Galaxies*, ApJ, 585, L117

Belokurov, V., Evans, N. W., Moiseev, A., King, L. J., Hewett, P. C., Pettini, M., Wyrzykowski, L., McMahon, R. G., Smith, M. C., Gilmore, G., Sanchez, S. F., et al. 2007: *The Cosmic Horseshoe: Discovery of an Einstein Ring around a Giant Luminous Red Galaxy*, ApJ, 671, L9

Bender, R., Burstein, D., & Faber, S. M. 1992: *Dynamically hot galaxies. I - Structural properties*, ApJ, 399, 462

Bender, R., Doebereiner, S., & Moellenhoff, C. 1988: *Isophote shapes of elliptical galaxies. I - The data*, A&AS, 74, 385

Bender, R. & Moellenhoff, C. 1987: *Morphological analysis of massive early-type galaxies in the Virgo cluster*, A&A, 177, 71

Bender, R., Saglia, R. P., & Gerhard, O. E. 1994: *Line-of-Sight Velocity Distributions of Elliptical Galaxies*, MNRAS, 269, 785

Bender, R., Saglia, R. P., Ziegler, B., Belloni, P., Greggio, L., Hopp, U., & Bruzual, G. 1998: *Exploring Cluster Elliptical Galaxies as Cosmological Standard Rods*, ApJ, 493, 529

Benítez, N. 2000: *Bayesian Photometric Redshift Estimation*, ApJ, 536, 571

Benítez, N., Ford, H., Bouwens, R., Menanteau, F., Blakeslee, J., Gronwall, C., Illingworth, G., Meurer, G., Broadhurst, T. J., Clampin, M., Franx, M., et al. 2004: *Faint Galaxies in Deep Advanced Camera for Surveys Observations*, ApJS, 150, 1

Bernabei, R., Belli, P., Cappella, F., Cerulli, R., Montecchia, F., Nozzoli, F., Incicchitti, A., Prosperi, D., Dai, C. J., Kuang, H. H., Ma, J. M., et al. 2004: *Dark Matter Particles in the Galactic Halo:*, International Journal of Modern Physics D, 13, 2127

Bernardi, M., Sheth, R. K., Annis, J., Burles, S., Eisenstein, D. J., Finkbeiner, D. P., Hogg, D. W., Lupton, R. H., Schlegel, D. J., SubbaRao, M., Bahcall, N. A., et al. 2003a: *Early-Type Galaxies in the Sloan Digital Sky Survey. III. The Fundamental Plane*, AJ, 125, 1866

Bernardi, M., Sheth, R. K., Annis, J., Burles, S., Eisenstein, D. J., Finkbeiner, D. P., Hogg, D. W., Lupton, R. H., Schlegel, D. J., SubbaRao, M., Bahcall, N. A., et al. 2003b: *Early-type Galaxies in the Sloan Digital Sky Survey. II. Correlations between Observables*, AJ, 125, 1849

Bertin, E. & Arnouts, S. 1996: *SExtractor: Software for source extraction.*, A&AS, 117, 393

Bertin, G., Liseikina, T., & Pegoraro. 2003: *Slow evolution of elliptical galaxies induced by dynamical friction. I. Capture of a system of satellites*, A&A, 405, 73

Bertin, G., Saglia, R. P., & Stiavelli, M. 1992: *Elliptical galaxies with dark matter. I - Self-consistent models. II - Optimal luminous-dark matter decomposition for a sample of bright objects*, ApJ, 384, 423

Blumenthal, G. R., Faber, S. M., Flores, R., & Primack, J. R. 1986: *Contraction of dark matter galactic halos due to baryonic infall*, ApJ, 301, 27

Blumenthal, G. R., Faber, S. M., Primack, J. R., & Rees, M. J. 1984: *Formation of galaxies and large-scale structure with cold dark matter*, Nat, 311, 517

Böhringer, H., Voges, W., Huchra, J. P., McLean, B., Giacconi, R., Rosati, P., Burg, R., Mader, J., Schuecker, P., Simiç, D., Komossa, S., et al. 2000: *The Northern ROSAT All-Sky (NORAS) Galaxy Cluster Survey. I. X-Ray Properties of Clusters Detected as Extended X-Ray Sources*, ApJS, 129, 435

Bolton, A. S., Burles, S., Koopmans, L. V. E., Treu, T., Gavazzi, R., Moustakas, L. A., Wayth, R., & Schlegel, D. J. 2008a: *The Sloan Lens ACS Survey. V. The Full ACS Strong-Lens Sample*, ApJ, 682, 964

Bolton, A. S., Burles, S., Koopmans, L. V. E., Treu, T., & Moustakas, L. A. 2006: *The Sloan Lens ACS Survey. I. A Large Spectroscopically Selected Sample of Massive Early-Type Lens Galaxies*, ApJ, 638, 703

Bolton, A. S., Burles, S., Schlegel, D. J., Eisenstein, D. J., & Brinkmann, J. 2004: *Sloan Digital Sky Survey Spectroscopic Lens Search. I. Discovery of Intermediate-Redshift Star-forming Galaxies behind Foreground Luminous Red Galaxies*, AJ, 127, 1860

Bolton, A. S., Treu, T., Koopmans, L. V. E., Gavazzi, R., Moustakas, L. A., Burles, S., Schlegel, D. J., & Wayth, R. 2008b: *The Sloan Lens ACS Survey. VII. Elliptical Galaxy Scaling Laws from Direct Observational Mass Measurements*, ApJ, 684, 248

Brainerd, T. G., Blandford, R. D., & Smail, I. 1996: *Weak Gravitational Lensing by Galaxies*, ApJ, 466, 623

Bravin, M., Bruckmayer, M., Bucci, C., Cooper, S., Giordano, S., von Feilitzsch, F., Höhne, J., Jochum, J., Jörgens, V., Keeling, R., Kraus, H., et al. 1999: *The CRESST dark matter search*, Astroparticle Physics, 12, 107

Bressan, A., Chiosi, C., & Fagotto, F. 1994: *Spectrophotometric evolution of elliptical galaxies. 1: Ultraviolet excess and color-magnitude-redshift relations*, ApJS, 94, 63

Brimioulle, F., Seitz, S., Lerchster, M., Bender, R., & Snigula, J. 2013: *Dark Matter Halo Properties from Galaxy-Galaxy Lensing*, ArXiv e-prints

Broadhurst, T., Benítez, N., Coe, D., Sharon, K., Zekser, K., White, R., Ford, H., Bouwens, R., Blakeslee, J., Clampin, M., Cross, N., et al. 2005: *Strong-Lensing Analysis of A1689 from Deep Advanced Camera Images*, ApJ, 621, 53

Bruzual, G. & Charlot, S. 2003: *Stellar population synthesis at the resolution of 2003*, MNRAS, 344, 1000

Bullock, J. S., Kolatt, T. S., Sigad, Y., Somerville, R. S., Kravtsov, A. V., Klypin, A. A., Primack, J. R., & Dekel, A. 2001: *Profiles of dark haloes: evolution, scatter and environment*, MNRAS, 321, 559

Cappellari, M., Bacon, R., Bureau, M., Damen, M. C., Davies, R. L., de Zeeuw, P. T., Emsellem, E., Falcón-Barroso, J., Krajnović, D., Kuntschner, H., McDermid, R. M., et al. 2006: *The SAURON project - IV. The mass-to-light ratio, the virial mass estimator and the Fundamental Plane of elliptical and lenticular galaxies*, MNRAS, 366, 1126

Cappellari, M., Emsellem, E., Krajnović, D., McDermid, R. M., Scott, N., Verdoes Kleijn, G. A., Young, L. M., Alatalo, K., Bacon, R., Blitz, L., Bois, M., et al. 2011: *The ATLAS^{3D} project - I. A volume-limited sample of 260 nearby early-type galaxies: science goals and selection criteria*, MNRAS, 413, 813

Cappellari, M., McDermid, R. M., Alatalo, K., Blitz, L., Bois, M., Bournaud, F., Bureau, M., Crocker, A. F., Davies, R. L., Davis, T. A., de Zeeuw, P. T., et al. 2012a: *Systematic variation of the stellar initial mass function in early-type galaxies*, Nat, 484, 485

Cappellari, M., McDermid, R. M., Alatalo, K., Blitz, L., Bois, M., Bournaud, F., Bureau, M., Crocker, A. F., Davies, R. L., Davis, T. A., de Zeeuw, P. T., et al. 2012b: *The Atlas3D project - XX. Mass-size and Mass-sigma projections of the Virial Plane of early-type galaxies: variation of morphology, kinematics, mass-to-light ratio and stellar initial mass function*, ArXiv e-prints

Carollo, C. M., de Zeeuw, P. T., van der Marel, R. P., Danziger, I. J., & Qian, E. E. 1995: *Dark matter in elliptical galaxies*, ApJ, 441, L25

Chabrier, G. 2003: *Galactic Stellar and Substellar Initial Mass Function*, PASP, 115, 763

Clowe, D., Gonzalez, A., & Markevitch, M. 2004: *Weak-Lensing Mass Reconstruction of the Interacting Cluster 1E 0657-558: Direct Evidence for the Existence of Dark Matter*, ApJ, 604, 596

Coe, D., Benítez, N., Broadhurst, T., & Moustakas, L. A. 2010: *A High-resolution Mass Map of Galaxy Cluster Substructure: LensPerfect Analysis of A1689*, ApJ, 723, 1678

Coe, D., Benítez, N., Sánchez, S. F., Jee, M., Bouwens, R., & Ford, H. 2006: *Galaxies in the Hubble Ultra Deep Field. I. Detection, Multiband Photometry, Photometric Redshifts, and Morphology*, AJ, 132, 926

Cohn, J. D., Kochanek, C. S., McLeod, B. A., & Keeton, C. R. 2001: *Constraints on Galaxy Density Profiles from Strong Gravitational Lensing: The Case of B1933+503*, ApJ, 554, 1216

Coles, J. 2008: *A New Estimate of the Hubble Time with Improved Modeling of Gravitational Lenses*, ApJ, 679, 17

Colley, W. N., Tyson, J. A., & Turner, E. L. 1996: *Unlensing Multiple Arcs in 0024+1654: Reconstruction of the Source Image*, ApJ, 461, L83

Corsini, E. M., Wegner, G., Saglia, R. P., Thomas, J., Bender, R., & Thomas, D. 2008: *Spatially Resolved Spectroscopy of Coma Cluster Early-Type Galaxies. IV. Completing the Data Set*, ApJS, 175, 462

Davis, M., Efstathiou, G., Frenk, C. S., & White, S. D. M. 1985: *The evolution of large-scale structure in a universe dominated by cold dark matter*, ApJ, 292, 371

de Grandi, S., Böhringer, H., Guzzo, L., Molendi, S., Chincarini, G., Collins, C., Cruddace, R., Neumann, D., Schindler, S., Schuecker, P., & Voges, W. 1999: *A Flux-limited Sample of Bright Clusters of Galaxies from the Southern Part of the ROSAT All-Sky Survey: The Catalog and LOG N-LOG S*, ApJ, 514, 148

De Lucia, G., Springel, V., White, S. D. M., Croton, D., & Kauffmann, G. 2006: *The formation history of elliptical galaxies*, MNRAS, 366, 499

de Vaucouleurs, G. 1948: *Recherches sur les Nebuleuses Extragalactiques*, Annales d'Astrophysique, 11, 247

Dekel, A., Stoehr, F., Mamon, G. A., Cox, T. J., Novak, G. S., & Primack, J. R. 2005: *Lost and found dark matter in elliptical galaxies*, Nat, 437, 707

Diego, J. M., Sandvik, H. B., Protopapas, P., Tegmark, M., Benítez, N., & Broadhurst, T. 2005: *Non-parametric mass reconstruction of A1689 from strong lensing data with the Strong Lensing Analysis Package*, MNRAS, 362, 1247

Diemand, J., Kuhlen, M., & Madau, P. 2007: *Formation and Evolution of Galaxy Dark Matter Halos and Their Substructure*, ApJ, 667, 859

Djorgovski, S. & Davis, M. 1987: *Fundamental properties of elliptical galaxies*, ApJ, 313, 59

Donnarumma, A., Ettori, S., Meneghetti, M., Gavazzi, R., Fort, B., Moscardini, L., Romano, A., Fu, L., Giordano, F., Radovich, M., Maoli, R., et al. 2011: *Abell 611. II. X-ray and strong lensing analyses*, A&A, 528, A73

Doroshkevich, A. G., Khlopov, M. I., Sunyaev, R. A., Szalay, A. S., & Zeldovich, I. B. 1981: *Cosmological impact of the neutrino rest mass*, Annals of the New York Academy of Sciences, 375, 32

Dressler, A. 1980: *Galaxy morphology in rich clusters - Implications for the formation and evolution of galaxies*, ApJ, 236, 351

Dressler, A., Oemler, Jr., A., Couch, W. J., Smail, I., Ellis, R. S., Barger, A., Butcher, H., Poggianti, B. M., & Sharples, R. M. 1997: *Evolution since Z = 0.5 of the Morphology-Density Relation for Clusters of Galaxies*, ApJ, 490, 577

Drory, N., Bender, R., Feulner, G., Hopp, U., Maraston, C., Snigula, J., & Hill, G. J. 2004: *The Munich Near-Infrared Cluster Survey (MUNICS). VI. The Stellar Masses of K-Band-selected Field Galaxies to z˜1.2*, ApJ, 608, 742

Drory, N., Feulner, G., Bender, R., Botzler, C. S., Hopp, U., Maraston, C., Mendes de Oliveira, C., & Snigula, J. 2001: *The Munich Near-Infrared Cluster Survey - I. Field selection, object extraction and photometry*, MNRAS, 325, 550

Dubinski, J. 1998: *The Origin of the Brightest Cluster Galaxies*, ApJ, 502, 141

Duffy, A. R., Schaye, J., Kay, S. T., Dalla Vecchia, C., Battye, R. A., & Booth, C. M. 2010: *Impact of baryon physics on dark matter structures: a detailed simulation study of halo density profiles*, MNRAS, 405, 2161

Dunkley, J., Bucher, M., Ferreira, P. G., Moodley, K., & Skordis, C. 2005: *Fast and reliable Markov chain Monte Carlo technique for cosmological parameter estimation*, MNRAS, 356, 925

Ebeling, H., Ma, C. J., Kneib, J.-P., Jullo, E., Courtney, N. J. D., Barrett, E., Edge, A. C., & Le Borgne, J.-F. 2009: *A spectacular giant arc in the massive cluster lens MACSJ1206.2-0847*, MNRAS, 395, 1213

EDELWEISS Collaboration, Armengaud, E., Augier, C., Benoît, A., Bergé, L., Blümer, J., Broniatowski, A., Brudanin, V., Censier, B., Chardin, G., Chapellier, M., et al. 2011: *Final results of the EDELWEISS-II WIMP search using a 4-kg array of cryogenic germanium detectors with interleaved electrodes*, Physics Letters B, 702, 329

Eggen, O. J., Lynden-Bell, D., & Sandage, A. R. 1962: *Evidence from the motions of old stars that the Galaxy collapsed.*, ApJ, 136, 748

Eichner, T., Seitz, S., & Bauer, A. 2012: *Golden gravitational lensing systems from the Sloan Lens ACS Survey - II. SDSS J1430+4105: a precise inner total mass profile from lensing alone*, MNRAS, 427, 1918

Einstein, A. 1916: *Die Grundlage der allgemeinen Relativitätstheorie*, Annalen der Physik, 354, 769

Einstein, A. 1917: *Kosmologische Betrachtungen zur allgemeinen Relativitätstheorie*, Sitzungsberichte der Königlich Preußischen Akademie der Wissenschaften (Berlin), Seite 142-152., 142

Einstein, A. 1922, Vier Vorlesungen über Relativitätstheorie (Braunschweig, Germany: Vieweg)

El-Zant, A., Shlosman, I., & Hoffman, Y. 2001: *Dark Halos: The Flattening of the Density Cusp by Dynamical Friction*, ApJ, 560, 636

Elíasdóttir, Á., Limousin, M., Richard, J., Hjorth, J., Kneib, J.-P., Natarajan, P., Pedersen, K., Jullo, E., & Paraficz, D. 2007: *Where is the matter in the Merging Cluster Abell 2218?*, ArXiv e-prints

Evrard, A. E. 1997: *The intracluster gas fraction in X-ray clusters - Constraints on the clustered mass density*, MNRAS, 292, 289

Fabbiano, G. 1989: *X rays from normal galaxies*, ARA&A, 27, 87

Faber, S. M. & Jackson, R. E. 1976: *Velocity dispersions and mass-to-light ratios for elliptical galaxies*, ApJ, 204, 668

Fadely, R., Keeton, C. R., Nakajima, R., & Bernstein, G. M. 2010: *Improved Constraints on the Gravitational Lens Q0957+561. II. Strong Lensing*, ApJ, 711, 246

Falco, E. E., Gorenstein, M. V., & Shapiro, I. I. 1985: *On model-dependent bounds on H(0) from gravitational images Application of Q0957 + 561A,B*, ApJ, 289, L1

Fixsen, D. J., Cheng, E. S., Cottingham, D. A., Eplee, Jr., R. E., Isaacman, R. B., Mather, J. C., Meyer, S. S., Noerdlinger, P. D., Shafer, R. A., Weiss, R., Wright, E. L., et al. 1994: *Cosmic microwave background dipole spectrum measured by the COBE FIRAS instrument*, ApJ, 420, 445

Focardi, P. & Malavasi, N. 2012: *The Effect of the Environment on the Faber-Jackson Relation*, ApJ, 756, 117

Friedman, A. 1922: *Über die Krümmung des Raumes*, Zeitschrift fur Physik, 10, 377

Fritz, A., Böhm, A., & Ziegler, B. L. 2009: *The evolution of field early-type galaxies in the FDF and WHDF*, MNRAS, 393, 1467

Fukugita, M., Hogan, C. J., & Peebles, P. J. E. 1998: *The Cosmic Baryon Budget*, ApJ, 503, 518

Gao, L., White, S. D. M., Jenkins, A., Stoehr, F., & Springel, V. 2004: *The subhalo populations of ΛCDM dark haloes*, MNRAS, 355, 819

Gavazzi, R., Treu, T., Koopmans, L. V. E., Bolton, A. S., Moustakas, L. A., Burles, S., & Marshall, P. J. 2008: *The Sloan Lens ACS Survey. VI. Discovery and Analysis of a Double Einstein Ring*, ApJ, 677, 1046

Gavazzi, R., Treu, T., Rhodes, J. D., Koopmans, L. V. E., Bolton, A. S., Burles, S., Massey, R. J., & Moustakas, L. A. 2007: *The Sloan Lens ACS Survey. IV. The Mass Density Profile of Early-Type Galaxies out to 100 Effective Radii*, ApJ, 667, 176

Geiger, B. & Schneider, P. 1999: *A simultaneous maximum likelihood approach for galaxy-galaxy lensing and cluster lens reconstruction*, MNRAS, 302, 118

Gelman, A., Carlin, J., Stern, H., & Rubin, D. B. 1995, Bayesian Data Analysis (Chapman & Hall/CRC)

Gerhard, O., Kronawitter, A., Saglia, R. P., & Bender, R. 2001: *Dynamical Family Properties and Dark Halo Scaling Relations of Giant Elliptical Galaxies*, AJ, 121, 1936

Ghigna, S., Moore, B., Governato, F., Lake, G., Quinn, T., & Stadel, J. 1998: *Dark matter haloes within clusters*, MNRAS, 300, 146

Giacconi, R., Murray, S., Gursky, H., Kellogg, E., Schreier, E., & Tananbaum, H. 1972: *The Uhuru catalog of X-ray sources.*, ApJ, 178, 281

Girardi, M., Borgani, S., Giuricin, G., Mardirossian, F., & Mezzetti, M. 1998: *The Observational Mass Function of Nearby Galaxy Clusters*, ApJ, 506, 45

Gladders, M. D. & Yee, H. K. C. 2000: *A New Method For Galaxy Cluster Detection. I. The Algorithm*, AJ, 120, 2148

Gnedin, O. Y., Kravtsov, A. V., Klypin, A. A., & Nagai, D. 2004: *Response of Dark Matter Halos to Condensation of Baryons: Cosmological Simulations and Improved Adiabatic Contraction Model*, ApJ, 616, 16

Golse, G. & Kneib, J.-P. 2002: *Pseudo elliptical lensing mass model: Application to the NFW mass distribution*, A&A, 390, 821

Goudfrooij, P., Hansen, L., Jorgensen, H. E., & Norgaard-Nielsen, H. U. 1994: *Interstellar matter in Shapley-Ames elliptical galaxies. II. The distribution of dust and ionized gas*, A&AS, 105, 341

Grillo, C., Eichner, T., Seitz, S., Bender, R., Lombardi, M., Gobat, R., & Bauer, A. 2010: *Golden Gravitational Lensing Systems from the Sloan Lens ACS Survey. I. SDSS J1538+5817: One Lens for Two Sources*, ApJ, 710, 372

Grillo, C., Gobat, R., Lombardi, M., & Rosati, P. 2009: *Photometric mass and mass decomposition in early-type lens galaxies*, A&A, 501, 461

Grillo, C., Gobat, R., Rosati, P., & Lombardi, M. 2008a: *Stellar mass estimates in early-type galaxies from lensing+dynamical and photometric measurements*, A&A, 477, L25

Grillo, C., Lombardi, M., & Bertin, G. 2008b: *Cosmological parameters from strong gravitational lensing and stellar dynamics in elliptical galaxies*, A&A, 477, 397

Grillo, C., Lombardi, M., Rosati, P., Bertin, G., Gobat, R., Demarco, R., Lidman, C., Motta, V., & Nonino, M. 2008c: *A twelve-image gravitational lens system in the z 0.84 cluster Cl J0152.7-1357*, A&A, 486, 45

Halkola, A., Hildebrandt, H., Schrabback, T., Lombardi, M., Bradač, M., Erben, T., Schneider, P., & Wuttke, D. 2008: *The mass distribution of RX J1347-1145 from strong lensing*, A&A, 481, 65

Halkola, A., Seitz, S., & Pannella, M. 2006: *Parametric strong gravitational lensing analysis of Abell 1689*, MNRAS, 372, 1425

Halkola, A., Seitz, S., & Pannella, M. 2007: *The Sizes of Galaxy Halos in Galaxy Cluster Abell 1689*, ApJ, 656, 739

Hoekstra, H., Yee, H. K. C., & Gladders, M. D. 2004: *Properties of Galaxy Dark Matter Halos from Weak Lensing*, ApJ, 606, 67

Host, O. 2012: *Galaxy cluster strong lensing: image deflections from density fluctuations along the line of sight*, MNRAS, 420, L18

Hubble, E. 1929: *A Relation between Distance and Radial Velocity among Extra-Galactic Nebulae*, Proceedings of the National Academy of Science, 15, 168

Hubble, E. P. 1936, Realm of the Nebulae, ed. Hubble, E. P.

Jesseit, R., Naab, T., & Burkert, A. 2002: *The Validity of the Adiabatic Contraction Approximation for Dark Matter Halos*, ApJ, 571, L89

Johnston, D. E., Sheldon, E. S., Wechsler, R. H., Rozo, E., Koester, B. P., Frieman, J. A., McKay, T. A., Evrard, A. E., Becker, M. R., & Annis, J. 2007: *Cross-correlation Weak Lensing of SDSS galaxy Clusters II: Cluster Density Profiles and the Mass–Richness Relation*, ArXiv e-prints

Jones, M. H., Lambourne, R., Adams, D. J., & University., O. 2004., An introduction to galaxies and cosmology / (Cambridge :: Cambridge University Press,)

Jullo, E., Natarajan, P., Kneib, J.-P., D'Aloisio, A., Limousin, M., Richard, J., & Schimd, C. 2010: *Cosmological Constraints from Strong Gravitational Lensing in Clusters of Galaxies*, Science, 329, 924

Kahn, F. D. & Woltjer, L. 1959: *Intergalactic Matter and the Galaxy.*, ApJ, 130, 705

Kaiser, N. & Squires, G. 1993: *Mapping the dark matter with weak gravitational lensing*, ApJ, 404, 441

Keeton, C. R. 2001a: *A Catalog of Mass Models for Gravitational Lensing*, ArXiv Astrophysics e-prints

Keeton, C. R. 2001b: *Cold Dark Matter and Strong Gravitational Lensing: Concord or Conflict?*, ApJ, 561, 46

Keeton, C. R. 2001c: *Computational Methods for Gravitational Lensing*, ArXiv Astrophysics e-prints

Kennicutt, Jr., R. C. 1992: *A spectrophotometric atlas of galaxies*, ApJS, 79, 255

Knapp, G. R. 1999: *Cold Gas and Star Formation in Elliptical Galaxies*, in Astronomical Society of the Pacific Conference Series, Vol. 163, Star Formation in Early Type Galaxies, ed. P. Carral & J. Cepa, 119

Knebe, A., Yahagi, H., Kase, H., Lewis, G., & Gibson, B. K. 2008: *The radial alignment of dark matter subhaloes: from simulations to observations*, MNRAS, 388, L34

Kochanek, C. S. 1991: *The implications of lenses for galaxy structure*, ApJ, 373, 354

Kochanek, C. S. 1993: *The Analysis of Gravitational Lens Surveys. II. Maximum Likelihood Models and Singular Potentials*, ApJ, 419, 12

Kochanek, C. S. 1994: *The dynamics of luminous galaxies in isothermal halos*, ApJ, 436, 56

Kochanek, C. S. 2004: *The Saas Fee Lectures on strong gravitational lensing*, ArXiv Astrophysics e-prints

Koester, B. P., McKay, T. A., Annis, J., Wechsler, R. H., Evrard, A., Bleem, L., Becker, M., Johnston, D., Sheldon, E., Nichol, R., Miller, C., et al. 2007: *A MaxBCG Catalog of 13,823 Galaxy Clusters from the Sloan Digital Sky Survey*, ApJ, 660, 239

Komatsu, E., Smith, K. M., Dunkley, J., Bennett, C. L., Gold, B., Hinshaw, G., Jarosik, N., Larson, D., Nolta, M. R., Page, L., Spergel, D. N., et al. 2011: *Seven-year Wilkinson Microwave Anisotropy Probe (WMAP) Observations: Cosmological Interpretation*, ApJS, 192, 18

Koopmans, L. V. E. 2006: *Gravitational Lensing Stellar Dynamics*, in EAS Publications Series, Vol. 20, EAS Publications Series, ed. G. A. Mamon, F. Combes, C. Deffayet, & B. Fort, 161–166

Koopmans, L. V. E., Bolton, A., Treu, T., Czoske, O., Auger, M. W., Barnabè, M., Vegetti, S., Gavazzi, R., Moustakas, L. A., & Burles, S. 2009: *The Structure and Dynamics of Massive Early-Type Galaxies: On Homology, Isothermality, and Isotropy Inside One Effective Radius*, ApJ, 703, L51

Koopmans, L. V. E., Treu, T., Bolton, A. S., Burles, S., & Moustakas, L. A. 2006: *The Sloan Lens ACS Survey. III. The Structure and Formation of Early-Type Galaxies and Their Evolution since z ˜ 1*, ApJ, 649, 599

Kormendy, J. & Bender, R. 2012: *A Revised Parallel-sequence Morphological Classification of Galaxies: Structure and Formation of S0 and Spheroidal Galaxies*, ApJS, 198, 2

Kronawitter, A., Saglia, R. P., Gerhard, O., & Bender, R. 2000: *Orbital structure and mass distribution in elliptical galaxies*, A&AS, 144, 53

Kroupa, P. 2001: *On the variation of the initial mass function*, MNRAS, 322, 231

Lacey, C. & Cole, S. 1993: *Merger rates in hierarchical models of galaxy formation*, MNRAS, 262, 627

Lagattuta, D. J., Fassnacht, C. D., Auger, M. W., Marshall, P. J., Bradač, M., Treu, T., Gavazzi, R., Schrabback, T., Faure, C., & Anguita, T. 2010: *Cosmic Evolution of Virial and Stellar Mass in Massive Early-type Galaxies*, ApJ, 716, 1579

Larson, D., Dunkley, J., Hinshaw, G., Komatsu, E., Nolta, M. R., Bennett, C. L., Gold, B., Halpern, M., Hill, R. S., Jarosik, N., Kogut, A., et al. 2011: *Seven-year Wilkinson Microwave Anisotropy Probe (WMAP) Observations: Power Spectra and WMAP-derived Parameters*, ApJS, 192, 16

Larson, R. B. 1974: *Dynamical models for the formation and evolution of spherical galaxies*, MNRAS, 166, 585

Lauer, T. R., Faber, S. M., Gebhardt, K., Richstone, D., Tremaine, S., Ajhar, E. A., Aller, M. C., Bender, R., Dressler, A., Filippenko, A. V., Green, R., et al. 2005: *The Centers of Early-Type Galaxies with Hubble Space Telescope. V. New WFPC2 Photometry*, AJ, 129, 2138

Limousin, M., Kneib, J. P., Bardeau, S., Natarajan, P., Czoske, O., Smail, I., Ebeling, H., & Smith, G. P. 2007a: *Truncation of galaxy dark matter halos in high density environments*, A&A, 461, 881

Limousin, M., Richard, J., Jullo, E., Kneib, J.-P., Fort, B., Soucail, G., Elíasdóttir, Á., Natarajan, P., Ellis, R. S., Smail, I., Czoske, O., et al. 2007b: *Combining Strong and Weak Gravitational Lensing in Abell 1689*, ApJ, 668, 643

Limousin, M., Richard, J., Kneib, J.-P., Brink, H., Pelló, R., Jullo, E., Tu, H., Sommer-Larsen, J., Egami, E., Michałowski, M. J., Cabanac, R., et al. 2008: *Strong lensing in Abell 1703: constraints on the slope of the inner dark matter distribution*, A&A, 489, 23

Limousin, M., Sommer-Larsen, J., Natarajan, P., & Milvang-Jensen, B. 2009: *Probing the Truncation of Galaxy Dark Matter Halos in High-Density Environments from Hydrodynamical N-Body Simulations*, ApJ, 696, 1771

Lin, Y.-T. & Mohr, J. J. 2004: *K-band Properties of Galaxy Clusters and Groups: Brightest Cluster Galaxies and Intracluster Light*, ApJ, 617, 879

Lynds, R. & Petrosian, V. 1986: *Giant Luminous Arcs in Galaxy Clusters*, in Bulletin of the American Astronomical Society, Vol. 18, Bulletin of the American Astronomical Society, 1014

Ma, C.-P. & Boylan-Kolchin, M. 2004: *Are Halos of Collisionless Cold Dark Matter Collisionless?*, Physical Review Letters, 93, 021301

Mandelbaum, R., Seljak, U., Cool, R. J., Blanton, M., Hirata, C. M., & Brinkmann, J. 2006: *Density profiles of galaxy groups and clusters from SDSS galaxy-galaxy weak lensing*, MNRAS, 372, 758

Maraston, C. 2005: *Evolutionary population synthesis: models, analysis of the ingredients and application to high-z galaxies*, MNRAS, 362, 799

Mathews, W. G. 1978: *The enormous mass of the elliptical galaxy M 87 : a model for the extended X-ray source.*, Lick Observatory Bulletin, 766, 1

Matković, A. & Guzmán, R. 2005: *Kinematic properties and stellar populations of faint early-type galaxies - I. Velocity dispersion measurements of central Coma galaxies*, MNRAS, 362, 289

Merritt, D. 1983: *Relaxation and tidal stripping in rich clusters of galaxies. I. Evolution of the mass distribution*, ApJ, 264, 24

Merritt, D. 1984: *Relaxation and tidal stripping in rich clusters of galaxies. II. Evolution of the luminosity distribution*, ApJ, 276, 26

Mo, H., van den Bosch, F., & White, S. 2010, Galaxy Formation and Evolution, Galaxy Formation and Evolution (Cambridge University Press)

Nair, S. 1998: *Modelling the 10-image lensed system B1933+503*, MNRAS, 301, 315

Narayan, R. 1998: *A review of astrophysical results from gravitational lensing*, New Astronomy Reviews, 42, 73

Narayan, R. & Bartelmann, M. 1996: *Lectures on Gravitational Lensing*, ArXiv Astrophysics e-prints

Natarajan, P., Kneib, J.-P., & Smail, I. 2002a: *Evidence for Tidal Stripping of Dark Matter Halos in Massive Cluster Lenses*, ApJ, 580, L11

Natarajan, P., Loeb, A., Kneib, J.-P., & Smail, I. 2002b: *Constraints on the Collisional Nature of the Dark Matter from Gravitational Lensing in the Cluster A2218*, ApJ, 580, L17

Navarro, J. F., Frenk, C. S., & White, S. D. M. 1997: *A Universal Density Profile from Hierarchical Clustering*, ApJ, 490, 493

Nelson, E. J., van Dokkum, P. G., Brammer, G., Förster Schreiber, N., Franx, M., Fumagalli, M., Patel, S., Rix, H.-W., Skelton, R. E., Bezanson, R., Da Cunha, E., et al. 2012: *Spatially Resolved Hα Maps and Sizes of 57 Strongly Star-forming Galaxies at z ~ 1 from 3D-HST: Evidence for Rapid Inside-out Assembly of Disk Galaxies*, ApJ, 747, L28

Nigoche-Netro, A., Aguerri, J. A. L., Lagos, P., Ruelas-Mayorga, A., Sánchez, L. J., & Machado, A. 2010: *The Faber-Jackson relation for early-type galaxies: dependence on the magnitude range*, A&A, 516, A96

Nigoche-Netro, A., Ruelas, A., & Sánchez, L. J. 2011: *The Dependence of the Faber-Jackson relation on the magnitude range*, in Revista Mexicana de Astronomia y Astrofisica Conference Series, Vol. 40, Revista Mexicana de Astronomia y Astrofisica Conference Series, 126–126

Ostriker, J. P. & Peebles, P. J. E. 1973: *A Numerical Study of the Stability of Flattened Galaxies: or, can Cold Galaxies Survive?*, ApJ, 186, 467

Oyaizu, H., Lima, M., Cunha, C. E., Lin, H., Frieman, J., & Sheldon, E. S. 2008: *A Galaxy Photometric Redshift Catalog for the Sloan Digital Sky Survey Data Release 6*, ApJ, 674, 768

Patnaik, A. R. & Kemball, A. J. 2001: *Sub-milliarcsec-scale structure of the gravitational lens B1600+434*, A&A, 373, L25

Peacock, J. A. 1999, Cosmological Physics, ed. Peacock, J. A.

Peletier, R. F., Davies, R. L., Illingworth, G. D., Davis, L. E., & Cawson, M. 1990: *CCD surface photometry of galaxies with dynamical data. II - UBR photometry of 39 elliptical galaxies*, AJ, 100, 1091

Peng, C. Y., Ho, L. C., Impey, C. D., & Rix, H.-W. 2002: *Detailed Structural Decomposition of Galaxy Images*, AJ, 124, 266

Peng, C. Y., Ho, L. C., Impey, C. D., & Rix, H.-W. 2010: *Detailed Decomposition of Galaxy Images. II. Beyond Axisymmetric Models*, AJ, 139, 2097

Perlmutter, S., Aldering, G., della Valle, M., Deustua, S., Ellis, R. S., Fabbro, S., Fruchter, A., Goldhaber, G., Groom, D. E., Hook, I. M., Kim, A. G., et al. 1998: *Discovery of a supernova explosion at half the age of the universe*, Nat, 391, 51

Postman, M., Coe, D., Benítez, N., Bradley, L., Broadhurst, T., Donahue, M., Ford, H., Graur, O., Graves, G., Jouvel, S., Koekemoer, A., et al. 2012: *The Cluster Lensing and Supernova Survey with Hubble: An Overview*, ApJS, 199, 25

Postman, M., Lubin, L. M., Gunn, J. E., Oke, J. B., Hoessel, J. G., Schneider, D. P., & Christensen, J. A. 1996: *The Palomar Distant Clusters Survey. I. The Cluster Catalog*, AJ, 111, 615

Press, W. H. & Schechter, P. 1974: *Formation of Galaxies and Clusters of Galaxies by Self-Similar Gravitational Condensation*, ApJ, 187, 425

Pu, S. B., Saglia, R. P., Fabricius, M. H., Thomas, J., Bender, R., & Han, Z. 2010: *Radially extended kinematics and stellar populations of the massive ellipticals NGC 1600, NGC 4125, and NGC 7619 . Constraints on the outer dark halo density profile*, A&A, 516, A4

Renzini, A. 2006: *Stellar Population Diagnostics of Elliptical Galaxy Formation*, ARA&A, 44, 141

Richard, J., Kneib, J.-P., Limousin, M., Edge, A., & Jullo, E. 2010a: *Abell 370 revisited: refurbished Hubble imaging of the first strong lensing cluster*, MNRAS, 402, L44

Richard, J., Smith, G. P., Kneib, J.-P., Ellis, R. S., Sanderson, A. J. R., Pei, L., Targett, T. A., Sand, D. J., Swinbank, A. M., Dannerbauer, H., Mazzotta, P., et al. 2010b: *LoCuSS: first results from strong-lensing analysis of 20 massive galaxy clusters at z = 0.2*, MNRAS, 404, 325

Riess, A. G., Filippenko, A. V., Challis, P., Clocchiatti, A., Diercks, A., Garnavich, P. M., Gilliland, R. L., Hogan, C. J., Jha, S., Kirshner, R. P., Leibundgut, B., et al. 1998: *Observational Evidence from Supernovae for an Accelerating Universe and a Cosmological Constant*, AJ, 116, 1009

Riffeser, A., Seitz, S., & Bender, R. 2008: *The M31 Microlensing Event WeCAPP-GL1/POINT-AGAPE-S3: Evidence for a MACHO Component in the Dark Halo of M31?*, ApJ, 684, 1093

Robertson, H. P. 1935: *Kinematics and World-Structure*, ApJ, 82, 284

Robertson, H. P. 1936a: *Kinematics and World-Structure II.*, ApJ, 83, 187

Robertson, H. P. 1936b: *Kinematics and World-Structure III.*, ApJ, 83, 257

Romanishin, W. 1986: *The Absolute Magnitude-Effective Radius Relation for Luminous Elliptical Galaxies*, AJ, 91, 76

Rozo, E., Rykoff, E. S., Evrard, A., Becker, M., McKay, T., Wechsler, R. H., Koester, B. P., Hao, J., Hansen, S., Sheldon, E., Johnston, D., et al. 2009: *Constraining the Scatter in the Mass-richness Relation of maxBCG Clusters with Weak Lensing and X-ray Data*, ApJ, 699, 768

Rubin, V. C. & Ford, Jr., W. K. 1970: *Rotation of the Andromeda Nebula from a Spectroscopic Survey of Emission Regions*, ApJ, 159, 379

Rusin, D. & Kochanek, C. S. 2005: *The Evolution and Structure of Early-Type Field Galaxies: A Combined Statistical Analysis of Gravitational Lenses*, ApJ, 623, 666

Rusin, D., Kochanek, C. S., Falco, E. E., Keeton, C. R., McLeod, B. A., Impey, C. D., Lehár, J., Muñoz, J. A., Peng, C. Y., & Rix, H.-W. 2003a: *The Evolution of a Mass-selected Sample of Early-Type Field Galaxies*, ApJ, 587, 143

Rusin, D., Kochanek, C. S., & Keeton, C. R. 2003b: *Self-similar Models for the Mass Profiles of Early-Type Lens Galaxies*, ApJ, 595, 29

Ryden, B. 2002, Introduction to Cosmology (Benjamin Cummings)

Rzepecki, J., Lombardi, M., Rosati, P., Bignamini, A., & Tozzi, P. 2007: *Strong lensing analysis of the cluster RCS0224-0002 at z = 0.77*, A&A, 471, 743

Saglia, R. P., Bertin, G., & Stiavelli, M. 1992: *Elliptical Galaxies with Dark Matter. II. Optimal Luminous–Dark Matter Decomposition for a Sample of Bright Objects*, ApJ, 384, 433

Saglia, R. P., Sánchez-Blázquez, P., Bender, R., Simard, L., Desai, V., Aragón-Salamanca, A., Milvang-Jensen, B., Halliday, C., Jablonka, P., Noll, S., Poggianti, B., et al. 2010: *The fundamental plane of EDisCS galaxies. The effect of size evolution*, A&A, 524, A6

Saha, P. & Williams, L. L. R. 1997: *Non-parametric reconstruction of the galaxy lens in PG 1115+080*, MNRAS, 292, 148

Saha, P. & Williams, L. L. R. 2004: *A Portable Modeler of Lensed Quasars*, AJ, 127, 2604

Saha, P. & Williams, L. L. R. 2006: *Gravitational Lensing Model Degeneracies: Is Steepness All-Important?*, ApJ, 653, 936

Salpeter, E. E. 1955: *The Luminosity Function and Stellar Evolution.*, ApJ, 121, 161

Sand, D. J., Treu, T., Smith, G. P., & Ellis, R. S. 2004: *The Dark Matter Distribution in the Central Regions of Galaxy Clusters: Implications for Cold Dark Matter*, ApJ, 604, 88

Sanderson, A. J. R., Ponman, T. J., Finoguenov, A., Lloyd-Davies, E. J., & Markevitch, M. 2003: *The Birmingham-CfA cluster scaling project - I. Gas fraction and the M-T_X relation*, MNRAS, 340, 989

Sanglard, V., Benoit, A., Bergé, L., Blümer, J., Broniatowski, A., Censier, B., Chabert, L., Chapellier, M., Chardin, G., Charvin, P., Collin, S., et al. 2005: *Final results of the EDELWEISS-I dark matter search with cryogenic heat-and-ionization Ge detectors*, Phys. Rev. D, 71, 122002

Sauer, T. 2010: *A brief history of gravitational lensing*, Einstein Online, 4, 1005

Schneider, P. 2006, Extragalactic Astronomy and Cosmology: An Introduction (Springer)

Schneider, P., Ehlers, J., & Falco, E. E. 1992, Gravitational Lenses, ed. Schneider, P., Ehlers, J., & Falco, E. E.

Schneider, P., Kochanek, C. S., & Wambsganss, J. 2006, Gravitational Lensing: Strong, Weak and Micro, ed. Schneider, P., Kochanek, C. S., & Wambsganss, J.

Schneider, P. & Rix, H.-W. 1997: *Quantitative Analysis of Galaxy-Galaxy Lensing*, ApJ, 474, 25

Schneider, P. & Seitz, C. 1995: *Steps towards nonlinear cluster inversion through gravitational distortions. 1: Basic considerations and circular clusters*, A&A, 294, 411

Seitz, S., Saglia, R. P., Bender, R., Hopp, U., Belloni, P., & Ziegler, B. 1998: *The z=2.72 galaxy cB58: a gravitational fold arc lensed by the cluster MS1512+36*, MNRAS, 298, 945

Sérsic, J. L. 1963: *Influence of the atmospheric and instrumental dispersion on the brightness distribution in a galaxy*, Boletin de la Asociacion Argentina de Astronomia La Plata Argentina, 6, 41

Silk, J. 1968: *Cosmic Black-Body Radiation and Galaxy Formation*, ApJ, 151, 459

Smail, I., Swinbank, A. M., Richard, J., Ebeling, H., Kneib, J.-P., Edge, A. C., Stark, D., Ellis, R. S., Dye, S., Smith, G. P., & Mullis, C. 2007: *A Very Bright, Highly Magnified Lyman Break Galaxy at z = 3.07*, ApJ, 654, L33

Smith, G. P., Ebeling, H., Limousin, M., Kneib, J.-P., Swinbank, A. M., Ma, C.-J., Jauzac, M., Richard, J., Jullo, E., Sand, D. J., Edge, A. C., et al. 2009: *Hubble Space Telescope Observations of a Spectacular New Strong-Lensing Galaxy Cluster: MACS J1149.5+2223 at z = 0.544*, ApJ, 707, L163

Song, J., Mohr, J. J., Barkhouse, W. A., Warren, M. S., Dolag, K., & Rude, C. 2012: *A Parameterized Galaxy Catalog Simulator for Testing Cluster Finding, Mass Estimation, and Photometric Redshift Estimation in Optical and Near-infrared Surveys*, ApJ, 747, 58

Soucail, G., Fort, B., Mellier, Y., & Picat, J. P. 1987: *A blue ring-like structure, in the center of the A 370 cluster of galaxies*, A&A, 172, L14

Sparke, L. S. & Gallagher, III, J. S. 2000, Galaxies in the universe : an introduction, ed. Sparke, L. S. & Gallagher, J. S., III

Springel, V., Di Matteo, T., & Hernquist, L. 2005: *Black Holes in Galaxy Mergers: The Formation of Red Elliptical Galaxies*, ApJ, 620, L79

Suyu, S. H. & Halkola, A. 2010: *The halos of satellite galaxies: the companion of the massive elliptical lens SL2S J08544-0121*, A&A, 524, A94

Suyu, S. H., Hensel, S. W., McKean, J. P., Fassnacht, C. D., Treu, T., Halkola, A., Norbury, M., Jackson, N., Schneider, P., Thompson, D., Auger, M. W., et al. 2012: *Disentangling Baryons and Dark Matter in the Spiral Gravitational Lens B1933+503*, ApJ, 750, 10

Suyu, S. H., Marshall, P. J., Auger, M. W., Hilbert, S., Blandford, R. D., Koopmans, L. V. E., Fassnacht, C. D., & Treu, T. 2010a: *Dissecting the Gravitational lens B1608+656. II. Precision Measurements of the Hubble Constant, Spatial Curvature, and the Dark Energy Equation of State*, ApJ, 711, 201

Suyu, S. H., Marshall, P. J., Auger, M. W., Hilbert, S., Blandford, R. D., Koopmans, L. V. E., Fassnacht, C. D., & Treu, T. 2010b: *Dissecting the Gravitational lens B1608+656. II. Precision Measurements of the Hubble Constant, Spatial Curvature, and the Dark Energy Equation of State*, ApJ, 711, 201

Suyu, S. H., Marshall, P. J., Blandford, R. D., Fassnacht, C. D., Koopmans, L. V. E., McKean, J. P., & Treu, T. 2009: *Dissecting the Gravitational Lens B1608+656. I. Lens Potential Reconstruction*, ApJ, 691, 277

Suyu, S. H., Marshall, P. J., Hobson, M. P., & Blandford, R. D. 2006: *A Bayesian analysis of regularized source inversions in gravitational lensing*, MNRAS, 371, 983

Swinbank, A. M., Bower, R. G., Smith, G. P., Wilman, R. J., Smail, I., Ellis, R. S., Morris, S. L., & Kneib, J.-P. 2007: *Resolved spectroscopy of a gravitationally lensed L* Lyman-break galaxy at z ~ 5*, MNRAS, 376, 479

Sykes, C. M., Browne, I. W. A., Jackson, N. J., Marlow, D. R., Nair, S., Wilkinson, P. N., Blandford, R. D., Cohen, J., Fassnacht, C. D., Hogg, D., Pearson, T. J., et al. 1998: *The complex gravitational lens system B1933+503*, MNRAS, 301, 310

Temi, P., Brighenti, F., & Mathews, W. G. 2008: *The Mid-Infrared Spectral Energy Distribution, Surface Brightness, and Color Profiles in Elliptical Galaxies*, ApJ, 672, 244

Thomas, D., Maraston, C., Bender, R., & Mendes de Oliveira, C. 2005: *The Epochs of Early-Type Galaxy Formation as a Function of Environment*, ApJ, 621, 673

Thomas, J., Saglia, R. P., Bender, R., Thomas, D., Gebhardt, K., Magorrian, J., Corsini, E. M., & Wegner, G. 2007: *Dynamical modelling of luminous and dark matter in 17 Coma early-type galaxies*, MNRAS, 382, 657

Thomas, J., Saglia, R. P., Bender, R., Thomas, D., Gebhardt, K., Magorrian, J., Corsini, E. M., & Wegner, G. 2009: *Dark Matter Scaling Relations and the Assembly Epoch of Coma Early-Type Galaxies*, ApJ, 691, 770

Thomas, J., Saglia, R. P., Bender, R., Thomas, D., Gebhardt, K., Magorrian, J., Corsini, E. M., Wegner, G., & Seitz, S. 2011: *Dynamical masses of early-type galaxies: a comparison to lensing results and implications for the stellar initial mass function and the distribution of dark matter*, MNRAS, 415, 545

Tinsley, B., Larson, R., Gehret, D., & University, Y. 1977, The Evolution of galaxies and stellar populations: conference at Yale University, May 19-21, 1977 (Yale University Observatory)

Toomre, A. & Toomre, J. 1972: *Galactic Bridges and Tails*, ApJ, 178, 623

Treu, T., Koopmans, L. V., Bolton, A. S., Burles, S., & Moustakas, L. A. 2006: *The Sloan Lens ACS Survey. II. Stellar Populations and Internal Structure of Early-Type Lens Galaxies*, ApJ, 640, 662

Treu, T. & Koopmans, L. V. E. 2004: *Massive Dark Matter Halos and Evolution of Early-Type Galaxies to z ̃ 1*, ApJ, 611, 739

Umetsu, K., Medezinski, E., Nonino, M., Merten, J., Zitrin, A., Molino, A., Grillo, C., Carrasco, M., Donahue, M., Mahdavi, A., Coe, D., et al. 2012: *CLASH: Mass Distribution in and around MACS J1206.2-0847 from a Full Cluster Lensing Analysis*, ApJ, 755, 56

van Dokkum, P. G., Brammer, G., Fumagalli, M., Nelson, E., Franx, M., Rix, H.-W., Kriek, M., Skelton, R. E., Patel, S., Schmidt, K. B., Bezanson, R., et al. 2011: *First Results from the 3D-HST Survey: The Striking Diversity of Massive Galaxies at z 1*, ApJ, 743, L15

van Dokkum, P. G. & van der Marel, R. P. 2007: *The Star Formation Epoch of the Most Massive Early-Type Galaxies*, ApJ, 655, 30

Vegetti, S. & Koopmans, L. V. E. 2009: *Bayesian strong gravitational-lens modelling on adaptive grids: objective detection of mass substructure in Galaxies*, MNRAS, 392, 945

Ventimiglia, G., Arnaboldi, M., & Gerhard, O. 2011: *The unmixed kinematics and origins of diffuse stellar light in the core of the Hydra I cluster (Abell 1060)*, A&A, 528, A24

Walker, A. G. 1937: *On Milne's Theory of World-Structure*, Proceedings of the London Mathematical Society, s2-42, 90

Walsh, D., Carswell, R. F., & Weymann, R. J. 1979: *0957 + 561 A, B - Twin quasistellar objects or gravitational lens*, Nat, 279, 381

Wambsganss, J. 1998: *Gravitational Lensing in Astronomy*, Living Reviews in Relativity, 1

Warnick, K., Knebe, A., & Power, C. 2008: *The tidal streams of disrupting subhaloes in cosmological dark matter haloes*, MNRAS, 385, 1859

Warren, S. J. & Dye, S. 2003: *Semilinear Gravitational Lens Inversion*, ApJ, 590, 673

Wayth, R. B. & Webster, R. L. 2006: *LENSVIEW: software for modelling resolved gravitational lens images*, MNRAS, 372, 1187

Wegner, G. A., Corsini, E. M., Thomas, J., Saglia, R. P., Bender, R., & Pu, S. B. 2012: *Further Evidence for Large Central Mass-to-light Ratios in Early-type Galaxies: The Case of Ellipticals and Lenticulars in the A262 Cluster*, AJ, 144, 78

Weidinger, T. 2010, Diplomathesis, Universitaets-Sternwarte Muenchen (USM)

Weijmans, A.-M., Krajnović, D., van de Ven, G., Oosterloo, T. A., Morganti, R., & de Zeeuw, P. T. 2008: *The shape of the dark matter halo in the early-type galaxy NGC 2974*, MNRAS, 383, 1343

Weinberg, S. 2008, Cosmology, ed. Weinberg, S. (Oxford University Press)

White, S. D. M., Frenk, C. S., & Davis, M. 1983: *Clustering in a neutrino-dominated universe*, ApJ, 274, L1

White, S. D. M. & Rees, M. J. 1978: *Core condensation in heavy halos - A two-stage theory for galaxy formation and clustering*, MNRAS, 183, 341

Wilman, D. J. & Erwin, P. 2012: *The Relation between Galaxy Morphology and Environment in the Local Universe: An RC3-SDSS Picture*, ApJ, 746, 160

Wright, C. O. & Brainerd, T. G. 2000: *Gravitational Lensing by NFW Halos*, ApJ, 534, 34

Wuyts, S., Förster Schreiber, N. M., Genzel, R., Guo, Y., Barro, G., Bell, E. F., Dekel, A., Faber, S. M., Ferguson, H. C., Giavalisco, M., Grogin, N. A., et al. 2012: *Smooth(er) Stellar Mass Maps in CANDELS: Constraints on the Longevity of Clumps in High-redshift Star-forming Galaxies*, ApJ, 753, 114

Xanthopoulos, E., Browne, I. W. A., King, L. J., Koopmans, L. V. E., Jackson, N. J., Marlow, D. R., Patnaik, A. R., Porcas, R. W., & Wilkinson, P. N. 1998: *The new gravitational lens system B1030+074*, MNRAS, 300, 649

York, D. G., Adelman, J., Anderson, Jr., J. E., Anderson, S. F., Annis, J., Bahcall, N. A., Bakken, J. A., Barkhouser, R., Bastian, S., Berman, E., Boroski, W. N., et al. 2000: *The Sloan Digital Sky Survey: Technical Summary*, AJ, 120, 1579

York, T., Jackson, N., Browne, I. W. A., Koopmans, L. V. E., McKean, J. P., Norbury, M. A., Biggs, A. D., Blandford, R. D., de Bruyn, A. G., Fassnacht, C. D., Myers, S. T., et al. 2005: *CLASS B0631+519: last of the Cosmic Lens All-Sky Survey lenses*, MNRAS, 361, 259

Young, L. M., Bureau, M., Davis, T. A., Combes, F., McDermid, R. M., Alatalo, K., Blitz, L., Bois, M., Bournaud, F., Cappellari, M., Davies, R. L., et al. 2011: *The ATLAS^{3D} project - IV. The molecular gas content of early-type galaxies*, MNRAS, 414, 940

Zhang, Y.-Y., Finoguenov, A., Böhringer, H., Kneib, J.-P., Smith, G. P., Kneissl, R., Okabe, N., & Dahle, H. 2008: *LoCuSS: comparison of observed X-ray and lensing galaxy cluster scaling relations with simulations*, A&A, 482, 451

Ziegler, B. L. & Bender, R. 1997: *The Mg(b)-sigma relation of elliptical galaxies at Z of about 0.37*, MNRAS, 291, 527

Zitrin, A., Bartelmann, M., Umetsu, K., Oguri, M., & Broadhurst, T. 2012a: *Miscentring in Galaxy Clusters: Dark Matter to Brightest Cluster Galaxy Offsets in 10,000 SDSS Clusters*, ArXiv e-prints

Zitrin, A. & Broadhurst, T. 2009: *Discovery of the Largest Known Lensed Images Formed by a Critically Convergent Lensing Cluster*, ApJ, 703, L132

Zitrin, A., Broadhurst, T., Barkana, R., Rephaeli, Y., & Benítez, N. 2011: *Strong-lensing analysis of a complete sample of 12 MACS clusters at z 0.5: mass models and Einstein radii*, MNRAS, 410, 1939

Zitrin, A., Rosati, P., Nonino, M., Grillo, C., Postman, M., Coe, D., Seitz, S., Eichner, T., Broadhurst, T., Jouvel, S., Balestra, I., et al. 2012b: *CLASH: New Multiple Images Constraining the Inner Mass Profile of MACS J1206.2-0847*, ApJ, 749, 97

Zwicky, F. 1933: *Die Rotverschiebung von extragalaktischen Nebeln*, Helvetica Physica Acta, 6, 110

Zwicky, F. 1937a: *Nebulae as Gravitational Lenses*, Phys. Rev. Lett., 51, 290

Zwicky, F. 1937b: *On the Probability of Detecting Nebulae Which Act as Gravitational Lenses*, Phys. Rev. Lett., 51, 679

Acknowledgments

Although I have the honor to finally put all the results together and submit it as my thesis, it would have been totally impossible without big contributions by many other people. As a matter of fact, not a single page of this thesis would exist without the help and support of a lot of persons.

First I would like to thank Ralf Bender for making this thesis possible at all and being my supervising professor. I would like to thank dearly my thesis advisor Stella Seitz for all of her time, encouragement, guidance and availability throughout all that years. I also want to thank her for all the suggestions and discussions which not only laid the foundations for this thesis, but also greatly improved not only this work, but also my understanding of astrophysics. Without these two, this thesis would only be a mere dream instead of an almost completed piece of work.

I owe a huge thank to all of my closer or more distant collaborators on the various projects in the last years, especially Anne Bauer, Claudio Grillo, Aleksi Halkola, Sherry H. Suyu for all their support and the work they put into the projects. It was a great pleasure to work with so many interested, motivated and stimulating people in all that time.

One of the big cornerstones of this work are the former and current members of the Lensing group here at the USM: Matthias Bierschenk, Fabrice Brimiuolle, Yi-Hao Chen, Natascha Greisel, Daniel Grün, Mike Lerchster, Anna Monna, Patricia Spinelli, Carsten Strübig, Thomas Weidinger. I want to thank them not only for their countless hours of help and discussions, but also for their friendship.

I want to thank all the former and current people at the USM for the great atmosphere at this institute. I helped a lot to be in this environment all these years. In fact I cannot remember a single day I did not enjoy being here. Particularly, I'd like to thank all the people sharing an office with me throughout all the last years, it was great fun. Last but not least I want to say thanks for all the different activities I had the pleasure to take part in.

I want to thank everybody for their help with suggestions and proof reading of this thesis. Besides all the people that helped a lot on the manuscript but are already mentioned (to whom I'm as thankful), I want to thank Cornelius Kaschinski and Tomer Czaczkes for their short–notice proof reading.

To Steffi Simon, Nicole Frank and Ute Breithaupt: It was a delight to share a flat with you! Thanks for the food, the time, the wine and the parties.

Fortunately enough, after thanking so many people explicitly and implicitly already, there are many more left to whom I owe a big thank you. I want to thank my friends, also the ones that are not yet included at several other entries earlier already, for all the hours well–spent in their company and their support when needed. It was always a great joy.

At last, I would like to thank my family for all their support and understanding during the time this undertaking needed to get completed. Nothing of this would have been possible

without you.

Then there is one person left to thank here: Julia, I want to thank you wholeheartedly for your love and patience, for your faith in me and for all the encouragement. Without you, all the efforts would have been meaningless.

Curriculum Vitæ

Name:	Thomas Martin Eichner
Citizenship:	German
Date of birth:	23 January 1982
Place of birth:	Erding, Germany

Education

- **2007–date, Ph.D in Astrophysics**
  University Observatory Munich, Faculty of Physics, Ludwig-Maximilians-Universität (USM-LMU)
  Munich, Germany

- **2001–2007, Diplom in Physics**
  Faculty of Physics, Ludwig-Maximilians-Universität
  Munich, Germany

- **2001, Abitur**
  Gymnasium Dorfen
  Dorfen, Germany